ICMAB
INSTITUT DE CIÈNCIA DE MATERIALS DE BARCELONA
EXCELENCIA SEVERO OCHOA
CSIC
CONSEJO SUPERIOR DE INVESTIGACIONES CIENTÍFICAS

UAB
Universitat Autònoma de Barcelona
Facultat de Ciències
Departament de Física

Doctoral Thesis

Superconducting Coated Conductors for Proton Beam Screens in High-Energy Particle Accelerators

Author:
Artur ROMANOV

Supervisors:
Prof. Teresa PUIG,
Dr. Joffre GUTIERREZ,

A dissertation submitted in fulfillment of the requirements
for the degree of Doctor of Philosophy

in the

Superconducting Materials and Large Scale Nanostructures Department (SUMAN)
Institut de Ciència de Materials de Barcelona (ICMAB-CSIC)

Tutor: Prof. Carles Navau Ros

Doctorat en Física
Departament de Física - Facultat de Ciències
Universitat Autònoma de Barcelona

April 2022

Artur Romanov

ICMAB-CSIC

Campus de la UAB, Bellaterra, Barcelona

aaeromanov@gmail.com

April 2022

ICMAB
INSTITUT DE CIÈNCIA DE MATERIALS DE BARCELONA
EXCELENCIA SEVERO OCHOA
CSIC
CONSEJO SUPERIOR DE INVESTIGACIONES CIENTÍFICAS

UAB
Universitat Autònoma de Barcelona
Facultat de Ciències
Departament de Física

Memòria que porta per títol **"Superconducting REBCO Coated Conductors for Proton Beam Screens in High-Field Particle Accelerators "** i presentada per aspirar al Grau de Doctor en Física per **Artur Romanov**

Autor:

Artur Romanov, M. Sc.

amb el vist i plau de: **Prof. Teresa Puig Molina**, Professora d'investigació del Institut de Ciències de Materials de Barcelona (ICMAB-CSIC); **Dr. Joffre Guttiérez Royo**, Científic Titular del Institut de Ciències de Materials de Barcelona (ICMAB-CSIC) i **Prof. Carles Navau Ros**, Agregat del Departament de Física de la Universitat Autònoma de Barcelona (UAB).

I per a que així consti, signen el present certificat.

PUIG MOLINA M.TERESA - DNI 39174185X
Firmado digitalmente por PUIG MOLINA M.TERESA - DNI 39174185X
Fecha: 2022.04.14 12:40:29 +02'00'

Firmado por Joffre Gutierrez Royo el día 15/04/2022

CARLES NAVAU ROS - DNI 43719418Y
Firmado digitalmente por CARLES NAVAU ROS - DNI 43719418Y
Fecha: 2022.04.18 16:16:20 +02'00'

Directora:
Prof. Teresa Puig Molina

Director:
Dr. Joffre Guttiérez Royo

Tutor:
Prof. Carles Navau Ros

Bellaterra, abril de 2022

UNIVERSITAT AUTÒNOMA DE BARCELONA

Abstract

Department of Physics
Institut de Ciència de Materials de Barcelona (ICMAB-CSIC)

Doctor of Philosophy

Superconducting Coated Conductors for Proton Beam Screens in High-Energy Particle Accelerators

by Artur ROMANOV

In order to drive high-energy research beyond the lifetime of the Large Hadron Collider (LHC), the European Organization for Nuclear Research (CERN) kicked off an R&D initiative for a 100 TeV proton-proton collider with 100 km circumference, the so-called Future Circular Collider (FCC). Part of the FCC study is to rethink the design of the beam screen, an accelerator component that houses the particle beam and thermally shields the cold bores of the steering magnets from the synchrotron radiation. The concept of the LHC beam screen is based on a stainless steel tube coated in its interior with copper. However, in the foreseen operating conditions of the FCC, i.e. 40-60 K, 16 T and 0-1 GHz proton bunch frequency, the copper coating might not display a low enough surface impedance to guarantee a stable beam. The only known material class, which exhibits a lower surface resistance at given conditions, is formed by superconductors.

Since January 2017, the Superconducting Materials and Large Scale Nanostructures group at the Material Science Institute in Barcelona (ICMAB-CSIC) started a collaboration with CERN to evaluate the suitability and optimization of $REBa_2Cu_3O_{7-\delta}$ (RE = rare-earth) coated conductors (CCs), a structure consisting of a superconducting material layer on top of a flexible, metallic substrate, as a possible beam screen coating alternative to copper.

In the framework of this thesis, we characterized the electrical properties of several commercially available REBCO CCs with both direct and high-frequency current excitation in a wide cryogenic range and at large magnetic fields up to 9 T, where we employed a Hakki-Coleman type dielectric resonator with resonant frequency 8 GHz for surface impedance measurements. Complementary to this, we explored the compatibility of REBCO CCs with vacuum and field-quality requirements within the FCC beam screen and developed an attachment technique which enables the large-scale coating of curved, metallic surfaces, like the beam screen chamber, with REBCO CCs. Generated results not only demonstrate that commercially available REBCO CCs fulfill the promise of exceptionally good high-frequency properties at measurement conditions, but also propose practical solutions to issues which previously hindered the usage of REBCO in the beam screen chamber or other high-field microwave applications.

Acknowledgements

Some words have to be spent on friends who surrounded me during the doctorate. The first people I met upon my arrival in Barcelona, Laia, Julia, Ana, Vish, Alejandro, Ferran, Juan Carlos, Alex, Mathieu and Juri, could not have been more welcoming. In fact, Juri and Mathieu offered me shelter in the secretly best room of their flat. This time went down in history as the foundation of a brotherhood whose vows were spoken over plates of Borscht. Later, Laia invited me to live in her flat which became my home. Thank you, guys!
The following years were unforgettable thanks to the friends I made and moments we shared. Shout out to: My office mates Ziliang, Julia, Raul, Monica, Sumi, Juri, Neil and Mario, my lunch mates Juri, Mathieu, Lavi and Aish, my party mates Juri, Mathieu, Alejandro, Lavi, Tato, Pamela, Nico, Pedro and Francesco. Not to forget my flat mates, coffee mates, hiking mates, ping-pong mates, chess mates, climbing mates, surfing mates, skiing mates or regular mates. All of them left great memories in me behind and made the time at the ICMAB so enjoyable. Thank you!

To my friends in Germany: Eugen, Fabian, Arthur, Gina, Ella, Rosita, Stephi, Nadja, Iwan, Olga, Sergej, Andi, Rudi, Britta, Benjamin, Christina, Linda and Maria. Thank you for always welcoming me with open arms and giving a sweet addition to my life in Barcelona. Each of our meet-ups felt like a little reunion party and I am looking forward to celebrate much more of those with you.

Der Schlussdank geht an meine Familie. Oma Mina, vielen Dank für das Verwöhnen. Julia und Viktor, danke für das Wegweisen. Anastasia und Dimitri, danke für eure Verlässlichkeit. Michael, danke für deine Brüderlichkeit. Julian und Caroline danke für den gemeinsamen Spaß. An meine Eltern, Alexander und Elena, die letzten Jahre waren mir eine Freude und Ihr habt sie mir ermöglicht. Danke für euer Vertrauen, eure Unterstützung und eure bedingungslose Liebe.

Contents

List of Abbreviations

a-C	Amorphous carbon
APC	Artificial pinning center
CC	Coated Conductor
CERN	European Organization for Nuclear Research
DC	Direct current
DR	Dielectric resonator
DUT	Device under test
EB-PVD	Electron-beam physical vapor deposition
FC	Field cooling
FCC-hh	Future Circular Collider hadron-hadron
FEM	Finite element method
GR	Gittleman-Rosenblum
HTS	High-temperature superconductors
ICMAB-CSIC	Institute of Materials Science of Barcelona
IFAE	Institute for High Energy Physics of Barcelona
ISD	Inclined substrate deposition
LHC	Large Hadron Collider
LMO	$LaMnO_{3+\delta}$
LTS	Low-temperature superconductor
PLD	Pulsed laser deposition
PPMS	Physical Property Measurement System
RADES	Relic Axion Detector Exploratory Setup
RE	Rare earth
REBCO	$REBa_2Cu_3O_{7-\delta}$
RF	Radio frequency
SC	Superconductor
SEM	Scanning electron microscopy
SEY	Secondary electron yield
SQUID	Superconducting Quantum Interference Device
SR	Synchrotron radiation
SUMAN	Superconducting Materials and Large Scale Nanostructures group at ICMAB
UPC	Polytechnic University of Catalonia
VM	Vortex motion
VNA	Vector network analyzer
VSM	Vibrating Sample Magnetometer
YBCO	$YBa_2Cu_3O_{7-\delta}$
ZFC	Zero-field cooling

List of Journal Articles

Published journal articles:

1. T. Puig, P. Krkotić, <u>A. Romanov</u>, J. O'Callaghan, D. A. Zanin, H. Neupert, P. C. Pinto, P. Demolon, A. Granadeiro Costa, M. Taborelli, F. Perez, M. Pont, J. Gutierrez & S. Calatroni. "Coated conductor technology for the beamscreen chamber of future high energy circular colliders." *Superconductor Science and Technology* 32.9 (2019): 094006. DOI: https://doi.org/10.1088/1361-6668/ab2e66

2. FCC collaboration. "FCC Physics Opportunities: Future Circular Collider Conceptual Design Report Volume 1." *European Physical Journal C* 79.6 (2019):474. DOI: https://doi.org/10.1140/epjc/s10052-019-6904-3

3. FCC collaboration. "FCC-ee: The Lepton Collider: Future Circular Collider Conceptual Design Report Volume 2." *European Physical Journal: Special Topics* 228.2 (2019):261-623. DOI: https://doi.org/10.1140/epjst/e2019-900045-4

4. FCC collaboration. "FCC-hh: the Hadron collider: future circular collider conceptual design report volume 3." *European Physical Journal: Special Topics* 228.4 (2019):755-1107. DOI: https://doi.org/10.1140/epjst/e2019-900087-0

5. FCC collaboration. "HE-LHC: The High-Energy Large Hadron Collider: Future Circular Collider Conceptual Design Report Volume 4." *European Physical Journal: Special Topics* 228.5 (2019):1109-1382. DOI: https://doi.org/10.1140/epjst/e2019-900088-6

6. <u>A. Romanov</u>, P. Krkotić, G. Telles, J. O'Callaghan, T. Puig, M. Pont, F. Perez, X. Granados, S. Calatroni, T. Puig & J. Gutierrez. "High frequency response of thick REBCO coated conductors in the framework of the FCC study." *Scientific Reports* 10.1 (2020): 094006. DOI: https://doi.org/10.1038/s41598-020-69004-z

7. P. Krkotić, <u>A. Romanov</u>, N. Tagdulang, G. Telles, , T. Puig, J. Gutierrez, X. Granados, S. Calatroni, F. Perez, M. Pont & J. O'Callaghan. "Evaluation of the nonlinear surface resistance of REBCO coated conductors for their use in the FCC-hh beam screen." *Superconductor Science and Technology* 35.2 (2022): 025015. DOI: https://doi.org/10.1088/1361-6668/ac4465

To be submitted journal articles:

1. G. Telles, <u>A. Romanov</u>, S. Calatroni, X. Granados, T. Puig & J. Gutierrez. "Field quality and surface resistance studies of a superconducting $REBa_2Cu_3O_{7-x}$ - Cu hybrid coating for the FCC beam screen." To be submitted.

2. FCC consortium collaboration. "Novel high-temperature superconducting coatings for large scale microwave applications." To be submitted.

Chapter 1

Introduction

The Large Hadron Collider (LHC) represents today's biggest particle accelerator in the world with 27 km circumference and approximately 8 T dipole magnets that are required to steer charged particles on a circular track [1, 2]. This facility allows collisions with 13 TeV. Its most spectacular accomplishment was the discovery of the Higgs boson in 2012 [3]. Nicknamed by the physicist Leon Lederman as the god particle [4], it explains how matter receives its mass and was the last missing piece to complete the standard model of particle physics. A year after its announcement, the theoretical proposal for the Higgs boson, made Independently by François Englert and Peter W. Higgs in 1964, was awarded with the Nobel Prize in Physics [5]. Since 2018, the LHC undergoes a long beam shutdown during which the machine is technically enhanced. The so-called high-luminosity upgrade will increase the likelihood for rare events during collisions and improve the statistical confidence of already discovered phenomena [6]. However, entirely new physics are expected to be locked behind energy frontiers unattainable by state of the art particle accelerators. To this end, the European Organization for Nuclear Research (CERN) launched studies addressing the successor of the LHC [7]. Among all possible options for a next generation particle accelerator, the Future Circular Collider-hadron hadron (FCC-hh) asserted itself as the most likely project to be realized [8]. Historically, the particle physics community pushed both the limits of knowledge and technology likewise and opted to continue with its tradition by recommending the most ambitious future for particle accelerators at CERN. The FCC-hh will be a ring roughly four times longer (100 km) and subjected to up to two times larger magnetic fields (16 T) than the LHC [9]. A topographical scheme of the two particle accelerators is presented in Fig. 1.1. The increased magnitudes will allow eight times bigger collision
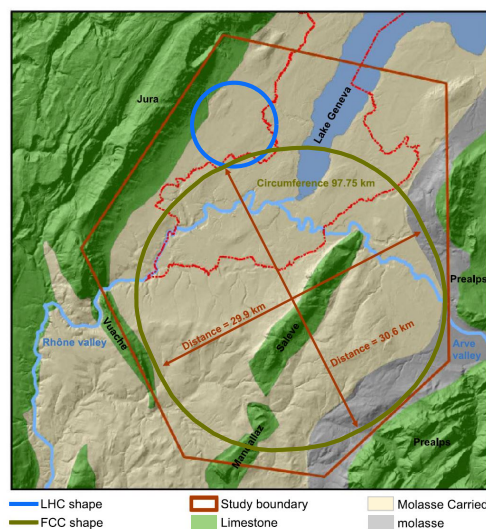
FIGURE 1.1: A map of the LHC trace, proposed FCC trace, local study boundaries and important geological factors. Adapted from [9] with kind permission of The European Physical Journal (EPJ).

energies of protons reaching 100 TeV. The unprecedented energy scale of the beam comes with repercussions. When steered by the magnets, charged particles will generate an immense amount of synchrotron light, 160 times higher than in the LHC, that requires a complete new design of the beam screen chamber [10].

The beam screen chamber is a stainless steel tube that houses the particle beam and thermally shields the superconducting magnets held at 1.9 K from synchrotron radiation. An illustration of the latest beam screen design is presented in Fig. 1.2. The close proximity to accelerated particles, in particular 10^{11} protons in 8 cm long bunches, gives rise
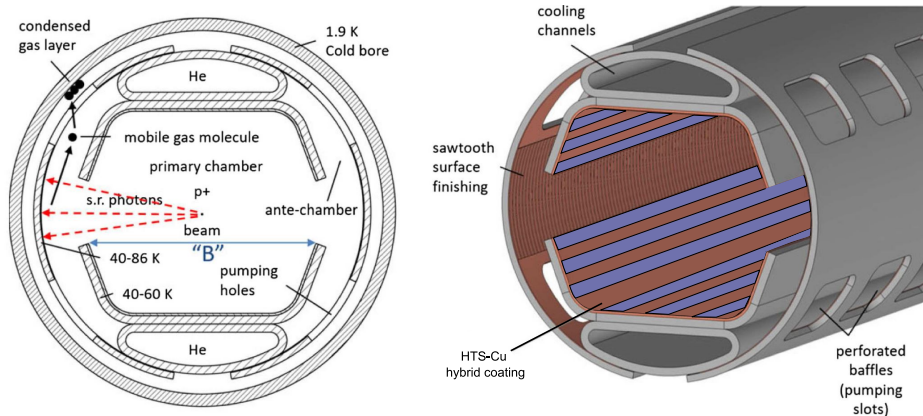
FIGURE 1.2: Latest beam screen chamber design. The HTS-Cu hybrid structure is a coating option that is going to be investigated in chapter 7 of this thesis. Adapted from [9] with kind permission of The European Physical Journal (EPJ).

to induced mirror charges in the metal oscillating with up to 1 GHz. The wake fields produced by the mirror charges interact electromagnetically with the protons and cause beam instabilities. In order to mitigate this effect, the chamber's interior is dressed with a highly conductive material. The beam coupling impedance, the quantity aimed for reduction, scales proportionally with the surface impedance of the beam facing material. Due to its high conductivity, abundance and proven use in electronics, copper is the coating of choice for the LHC. However, the increased magnitude of synchrotron radiation within the FCC demands an increase of operational temperature of the beam screen chamber in order to keep the refrigeration costs sustainable. The rise from 20 K in the LHC to prospected 40-60 K in the FCC-hh is considerable and renders the copper coating critically resistive. At this temperature, the surface impedance of copper might lie above the threshold that guarantees a stable beam operation [11]. The material class known to significantly undercut the surface impedance of copper is constituted by superconductors. In fact, the framework of operation, elevated temperatures and extremely large fields, narrows down suitable coating alternatives to high-temperature superconductors (HTS).

As part of the FCC study, CERN commissioned two investigations on potential HTS usage for the application. One explores the possibility of thallium-based superconductors as coating candidate [12, 13], the other the potential of $REBa_2Cu_3O_{7-\delta}$ (REBCO, with RE = rare earth)-based coated conductors (CCs) for the new beam screen chamber [14, 15]. The latter endeavour forms the heart of this PhD thesis and was conducted at the Institute of Materials Science of Barcelona (ICMAB-CSIC) within a consortium consisting of experts from ALBA Synchrotron, Polytechnic University of Catalonia (UPC), The Institute for High Energy Physics (Institut de Fisica d'Altes Energies, IFAE) of Barcelona and CERN. Second-generation high-temperature superconductor tapes, or simply coated conductors, is a laminar structure with a several tens of microns thick metallic base, followed by functional oxide buffer layers on top of which microns of bi-axially textured REBCO superconductor is grown. The HTS is terminated by Ag and when demanded with an additional Cu layer or jacket. In Fig. 1.3, a scheme of described CC is shown.

Stabilizing Cu (~20μm)

REBCO layer (1 - 3μm)

Buffer layers (0.2 - 1μm)

Protective Ag (~2μm)

Metallic substrate (40 - 100μm)
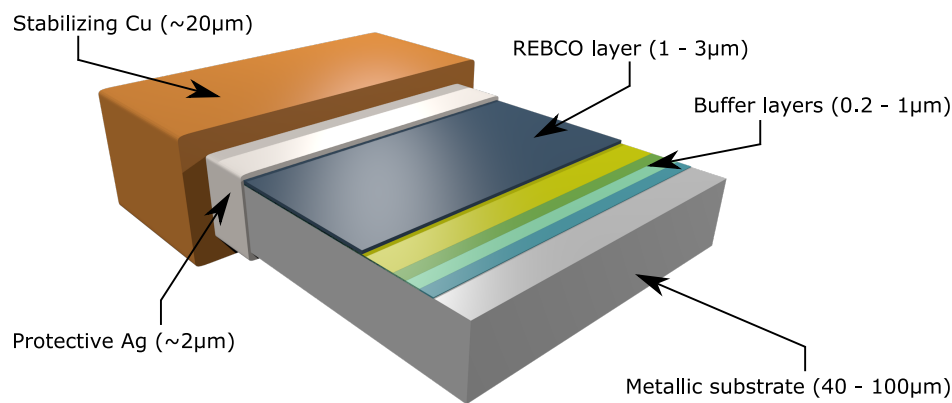
FIGURE 1.3: Schematic depiction of RE based HTS wire, known as coated conductor. The structure is demonstrated by jutting out the laminar layers, which are labeled and quantified in terms of their typical thickness.

The penetration into the market succeeded in areas where the extremely large current-carrying capacity of REBCO does not face any competition. Today, the largest volume of CCs finds its customer in high-field magnets [16], operated at low temperatures (below 10 K) and at magnetic fields above 10 T. However, applications like rotating machines, used at 20-40 K and above 1 T, power cables and fault current limiters, operation window spans 65-77 K and below 0.1 T, comprise commercial corner stones, too [17]. As a consequence, REBCO's superconducting properties have been studied in and optimized to these specific direct current regimes.

While superconductors are no newcomers to the field outside of direct current, most notably elemental niobium is used as coating for radio frequency (RF)-cavities [18], HTS pick up coils are employed to increase the signal-to-noise ratio for nuclear magnetic resonance [19] and HTS antennas are applied for low-noise and narrow-band receivers [20], the technological demand was mainly entrenched in high-frequency and zero applied field regimes. The advent of high-frequency, high magnetic field applications, like the beam screen chamber of the FCC-hh or haloscopes for the search of cold dark matter, at which the superconducting state of low-temperature superconductors (LTS) like Nb breaks down, brings HTS into new spotlight. Different from conventional superconductors, magnetic field can penetrate the HTS as quantized flux threads rendering the superconductor into the so-called mixed state. This phenomenon allows superconductivity to survive even strong magnetic fields. As a consequence, the interest to study the superconducting properties at high frequencies and high magnetic fields has reached new heights.

In this thesis, we characterize several commercially available REBCO CCs with respect to its compatibility with the beam screen chamber of the FCC-hh. One of the key figures in this study is the surface impedance of the coating material as it is directly related to the beam stability. Within our consortium, colleagues undertook the challenging task to design and build a device tailored to measure the macroscopic high-frequency response of highly conductive samples like copper or REBCO CCs at cryogenic temperatures and high magnetic fields. The result is a dielectric loaded resonator (DR) that can fit into a cryostat, surrounded by a 9 T-magnet, and allows replacement of its cavity endplates by roughly $12 \times 12 \, \text{mm}^2$ samples. Information about the material's surface impedance can be deduced from modifications to the quality factor and resonant frequency of the cavity, both measurands of the system. Since dimensions of the resonator are restricted by the bore diameter $\varnothing \approx 25 \, \text{mm}$ of available cryostat, the choice of dielectric is limited to rutile (TiO_2) because of its capability to focus the electromagnetic field within the cavity strong enough to discard contributions from the metallic enclosure. The geometry of the DR fixes the resonant frequency of characterizing TE_{011} mode to around 8 GHz, significantly above the 1 GHz excitation frequency in the FCC-hh. At the start of the thesis, only few experimental data on the surface resistance of commercial thick REBCO CCs was available in

literature and to our knowledge, no comparative study between various CCs at high magnetic fields. No data at all on the surface reactance of mentioned CCs could be found. Over the course of this work, we characterized REBCO tapes in terms of both surface resistance and surface reactance, the real and imaginary part of the surface impedance, at 8 GHz in a wide temperature range 10-70 K and up to 9 T where we compared it to copper. At 8 GHz, 50 K and 9 T, the closest FCC-hh conditions realizable with our setup, the surface resistance of best performing CCs undercuts copper by more than a factor of 4.5. Modelling suggest that the performance advantage tilts further into REBCO's favor at FCC conditions, where REBCO could outperform copper in terms of surface resistance by up to a factor of 70. Employment of impedance transformation allows us to estimate the contributions of the layers below REBCO to the overall measured surface impedance which amount only few percent at experimental conditions. In addition, by extracting and comparing high frequency vortex parameters of several REBCO films, we are able to suggest microstructural features beneficial for the operation at high frequencies and large magnetic fields, a regime to which, until recently, the CCs industry had no reason to adopt.

A major issue relates to the attachment of REBCO to the beam screen chamber. The coating of even curved RF cavities with elemental niobium works well using either Nb foil or by sputter deposition. In contrast, REBCO requires stringent controlled elemental stoichiometry, temperature and oxygen partial pressure during growth in addition to epitaxy, so a highly textured template, for highest performing properties to emerge. This fact makes it virtually impossible to grow epitaxial REBCO directly on curved cavities or other metallic chambers. Ahn et al. [21] demonstrated that gluing REBCO CCs to RF cavities yields high quality factors in the coated cavity and bypasses the problem of direct growth. We developed an alternative coating technique that is based on upside down soldering of Cu coated REBCO tapes to metallic walls and subsequent delamination of the substrate from the REBCO layer. This approach is advantageous in terms of exposed surface side as will be explained in the thesis and is proposed as a coating solution for the FCC-hh beam screen chamber.

More points on a checklist that a superconducting coating candidate has to fulfill like sustaining 25 A peak currents at extreme FCC-hh conditions, tolerance to synchrotron radiation or suppression of electron cloud generation are addressed and discussed in more detail in this work. Without further ado, the thesis is structured as follows

- **Chapter** 2 encompasses relevant fundamental concepts in pursuit of facilitating the reader the interpretation of generated results.

- **Chapter** 3 presents details about the experimental setups, applied data treatment and material processing. It includes a introduction to the high frequency characterization measurement system, part of which are the vector network analyzers, the dielectric loaded resonator and the PPMS, a short summary of the used magnetometers and reports about sample fabrication for and technicalities of direct current (DC) transport characterization.

- **Chapter** 4 introduces the architecture of analyzed CCs, explaining the purpose of each layer in the laminar structure. Special focus is put on growth characteristics that yield differences in microstructure. DC-transport and magnetization analysis reveal a wide range of superconducting properties among the REBCO films. We link them to corresponding microstructures and discuss whether magnitudes of DC-properties meet the threshold values imposed by the FCC-hh.

- **Chapter** 5 continues with analysis of high-frequency properties. The surface resistance of eight different CCs is compared with copper's as a function of magnetic field up to 9 T at 8 GHz, 50 K. In this regime, the most optimized superconductivity technology out-performs copper by a factor more than 2, proving its potential as a coating alternative. High-frequency pinning property extraction is performed in the realm of a mean-field model, the Gittleman-Rosenblum model, and demonstrates a large variety of magnitudes which is associated to differences in REBCO microstructure. A section is dedicated to the correct interpretation of surface reactance measurements of thick REBCO films with a DR. Understanding all possible contributions to the resonant

frequency and taking sample mounting precautions is key in order to generate reliable data. Finally, based on extrapolations, we discuss what high-frequency performance of CCs and copper to expect at FCC-hh conditions.

- **Chapter** 6 proposes a coating solution for the beam screen chamber. A sequence based on upside-down soldering copper covered CCs to a curved metallic wall and a subsequent exfoliation of the substrate from the REBCO layer has proven itself as practicable attachment technique. The exposed bottom side of the REBCO displays no significant ripping damage in the sample center but excellent pinning performance, even improved with respect to the usually characterized top surface. The role of residual buffer layers on delaminated bottom surfaces is analyzed in terms of its high-frequency response.

- **Chapter** 7 addresses a series of additional issues associated to the use of CCs in a high-energy particle accelerator beam screen chamber. Residing within the beam screen chamber, superconducting currents of REBCO can decrease the field homogeneity, an important factor endangering the beam stability. We demonstrate that converting CCs into hybrid coatings, consisting of alternating REBCO and Cu stripes, decreases the superconducting currents to acceptable values while maintaining low surface resistances. Second, the electron cloud generation is a common problem to occur within particle accelerators. In the past, strategies were developed to prevent this problem. In collaboration with CERN, we tested the compatibility of CCs with surface cleaning and thin layers of amorphous carbon, both cures for high secondary electron yields. Third, interactions between synchrotron radiation and the superconducting state is not well studied yet. After exposing CCs for several weeks to synchrotron light at ALBA synchrotron, the critical current density and critical temperature were compared with the initial state to estimate possible material degradation.

- **Chapter** 8 concludes the thesis with summarizing the results and bringing them into a bigger context.

Chapter 2

Theoretical background

In this chapter, the reader will be provided with a short introduction to the most meaningful phenomena related to superconductivity, a discussion on the structural properties of REBCO, the material under investigation, and brief treatise of high-frequency electrodynamics. These subjects combined are supposed to serve as a theoretical backbone to follow the interpretation of generated results.

2.1 Superconductivity and its milestone

In the following, a timeline is given that touches upon selected discoveries and theories related to superconductivity. Note that this overview has by no means the ambition to represent a complete history of superconductivity but is rather a vehicle to establish concepts, important for this thesis, in a quick way.

- **Discovery of superconductivity in 1911 [22]:** Three years after the successful He liquefaction, the dutch physicist Heike Kammerlingh Onnes made a striking observation. Unlike expected from ordinary metals whose electrical resistance decreases gradually when approaching absolute zero temperature, the resistance of mercury dropped abruptly to zero below a critical temperature T_c, a phenomenon unseen at this time. Anecdotally, this finding was so groundbreaking that Onnes and his team of researches considered a short-circuit to be the most plausible explanation. Luckily, experimental refinements led to a more interesting conclusion: mercury reached a new thermodynamic state characterized by zero electrical DC resistance which was later coined as the superconductive state.

- **Meissner Effect in 1933 [23, 24]:** 22 years after its discovery, Meissner and Ochsenfeld revolutionized the understanding of superconductivity. Having a zero DC resistance, superconductors have been regarded as perfect conductors. With Faraday's law $\oint \boldsymbol{E} \, d\boldsymbol{l} = -\frac{\partial \Phi}{\partial t}$, any loop consisting of perfect conductor prevents a change of magnetic flux lines. This argument can be extended to a bulk specimen of a perfect conductor. A bulk sample can be modulated as a infinite amount of conducting paths. Since the flux through each path is fixed, it follows that the rate of magnetic flux density within the bulk conductor is zero. Thus, exposing a superconductor in its normal state to a magnetic field and then cooling down below T_c results in a freezing of the magnetic field inside the superconductor assuming perfect conductor behavior. Meissner and Ochsenfeld demonstrated that this did not happen. Rather all the magnetic field gets expelled from the interior of a superconductor and allows penetration only in a narrow layer with thickness λ_L, later labeled as the London penetration depth, when chilled below T_c. So, in addition to zero DC resistance, superconductors are characterized by perfect diamagnetic behavior, the so-called Meissner effect. The existence of such reversible Meissner state implies that superconductivity will be destroyed beyond a critical field H_c, a field that carries the energy difference between the normal and superconducting state in zero field, known as the condensation energy of the superconducting state.

- **Two-fluid model in 1934 [25]:** Proposed by Gortor and Casimir, the two-fluid model succeeds in describing important concepts of superconductivity by replacing normal electrons as charge carriers with two fluids consisting of electron-like quasiparticles and a superfluid condensate of electrons. While not covering the entire microscopic picture, it can be used in combination with established models and equation to derive superconducivity phenomena in a descriptive way as done in section 2.5.2.

- **London theory in 1935 [26, 27]:** The brothers Fritz and Heinz London postulated two constitutive relations for superconductors that describe mathematically the influence of electric and magnetic fields on the supercurrent, contrasting Ohm's law for regular conductors. Even though these equations are based on physical intuition rather than a formal derivation from accepted laws, they entail both the perfect conductivity and Meissner effect in superconductors in a elegant and simple form. An unsound and not rigorous derivation of the London equations is given in section 2.5.2.

- **Ginzburg-Landau (GL) theory in 1950 [28]:** Bothered by the inability of the phenomenological London equations to determine the surface tension between normal and superconducting state or to describe the breakdown of superconductivity by a magnetic field or current, the soviet physicists Vitaly Ginzburg and Lev Landau put forward a complex pseudo wave function $|\psi|$ as an order parameter within Landau's theory of second-order phase transitions. This $|\psi|$ describes the local density of superconducting electrons according to $|\psi|^2 = n_s$, where n_s is the charge carrier density of superconducting electrons. Under inclusion of variation principles and series expansions, they could derive a Schrödinger-like equation for the order parameter and address the shortcomings they lamented. The GL theory introduces the temperature coherence length $\xi(T)$, the distance upon which the superconducting electron density decays at an interface of the superconducting and normal state. Far below T_c, $\xi(T) \approx \xi_0$, where ξ_0 is the temperature independent coherence length as introduced by Pippard [29]. The coherence length constitutes, together with the London penetration depth λ_L, the so-called GL parameter κ according to

$$\kappa = \frac{\lambda_L}{\xi}. \tag{2.1}$$

  The GL parameter κ varies rather slowly with temperature, in first approximation according to $(1 + (T/T_c)^2)^{-1}$ [30]. For classical elemental superconductors $\lambda_L \approx 50\,\text{nm}$ and $\xi \approx 300\,\text{nm}$, thus $\kappa \ll 1$, associated to a positive surface energy. The GL parameter helped, later in time, to formally distinguish two sorts of superconductors that differ in the magnitudes of κ, as described in section 2.2.

- **BCS theory in 1957 [31]:** John Bardeen, Leon Cooper and John Robert Schrieffer shaped the understanding of superconductivity with the first microscopic theory. The genius of their theory lies in the realization that two electrons with opposite momentum and spin interact attractively with each other, if the energy difference between the electronic states involved is smaller than the phonon energy $\hbar\omega$. In other words, in the superconducting state, electrons form pairs, coined as Cooper pairs, because the attractive force mediated by lattice vibrations dominates the repulsive Coulomb interaction. Cooper pairs behave as bosons and fall into a coherent ground state forming a Bose-Einstein condensate. Electrons in the Bose-Einstein condensate travel without scattering. Not only does the theory confirm that superconductivity is a second-order phase transition and the dependence of T_c on the isotopic mass (which is connected to lattice vibrations). It also predicts the minimum energy required to break a Cooper pair $E(T) = 2\Delta(T)$. This energy is related to the energy gap between the ground state and superconducting state Δ, whose existence was only assumed at that time.

- **Discovery of HTS in 1986 [32]:** Before 1986, many believed that superconductivity was restricted to metals and their alloys with limited T_c around 25 K. Hence, the discovery of superconductivity in a ceramic Ba-La-Cu-O system with T_c in the 30 K range by Goerg Bednorz[1] and Karl Müller caused another paradigm shift in the community. It prompted a rally in search for high-T_c superconductivity in a new material class, the so-called cuprates, and arguably culminated in the discovery of $YBa_2Cu_3O_{7-\delta}$ (YBCO)[2] [34] in 1987, whose critical temperature was measured to be $T_c = 93$ K, well above the boiling point of liquid nitrogen (77 K). The liquid nitrogen coolant is more abundant, easier to liquefy and store than helium which makes the maintenance of superconductivity in HTS like YBCO much cheaper. In contrast to metallic superconductors, HTS materials are usually layered, anisotropic and exhibit strongest superconductor behavior in preferred planes. Although they obey the same general phenomenology as classic superconductors, the microscopic mechanism mediating superconductivity at such high temperatures is still not understood.

2.2 Type-I and type-II superconductors

The GL theory with its general principles of second-order phase transitions allows an important distinction between two sorts of superconductors when exposed to critical magnetic fields. The key quantity here is the surface energy associated with the normal-state to superconducting-state interface. Per unit area of interface, the surface energy is $\gamma \propto H_c^2 \delta$, where H_c is the critical field that transforms the superconductor from the Meissner state into the normal state and the length $\delta \approx \xi - \lambda_L$ relates coherence length and penetration length to each other [30].

If δ and thus the surface energy is positive, then the superconductor maintains a stable equilibrium of macroscopic volumes of the two phases. Elemental metal superconductors like Hg or Nb exhibit exactly this behavior with $\xi > \lambda_L$ and are nowadays categorized as type-I superconductors or simply conventional superconductors. Ginzburg and Landau showed that the GL parameter $\kappa = \frac{\lambda_L}{\xi}$ can be used as an precise indicator for the sign of surface energy. At $\kappa = 1/\sqrt{2}$, a crossover from positive to negative surface energy occurs. By the time of their work, only type-I superconductors were studied and negative surface energies were just treated as a theoretical construct.

In 1957, Alexei Abrikosov philosophized about negative surface energies in real superconductors and came to the conclusion that the behavior of such superconductor in magnetic field must be significantly different [35]. To gain a more favourable energetic state, the interfaces between normal and superconducting state would start to multiply. This is what is found in type-II superconductors[3] where a new phase emerges beyond the Meissner state, the Shubnikov or mixed state, when magnetic fields exceed the lower critical field H_{c1}. The new phase favours the penetration of so-called vortices (or fluxons), quantized magnetic field tubes with flux $\Phi_0 = \frac{h}{2e} \approx 2.07 \times 10^{-15}$ Tm^2, whose core is in fist approximation normal conducting, of diameter $\varnothing = 2\xi$ and outlined by a circular supercurrent J_s. A schematic drawing of a vortex can be found in Fig. 2.1. Increase of applied magnetic field results in an increase of the flux density in the superconductor. When the upper critical field

$$H_{c2} = \frac{\Phi_0}{2\pi\xi^2} \tag{2.2}$$

---

[1]During a summer school (EASISchool 1) at the Technical University of Vienna in 2018 [33], I had the opportunity to meet Georg Bednorz in person and listen to a lecture entitled 'From low - to high T_c superconductors' given by him. Especially interesting was his story about how the discovery of HTS caused initial backlash from respectable experts in the field of superconductivity. The T_c in the investigated cuprate exceeds the maximum limit predicted by the BCS theory and was thus met with scepticism. Many thanks go out to the organizers of the event and Prof. Teresa Puig for proposing the school to me.

[2]YBCO is the most prominent candidate of the rare-earth based cuprates summarized as REBCO.

[3]The distinction between type-I and type-II superconductors was initiated by A. Abrikosov.
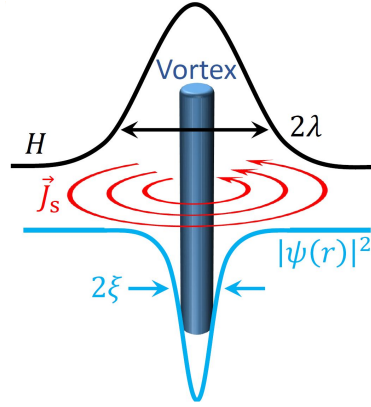
FIGURE 2.1: A drawn representation of a vortex. The order parameter $|\psi|^2$ drops to zero at the axis of the flux tube resulting in an approximated normal core radius of ξ. Suppercurents J_s shield the flux line from penetrating into the sample further than λ_L. Reprinted from [36] with permission.

is reached, the cortex cores overlap and the material is rendered through a second-order phase transition into the normal state. Since vortices penetrate type-II superconductors only partially, the diamagnetic energy cost of keeping the field out is small, so H_{c2} can be much greater than the thermodynamic H_c. This property has led to an expansion of superconductivity applications, one of which is the realization of high-field superconducting magnets [37]. Typical representatives of type-II superconductors are metallic alloys like NbTi or NbSn$_3$ and all HTS. In Fig. 2.2, we present phase diagrams of both types of superconductors.
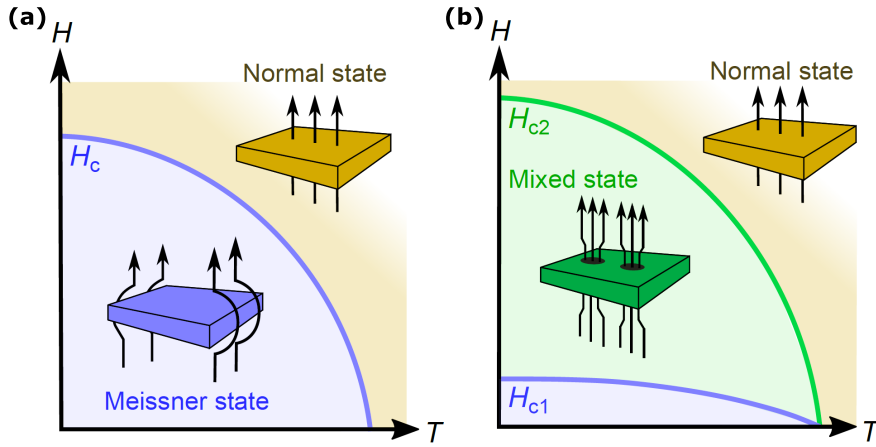
FIGURE 2.2: Magnetic phase diagram for type-I (a) and type-II (b) superconductors. Adapted from [36] with permission.

Essmann and Träuble found in 1967 [38] that the vorticies distribute themselves in a hexagonal lattice with density $n_v = \frac{\mu_0 H}{\Phi_0}$ when penetrating the type-II superconductor. The hexagonal side length a_Δ, see Fig. 2.3, relates to the applied magnetic field according to [39]

$$a_\Delta^2 = \frac{2}{\sqrt{3}} \frac{\Phi_0}{\mu_0 H}. \tag{2.3}$$

Note that a precise theoretical description of the hexagonal vortex lattice exists only for homogeneous materials, since the lattice exhibits usually distortions and defects.
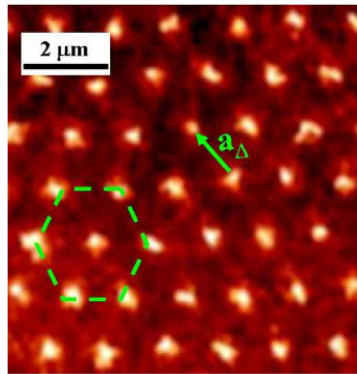
FIGURE 2.3: Magnetic bitter decoration of the vortex lattice in a YBCO single crystal sample. Adapted from [40] with permission.

2.3 Vortex matter

This section gives a very brief introduction into the behavior of vortices in type-II superconductors focusing on the HTS REBCO when exposed to a magnetic field and carrying a transport current. Presented discourse is based on introductory textbooks [30, 41, 42] and previous PhD theses of the SUMAN group at the ICMAB [36, 43, 44].

2.3.1 Vortex pinning

Type-II superconductors have huge potential for practical applications, such as the mentioned high magnetic field solenoids or energy storage devices among others, due to their high upper critical fields. However, the interplay between currents and flux lines in the mixed state results in a Lorentz-like force with form

$$\boldsymbol{F}_L = \boldsymbol{J} \times \boldsymbol{B}, \tag{2.4}$$

where $\boldsymbol{J}$ is the transport current density flowing through the superconductor. Drift of the vortices would generate an associated electric field and cause dissipation in the material, because of its normal core [39]. In this case, the superconductor would loose its desirable property of perfect conductivity. A strategy to counter this effect is to pin the vortices with inhomogeneities in the microstructure of the material and crystal defects. An important quantity that defines the applicability of a superconductor is the critical current density J_c. It is defined as the current density that causes a Lorentz-like force big enough to match the pinning force per unit volume applied by the defects on the flux lines $\boldsymbol{F}_p$ according to

$$\boldsymbol{F}_p = \boldsymbol{J}_c \times \boldsymbol{B}. \tag{2.5}$$

The structural inhomogeneities in the material give rise to a local reduction in the order parameter $|\psi|^2$. As a result, when a vortex docks on a pinning center, it can lower its free energy. The energy saved by a pinned vortex is known as the temperature and field dependent pinning energy $U_p \propto B_c^2 V_i$ [39], and it is proportional to the intersection volume V_i between the pinning center and the flux line. For pinning centers to be effective in HTS, their size should be on the scale of ξ. This kind of pinning coined core pinning.

In HTS like REBCO or other type-II superconductors (SC), defects can be desired for improvement of superconducting performance, however, they must not lead to grain discontinuity that decreases percolation currents. Since ξ in REBCO is of the order of a few nm, many structural and atomic defects occurring naturally in the growth process

qualify as pinning centers. The task to engineer predominantly pinning effective defects[4] while avoiding those that compromise current percolation and grain connectivity is a very challenging one and leads to a rich variety of REBCO microstructures optimized for specific applications as discussed in chapter 4. Defects are usually categorized according to their dimensionality and an overview of typical inhomogeneities is presented in Fig. 2.4 and discussed in detail in [45, 46].
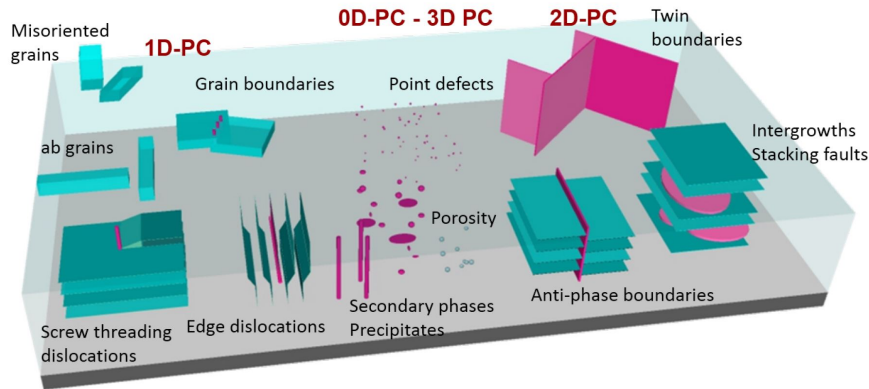
FIGURE 2.4: Schematic drawing of typical defects in the REBCO microstructure arranged according to their dimensionality. Defects acting as pinning centers (PC) are colored in pink. Adapted from [44] with permission.

Defects smaller than the coherence length ξ, for example, interstitials, impurity atoms or interchange of rare-earth and barium atoms, are of zero dimension (0D). Together with the 3D disturbances of order ξ, such as precipitates, nanoparticles and its associated strained regions or voids, 0D defects form the so-called isotropic defects since they contribute to pinning irrespective of the magnetic field direction. Isotropic imperfections are usually distributed randomly and thus are named uncorrelated. In contrast, anisotropic defects, also named correlated defects, are of 1D and 2D and give pinning a direction dependence. Dislocations and columnar defects are regarded as 1D irregularities, while defects such as small angle grain boundaries, anti-phase boundaries and surfaces of large precipitates have two dimensions.

It should be noted that not all defects are desirable. Large defects such as misoriented REBCO grains, coarsened secondary phases or porosity can decrease the superconducting cross section and reduce the current percolation. In a high performing REBCO film, these kind of microstructural features are avoided. We discuss the defect landscape of studied CCs in chapter 4.

2.3.2 Magnetic phase diagram

Depending on the microstructural disorder, temperature and magnetic field, HTS display different vortex liquid and solid phases when rendered into the mixed state, see Fig. 2.5. In single crystal samples, that are clean and virtually defect-free, a vortex lattice, also known as Abrikosov lattice, is observed at low temperatures. Samples full of uncorrelated point defects exhibit a vortex glass state which is reduced in its long-range translational and orientational symmetry. This state promotes line wandering. In contrast, correlated defects like columnar defects or twin boundaries put the vortices into a Bose glass state where vortices are rather localized. These three states are considered as solid phases and differ from each other in their degree of vortex-vortex and vortex-pin interaction. The former favours an ordered lattice state, while the latter a glass.

---

[4]The effectiveness of a defect for pinning is temperature and field dependent.
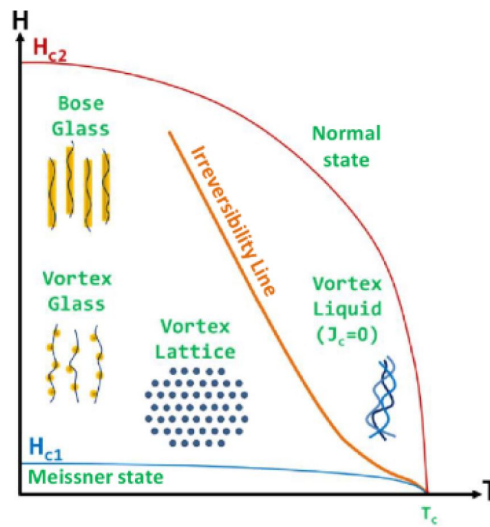
FIGURE 2.5: Qualitative magnetic phase diagram with some of the most important solid vortex phases separated by the irreversiblity line from the liquid vortex state. Adapted from [44] with permission.

At high temperatures, thermal energies start to overwhelm vortex-vortex and vortex-pin interactions and melt the vortex solid into a liquid phase. The phase transition is represented as a concave upwards line in the magnetic phase diagram, see Fig. 2.5. The line is denoted melting line if the specimen is a highly homogeneous and defect free crystal. In this case the transition is of first-order. For defect rich samples, like the CCs studied in this thesis, the transition is of second-order and phase separating line is called irreversibility line.

Beyond the irreversibility line, the material, though superconducting in the sense of non-zero order parameter, is found in a resistive state, corresponding to easy flux flow. In the flux-flow region, the pinning is so weak that the material is always close to the equilibrium flux distribution which allows a reversible vortex movement. Naturally, the technological applicability of type-II superconductors is limited by the irreversibility line. Successful strategies to shift the irreversibility line to higher temperatures involve the introduction of correlated defects into the microstructure [42].

2.3.3 Bean's critical state model

In the mixed state of a defect free type-II superconductor, magnetic vortices arrange themselves in a homogeneous hexagonal lattice minimizing the interaction between flux lines. The presence of microstructural defects, however, leads to flux pinning. These pinning centers oppose the free penetration and removal of vortices within the superconductor when exposed to a magnetic field. This results in flux density gradients and magnetic hysteresis. C. P. Bean proposed a macroscopic critical state model that explains the magnetic properties in the material [47].

In its simplest form, the model assumes the specimen to be a infinitely long slab with width w, where thermal forces are neglected and $B_{c1} = 0$ [48]. When considering a virgin slab (zero-field cooled), flux lines will start entering the specimen from its edges, moving to the center as we increase the magnetic field. Bean assumed the non-homogeneous flux distribution to be always in its critical state, i.e. the magnetic field gradient is maximum in all points within the sample, in the sense that the magnetic pressure exerted from the interaction between vortices matches exactly the pinning forces. This maximum field gradient causes the current density to be either critical $J = \pm J_c$ in vortex-populated regions or zero in the volume that vortices have not reached. Fig. 2.6 depicts an illustration of described field penetration for an applied field $H < B_s/\mu_0$, where B_s is characteristic full penetration field, i.e. the field strength at which the two critical states formed at the edges meet in the center.

Magnetization profiles generated in a zero-field cooled, infinitely long cylinder with radius $d/2$ are given for specific
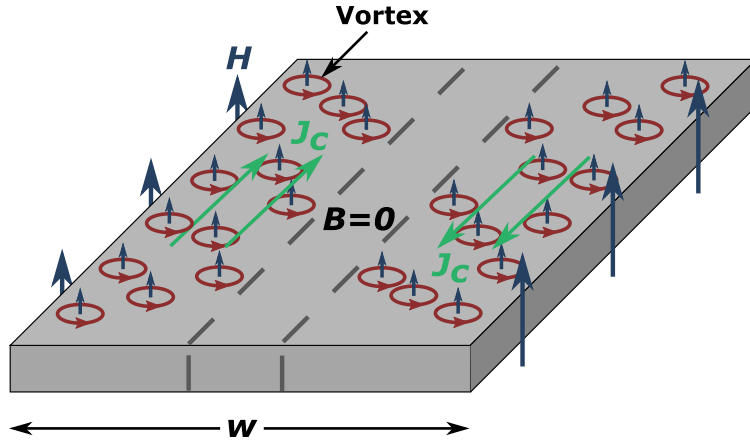
FIGURE 2.6: Introduction of vortices according to the critical state in an type-II superconductor in shape of a slab with width w and infinite length. The applied magnetic field is $H < B_s/\mu_0$. The critical current density J_c arises as an intrinsic property from the overlapping supercurrents of the non-homogeneous vortex distribution. Recreated from [49].

magnetic field values in Fig. 2.7 **(a)**.

The saturation magnetization $-M_{sat}$ of the sample is reached when the full penetration field $H_s = B_s/\mu_0$ is applied. Upon further increase of applied field, the total flux density in the specimen rises while maintaining at all time the maximum flux gradient. The slope of the magnetization gives the direction of J_c. A negative slope indicates a flow into the reading plane and vice versa. The inverse magnetization process is shown in Fig. 2.7 **(b)**. Beginning from $H = 2B_s/\mu_0$, the applied magnetic field is decreased. Flux lines will start leaving the superconductor by its edges, reversing the magnetic flux gradient and hence the current direction. When the applied field reaches zero, a significant amount of flux remains trapped in the superconductor. The flowing currents within the specimen cause the superconductor to be positively magnetized. The sample magnetization is fully saturated in the specific case of coming from fields $H \geq 2B_s/\mu_0$. So, as the external field is cycled, the magnetization $M - H$ curve becomes a hysteretic loop.
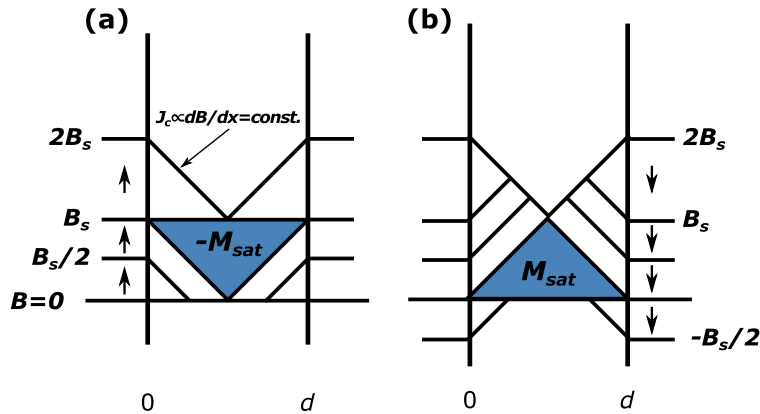
FIGURE 2.7: Internal magnetization profiles of an infinite cylindrical superconducting sample with radius $d/2$ subjected to an increasing **(a)** and decreasing **b()** magnetic field. $H = B_s/\mu_0$ is the maximum external field that can be screened out at the midplane of the superconductor and corresponds to saturated magnetization. Recreated from [48].

It can be shown that the critical current density for an infinite cylinder with the magnetic field applied perpendicular to the sample plane can be derived within the critical state model to be [41]

$$J_c = \frac{3\Delta M}{2R},$$

(2.6)

where R is the radius of the cylinder and ΔM corresponds to the hysteresis magnetization loop $M - H$ when it is saturated. In subsection 3.2.3, we will discuss the determination of J_c from a measured magnetization loop in a REBCO CC.

2.4 Crystal structure of REBCO

The "123" class cuprates $RE_1Ba_2Cu_3O_{7-\delta}$ (REBCO), where the RE stands for rare earth elements and can represent candidates like Y, La, Nd, Sm, Eu, Gd, Ho, Er and Lu, crystallize in a highly layered and anisotropic structure [30]. In particular, it is a triple perovskite-like structure[5] whose unit cell, as shown for YBCO in Fig. 2.8, can be imagined as a $YCuO_{3-1}$ perovskite-like sandwiched by two $BaCuO_{3-(0.5+\delta)}$ perovskite-likes while sharing the CuO_2 planes. Considering this, the amount of oxygen atoms in REBCO reduces from nine, as expected from three regular perovskites, to $7 - \delta$.
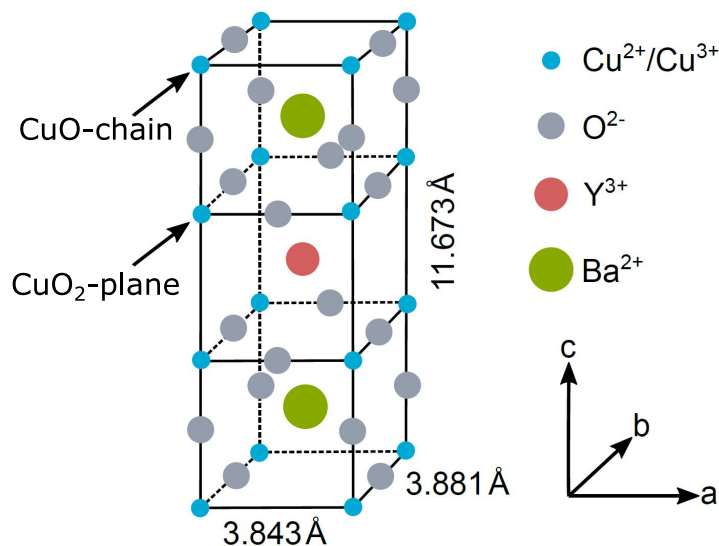
FIGURE 2.8: Orthorhombic $Y_1Ba_2Cu_3O_{7-\delta}$ unit cell. The stacking of planes in the c-direction starting from the lowest is as follows: $CuO_{1-\delta}$, BaO, CuO_2, Y, CuO_2, BaO, $CuO_{1-\delta}$. Adapted from [36] with permission.

The BaO planes separate the CuO_2-planes from the $CuO_{1-\delta}$ layers, that is responsible for the oxygen deficiency δ in REBCO. The average occupancy of the oxygen sites in the $CuO_{1-\delta}$ plane ranges from 0 ($\delta = 1$) to 1 ($\delta = 0$) which corresponds to a fully depleted and loaded state, respectively. The oxygen depletion level δ determines the crystal structure of REBCO [50]. If δ is greater than 0.65, the few oxygen atoms distribute themselves randomly in the $CuO_{1-\delta}$ plane resulting in a tetragonal symmetry with equal lattice parameters $a = b$. This state presents an insulating behavior in an antiferromagnetic phase [51]. For $\delta \leq 0.65$, there are enough oxygen atoms to form chains with the copper along the b-axis upon which a transition to orthorhombic structure with $a < b$ occurs, which corresponds to a metallic-superconductor state. Within the orthorhombic crystal structure, the oxygen content represented by δ has profound impact on the critical temperature of the film, due to its link to the carrier concentration as shown for YBCO in Fig. 2.9.

The strong sensitivity to carrier doping and the fact that cuprates like REBCO are only superconducting in a limited range of δ is stated as one of the main reasons for discovering high temperature superconductors with such an delay

---

[5]A perovskite structure is adopted by many oxides with the chemical formula ABO_3, where A and B are cations of different sizes and O stands for oxygen.
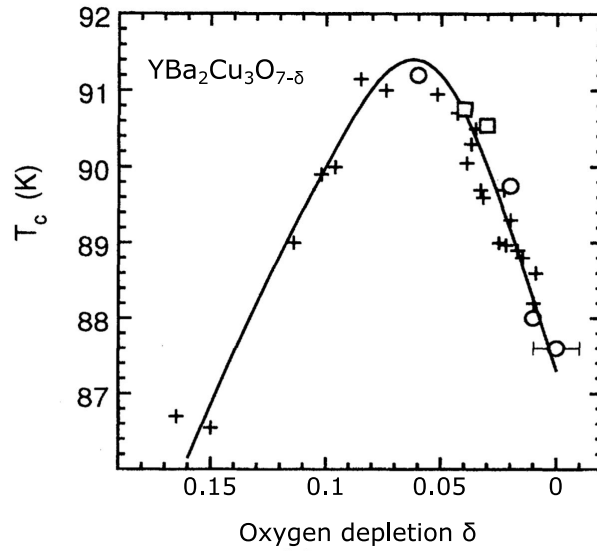
FIGURE 2.9: The variation of critical temperature T_c with the oxygen content for YBCO. Adapted from
[52] with permission.

with respect to the initial finding of superconductivity [41]. Electronic features resulting from the layered triple perovskite structure in REBCO are listed in the following.

- The charge transport takes place in the CuO_2 plane lying normal to the c-axis. Due to the sharp localization of the carriers within the planes, REBCO, and cuprates in general, display extremely anisotropic properties with poor conductivity in the c-direction. An important contributor to the electronic transport, as expected from the strong influence of δ, are the b-axis directed CuO chains. They contain free charge carriers from hole doping which are coupled through a charge transfer mechanism to the CuO_2 planes. The quasi-2D nature of REBCO requires a biaxial epitaxial growth with minimal grain misalignment to reach the best possible superconducting properties.

- Compared with a regular metals, the charge carrier density in REBCO is relatively low. The less heavy screening, causes a large London penetration depth $\lambda_L^{ab}(0\,K) = 150\,nm$ [53] for current flow within the $a - b$ plane and even a larger in c-direction $\lambda_L^c(0\,K) = 890\,nm$ [41].

- REBCO like all cuprates exhibit extremely short coherence lengths $\xi^{ab} = 2\,nm$ and $\xi^c = 0.3\,nm$ [41]. On the one hand, it makes thermal fluctuations quite strong and on the other hand, it gives nanometric defects like impurity concentrations, grain boundaries or artificially added nanoparticles importance, as they can contribute to vortex pinning. The extreme mismatch with the penetration depth causes the GL parameter to be $\kappa > 50$ making REBCO an extreme type-II superconductor.

2.5 High-frequency electrodynamics

This section aims to provide general knowledge on how materials, here restricted to conductors and superconductors, respond to an non-static electromagnetic field on a macroscopic scale. From fundamental concepts, we will derive explicit expressions for parameters that describe the interaction involved, namely the skin depth and surface impedance of a conductor. Presented deductions are based on [30, 54–56].

2.5.1 Conductors

Starting point is an electromagnetic plane wave propagating through vacuum that impinges perpendicularly the surface of a conductor with infinite expansion into a half space. A sketch of outlined situation with a reference coordinate system is given in Fig. 2.10. Maxwell's equations describe the interaction of conductor and electromagnetic field
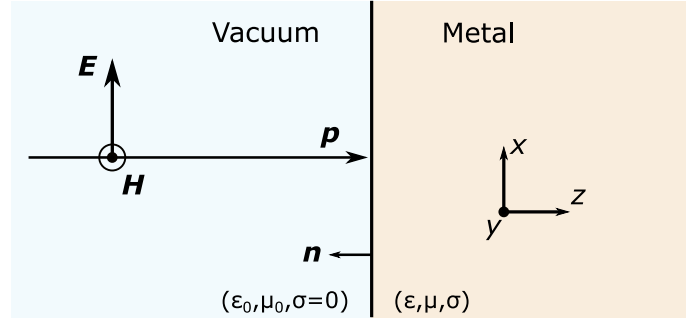
FIGURE 2.10: A plane wave with electric field strength vector E and magnetic field strength vector H impinging the surface of a conductor with normal vector n. The wave propagation vector is named p. Recreated from [55].

$$\nabla \cdot \boldsymbol{D} = \rho_c \tag{2.7}$$

$$\nabla \cdot \boldsymbol{B} = 0 \tag{2.8}$$

$$\nabla \times \boldsymbol{E} = -\frac{\partial \boldsymbol{B}}{\partial t} = -i\omega\mu\boldsymbol{H} \tag{2.9}$$

$$\nabla \times \boldsymbol{H} = \frac{\partial \boldsymbol{D}}{\partial t} + \boldsymbol{J} = i\omega\varepsilon\boldsymbol{E} + \sigma\boldsymbol{E} = (i\omega\varepsilon + \sigma)\boldsymbol{E}, \tag{2.10}$$

where $\boldsymbol{H} = \boldsymbol{H}_0 e^{i\omega t}$ is the magnetic field strength vector, $\boldsymbol{E} = \boldsymbol{E}_0 e^{i\omega t}$ the electric field strength vector with sinusoidal time dependencies, $\boldsymbol{B}$ the magnetic flux density vector, $\boldsymbol{D}$ the electric displacement vector and ρ_c the charge carrier density. In the following, a source-free conductor is assumed, so that the charge carrier density $\rho_c = 0$. The constitutive relations

$$\boldsymbol{D} = \varepsilon\boldsymbol{E} \tag{2.11}$$

$$\boldsymbol{B} = \mu\boldsymbol{H} \tag{2.12}$$

$$\boldsymbol{J} = \sigma\boldsymbol{E} \tag{2.13}$$

indicate that the response of an electromagnetic material to an electromagnetic field can be described by three constitutive parameters, namely the complex permittivity $\varepsilon = \varepsilon' - i\varepsilon''$, the complex permeability $\mu = \mu' - i\mu''$ and the conductivity of the material σ. They also give the distance to which the electromagnetic field penetrates into the conductor as we will see later. By applying the curl operator to eq. (2.9) and eq. (2.10), exploiting the vector calculus identity $\nabla \times (\nabla \times \boldsymbol{A}) = \nabla(\nabla \cdot \boldsymbol{A}) - \nabla^2\boldsymbol{A}$ and under consideration of eqs. (2.7) and (2.8), we obtain

$$\nabla^2\boldsymbol{E} = i\omega\mu(i\omega\varepsilon + \sigma)\boldsymbol{E} \tag{2.14}$$

$$\nabla^2\boldsymbol{H} = i\omega\mu(i\omega\varepsilon + \sigma)\boldsymbol{H}. \tag{2.15}$$

In the context of the thesis, we deal with highly conductive materials for which $\sigma \gg \omega\varepsilon$, meaning that the conductive current is much bigger than the displacement current, so that eqs. (2.14) and (2.15) are simplified to

$$\nabla^2 \boldsymbol{E} = i\omega\mu\sigma\boldsymbol{E} \tag{2.16}$$

$$\nabla^2 \boldsymbol{H} = i\omega\mu\sigma\boldsymbol{H}. \tag{2.17}$$

As defined in Fig. 2.10, the traveling wave is characterized by electric and magnetic field being perpendicular to each other and its direction of propagation. Setting arbitrarily $t = 0$, fixing the propagation into the z-directions and $\mathbf{E} = (E_x\mathbf{e}_x, 0, 0)$, we can rewrite previous expressions to

$$\frac{\partial^2 E_x}{\partial z^2} = i\omega\mu\sigma E_x \tag{2.18}$$

$$\frac{\partial^2 H_y}{\partial z^2} = i\omega\mu\sigma H_y. \tag{2.19}$$

A solution to these equations has the form

$$E_x = E_0 e^{-\gamma z}, \tag{2.20}$$

where the time dependence is $e^{i\omega t}$ but has been dropped here for simplification, E_0 is the electric field strength at the surface of the conductor, so at $z = 0$, and γ is the complex propagation constant

$$\gamma = \alpha + i\beta = \sqrt{i\omega\mu\sigma} = (1+i)\sqrt{\frac{\omega\mu\sigma}{2}}. \tag{2.21}$$

The real part α is denoted as the attenuation constant, the imaginary part β as the phase constant. The so-called skin depth δ_s is defined as

$$\delta_s = \frac{1}{\alpha} = \sqrt{\frac{2}{\omega\mu\sigma}} \tag{2.22}$$

and describes the distance the electromagnetic field travels into a highly conductive material before it decays by factor e^{-1}. At microwave frequencies, the order of the skin depth for metals is 10^{-7} m. Plugging eqs. (2.21) and (2.22) into the solution of the electric field intensity (2.20) and its magnetic field intensity counterpart, we get

$$E_x = E_0 e^{-\frac{1+i}{\delta_s}z} \tag{2.23}$$

$$H_y = H_0 e^{-\frac{1+i}{\delta_s}z}. \tag{2.24}$$

With this, we can express eq. (2.9) as

$$\frac{\partial E_x}{\partial z} = -i\omega\mu H_y \Rightarrow H_y = \frac{i}{\omega\mu}\frac{\partial E_x}{\partial z} = \frac{i}{\omega\mu}\left(-\frac{(1+i)}{\delta_s}\right)E_0 e^{-\frac{1+i}{\delta_s}z} = \frac{(1-i)}{\omega\mu\delta}E_0 e^{-\frac{1+i}{\delta_s}z}. \tag{2.25}$$

With the definition of the skin depth, we can write $\omega = \frac{2}{\mu\sigma\delta_s^2}$ and insert it into above relation to get

$$H_y = \frac{(1-i)\delta_s\sigma}{2}E_0 e^{-\frac{1+i}{\delta_s}z}. \tag{2.26}$$

The presented derivation allows us to give an explicit expression for the in general defined surface impedance $Z_s = R_s + iX_s = \frac{E_\parallel}{H_\parallel}$, where the real part of the surface impedance is denoted surface resistance R_s, the imaginary part is named surface reactance X_s and $E_\parallel$ and $H_\parallel$ are the electric field intensity and magnetic field intensity components

tangential to the surface of the conductor, as:

$$Z_s = \frac{E_\parallel}{H_\parallel} = \frac{E_x}{H_y} = \frac{E_0 e^{-\frac{1+i}{\delta_s} z}}{\frac{(1-i)\delta_s \sigma}{2} E_0 e^{-\frac{1+i}{\delta_s} z}} = \frac{2}{(1-i)\delta_s \sigma} = \frac{(1+i)}{\sigma \delta_s} = \sqrt{i\omega\mu\rho}, \tag{2.27}$$

with $\sigma = \frac{1}{\rho}$ and ρ the electrical resistivity of the conductor. For normal conductors, the conductivity σ is a real number and the surface resistance R_s and surface reactance X_s have the same magnitude $R_s = X_s = \sqrt{\frac{\mu\omega}{2\sigma}}$, see eq. (2.27), that scale with $\omega^{1/2}$.

2.5.2 Superconductors

In order to derive fundamental expressions and ideas describing superconductors, the two-fluid model is introduced in the paragraph **Two-fluid model**. With the aid of mentioned model and previous derivations for conductors, we will be able to describe the interaction of electromagnetic fields with superconductors as shown in paragraph **Surface impedance without applied magnetic field**. Following examinations are based on [30, 54, 57, 58].

Two-fluid model

In contrast to normal metals in which current is carried by electrons, it is assumed that there are two types of fluids involved in the charge transport of a superconductor: normal electrons, also known as quasiparticles, corresponding to a carrier density n_n and electron pairs, also known as Cooper-pairs or superconducting carriers, with carrier density n_s whose coupling is mediated by lattice vibrations that allows scattering-free travel. The total carrier density is defined as $n = n_s + n_n$ and displays an increasing pair electrons to normal electrons fraction with decreasing temperature according to [59]

$$n_s = n \cdot \left(1 - \left(\frac{T}{T_c}\right)^4\right) \tag{2.28}$$

$$n_n = n \cdot \left(\frac{T}{T_c}\right)^4. \tag{2.29}$$

Note that the electron pair density n_s approaches zero at the transition temperature T_c.

It is worthwhile to consider the equations of motion for the two charge carrier densities under the influence of an applied electric field $\boldsymbol{E}$. The force acting on an electron pair is given by

$$2m\frac{d\boldsymbol{v}_s}{dt} = -2e\boldsymbol{E} \tag{2.30}$$

with m being the electron mass, $\mathbf{v}_s$ the velocity of the paired electrons and e the electron charge. An additional force from the scattering with the atom cores acts on the normal electrons so that we have

$$m\frac{d\boldsymbol{v}_n}{dt} + m\frac{\boldsymbol{v}_n}{\tau} = -e\boldsymbol{E}, \tag{2.31}$$

where $\mathbf{v}_n$ is the electron velocity and τ the momentum relaxation time describing the magnitude of losses. The current densities of electron pairs and normal electrons can be written respectively as

$$\mathbf{J}_s = -n_s e \mathbf{v}_s \tag{2.32}$$

$$\mathbf{J}_n = -n_s e \mathbf{v}_n. \tag{2.33}$$

Further algebraic manipulations allows non-rigorous deduction of meaningful concepts. Let us consider that the unpaired electron density n_n is negligibly small, a reasonable assumption at low temperatures. In this case, it is sufficient to consider only eq. (2.30) and inserting eq. (2.32) into it yields the first London equation [26]:

$$\Lambda \frac{\partial \mathbf{J}_s}{\partial t} = \mathbf{E} \tag{2.34}$$

with $\Lambda = \frac{m}{n_s e^2}$. This equation postulates the relaxation time τ for electron pairs to be infinite, so no scattering between charge carrier and defects take place. It successfully describes the transport process in a superconductor in a phenomenological way. Taking now the curl of eq. (2.34) and considering Faraday's law $\nabla \times \mathbf{E} = -\frac{\partial \mathbf{B}}{\partial t}$ yields

$$\Lambda \frac{\partial}{\partial t} (\nabla \times \mathbf{J}_s) = -\frac{\partial \mathbf{B}}{\partial t}. \tag{2.35}$$

Integrating with respect to time and setting the integration constant to zero[6] gives the second London equation

$$\Lambda \nabla \times \mathbf{J}_s = -\mathbf{B}. \tag{2.36}$$

Applying a curl to eq. (2.36) and exploiting Ampere's law $\nabla B = \mu_0 \mathbf{J}$ gives an useful representation of the second London equation according to

$$\nabla^2 \mathbf{B} = \frac{1}{\lambda_L^2} \mathbf{B}, \tag{2.37}$$

where $\lambda_L = \sqrt{\frac{m}{\mu_0 n_s e^2}}$ is the so-called London penetration depth. Eq. (2.37) implies that the magnetic field is screened exponentially from the interior of the superconductor with λ_L, which describes the Meissner effect. Inserting the temperature dependence of n_s (see eq. 2.28) into λ_L reveals the corresponding temperature response as

$$\lambda_L = \lambda_L(0) \left[1 - \left(\frac{T}{T_c} \right)^4 \right]^{-1/2}. \tag{2.38}$$

The penetration depth has a minimum $\lambda_L(0)$ at 0 K and amounts for YBCO around 150 nm [53].

Let us now assume the normal carrier density to be relevant and time dependent electromagnetic fields varying in sinusoidal manner. This gives

$$\mathbf{J}_s = \mathbf{J}_{s,0} e^{i\omega t}, \quad \mathbf{J}_n = \mathbf{J}_{n,0} e^{i\omega t}, \quad \mathbf{E} = \mathbf{E} e^{i\omega t}. \tag{2.39}$$

Substituting eqs. (2.32) and (2.33) into the corresponding equations of motions (2.30) and (2.31) while considering the new time dependencies yield explicit expressions for the current densities. Summing them up yields the total current density as

$$\mathbf{J}_0 = \mathbf{J}_{n,0} + \mathbf{J}_{s,0} = \left[\frac{n_n e^2 \tau}{m(1 + \omega^2 \tau^2)} - i \left(\frac{n_s e^2}{\omega m} + \frac{n_n e^2 \tau^2 \omega}{m(1 + \omega^2 \tau^2)} \right) \right] \mathbf{E}_0. \tag{2.40}$$

---

[6]Main reasoning comes from the fact that the second London equation does require a constant to describe experimental results.

With this expression, we can introduce the complex two-fluid conductivity σ_{2f} according to

$$\boldsymbol{J}_0 = \sigma_{2f}\boldsymbol{E}_0 = (\sigma_1 - i\sigma_2)\boldsymbol{E}_0, \tag{2.41}$$

where

$$\sigma_1 = \frac{n_n e^2 \tau}{m(1 + \omega^2 \tau^2)} \quad \text{and} \quad \sigma_2 = \frac{n_s e^2}{\omega m} + \frac{n_n e^2 \tau^2 \omega}{m(1 + \omega^2 \tau^2)}. \tag{2.42}$$

Figure 2.11 shows the electrical circuit analogue to the current flow within a superconductor. It can be represented as a parallel connection consisting of a parallel resistor R_n and inductor L_n, which corresponds to the normal fluid, and a pure lossless inductor L_s, which corresponds to the superfluid channel. At zero frequency all of the current flows trough the inductors and there is no Ohmic loss, known as the most famous property of a superconductor. At non-zero frequencies the inductive part of the circuit becomes highly reactive and current is shunted into the resistive channel. This explains phenomenologically why a superconductor is not lossless outside of the DC-regime. More accurate methods based on BCS theory exist in order to derive the complex conductivity, that take fundamental material parameters into account and can be found in the following reference [30, 41, 60] but are outside of this thesis' scope.
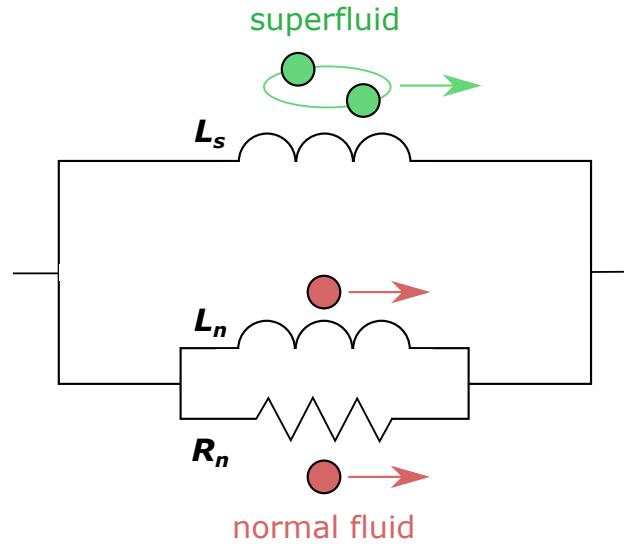
FIGURE 2.11: Electrical circuit analogue that describes the current flow in superconductors by means of the two-fluid model. Figure recreated from [58].

Surface impedance without applied magnetic field

Having understood the concept of two-fluid conductivity, it is worthwhile to return to the solution of the wave equations (2.18) and (2.19) as derived in subsection 2.5.1:

$$E_x = E_0 e^{-\gamma z} \tag{2.43}$$

$$H_y = H_0 e^{-\gamma z}, \tag{2.44}$$

with propagation coefficient $\gamma = \alpha + i\beta = \sqrt{i\omega\mu\sigma}$. Substituting the complex conductivity σ_{2f} (see eq. (2.41)) into the propagation coefficient, yields

$$\gamma = \sqrt{i\omega\mu\sigma_{2f}} = \sqrt{i\omega\mu(\sigma_1 - i\sigma_2)}. \tag{2.45}$$

This can be written as

$$\gamma = \sqrt{i\omega\mu(-i\sigma_2)(\frac{\sigma_1}{-i\sigma_2}+1)} = \sqrt{\omega\mu\sigma_2}\sqrt{1+i\frac{\sigma_1}{\sigma_2}}. \tag{2.46}$$

For temperatures well below the transition temperature, the supercurrent dominates the normal charge carriers so that $\sigma_2 \gg \sigma_1$. Executing a Taylor expansion on the second term in eq. (2.46) around $\frac{\sigma_1}{\sigma_2} = 0$ allows to separate the real and imaginary part of the propagation coefficient according to

$$\gamma = \alpha + i\beta = \sqrt{\omega\mu\sigma_2}\left(1+i\frac{\sigma_1}{2\sigma_2}\right). \tag{2.47}$$

Similar to the skin depth δ_s for conductors, the inverse of γ's real part gives the characteristic depth at which a impinging electromagnetic wave exponentially decays by a factor e^{-1}. It is called the London penetration depth λ_L and is given by

$$\lambda_L = \frac{1}{\alpha} = \frac{1}{\sqrt{\omega\mu\sigma_2}}. \tag{2.48}$$

An equivalent derivation of λ_L resulted in eq. (2.37). It should be noted that well below the transition temperature, λ_L is frequency independent since $\sigma_2 \propto 1/\omega$, see eq. (2.42).

We can now return to the deduced surface impedance expression for conductors, see eq. (2.27) and substitute with the two-fluid conductivity σ_{2f} according to

$$Z_s = \sqrt{\frac{i\omega\mu}{\sigma_{2f}}} = \sqrt{\frac{i\omega\mu}{(\sigma_1 - i\sigma_2)}}. \tag{2.49}$$

In an analogous way to the propagation coefficient, so re-arranging terms, assuming $\sigma_2 \gg \sigma_1$ and expanding, allows to isolate the real and imaginary part of the surface impedance

$$Z_s = R_s + iX_s = \sqrt{\frac{\omega\mu}{\sigma_2}}\left(\frac{\sigma_1}{2\sigma_2}+i\right). \tag{2.50}$$

The resistive and reactive parts can be extracted as

$$R_s = \sqrt{\frac{\omega\mu}{\sigma_2}}\frac{\sigma_1}{2\sigma_2} \qquad X_s = \sqrt{\frac{\omega\mu}{\sigma_2}}. \tag{2.51}$$

In order to see the frequency dependencies clearer, the σ_2 from eq. (2.48) can be substituted:

$$R_s = \frac{\omega^2\mu^2\sigma_1\lambda_L^3}{2} \qquad X_s = \omega\mu\lambda_L. \tag{2.52}$$

So, the the two-fluid model leads to the prediction that the surface resistance is proportional to ω^2, whereas the frequency dependence for metals is $\sqrt{\omega}$ as shown in eq. (2.27). This means that the surface resistance of a superconductor decreases much more rapidly with frequency than the normal conductor counterpart which will become relevant later in the discussions of chapter 5. At lower frequencies, the surface resistance of superconductors are much smaller than for normal metals but as the frequency increases it eventually surpasses the values of metals. The crossover frequency, so the frequency at which the superconductor surface resistance becomes larger than metals, amounts for copper and a thin film of HTS several hundred gigahertz [57].

2.5.3 Phenomenological formulation of surface resistance for type-II SC

Leaving the realm of classical type-I superconductors and examining HTS, a new phase occurs when increasing the outer magnetic field above the lower critical field H_{c1}. In fact, in order to describe the surface impedance of a type-II SC, the movement of vortices in the mixed state has be taken into account. We consider the expression for the experimental surface resistance of a type-II superconductor as a function of RF field H_{rf}, externally applied flux density B and temperature T [11]:

$$R_s(H_{rf}, B, T) = R_{BCS}(H_{rf}, 0, T) + R_{res}(H_{rf}, 0, 0) + R_{fl}(H_{rf}, B, T) \tag{2.53}$$

with BCS formalism deduced component R_{BCS}[7] that depends on the gap parameter of the superconductor [61] and the, in general, field and temperature independent residual surface resistance R_{res} resulting from impurities and defects. It has been experimentally found that $R_{res} \propto \omega^2$ in high-T_c SC [62, 63]. The externally applied magnetic field dependence enters through R_{fl} which represents the losses induced by the movement of vortices, also known as fluxons, when rendered to the mixed state [11, 64]. For cuprates the vortex cores are of radius $\xi \sim$ nm, known as the coherence length as was introduced in section 2.1. The last term is subject of many theories [65, 66] and will be integral part of our high-frequency analysis.

Vortex-motion model

As described by equation (2.53), the microwave response with applied magnetic field is driven by the movement of fluxons in the superconductor. Consider a single vortex from an externally applied magnetic field $B = n\Phi_0$, n is the number of fluxons per unit area, in a type-II superconductor under a harmonic transport current density $\boldsymbol{J} = J_0 \exp(i2\pi\nu t)\,\boldsymbol{n}_{a,b}$ with J_0 not close to the critical current density J_c. Here, ν is the current frequency in the range of $1-100\,\text{GHz}$ and $\boldsymbol{n}_{a,b}$ a unit vector perpendicular to the applied magnetic field with unit vector $\boldsymbol{n}_c$. The vortex will be exposed to a Lorentz force $\boldsymbol{F}_L = \boldsymbol{J} \times \Phi_0\,\boldsymbol{n}_c$ exerted by the interplay with the electrical current. However, under the presence of pinning sites, the vortex motion is constrained by pinning potential wells. This results in a pinning force $\boldsymbol{F}_p = -k_p\boldsymbol{x}$ which can be assumed to be linear to its vortex displacement $\boldsymbol{x}$. The pinning constant or Labusch parameter k_p defines the curvature of the pinning potential U_c $(k_p)_{\text{rigid}} \approx L_c^{-1}(d^2U_c/dx^2)$ (in the limiting case of rigid vortices with infinite line tension), here L_c is the average distance between pinning sites along the vortex length [67]. Additionally, the moving normal conducting vortex core gives rise to a viscous force $\boldsymbol{F}_v = -\eta\dot{\boldsymbol{x}}$, with η being the vortex viscosity. It can be understood either as a conversion of Cooper pairs to quasiparticles where energy is lost [30] or Joule dissipation within the vortex core [31]. By considering the fluxon mass to be very small [68] and neglecting it, the equation of motion for a single vortex becomes [67, 69]

$$\eta\dot{\boldsymbol{x}} + k_p\boldsymbol{x} = \boldsymbol{J} \times \Phi_0\,\boldsymbol{n}_c + f_{th}, \tag{2.54}$$

where f_{th} is a thermal stochastic force. This equilibrium of forces is valid for not too large vortex displacements $\boldsymbol{x}$ in relation to the size of the potential wells within the superconductor. Moreover, nonlinearities are not considered in this model [69] and are discussed in the context of the FCC-hh elsewhere [70, 71]. The response function to eq. (2.54) can be written in generalized form as [69]

$$\rho_{vm,\chi} = \rho'_{vm,\chi} + i\rho''_{vm,\chi} = \frac{\Phi_0 B}{\eta}\frac{\chi + i\nu_0/\nu_c}{1 + i\nu_0/\nu_c}, \tag{2.55}$$

---

[7]An explicit representation of this component is given in eq. (2.52).

where v_0 is the resonant frequency. The adimensional normalized creep factor $\chi(T,H)$ considers thermal activation which cause vortices to jump out of their pinning sites. For $\chi \approx 0$ vortices stay unaffected by thermal force and for $\chi \approx 1$ the thermal force renders pinning potential completely ineffective [66, 69]. The material characteristic frequency v_c, denoted v_p in the absence of thermal effects, is proportional to the pinning strength and separates microwave dissipation regimes within the superconductor. Eq. (2.55) represents with three parameters χ, v and v_c a highly complex function which, when only related to two independent data sets stays underdetermined. A suitable approach to determine all three parameters is the measurement of $R_s(H)$ and $X_s(H)$ at several measurement frequencies as discussed in [72].

Although, thermal activation plays for REBCO especially at temperatures close to T_c a significant role [66, 72], for intermediate temperatures, it can be useful to neglect the flux creep in order to decrease the degrees of freedom in eq. (2.55). For no thermal force $f_{th} = 0$ limit, eq. (2.55) simplifies the vortex-motion resistivity to

$$\rho_{vm} = \rho'_{vm} + i\rho''_{vm} = \rho_{ff}\frac{1}{1 - iv_p/v_0} = \frac{B\Phi_0}{\eta}\frac{1}{1 - iv_p/v_0}, \tag{2.56}$$

which is known as the Gittleman-Rosenblum (GR) model, named after its founding fathers [65]. $v_p = \frac{k_p}{2\pi\eta}$ denotes the depinning frequency, that is the material characteristic frequency above which the vortex response changes from the pinning to the flux-flow regime. The former is dominated by reactive, the latter by resistive contributions. At $v_0 \ll v_p$ the vortex motion resistivity is in first approximation completely imaginary with $\rho_{vm} = i2\pi v B\Phi_0/k_p$. $v_0 \gg v_p$ reaches the extreme of the flux-flow regime in which $\rho_{vm} = \rho_{ff}$.

We plot the frequency behavior of eq. (2.55) and (2.56) in Fig. 2.12 in order to visualize the two mentioned dissipation regimes and point out the differences between both models. On the one hand, the creep model approaches $\rho'_{vm,\chi} = \rho_{ff} \cdot \chi \neq 0 = \rho'_{vm}$ at extremely low frequencies. On the other hand, when considering creep, the peak value of the imaginary part is decreased by the factor $(1 - \chi)$ as compared to the GR model. In the following, we will always refer to the vortex motion in the context of zero creep.
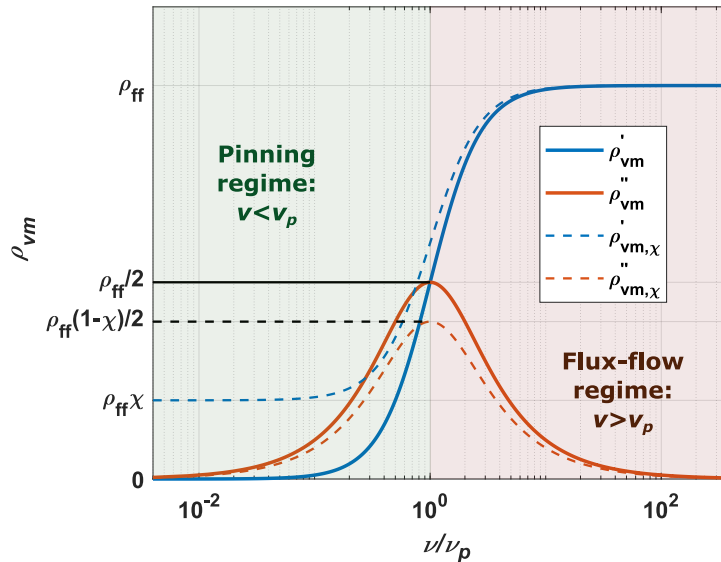
FIGURE 2.12: The vortex motion resistivity without (ρ_{vm}) and under ($\rho_{vm,\chi}$) consideration of flux creep with $\chi = 0.2$, corresponding to $\approx 50\,\mathrm{K}$ [66, 72]. The characteristic frequency v_c or, in case of $\chi = 0$, depinning frequency v_p separates the pinning, low-loss, from the flux-flow, high-loss regime. Visualization inspired by [69].

Having elaborated the microwave response of the vortex motion, the total surface impedance of a type-II superconductor in the mixed state can be expressed analogously to metals as shown in eq. (2.27) but assuming a complex resistivity $\tilde{\rho}$:

$$Z_s = \sqrt{i\omega\mu\tilde{\rho}}. \tag{2.57}$$

In general, $\tilde{\rho}$ holds contributions from the normal/super fluid charge transport [73] and the dissipative movement of vortices [66]. The two-fluid model $\sigma_{2f} = \frac{1}{\rho_{2f}} = \sigma_1 - i\sigma_2$ describes the first contribution and the Gittleman-Rosenblum model with its vortex motion resistivity ρ_{vm} the second part. Thus, the complex resistivity results to [73]

$$\tilde{\rho} = \rho_{2f} + \rho_{vm} = \frac{1}{\sigma_1 - i\sigma_2} + \rho_{vm}. \tag{2.58}$$

For $T \ll T_c$, this is assumed throughout the microwave measurement analysis, the two-fluid conductivity tends towards the super fluid, with $\sigma_1 \ll \sigma_2$, and we can write in a first approximation $\rho_{2f} = i/\sigma_2$. Holding on to eq. (2.57), the surface impedance yields

$$Z_s = \sqrt{i\omega\mu_0\tilde{\rho}} \simeq \sqrt{\omega\mu_0(-\frac{1}{\sigma_2} + i\rho_{vm})}, \tag{2.59}$$

with $1/\sigma_2 = \omega\mu_0\lambda_L^2$. Without an applied external field $\rho_{vm} = 0$, the entire surface impedance becomes reactive $Z \simeq \sqrt{-\omega\mu_0/\sigma_2} = i\omega\mu_0\lambda_L$. With this, we can express the surface resistance originating only from vortex movement as

$$R_{vm} = R_s(T,B) - R_s(T,0) = \Delta R_s = i\omega\mu_0\sqrt{\lambda_L^2 - \frac{i}{\omega\mu_0}\rho_{vm}}. \tag{2.60}$$

This expression becomes relevant in chapter 5, where we fit measured ΔR_s in order to obtain the depinning frequency ν_p of characterized REBCO CCs.

Chapter 3

Experimental Methods

In this chapter, an introduction to utilized measurement techniques and sample fabrication methods will be given. It is divided into three sections. The dielectric resonator measurement system, with which we characterize the high-frequency response of REBCO CC as a function of magnetic field at cryogenic temperatures, is described in section 3.1. Therein, subsection 3.1.4 is dedicated to the data acquisition and raw data treatment of corresponding measurements. The two used magnetometers are detailed together with examples of typical measurements in section 3.2. Finally, we provide some background on DC-transport characterization in 3.3. The sample fabrication to create an electrical circuit for low temperature transport experiments is explained in subsection 3.3.2.

3.1 Dielectric resonator measurement system

The acquisition of REBCO coated conductor's surface impedance data is realized with a setup consisting of a a two-port vector network analyzer (VNA), a custom built dielectric resonator and a Physical Property Measurement System (PPMS) by Quantum Design. Fig. 3.1 provides a scheme of the experimental layout. The three main components of this setup are discussed separately in the following sections.
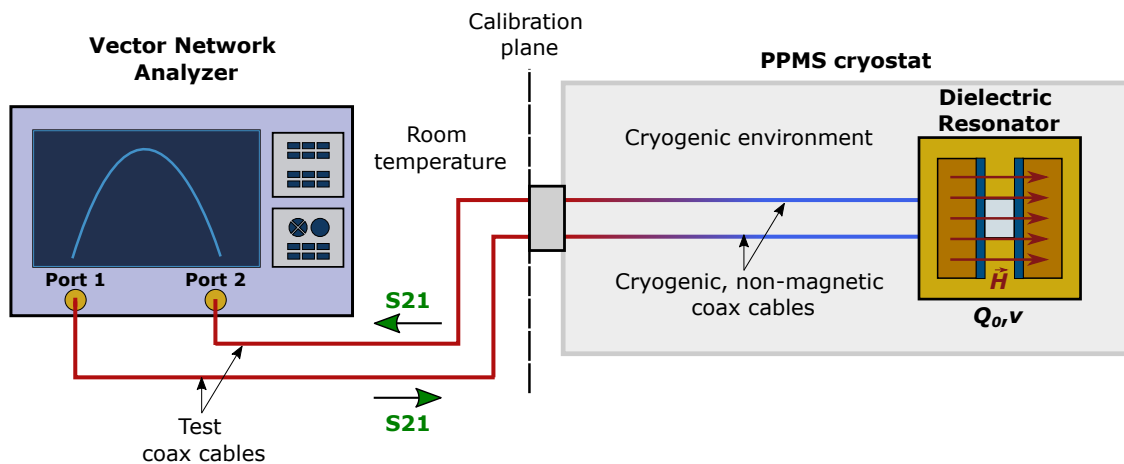
FIGURE 3.1: Scheme of experimental setup consisting of a two port vector network analyzer (VNA), a cryostat which is part of the PPMS and the dielectric resonator (DR). The coaxial cables leading up to the cryostat are calibrated before each microwave measurement. The cables from the cryostat head to the DR are inaccessible and in addition, subject to changing temperature gradients. This part of the transmission line stays uncalibrated and affects the measured scattering coefficients (S-parameters). Effects resulting from cross talk between the couplers or phase delay of the uncalibrated lines are met by using a special fitting strategy for the scattering parameter S_{21} that takes non-idealities into account. The green arrows labeled S_{21} give the signal flow for this particular S-parameter.

3.1.1 Vector Network Analyzers

Measurement principle

A vector network analyzer represents an high-accuracy instrument that combines mainly a microwave power source, signal separation devices and detectors for determination of network parameters such as the scattering coefficients, known as S-parameters [54]. The S-parameters describe how a device under test (DUT) affects the excitation signal, the amplitudes and phase angles of waves (vector in complex plane), that is transmitted or reflected in forward or reverse direction [74, 75]. The mathematical equivalent of it gives a scattering matrix $\boldsymbol{S}$ constituted by S-parameters $S_{i,j}$ which relates incident waves a_i to reflected waves b_i. For a two-port network, the network exclusively used in this work, we can write

$$\begin{pmatrix} b_1 \\ b_2 \end{pmatrix} = \begin{pmatrix} S_{11} & S_{12} \\ S_{21} & S_{22} \end{pmatrix} \times \begin{pmatrix} a_1 \\ a_2 \end{pmatrix}. \tag{3.1}$$

Here, the waves a_i, b_i with $i = 1, 2$ can be defined in terms of power waves as [76]

$$a_i = \frac{V_i + Z_i I_i}{2\sqrt{|\mathrm{Re}(Z_i)|}} = \frac{V_i^+}{2\sqrt{|\mathrm{Re}(Z_i)|}}, \quad b_i = \frac{V_i - Z_i^* I_i}{2\sqrt{|\mathrm{Re}(Z_i)|}} = \frac{V_i^-}{2\sqrt{|\mathrm{Re}(Z_i)|}}, \tag{3.2}$$

where V_i and I_i denote the voltage and the current at the i-th port, Z_i the port impedance and Z_i^* its complex conjugate. The VNA basically measures the two forward traveling waves a_1 and a_2 and two reverse traveling waves b_1 and b_2 independently.

Some limiting cases help with the interpretation of $S_{i,j}$:

- For a forward measurement ($|a_1| > 0$) and matched DUT port 2 ($a_2 = 0$), S_{11} defines the reflection coefficient of DUT port 1 as $S_{11} = b_1/a_1 = V_1^-/V_1^+$.

- For a forward measurement ($|a_1| > 0$) and matched DUT port 2 ($a_2 = 0$), S_{21} defines the forward transmission coefficient as $S_{21} = b_2/a_1$. Given that the characteristic impedances of the two ports are the same $Z_1 = Z_2$, we can write $S_{21} = b_2/a_1 = V_2^-/V_1^+$.

- For a reverse measurement ($|a_2| > 0$) and matched DUT port 1 ($a_1 = 0$), S_{22} defines the reflection coefficient of DUT port 2 as $S_{22} = b_2/a_2 = V_2^-/V_2^+$.

- For a reverse measurement ($|a_2| > 0$) and matched DUT port 1 ($a_1 = 0$), S_{12} defines the reverse transmission coefficient as $S_{12} = b_1/a_2$. Given that the characteristic impedances of the two ports are the same $Z_1 = Z_2$, we can write $S_{12} = b_1/a_2 = V_1^-/V_2^+$.

We show a chart with the signal flow corresponding to a two-port network with ideal source-load match in Fig. 3.2.
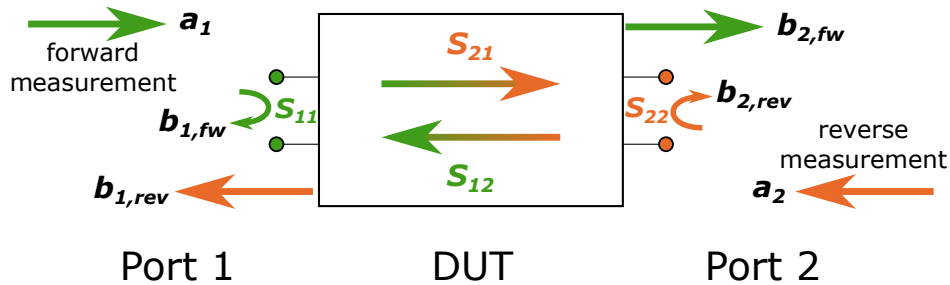
FIGURE 3.2: Visualization of signal flow and S-parameters in an ideally matched source load ports network. Figure recreated from [75].

For all microwave experiments within this thesis, the four scattering coefficients $S_{i,j}$, with $i, j = 1, 2$, serve as the raw data from which all surface impedance data presented in the following chapters are deduced.

Employed VNAs

Over the course of this PhD, we took two different VNAs into operation. The specifications of the used VNAs are gathered from data sheets of the providers [77, 78] and listed in table 3.1.

	Keysight FieldFox N9918A	**Rohde & Schwarz ZNB 20**
Frequency range	30 kHz-26.5 GHz	100 kHz-20 GHz
Frequency accuracy	± 0.7 ppm (spec) $+ \pm 1$ ppm/yr, will not exceed ± 3.5 ppm	± 0.5 ppm (spec) $+ \pm 1$ ppm/yr
Extended power range (8 GHz)	-15 dBm	-30-12 dBm
OS	Custom OS	Windows
Measurement speed	Reference	3-5× faster
Dynamic range (8 GHz)	95 dB (spec)	>120 dB (spec)
Type	Handheld	Stationary VNA

TABLE 3.1: A list of relevant specifications of the VNAs employed in this thesis.

Without additional software, each measurement point, the S-parameters as a function of frequency at specific temperature and magnetic field, has to be recorded manually with the corresponding VNAs. We developed Python based scripts in order to improve and automatize the measurement procedure. The main features of mentioned programs are

- Establishing communication between the VNAs and the PC in the low temperature lab of the ICMAB.

- Allowing to remote-control the VNAs.

- Automatized measurement loop involving the tracking, measurement and saving of resonance curves.

- Real time visualization of loaded Q-value Q_l and resonant frequency ν_0 as a function of time and magnetic field (R&S script).

A measurement script for the portable Keysight FieldFox N9918A, named DRΩMS, was written by members of the project consortium. A user manual of the same name intended to assist users with its operation was created and can be found in the consortium repository [79].

An additional Python program was developed for the Rohde & Schwarz ZNB 20 with the support of Dr. Bernat Bozzo by me. It is based on a Github library created by a user called Terrabits and described as an instrument control library for general purpose Rohde & Schwarz instruments, and in particular the vector network analyzer [80]. Additional inspiration was taken from DRΩMS and the measurement procedures of the engineering department, section of applied physics group in Roma Tre University. As compared to the DRΩMS software, we implemented the possibility of magnetic field sweeps that can be measured three times faster with an eight times higher point density, save and reliable data storage on the PPMS computer, instead of an external pen drive, and real time data plotting of measureands, a feature especially useful for surface reactance measurements.

The file named 'vna_plotting_script.py' starts the measurement loop and is saved on the computer of the PPMS II.

3.1.2 Dielectric Resonator

Different from non-resonant methods, known as a broadband technique, where information about electromagnetic properties of materials over a frequency range can be obtained, a resonant method is used to get knowledge about the permittivity, permeability or surface impedance of materials at one single or several discrete frequencies [54].

In this thesis, we use a Hakki-Coleman type dielectric loaded resonator [81] with resonant frequency $\nu_0(50\,\text{K}) \approx 8\,\text{GHz}$ to measure the high-frequency response of the coated conductor samples at $10\,\text{K}$ to $70\,\text{K}$ and fields up to $9\,\text{T}$. It is a transmission type resonating structure where samples under investigation replace the end walls of a well known resonator cavity upon which the resonant frequency and quality factor of the resonator will be changed. Then, the electromagnetic properties of the sample can be derived from the changes of the resonant frequency and quality factor of the resonator [54].

The resonator was designed and optimized for operation at low temperatures and large magnetic fields by members of the project consortium [82].

It consists of a $37\,\text{mm}$ long, hollow metallic cylinder with an outer diameter $\varnothing_{\text{resonator}} = 24\,\text{mm}$, the dimensions have been chosen in order to fit the cylinder into the cryostat bore. The actual cavity is of height $h = 3\,\text{mm}$ and radius $a = 11\,\text{mm}$ which we load with a dielectric TiO_2 rod of height $h = 3\,\text{mm}$ and radius $r = 2\,\text{mm}$ and terminate by two $12\,\text{mm} \times 12\,\text{mm}$ HTS sample squares on brass blocks. The elements are clamped together by CuBe springs forming a cylinder cavity with the dielectric terminated axially by the specimen under investigation that can structurally sustain material expansions and contractions in a wide cryogenic temperature range. Electromagnetic waves are guided into the cavity and picked up by two laterally inserted coaxial cables with coupling loops at its end whose insertion length is adjustable. On the basis of boundary conditions, the annular cavity geometry with $h < 2.1 \cdot r$ [54] allows for a TE_{011} working mode excitation with circular electric field line distribution (see Fig. 3.3 **(c)** or [83]) that drives currents through the *ab*-planes of studied REBCO superconductors. We provide a scheme of the DR in Fig. 3.3 **(a)**-**(b)** and a more detailed characterization of the resonator system is given in [82].

The defining quantities of a resonance are the resonant frequency ν_0, the frequency at which induced electromagnetic fields oscillate with greatest amplitude, and the unloaded quality factor or simply Q-factor Q_0, a dimensionless parameter representing the ratio between time-average stored energy W and energy loss per second P_r [74] with

$$Q_0 = \frac{\omega_0 W}{P_r}, \tag{3.3}$$

where $\omega_0 = 2\pi\nu_0$ is the angular resonant frequency. Energy dissipation occurs both in every conductive cavity surface and the loaded dielectric volume so that the power P_r can be expressed as

$$P_r = \sum_i P_{c,i} + P_d. \tag{3.4}$$

$P_{c,i}$ is the power loss arising from surface currents J_s running through conductive surface S_i of the cavity given by

$$P_{c,i} = \frac{R_{s,i}}{2} \int_{S_i} |J_s|^2 \, dS. \tag{3.5}$$

Here, $R_{s,i}$ corresponds to the surface resistance of conductive surface S_i. The power dissipated in the dielectric volume V can be expressed as

$$P_d = \frac{\omega_0}{2} \int_V \varepsilon' \varepsilon_0 \tan(\delta) |E|^2 \, dV. \tag{3.6}$$

In this equation, ε' is the real part of the permittivity of the dielectric $\varepsilon = \varepsilon' - i\varepsilon''$, ε_0 the vacuum permittivity, the loss tangent of the dielectric material is defined as $\tan(\delta) = \frac{\varepsilon''}{\varepsilon'}$ and E is the electric field at resonance.

Plugging eq. (3.4) into the inverse of eq. (3.3) gives

$$\frac{1}{Q_0} = \frac{\sum_i P_{c,i} + P_d}{\omega_0 W} = \sum_i \frac{1}{Q_{c,i}} + \frac{1}{Q_d} \tag{3.7}$$

(a)

Top lid

Coaxial transmission lines

Resonator body

Rutile cylinder

Twin samples on brass blocks

Spring

Bottom lid

(b) Rutile cylinder

Coupling loops

Sample

(c)

H

E

TE_{011} mode
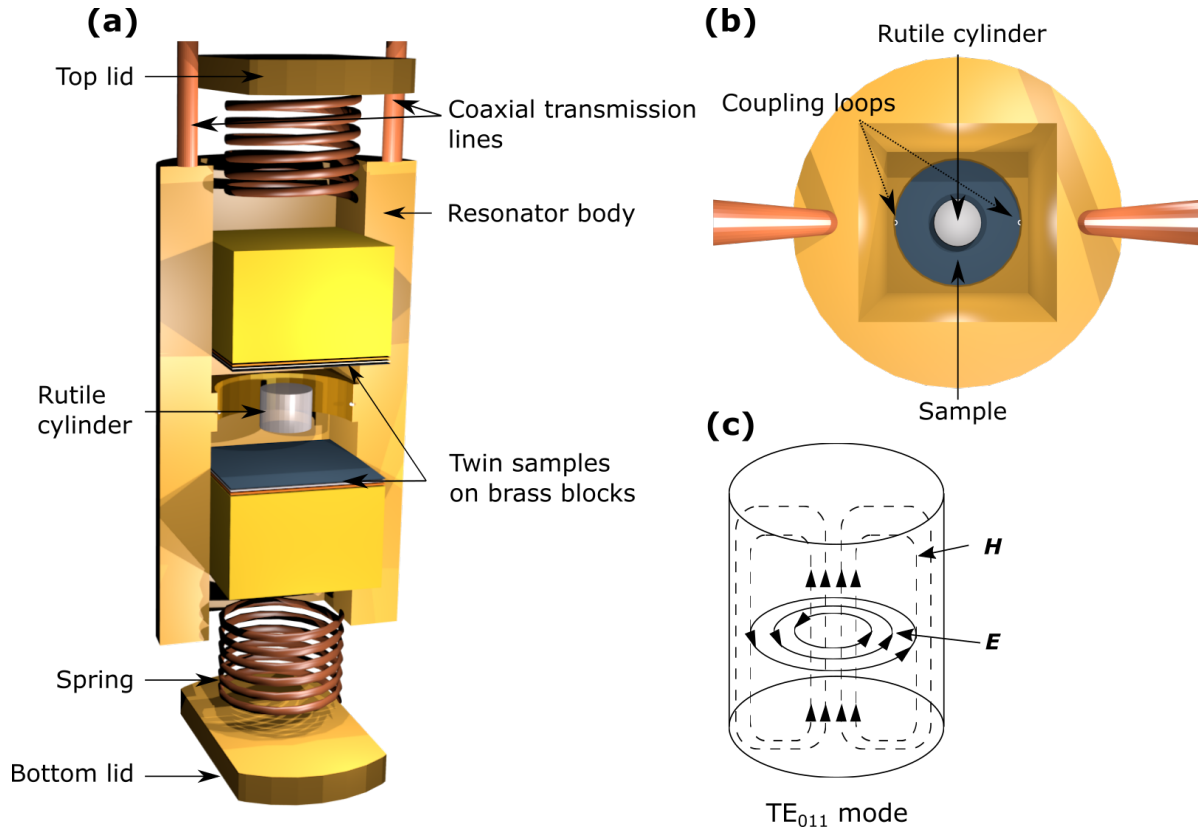
FIGURE 3.3: **(a)** Cross section of resonator body with important components that constitute our resonant system. Pressing the lids on the resonator body creates a rutile loaded cylinder cavity with samples as endplates. **(b)** Top view of half assembled resonator with the TiO_2 rod centered on a sample. **(c)** Schematic field distribution of TE_{011} mode. Redrawn from [54].

and under consideration of eq. (3.5) and eq. (3.6) we get

$$\frac{1}{Q_{c,i}} = \frac{R_{s,i} \int_{S_i} |J_s|^2 \, dS}{2\omega_0 W} = \frac{R_{s,i}}{G_i}, \tag{3.8}$$

where $G_i = \frac{2\omega_0 W}{\int_{S_i} |J_s|^2 \, dS}$ denotes the geometrical factor of the i-th surface and

$$\frac{1}{Q_d} = \frac{\int_V \varepsilon' \varepsilon_0 \tan(\delta) |E|^2 \, dV}{2W} = p \tan(\delta), \tag{3.9}$$

with $p = \frac{\int_V \varepsilon' \varepsilon_0 |E|^2 \, dV}{2W}$ being the filling factor, respectively. Here we have to assume that the dielectric rod under test is linear, isotropic, homogeneous, and nonmagnetic.

For a resonator coupled to external transmission lines, the so called loaded Q-factor Q_l has to be considered with

$$\frac{1}{Q_l} = \frac{1}{Q_0} + \frac{1}{Q_{ex}} = \frac{1}{Q_0}(1 + \sum \beta_i), \tag{3.10}$$

where Q_0 is the unloaded Q-factor, which takes only losses in the resonator into account and Q_{ex} is the Q-factor corresponding to losses in the external transmission lines and coupling elements [74]. The external losses can be

summarized in the coupling coefficients β_i. In our two-port system with unequal coupling

$$\beta_1 = \frac{1 - S_{11}}{S_{11} + S_{22}}, \tag{3.11}$$

$$\beta_2 = \frac{1 - S_{22}}{S_{11} + S_{22}}, \tag{3.12}$$

S_{11} and S_{22} are the S-parameters measured at resonant frequency [84]. The magnitude of β_i describes the coupling between external circuit and resonator. At an over-coupling setup $\beta_i > 1$, the energy dissipation in the transmission lines is larger than in the cavity. $\beta_i = 1$ describes a state with equal energy dissipation in the external circuit and resonator and is denoted critical coupling. For $\beta_i < 1$, we have an under-coupling state where the energy dissipation in the external load is smaller than in the resonator [54]. Naturally, the determination of β_i represents a source of errors, so that an error optimized system features $\beta_i \sim 0$, hence, $Q_l \approx Q_0$ [85]. Throughout this thesis, our resonator stayed in the under-coupling regime with $\beta_i \approx 0.1 - 0.8$ for which $Q_l \neq Q_0$. A common technique to tune the coupling is the variation of coupling loop insertion into the resonator [56].

For our specific case, of a metallic resonator body terminated by REBCO CC samples and loaded with a dielectric disk, the unloaded quality factor Q_0 relates to the losses within the resonator in the following way [82, 86] (compare with eqs. (3.7)-(3.9))

$$\frac{1}{Q_0} = \frac{R_s^{\mathrm{CC},1}}{G^{\mathrm{CC},1}} + \frac{R_s^{\mathrm{CC},2}}{G^{\mathrm{CC},2}} + \frac{R_s^{\mathrm{m}}}{G^{\mathrm{m}}} + p \tan \delta. \tag{3.13}$$

The first three terms of the sum are losses caused by the exposed conductive surfaces within the cavity, where the superscripts 'CC,1', 'CC,2' and 'm' stand for the coated conductors terminating the cavity and metallic enclosure, respectively. Because of rutile's much higher relative permittivity[1] $\varepsilon_r'(8\,\mathrm{GHz}, 50\,\mathrm{K}) \approx 111$ than the one of the surrounding medium, vacuum, the electromagnetic field is mainly focused in the dielectric. Thus, $p \approx 1$ and we are allowed to discard the contributions from the lateral metallic walls $\frac{R_s^{\mathrm{m}}}{G^{\mathrm{m}}} \approx 0$. Given the high homogeneity of commercially available coated conductors, we can assume top and bottle sample to be identical and write $\frac{R_s^{\mathrm{CC},1}}{G^{\mathrm{CC},1}} \approx \frac{R_s^{\mathrm{CC},2}}{G^{\mathrm{CC},2}} = \frac{R_s^{\mathrm{CC}}}{G}$ to end up with

$$R_s^{\mathrm{CC}}(T, B) = \frac{G}{2} \cdot \left[\frac{1}{Q_0(T, B)} - \tan \delta(T) \right]. \tag{3.14}$$

The procedures for numerical and empirical determination of G are described in [82], whereas $\tan(\delta)(T)$ is adopted from [87]. The numeric values used throughout this thesis are given as a function of temperature in appendix A. The erros on the R_s values for the different CCs shown are estimated following a careful analysis of the error sources (see the supplementary information of [14]). From this analysis we have determined that the error we commit in the determination of the values of R_s for the different CC providers is at maximum 10%. Note that this error is dominated by the non-homogeneity of the samples, i.e. by Q_0, and the exact placement of the cylinder that changes from one measurement to another.

In analogy to the surface resistance, the imaginary part of the surface impedance $Z_s = R_s + iX_s$ can be extracted from microwave measurements, too. The reactive response of a resonator reflects in the resonant frequency ν_0 according to [88],[86]:

$$-2\frac{\Delta \nu_0}{\nu_{0,\mathrm{ref}}} = \frac{\Delta X_s^{\mathrm{CC},1}}{G^{\mathrm{CC},1}} + \frac{\Delta X_s^{\mathrm{CC},2}}{G^{\mathrm{CC},2}} + \frac{\Delta X_s^{\mathrm{m}}}{G^{\mathrm{m}}} + p\frac{\Delta \varepsilon_r'}{\varepsilon_{r,\mathrm{ref}}'}, \tag{3.15}$$

where X_s is the surface reactance, ε_r' the real part of the relative dielectric permittivity. By Δx we mean the difference

---

[1]The relative permittiviy is a dimensionless quantity defined by $\varepsilon_r = \frac{\varepsilon}{\varepsilon_0} = \frac{\varepsilon' - i\varepsilon''}{\varepsilon_0} = \varepsilon_r' - i\varepsilon_r'' = \varepsilon_r'(1 - i\tan(\delta))$.

of a quantity from it's reference value x_{ref}. Using the same approximations made already for the surface resistance, we get

$$\Delta X_s^{\text{CC}}(T, \Delta T, B, \Delta B) = -G \left[\frac{\Delta v_0(\Delta T, \Delta B)}{v_{0,\text{ref}}(T, B)} + \frac{p}{2} \frac{\Delta \varepsilon_r'(\Delta T)}{\varepsilon_{r,\text{ref}}(T)} \right]. \tag{3.16}$$

The uncertainty in the surface reactance is, in a first approximation, dominated by the non-homogeneity of the samples and alignment uncertainties of the rutile disk and stays below 10 %.

3.1.3 Physical Properties Measurement System

In the context of large-field, high-frequency characterization of REBCO CCs, some essential elements of the PPMS have to be explained[2].

- **Dewar:** The dewar represents a special type of vacuum vessel used for storage of cryogens. The liquid-helium bath is jacked by a primarily aluminium built outer flask that gets evacuated in order to minimize the heat transfer with the environment.

- **PPMS probe:** The probe is composed of several concentric stainless steel tubes decorated with sophisticated electronic components and immersed into the liquid-helium bath of the dewar. Major components of the probe are the sample chamber (surrounded by a cooling annulus and several vacuum tubes) with sample space bore diameter $\varnothing \approx 25\,\text{mm}$ that limits the x-y dimensions of the resonator, temperature regulating impedance assembly, and the superconducting solenoid NbTi 9 T magnet. The top part of the probe protrudes out of the dewar and is referred to as the probe head. When the resonator, which hangs on coax cables, is introduced into the sample space, the access port is sealed by clamping an O-ring between flanges of the PPMS probe head and the transmission line fixture.

- **Model controllers:** The Model 6000 PPMS Controller is an integrated user interface that houses the electronics and the gas-control valves for the PPMS. Gas valves and gas lines inside the Model 6000 are used to control temperature. The Model 6700 Magnet Controller allows the control of the magnet.

Multivu, a software developed by Quantum Design, allows with the aid of the model controllers the adjustment of both the temperature, it is homogeneous in a volume starting at the blind puck sitting on the pins of the sample chamber and extending 10 cm higher, through considered liquid-helium flow into the cooling annulus, and of the magnetic field which has its its center 5.4 cm above the sample puck. Set temperatures correspond to the one measured close to the sample puck. An additional CERNOX thermometer was mounted within the resonating structure which allows monitoring the thermal state of the samples under investigation, however, it is not used for temperature control because of its high magnetoresistance. A full thermalization of the resonator, which means limiting the temperature drift to $\sim 10\,\text{mK}/15\text{min}$[3], takes approx. 2-3 h and an almost constant temperature offset of 7 K between thermometer at the sample puck and thermometer at the resonator prevails in the range $T_{reso} = 20 - 70\,\text{K}$.

The resonator is designed in such a way that, when sunken into the sample space of the PPMS probe, the bottom mass touches the puck in order to establish better heat transfer. The length of the coaxial cables is adjusted so that the resonating cavity resides approximately in the center of magnetic field. A schematic cross section of the resonator inserted into the PPMS probe is given in Fig. 3.4. Inserting the DR into the PPMS probe, we are able to flexibly set up specific temperatures and magnetic field densities with homogeneous distributions in the vicinity of the characterizing twin samples in order to characterize the surface impedance of REBCO CCs at cryogenic temperatures and large magnetic fields.

---

[2]Setup details are taken from the PPMS Hardware Manual [89].

[3]This temperature drift is only achievable for PPMS set temperatures $T_{PPMS}^{set} \geq 23\,\text{K}$. At lower temperatures, heat transfer provoked by the coax cables prevents to reach such stable drift values.
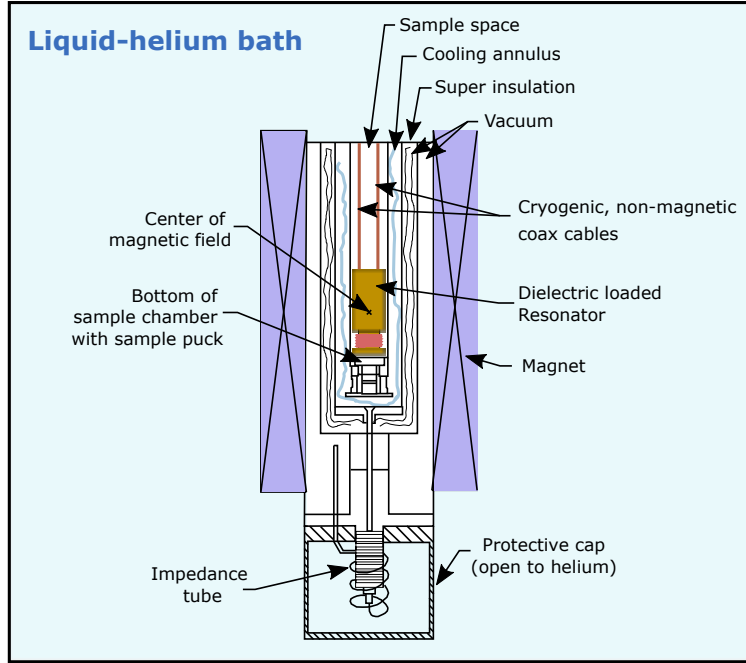
FIGURE 3.4: Cross section of bottom part of PPMS probe while housing the DR. Major components
are labeled. Inspired by drawing from [89].

3.1.4   Data treatment and setup conditions

Determination of Q-Factor and resonant frequency

In subsection 3.1.2, it has been demonstrated that the surface impedance $Z_s = R_s + iX_s$ of samples under study reflects
itself in the measurable Q-factor Q_l and resonant frequency v_0 of a resonating mode. To this end, it is essential to
establish a reliable and precise procedure for measurand determination.

Starting with the equation of motion of a simple resonator circuit, Laplace transforming it and solving for the trans-
fer function, one obtains with some approximations[4] the complex transmission coefficient S_{21}, the voltage ratio of
transmitted voltage to the incident voltage, as a function of frequency in ideal conditions as [85, 90, 91]

$$S_{21}(v) = \frac{S_M}{1 + 2iQ_l \frac{v - v_0}{v_0}}, \tag{3.17}$$

where $S_M = S_{21}(v_0)$ corresponds to the point with maximum magnitude. For an undercoupled setup, $\beta_1 \sim \beta_2 \ll 1$
[85], the modulus of eq. (3.17) gives

$$|S_{21}(v)| = \frac{|S_M|}{\sqrt{1 + 4Q_l^2 (\frac{v - v_0}{v_0})^2}}. \tag{3.18}$$

This equation describes a Lorentzian bell with resonant frequency located at the maximum of the magnitude. In Fig.
3.5, we show the measured transmission coefficient magnitude $|S_{21}|$ offset by $|S_M|$ for a measured coated conductor
that clearly resembles a Lorentzian curve. The most straightforward and from a computational viewpoint most efficient
strategy to obtain Q_l and v_0 is the -3.01 dB method [91]. It consists of linking the position of the peak maximum to v_0
and determining the bandwidth $BW = v_0/Q_l$ of the resonance curve, the distance between the half power ratio points,
in order to relate it to the loaded Q-Factor Q_l. However, this method, relies on discrete points and ideal measurement
conditions which can give poor results in real experimental scenarios or small signal to noise ratios.

---

[4]A complete derivation can be found in [90].
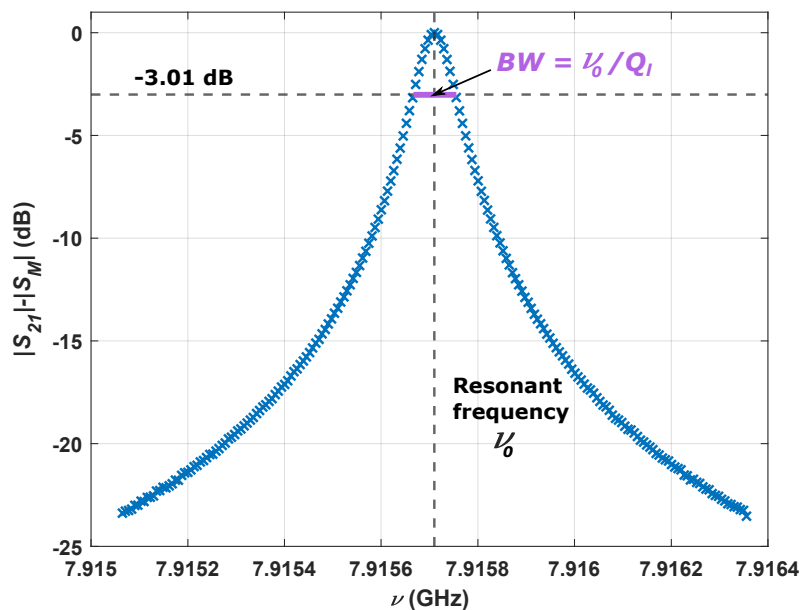
FIGURE 3.5: The magnitude of the transmission coefficient S_{21} in dB representation offset by its maximum value as a function of frequency of SuperOx APC coated conductor measured at $50\,K$ without applied field. The horizontal dashed line indicates $-3.01\,dB$, the purple horizontal line gives the bandwidth of the resonance curve BW and the dashed vertical line runs through the maximum value $|S_M|$ and corresponds to the resonant frequency v_0.

In addition, this simple approach does not take non-idealities into account, that can arise at measurement conditions. Two perturbations are the most common to occur. On the one hand, cross coupling (also known as cross talk) between cables and coupling elements and on the other hand, phase delays because the coupling ports of the resonator do not necessarily coincide with the plane of the measurement [56, 91] (which is usually tried to be minimized by calibrating the transmission lines [92]). The so-called Fano resonance model considers both effects by adding a complex number $S_X = S_{cR} + iS_{cX}$, representing cross talk, and a constant phase delay ϕ to the ideal Lorentz curve to yield [91]

$$S_{21}(v) = \left(\frac{S_M}{1 + 2iQ_l \frac{v - v_0}{v_0}} + S_X \right) e^{i\phi}. \tag{3.19}$$

The constant S_X gives the ideal Lorentzian of $|S_{21}|$ an asymmetric shape, whereas the phase delay does not affect the magnitude of S_{21} but its phase (remember S_{21} is a complex number). Fitting eq. (3.19) with six real fitting parameters to the transmission parameter S_{21} in the complex plane following the least-squares Levenberg-Marquardt algorithm [93, 94], referred here to as the complex fit model, is considered as the most accurate and precise technique, especially at small signal to noise ratios [56, 91, 95].

A simplified fit to the magnitude of $|S_{21}|$ with the modulus of eq. (3.19), called the absolute fit model, offers itself as a possible alternative. It was demonstrated in [56] that for Monte-Carlo simulated curves with $Q_{nominal} = 10000$, $v_{0,nominal} = 15\,GHz$, $S_X = 0.010 + i0.015$ (this cross talk introduces considerable asymmetry into $|S_{21}|$ as seen in Fig. 1 within [85]) and $\phi = \pi/19$ and signal to noise ratios $SNR > 10$ (see definition of SNR in [91]), the absolute fit and complex fit model both yield $|Q_{fit} - Q_{nominal}|/Q_{fit} < 1\%$ and $|v_{0,fit} - v_{0,nominal}|/v_{0,fit} < 0.1\,ppm$. Considering our upper boundary error on R_s and X_s which amount 10%, the absolute fit model satisfies our accuracy and precision demands excellently with the additional benefit of being faster and more computational cost efficient than the complex fit. Thus, this method was chosen in this thesis for the reliable determination of Q_l and v_0. We show the same data

points from Fig. 3.5 fitted with the modulus of eq. (3.19) in Fig. 3.6.
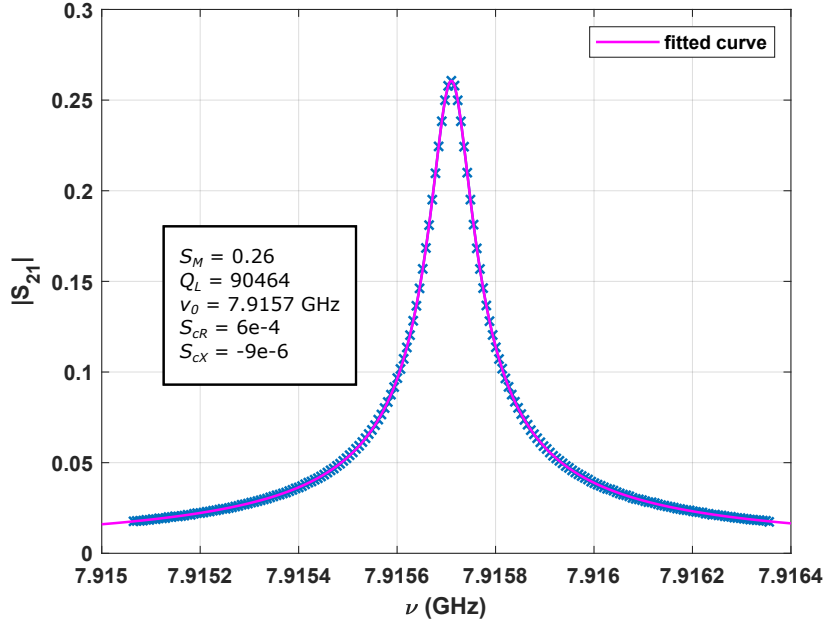
FIGURE 3.6: The modulus of the transmission coefficient S_{21}, blue crosses, measured for SuperOx APC CC at 50 K and without applied magnetic field together the modulus of eq. (3.19) used as a fit function, purple line. The inset displays the converged fitting parameters. The small S_{cR} and S_{cX} are in accordance with the symmetric shape of the Lorentzian.

The fit displays splendid accordance with the measurement data and a similar fitting quality for all other $|S_{21}|$ recorded in this thesis.

Data acquisition

In the following we condensate all essential setup conditions for the acquirement of surface impedance data used within this thesis in form of bullet points.

- **RF-Power:** The used RF power of -15 dBm translates to $H_{\max} = 28.68\,\text{A/m}$ or $0.036\,\text{mT}$ field in the cavity [96]. We have previously demonstrated that this power corresponds to the linear regime for pristine coated conductors as the measured surface resistance is mostly independent of the field amplitude [15]. A power dependence study with larger RF-powers, close to the ones expected in the beam screen chamber of the FCC-hh, was recently conducted within our consortium [71] but is outside of this thesis' scope.

- **Frequency span:** It was shown in [56] that the frequency span of measured S-Parameters can have an impact on the accuracy and precision of obtained Q_l and ν_0. A too narrow span disregards the full dynamic of resonance curves, while wide frequency spans sacrifice point density that leads to poorer fits. Within our measurement procedure, we fix the frequency span to be ten times the resonance curve's bandwidth BW at the first measurement point, i.e. at the beginning of a magnetic field sweep or a temperature sweep, and keep this frequency span until the sweep finishes. In all cases, we choose 201 as the number of points for each S-Parameter sweep, in order to establish a good compromise between measurement accuracy and speed. Alimenti simulated the relative uncertainties of loaded Q-factor $\sigma_{Q_l,r} = \sigma_{Q_l}/Q_l$ and relative uncertainty of resonant frequency $\sigma_{\nu_0,r} = \sigma_{\nu_0}/Q_l$ as a function of frequency spans when fitting resonance curves that consists of 1600 simulation points and have varying degrees of non-idealities with the absolute fit model [56]. He found an absolute minimum of $\sigma_{Q_l,r}$ when choosing the frequency span to be about six times the resonance bandwidth BW and an absolute minimum for

$\sigma_{v_0,r}$ when choosing the frequency span to be about four times the resonance bandwidth BW. Nevertheless, varying the frequency span between 3 times and 10 times the resonance peak's bandwidth BW changed $\sigma_{Q_l,r}$ by only 0.03 % and $\sigma_{v_0,r}$ by only 0.01 %. Thus, the uncertainties we introduce by fixing frequency span to $10 \cdot BW$ stay quite small and are irrelevant when assuming the upper error limit on the surface resistance and reactance to be 10 %, as mentioned above.

- **Intermediate frequency bandwidth:** The dynamic range of a VNA can be increased by lowering the bandwidth of the digital intermediate frequency (IF) filter which suppresses the noise level around the measurement frequency. However, the measurement time increases with smaller filter bandwidths. For small bandwidths, the measurement time is governed by the filter settling time, which is inversely proportional to the bandwidth [75]. We set the intermediate frequency bandwidth (IFBW) of the VNA to 1 kHz for all acquired high frequency data within this thesis. The Q-factor and resonant frequency acquired with IFBW = 1 kHz deviate less than by 0.1 % from the values acquired with IFBW = 0.1 kHz for SuperOx CC at 70 K and 9 T. The mean acquisition time of the four S-parameters S_{11}, S_{21}, S_{12} and S_{22} with IFBW = 1 kHz amounts about 4.5 s.

- **Calibration:** Transmission lines, the part from the VNA ports to the cryostat (see calibration plane in Fig. 3.1) are always subject to a calibration process before starting acquisition of *S*-parameters in order to minimize systematic and reproducible errors. For this, we set the frequency sweep range to 7.6 GHz to 8.1 GHz and execute the TOSM (Through–Open–Short–Match) (see [75]) calibration with a ZN-Z135 calibration kit standard. Based on this calibration, the derived error correction terms get intrapolated when limiting the frequency range to a single resonance peak with span $10 \cdot BW$.

- **Field sweeps:** The acquisition of Q-factor and resonant frequency as a function of magnetic field at fixed temperatures is carried out with the following sequence. From 0 T, we start with sweeping up the magnetic field to a desired magnetic field $H_{des.}$. Then, we sweep the magnetic field from desired magnetic field $H_{des.}$ back to 0 T. The sweep up and sweep down magnetic field branches correspond to a sample in zero-field cooled state and field cooled state, respectively. Finally, in order to minimize the effect of trapped fields, the superconducting external field magnet is demagnetized, i.e. the magnet is set to -1 T and subsequently to 0 T in oscillating mode. A typical magnetic field profile of a surface impedance field sweep, as described here, is shown in Fig. 3.7. The magnetic field is always applied normal to the sample substrate and ramped with 180 Oe/s.
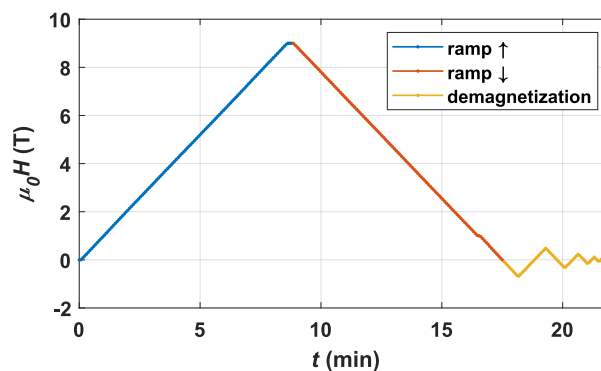
FIGURE 3.7: Shown is the applied magnetic field as a function of time corresponding to a field sweep experiment at fixed temperatures for surface impedance data acquisition. The sequence of the applied magnetic field is the following. First, we ramp the magnetic field up from 0 T to a desired magnetic field, here 9 T,(blue line). Second, we ramp down the magnetic field from the desired magnetic field back to zero field (red line). Finally, a demagnetization process is executed (yellow line).

3.2   Magnetometers

We perform non-invasive induction measurements of CCs under study using two different magnetometers. In particular, with the Quantum Design Magnetic Property Measurement System (MPMS) XL-7 SQUID DC and with the Vibrating Sample Magnetometer (VSM) option for the PPMS.

3.2.1   MPMS XL-7 SQUID DC magnetometer

The MPMS is as a family of analytical instruments to measure magnetic properties of small samples over a broad range of temperatures and magnetic fields [97]. Main components are a vacuum cryostat allowing stable experimental temperatures in a range $1.8 - 400$ K, a superconducting magnetic reaching fields up to 7 T, a motion control system to move the sample and a second-order gradiometer with superconducting pick-up coils coupled to a direct current Superconducting Quantum Interference Device (SQUID) that handle the extremely sensitive magnetic moment reading. The sample under investigation is mounted perpendicular to the applied magnetic field and moved during operation along the superconducting pickup coils, inducing currents $\Delta I = \Delta\Phi/L$, where ΔI is the current induced by the flux change $\Delta\Phi$ and L is the circuit's inductance [98]. It is important to note that the induced current is independent of the rate of flux change, thus samples can be moved arbitrarily slowly without performance degradation. The signal is amplified by the SQUID sensor which serves a very high sensitive current-to-voltage converter. With the proper magnetic shielding this system allows to resolve magnetic moments as low as 1×10^{-8} emu even at 7 T applied field [98].

The data was recorded using the Reciprocating Sample Option (RSO). In this type of measurement, the sample is displaced periodically around a reference position within the coils which results in an oscillating current profile. The frequency of the sample movement is set to 4 Hz and one measurement point is an average over 25 cycles.

3.2.2   Vibrating Sample Magnetometer option

The Vibrating Sample Magnetometer option is a modular expansion that is fully compatible with the PPMS. It primarily consists of a VSM linear motor transport (head) responsible for vertical sample translations, pick-up coils arranged in a first-order gradiometer within a puck for magnetic moment detection and corresponding electronics [99]. Within the gradiometer pick-up coil samples are vibrated typically with 2 mm amplitude at 40 Hz. The changing magnetic flux will induce a voltage drop in the coils according to Faraday's law of induction

$$V_{coil} = -\frac{d\Phi}{dt} = -\left(\frac{d\Phi}{dz}\right)\left(\frac{dz}{dt}\right), \tag{3.20}$$

with Φ the magnetic flux within the pick-coil, z the displacement from a reference position and t the time. For a sinusoidal sample movement, the coil voltage is proportional to a calibration constant C, the amplitude of the oscillation A, its angular frequency ω and the magnetic moment of the sample m, thus

$$V_{coil} = CA\omega m \cdot sin(\omega t). \tag{3.21}$$

The output of the pick-up coil is amplified and lock-in detected with a VSM detection module. This reading technique leads with the large bore coilset, which is used throughout this thesis, to a magnetic moment sensitivity of 1.5×10^{-6} emu. Being compatible with the PPMS, the VSM option allows fast and sensitive measurements of the sample magnetization in conditions realizable within the PPMS, i.e. in a temperature range 1.8-400 K and up to magnetic fields of 9 T. In addition, the higher oscillation frequency as compared to the SQUID allows for faster acquisition of magnetic moments and thus reduces the effect of thermally induced magnetic flux creep.

3.2.3 Typical magnetization measurements

Magnetization loops

In Fig 3.8, we present a full magnetization loop of a SuperPower CC sample acquired at 20 K with the VSM option of the PPMS. In this specific case, the following five magnetic branches (**I-V**) are measured.

- Branch **I**: Magnetic field sweep from 0 T to maximum positive field 9 T.

- Branch **II**: From 9 T gradual removal of magnetic field.

- Branch **III**: Magnetic field sweep from 0 T to maximum negative field -9 T.

- Branch **IV**: From -9 T gradual removal of magnetic field.

- Branch **V**: Magnetic field sweep from 0 T to field $> 2H'$.

Following Bean's critical state model, we can calculate the critical current I_c of a rectangular slab with width w, length l and thickness t from its fully saturated magnetization loop width $\Delta\mu(H) = \mu_{sat}^+(H) - \mu_{sat}^-(H)$, where $\mu_{sat}^+(H)$ and $\mu_{sat}^-(H)$ are the positive and negative branch of the magnetic moment, respectively, according to [100]

$$I_c(T,H) = wt \frac{\Delta\mu(T,H)}{w(1 - \frac{w}{3l})}. \tag{3.22}$$

Note that paramagnetic contributions from the CC substrate to the magnetization curves are cancelled out in the determination of $\Delta\mu$ and leave $J_c(H)$ unaffected. All magnetic moment loops presented in the thesis are recorded with the VSM option of the PPMS.
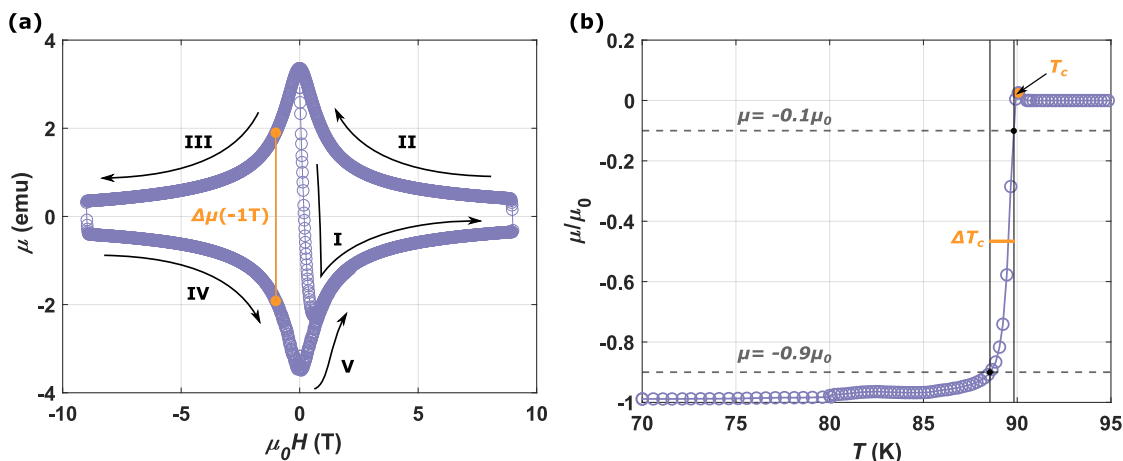
FIGURE 3.8: Magnetization measurements of a SuperPower CC acquired with introduced magnetometers. **(a)** Shown is a full magnetization loop recorded at 20 K with the VSM option. The greek numbers (**I-V**) refer to the sequential order with which the branches are generated. Orange points connected by orange line highlight the width of the magnetization loop at -1 T. **(b)** Normalized magnetization of sample in Meissner state as a function of temperature. The sample is zero-field cooled to 70 K, a small magnetic field 0.2 mT is applied that renders the sample into the Meissner state, and finally warmed up with 0.5 K/min. The onset of magnetization marks the critical temperature T_c (orange point), the transition width ΔT_c (orange line) can be deduced from the distance between the cross sections of $\mu = 0.9\mu_0$ and $\mu = 0.1\mu_0$ with the magnetization curve. Experiment was carried out with a SQUID.

Diamagnetic response

In order to measure the critical temperature T_c and its transition width ΔT_c of a superconducting film with macroscopic dimensions, the sample under investigation is zero-field cooled. Once the starting temperature is reached, an extremely small magnetic field 0.2 mT is applied that provokes the superconductor to fully shield its interior from the external field, i.e. enter the Meissner state. During warming the sample with 0.5 K/min, the magnetic moment of the sample is measured. Since the superconductor turns above T_c into its normal state and looses its diamagnetic signal, we define T_c as the temperature at which the magnetization has its onset. The transition width ΔT_c is here defined as the distance between the temperatures at which the magnetic moment drops to 90 % and 10 % of its extrapolated value at 0 K μ_0. An exemplary measurement corresponding to SuperPower CC is presented in 3.8 **(b)**.

3.3   DC-transport characterization

3.3.1   Experimental means

We employed the PPMS in order to perform electric transport measurements. As already introduced in subsection 3.1.3, a 9 T superconducting magnet and a helium cryostat, which allows for accurate temperature control between 1.8 K and 400 K, are part of the device. For electrical sample characterization, the system includes a nano-voltmeter and a dc/ac current source that can provide currents as low as 1 µA and as high as 2 A with a 0.1 µA resolution. When attaching the CC sample, precautions are taken. Due to the conducting metallic substrate, two squares of sticker paper are placed between sample and a metallic gold covered puck with the purpose to cut electrical contact. Thermal conduction is optimized by applying GE varnish to the sample bottom. Connecting the sample electrically with the puck is realized by means of silver wires with diameter $\varnothing = 50$ µm that are attached to the contact pads with Ag conductive paint. A photograph through the lense of a magnifying glass shows a prepared sample puck in Fig. 3.9.
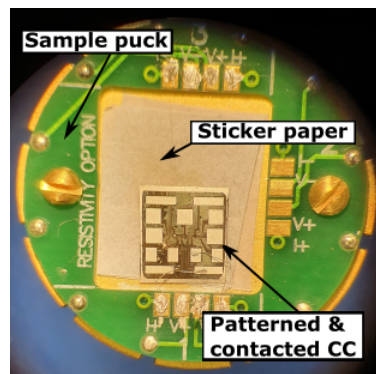
FIGURE 3.9: Top view of a contacted CC sample with well defined bridges attached to sample puck for electrical resistance characterization. Photograph taken through lens of magnifying glass.

As a reference for the set temperature, a thermometer is mounted right below the puck in the sample chamber of the PPMS probe.

3.3.2   Sample configuration

We carried out electrical resistance characterization of REBCO CCs samples in two main configurations, either on pattered samples with well defined bridges or in Van der Pauw geometry. Both techniques are based on 4-point probing to rule out resistance contributions from contacts and leads, and yield equivalent results. In the following, we provide some background to the corresponding configurations.

Patterned bridges

For a material with uniform and known length l, width w and thickness t, the electrical resistivity ρ can be derived from a measured point-point resistance R according to

$$\rho = \frac{wt}{l}R, \tag{3.23}$$

which goes back to G. S. Ohm and his electrical circuit experiments where he discovered the relation between electromotive force, current and resistance in the early nineteenth century [101]. Because of REBCO's enormous current-carrying capabilities, films are usually manipulated into narrow bridges containing structures when faced with electrical pinning properties measurements. A smaller material cross section allows for smaller characterizing currents and hence, minimizes the effect of Joule heating. Although *IV*-curves measurements (see [36, 44, 48] for group internal work on this) for determination of J_c are outside of this thesis' focus, we processed samples with photolithography into structures with $\sim 10 - 100\,\mu$m wide bridges that are fit for future *IV*−curves studies. These samples allow also for determination of electrical resistivity according to eq. (3.23) whose realization steps are going to be reported in the following.

The starting point is always a CC cut into a square shape (side lengths depend on the size of the mask and range between $5 - 8\,\mu$m). We begin with explaining the procedure that corresponds to a naked CC, i.e. a CC stripped off its Ag and Cu layers as provided by some manufacturers. Illustrations of processing steps that support the protocol are given in Fig. 3.10.
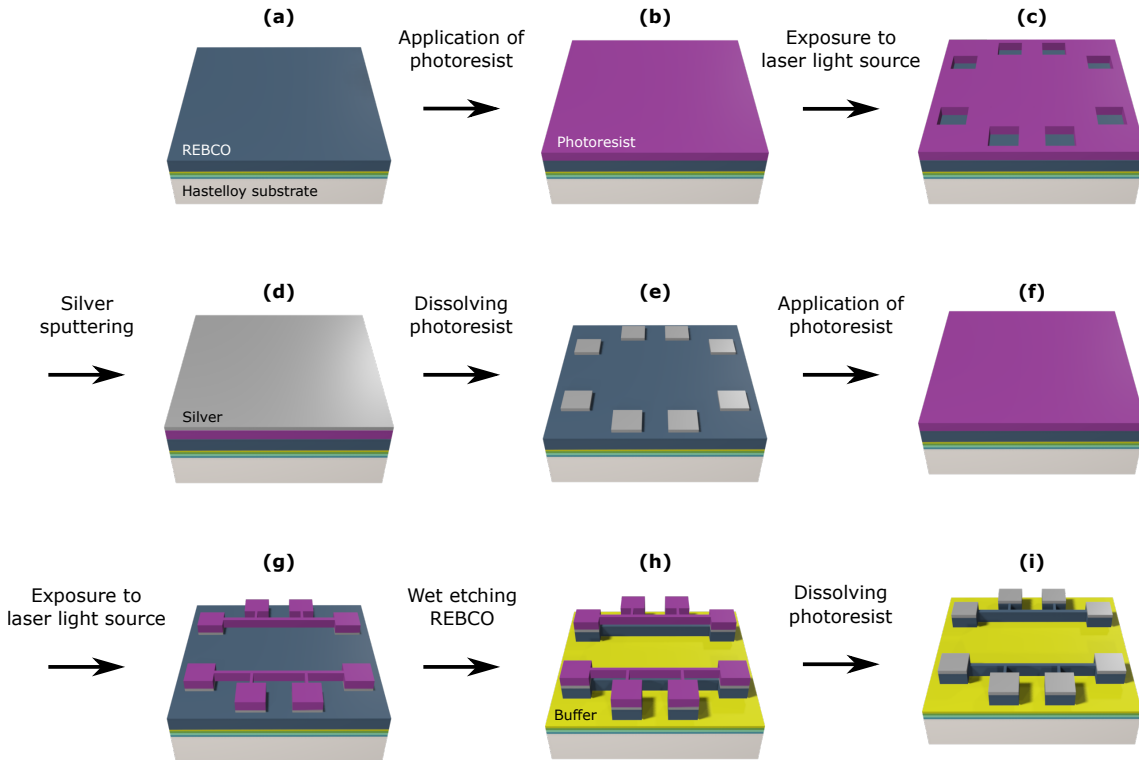
FIGURE 3.10: Illustrations of sample stages when running through process steps that yield a completed electrical circuit for low temperature transport characterization of REBCO. Details are provided in the text.

1. **Creating micro mask for contacts:** The film is first cleaned with acetone in a ultrasonic bath to get rid of organic and ionic impurities (see Fig. 3.10 **(a)**). Next step is spin-coating the sample with a positive photoresist, Microposit(TM) Shipley 1813 (TM), at $a = 5000\,\text{rpm/s}$ and $v = 12\,500\,\text{rpm}$ for 25 s in order to homogenize the resist thickness to $\approx 1\,\mu\text{m}$. Subsequently, the CC is placed on a hot plate kept at 95 °C during 60 s to remove organic solvents from the resist, known as curing (see Fig. 3.10 **(b)**). In a micro-writer by Durham Magneto Optics Ltd., as can be found in the Nanoquim clean room facility, the sample is aligned with a designed mask whose pattern is intended to get transferred to the resist. Then a 385 nm laser light-source operating at spatial resolution $1 - 5\,\mu\text{m}$, illuminates the photosensitive resist through the mask. Stirring the exposed mask in a developer solution (Microposit MF 319) for 45 s removes the activated areas of the photoresist (see Fig. 3.10 **(c)**).

2. **Contact preparation:** Silver deposition takes place in a TSST sputter system, again part of the Nanoquim clean room facility. The masked specimen is passed through a load-lock into the vacuum chamber where a 300-500 nm thick Ag layer is sputtered on the sample (see Fig. 3.10 **(d)**). During deposition a 0.1 mbar argon atmosphere and 350-400 V voltage between target and sample holder are kept. Areas where the silver is not intended to stay get removed in the lift-off process. The sample is cleaned with acetone in a ultrasonic bath during few seconds which carries away all the Ag sitting on resist, leaving behind the Ag deposited directly on the REBCO surface (see Fig. 3.10 **(e)**). In order to minimize Joule heating during electrical characterization at low temperatures, low contact resistance or interface resistance between the silver and superconductor are desired. To this end, the sample undergoes thermal treatment inside a quartz tube in a tubular furnace at 450 °C for 1 h in 0.12 L/min oxygen flow. The exact temperature profile is given in Fig. 3.11. At this annealing conditions only small modifications to the micostructure are expected [102].
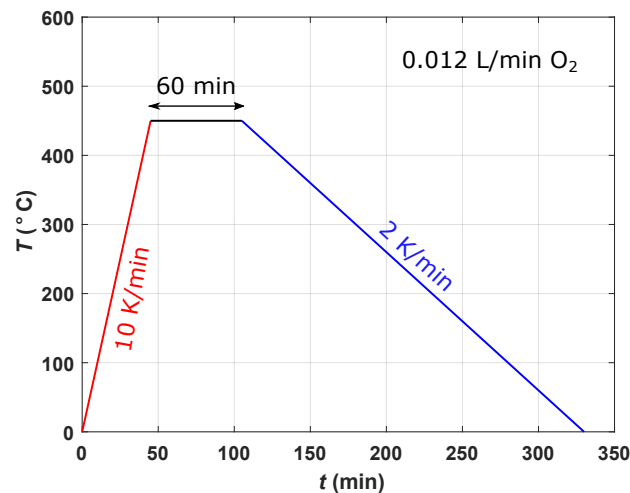
FIGURE 3.11: Thermal profile of Ag contacts annealing process.

3. **Patterning bridges:** In a second photoresist work, a new mask is created. This time with a pattern that outlines the entire electrical circuit, i.e. narrowed REBCO bridges, REBCO contact leads and the Ag contacts itself (see Fig. 3.10 **(g)**). The procedure runs analogously to the descriptions given earlier. Once the new mask is developed, one final step remains: the etching of excess REBCO in water diluted H_3PO_4. All REBCO which is unprotected by the photoresist is etched away transferring the micropattern of the resist to the sample (see Fig. 3.10 **(h)**). A common problem to occur with wet etching techniques is the over-etching. It is the undeliberate thinning of the REBCO bridges beyond the nominal values owing to the acid leaking below the photoresist and

attacking there the superconductor. This effect can be minimized by using solutions with moderate etching rates. We found freshly prepared 1:20 H_3PO_4:H_2O save to use as it has an etching rate of about $5\,nm/s$. Finally the residual photoresist can be removed with acetone. An example of a patterned sample is shown schematically in Fig. (see Fig. 3.10 (**h**)) and through a microscope in Fig. 3.12.
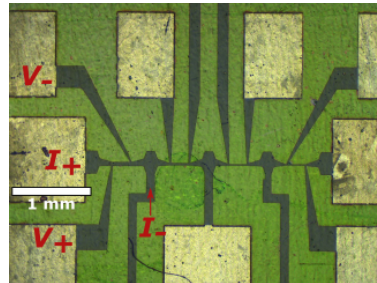
FIGURE 3.12: Optical microscope image of CC after deposition of Ag contacts (shiny yellow) and processing the REBCO (dark grey) into well defined bridges and contact leads. The greenish area are exposed buffer layer which usually lie below the REBCO. The current and voltage labels represent the correct contacting for a 4-point resistance measurement of the first bridge. Shown sample is based on a SuperOx CC.

CC manufacturer have some flexibility in which form they provide their CCs. Typical types are naked CCs, i.e. no Ag and Cu capping, or CCs with either Ag or Ag+Cu deposited on REBCO. Using Ag terminated CCs for electrical transport characterization can be advantageous with regard to the sample preparation. Silver employed by the providers serves as a catalyst for oxygen transfer during the oxygenation process carried out with a temperature profile that yields extremely low contact resistances. The possibility of exploiting the Ag deposited by manufacturer as electrical contacts would save us the sputtering process and thermal treatment associated to the Ag annealing.

To this end, we developed a completely top-down micropatterning routine that starts with an Ag covered CC and yields a sample ready for electrical transport measurements. Fig. 3.13 illustrates the most relevant stages during the sample processing.

1. **Patterning bridges:** Since silver is already present in the stack of layers (see Fig. 3.13 (**a**)), the first photolithography measure is drawing the outline of the finished electrical circuit onto hardened photoresist. Once the mask is developed (see Fig. 3.13 (**c**)), the unprotected Ag is etched with a solution of 1:1:x NH_3:H_2O_2:H_2O, with $x = 4 - 20$ controlling the reaction violence. The now exposed REBCO (see Fig. 3.13 (**d**)) is in turn wet etched, too. Here, special care has to be taken, due to risk of over-etching. After removing the resist, the pattern of the photolithography mask is transferred to the Ag+REBCO layers (see Fig. 3.13 (**f**)).

2. **Removing residual silver:** The next step targets the elimination of the Ag shunt above the REBCO bridges. Engaging with micropatterning, a new mask is created that covers only the contact areas (see Fig. 3.13 (**h**)). Exposed silver is then etched away with described solution (see Fig. 3.13 (**i**)). The processing has finished after dissolving the resist in acetone (see Fig. 3.13 (**j**)).

Van der Pauw method

In 1958, J. L. van der Pauw addressed the issue of labor-intensive preparation of samples into specific forms (bar or bridge) before an electrical sample characterization was possible. In his report, he elaborated on a theorem, the Van der Pauw method, that allows the measurement of the specific resistivity and Hall effect of conducting discs with arbitrary shape [103]. The proposed theorem applies for conducting samples that fulfill four conditions.
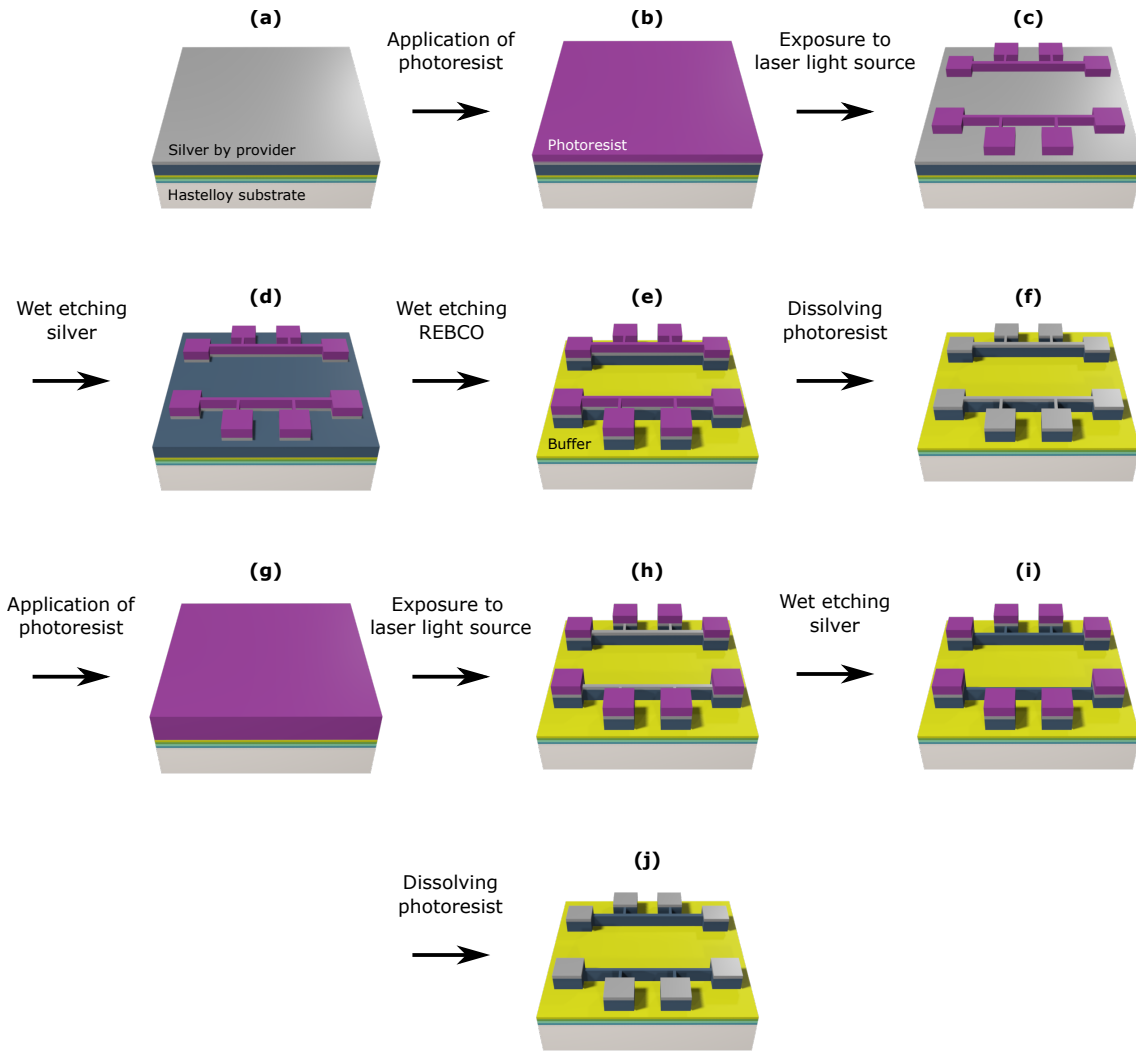
FIGURE 3.13: Illustrations of sample stages when running through process steps starting with an Ag coated CC and ending up with a completed electrical circuit for low temperature transport characterization of REBCO. Details are provided in the text.

1. The contacts are placed on the sample edges.

2. The contacts are sufficiently small. It can be shown that a finite contact size with diameter d introduces an error on the calculated specific resistivity according to $\sigma_\rho/\rho \sim d^2/D^2$, where D is the sample diameter [103].

3. The sample must not exhibit isolated holes.

4. The sample exhibit a homogeneous film thickness.

Having an eligible sample, it is possible to calculate the specific resistivity ρ, as a function of two measured resistances $R_{\mathrm{AB,CD}}$ and $R_{\mathrm{BC,DA}}$ and film thickness t according to

$$\rho = \frac{\pi \cdot t}{\ln 2} \frac{R_{\mathrm{AB,CD}} + R_{\mathrm{BC,DA}}}{2} f\left(\frac{R_{\mathrm{AB,CD}}}{R_{\mathrm{BC,DA}}}\right). \tag{3.24}$$

The first two indices of the resistance quantity define the contacts between which the current is applied and the second two between which the voltage is read. In particular, we have

$$R_{\text{AB,CD}} = \frac{V_{\text{D}} - V_{\text{C}}}{I_{\text{AB}}}, \tag{3.25}$$

$$R_{\text{BC,DA}} = \frac{V_{\text{A}} - V_{\text{D}}}{I_{\text{BC}}}. \tag{3.26}$$

The correction factor $f(\frac{R_{\text{AB,CD}}}{R_{\text{BC,DA}}})$ is calculated by solving

$$\cosh(\frac{R_{\text{AB,CD}}/R_{\text{BC,DA}} - 1}{R_{\text{AB,CD}}/R_{\text{BC,DA}} + 1} \frac{\ln 2}{f}) = \frac{1}{2} \exp \frac{\ln 2}{f} \tag{3.27}$$

and is a function of the resistance ratio which starts at one for $\frac{R_{\text{AB,CD}}}{R_{\text{BC,DA}}} = 1$ and decreases towards zero for $\frac{R_{\text{AB,CD}}}{R_{\text{BC,DA}}} > 1$ [103]. For in this thesis presented data, f usually stays within less than 1 % close to 1. We display a scheme of samples in van der Pauw geometry in Fig. 3.14.
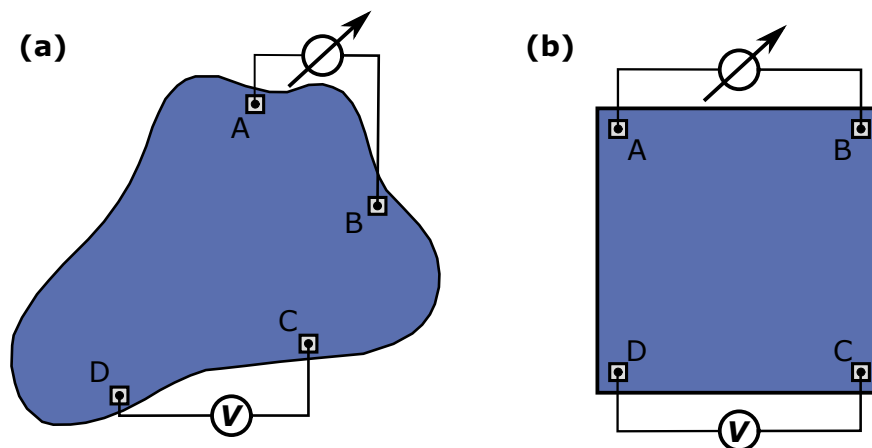
FIGURE 3.14: Schematic representation of samples in van der Pauw geometry with contacts A,B,C and D. Source and voltmeter are applied to measure $R_{\text{AB,CD}}$. **(a)** A sample of arbitrary shape. **(b)** A squared samples as used for resistivity characterization in this thesis.

For characterization with the Van der Pauw method, CCs are cut into approx $5 \times 5\,\text{mm}^2$ pieces. A photoresist mask designed to define the area and location of the contacts is deposited on to the sample. By means of DC-magnetron sputtering, we cover the masked CC with a thin layer (approx. $300\,\text{nm}$) of Ag. Cleaning the sample with acetone, the photoresist dissolves and removes all the unintentional Ag from the surface, leaving only well defined contacts behind. Here, the contacts are chosen to be $0.5 \times 0.5\,\text{mm}^2$ in area and placed into the sample corners keeping a distance of $300\,\mu\text{m}$ from the edges. Prepared samples resemble schematically the illustration in Fig. 3.14 **(b)**.

Chapter 4

Architectures and superconducting properties of REBCO coated conductors

Nowadays, a wide variety of second generation coated conductors produced in large scales (several thousands of km per year [104, 105]) are available on the market. In attempts to unlock the huge potential of REBCO, the industry has diversified and matured the CC technology immensely by developing different REBCO tape architectures and efficient production plants [106]. Growth process tuning and quality control tools gave rise to a new discipline for material scientists in this sector: microstructure engineering of the superconductor. Depending on the targeted application, suppliers grow either highly ordered, rather clean HTS for optimized operation at zero field and high temperatures or trigger imperfections like normal-conducting precipitations [107], dislocations [108] and/or add non-superconducting particles to introduce nanoscale defects into the REBCO matrix. Latter are known as artificial pinning centers (APCs) and reduce vortex mobility which improves performance at high magnetic fields [109]. The richness in available applications for REBCO CCs, power cables, rotating machines, high-field magnets (to name a few), propagates to the variety in optimal microstructures. However, the contextualization of REBCO CCs in the realm of microwave applications is new and thus, marks the field where the potential for microstructure optimization is still untapped. This fact incites the motivation to study a range of different CCs as potential beam screen coating. A goal of this thesis is to identify the most beneficial defects and propose a microstructure optimization recipe to the suppliers targeting this specific application at high frequencies. This chapter builds the foundation of our aim by studying the superconducting properties in DC regime demonstrating links to REBCO microstructure. Moreover, the DC properties of studied superconductors are examined in terms of possible operation in the FCC-hh beam screen chamber. They have to guarantee lossless operation despite challenging conditions. This aspect will be investigated, too.

Six industrial providers, Bruker HTS GmbH, Fujikura Ltd., SuNAM Co. Ltd., SuperOx, SuperPower Inc. and THEVA Dünnschichttechnik GmbH, participate with eight CCs in this work.

The first gatekeepers to check the compatibility of CCs with the beam screen chamber are the envisioned 25 A image currents induced by proton brunches at 16 T dipole field and 50 K operation temperature within the FCC-hh. These represent extreme conditions for the superconductor to sustain the superconducting state and implicitly, the potential advantages over copper. In order to generate lucidity, we characterize the classical superconducting properties of the REBCO layers. First, we extract material specific resistivities, critical temperatures and irreversibility fields with self and in-field resistance versus temperature measurements as shown in section 4.2. Second, we calculate the critical current density as a function of magnetic field up to 9 T at several cryogenic temperatures by means of inductive measurements in section 4.3. Besides testing for maximum current carrying capability, we will draw links between microstructure and in-field behavior of the CCs by fitting the $J_c(H)$ curves. Generated conclusions on the interplay between microstructure and superconducting properties in DC regime will be picked up in the next chapter, where we

analyze the high frequency properties of REBCO CCs under study.

Before jumping to the electrical characterization, we start by introducing the CCs' architectures and growth methods that carry implications for the microstructures in section 4.1.

4.1   Architectures of studied REBCO CCs

The eight CCs studied within this thesis are provided by six different manufacturer, that produce pieces of hundreds of meters length [110] with industrial throughput [106]. The corresponding characterizing key parameters and tape architectures are listed in table 4.1. The relevance of given characteristics is broken down in the following.

Samples	REBCO layer	Artificial pinning centers	Growth techn.	Buffer	Substr.
Bruker [111, 112]	YBCO (1.6 µm)	BZO nanorods	PLD	Y-stabil. Zr (2 µm)/ CeO$_2$ (70 nm)	Stain. steel (100 µm)
Fujikura [113]	GdBCO (1.8 µm)	-	PLD	Al$_2$O$_3$/Y$_2$O$_3$/MgO/ CeO$_2$ (700 nm)	Hastelloy (75 µm)
Fujikura APC [114]	EuBCO (2.5 µm)	BHO nanorods	PLD	Al$_2$O$_3$/Y$_2$O$_3$/MgO/ CeO$_2$ (700 nm)	Hastelloy (50 µm)
SuNAM [115, 116]	GdBCO (1.5 µm)	-	RCE-DR	Al$_2$O$_3$(40 nm)/Y$_2$O$_3$(7 nm)/ MgO(10 nm)/MgO(20 nm)/ LMO(20 nm)	Hastelloy (100 µm)
SuperOx [117, 118]	GdBCO (0.9 µm)	-	PLD	Al$_2$O$_3$(50 nm)/Y$_2$O$_3$(40 nm)/ MgO(6 nm)/LMO(40 nm)/ CeO$_2$(150 nm)	Hastelloy (60 µm)
SuperOx 2 [104]	YBCO (3 µm)	Y$_2$O$_3$ nanoparticl.	PLD	Al$_2$O$_3$(40 nm)/Y$_2$O$_3$(7.5 nm)/ MgO(6 nm)/MgO(100 nm)/ LMO(40 nm)	Hastelloy (40 µm)
SuperPower [119, 120]	[Gd,Y]BCO (1.3 µm)	BZO nanorods	MOCVD	MgO(10 nm)/MgO(30 nm)/ LMO (30 nm)	Hastelloy (50 µm)
Theva [121–123]	GdBCO (up to 2.8 µm)	-	EB-PVD	ISD MgO(2.5 µm)/ MgO(300 nm)	Hastelloy (100 µm/ 50 µm)

TABLE 4.1: Characterizing parameters and stack architectures of analyzed CCs.

The choice of rare-earth element sets the upper limit of achievable critical temperature T_c and can have an impact of the irreversibility field. The REBCO film thickness, determined with a profilometer for samples with etched steps, scales the expected current carrying capabilities and magnetic moments of magnetized samples given a J_c.

The artificial pinning centers can constitute an important part of REBCO's microstructure. They represent non-superconducting phases which are deliberately added to the initial REBCO composition in order to achieve better vortex pinning. The non-superconducting phases, here for example, the perovskites BaZrO$_3$ (BZO) and BaHfO$_3$ (BHO) or the Y$_2$O$_3$, which belong to the phase diagram of YBCO, are used. They have to be of diameter $\approx \xi$ in order to offer vortex immobilization. Their distribution is homogeneous and the average distance among them is 10-30 nm. This nanotechnology is especially applied for CCs which target operation in high magnetic field applications [46].

One of the main determinants for the type of grown REBCO microstructure is the growth technique. It relates to the degree of supersaturation during the film growth, growth kinetics and direction [17]. Pulsed laser deposition (PLD) [124] favors with high deposition rates an abundance of very mobile atoms and thus, high supersaturation

levels. It yields high nucleation rates, fine crystallites and strong drive for vertical growth. Defect hallmarks are 2D grain boundaries and optionally, APCs through the addition of non-stochiometric functional oxides in the growth process resulting in columnar rods [125] and randomly distributed 3D particles [126]. These APCs can be grown heteroepitaxially with REBCO [127]. The defect density of associated films is very large and operation best suited to in-field applications.

Theva produces their HTS tapes by a electron-beam physical vapor deposition (EB-PVD) technique in the so-called inclined substrate deposition (ISD) geometry. Importantly, the first MgO buffer layer is thermally evaporated and reactively grown on a Hastelloy substrate that is tilted by 25-30° with respect to the incoming MgO vapour [128]. Due to shadowing effects, only MgO grains with good in-plane alignment and a distinct surface angle survive leaving a terraced surface [129]. An additional thin MgO layer, deposited in normal incidence, homogenizes the surface for subsequent GdBCO growth. GdBCO nucleates on the inclined (200) MgO plane which features a *c*-axis inclined by roughly 27° to the substrate normal and lateral overgrowth of secondary phases or misoriented grains, due to the staircase structure of the ISD MgO layer resulting in very high active HTS thicknesses [122]. Growth on staircase MgO terraces limits the grain sizes of the HTS to the size of the terraces which is in the order of 200 nm [129]. Although, physical vapor deposition is linked to high to moderate supersaturation growth, characteristics of associated microstructures are superimposed by the mentioned features typical for ISD.

MOCVD, short for metal-organic chemical vapour deposition, uses a precursor gas mixture which undergoes pyrolysis before it is injected through showerheads on hot substrates. Multizone showerheads with each zone plumbed to different precursor composition allows continuous time and spatial variation of the film composition [130]. The growth is associated to moderate supersaturation and the same defect types occur as found for PLD growth but with a lower density [17].

Reactive co-evaporation deposition and reaction (RCE-DR) [115, 131] counts as a low supersaturation method. First, amorphous precursor films are co-evaporated with an e-gun at low temperatures under low oxygen pressure. The second step consists of a ex-situ reaction to transform the precursor film via a liquid reaction into REBCO under elevated temperatures and high oxygen pressure. With an off-stoichiometric composition, precipitations of secondary phases can be triggered. Owing to the low supersaturation and the 2D-like REBCO growth, uncorrelated defects like randomly distributed 0D point-like defects and big 3D nanoparticles prevail instead of columnar defects [17]. These samples with overall lower defect densities exceed at high temperatures and low fields operation.

We show in Fig. 4.1 a visual representation of the typical microstructural features corresponding to the growth methods as reported in [17].

In addition, the processing method serves also as an indicator for production pricing since the costs associated with vacuum and laser equipment or operation are considered to be higher than chemical methods.

Each layer of the buffer layers fulfills a specific function, e.g. passivation, planarization and texturing. The buffer layer sequence given in table 4.1 begins with layer closest to substrate and ends with layer closest to REBCO. For the specific case of characterizing the bottom surface of REBCO in the context of CC assembly to metallic surfaces for high-frequency applications, see chapter 6, the type of used buffer layers becomes relevant from a microwave performance viewpoint.

The last characteristic we provide is the substrate and its thickness. The limitations of substrates are governed by the necessity for biaxially textured REBCO growth compatibility. The substrate thickness is another important parameter. The superconducting performance J_c is often normalized by the total CC thickness to give rise to the engineering critical current density J_e that reflects the achievable power density of devices consisting of several stacked CCs. Consequently, thinner substrates can reduce the costs of CC based devices because of its higher J_e. This factor has led
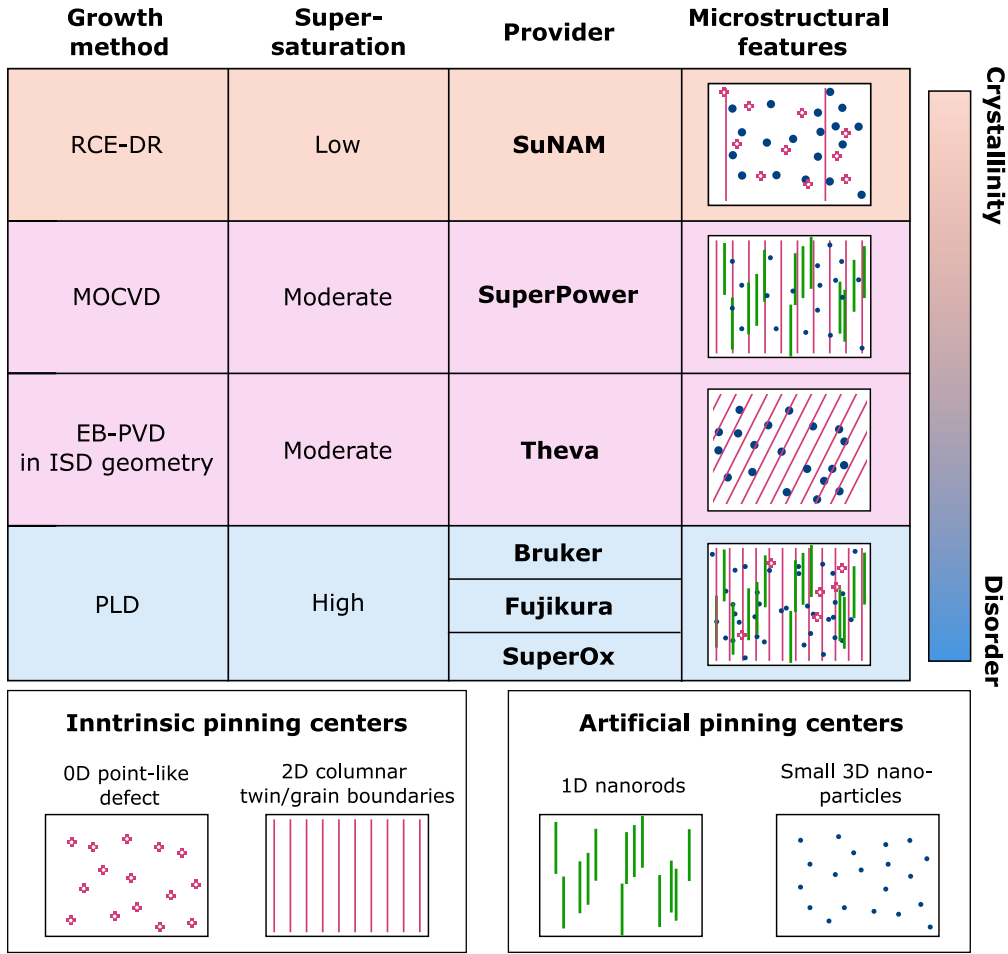
FIGURE 4.1: A schematic linking of growth method to typically generated REBCO microstructure. Upon increase of supersaturation, the amount of correlated pinning centers rises (2D grain boundaries and potentially 1D nanorods), i.e. the disorder. On the one hand, it might cause current blocking, but on the other hand, more defects are available for vortex pinning. The amount, dimension and distribution of generated defects can be tuned within each growth method. For example, Fujikura provides one CC with BHO nanorods (denoted Fujikura APC) and one CC without any APCs (denoted simply Fujikura), although both CCs are grown with PLD. A similar case is made for SuperOx who grow their CC with PLD, too. One type of their CC has small and randomly distributed Y_2O_3 nanoparticles acting as APCs (named SuperOx 2), their other CC type does not employ any APCs (denoted simply SuperOx). Note that rather big 3D nanoparticles, for example secondary phases, can emerge natively during growth (see SuNAM or Theva) and hence, are not considered as APCs. Visualization inspired by [17].

to substrate thickness reduction initiatives within the community [132].

4.2   Characterization of electrical properties from resistance measurements

4.2.1   Resistivity and critical temperature

An integral part of superconducting property characterization resides in electrical resistance measurements. At zero-applied field, one can extract the resistivity curve $\rho(T)$, the critical temperature T_c as well as its transition width ΔT_c. All three are control parameters for the film quality and outline the maximum operation temperature for superconductivity applications without applied magnetic field.

We present the electrical *ab*-plane resistivities ρ^1 as a function of temperature at zero applied magnetic field for all studied CCs in Fig. 4.2 **(a)**.
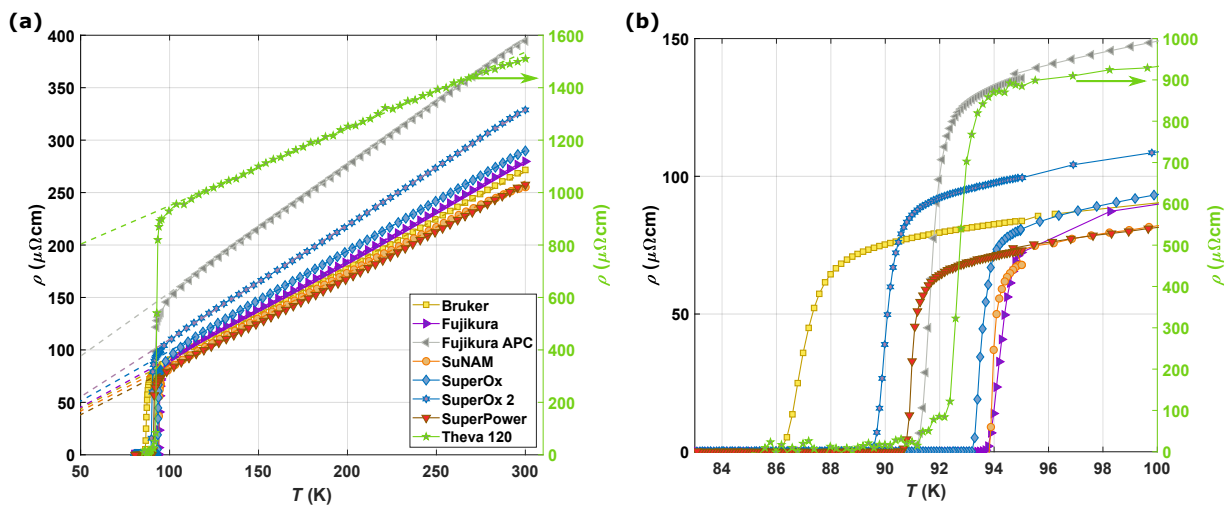
FIGURE 4.2: Characterization of transport properties based on electrical resistance measurements. **(a)** The resistivity ρ as a function of temperature at zero applied field for all studied CCs. The normal-state resistivity below the superconducting transition is extrapolated from linearly fitting the decrease in $\rho(T)$ within the temperature range 105 K-285 K and is displayed as dashed lines. **(b)** Zoom into the superconducting transition. The differences in T_c and ΔT_c among the samples are well appreciable. Both figures share the same legend and the right ordinate corresponds to Theva 120.

In the normal-state, so for temperatures above T_c, the resistivity follows a linear, metal-like behavior as observed for optimally doped YBCO samples [133, 134]. In order to acquire normal-state resistivity for temperatures below T_c, which will become important in chapter 5, we fit the linear resistivity behavior between 105 K and 285 K to describe the normal-state resistivity according to

$$\rho_n(T) = c \cdot T + \rho_0, \qquad (4.1)$$

where ρ_0 represents the resistivity at absolute zero temperature and c the resistivity slope.

The normal-state resistivities vary considerably among the CCs and represent electronic scattering with different defect landscapes [135] and hole doping states of REBCO [133]. Although the introduction of APCs to the superconductor causes defects in the REBCO matrix, it does not necessarily govern the measured resistivity as visible for two tapes that incorporate both APC nanorods. Fujikura APC marks the second highest $\rho(300\,\text{K})$, while SuperPower displays the lowest $\rho(300\,\text{K})$. This trend remains valid down to temperatures below T_c as visible in the linearly extrapolated normal-state resistivity shown in Fig. 4.2 **(a)**. Hence, the differences in $\rho(T)$ cannot be exclusively ascribed to the introduction of APC but depend on the electron scattering with the overall microstructure, crystallinity and doping state of the sample.

Presented data is in accordance with previously reported values for high crystalline quality, close to optimally doped YBCO [133, 136]. With the exceedingly high normal-state resistivity, the CC by Theva presents an exception. The *c*-axis of this REBCO tape is tilted by 27 degrees with respect to the substrate normal, transversely to the tape length [122]. For this sample the resistivity was measured in Van der Pauw geometry (see paragraph 3.3.2), so current flow was driven both within *ab*-planes and along the *c*-axis. Owing to the intrinsic electronic mass anisotropy of REBCO, electrons flowing along the *c*-axis have a higher effective mass than those flowing along the *ab*-planes which explains the increased resistivity [14]. We should note that the electric field distribution of the TE_{011} mode in our DR gives rise to analogous inter *ab*-planes current flow for Theva samples.

---

[1]Calculated according to eq. (3.23) and eq. (3.24).

A zoom into the superconducting transition is displayed in Fig. 4.2 **(b)**. We determine both the critical temperature T_c and the superconducting transition width ΔT_c from $\rho(T)$, taking into account the temperature gradient $\frac{d\rho}{dT}$. T_c follows the maximum derivation criterion, as described in [137], and ΔT_c is extracted from the derivation peak's full width at half maximum. As way of example, we visually demonstrate the determination method of T_c and ΔT_c for SuperOx 2 CC in Fig. 4.3. An overview of the calculated T_c and ΔT_c can be found in table 4.2.
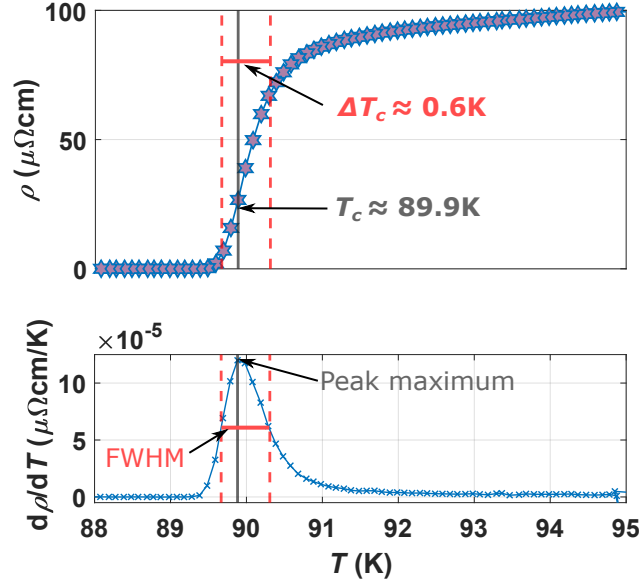
FIGURE 4.3: Visual demonstration of how we determine T_c and ΔT_c from $\rho(T)$. Shown data corresponds to SuperOx 2.

The transition temperature lies for all CCs, as expected, around 90 K. Referencing the envisioned 50 K beam screen operation temperature, the high critical temperature of REBCO CCs towers above the required threshold and entitles this material class as a natural beam screen coating option. Not of highest relevance for the FCC-hh but interesting from a scientific standpoint, the transition temperature between studied CCs vary by more than 7 K. This large spread in T_c suggests that some providers have optimized their CCs for specific applications in a way where sacrifices in T_c have been taken to gain in other quantities.

As a highly correlated electron system, REBCO's complex phase diagram is spanned by the temperature T and doping level p (which is controlled by the oxygen deficiency δ) [51]. The phase diagram shows that superconductivity occurs for a narrow range of p in which T_c follows approximately a dome shape whose maximum marks the optimally doped state. The two shoulders correspond to the under- and overdoped region of superconductivity. As an extension of this, the choice of employed rare-earth affects T_c, too. It is reported that for slightly overdoped samples, increasing the ionic radius of the rare-earth causes strain-induced charge redistribution between the charge reservoir and the transport carrying CuO_2 planes resulting in lower charge carrier density n and an increase of T_c [138].

In agreement with it, we measure $T_c < 91$ K for Y (smallest ionic radius) based CCs, for SuperPower with Y-Gd mixed rare-earth $T_c = 91$ K and for Gd or Eu (largest ionic radii) based CC $T_c > 91$ K.

The transition width ΔT_c is for all CCs quite sharp and ranges between 3 K and 1.1 K. Small ΔT_c, below 2 K, point usually towards close to optimal oxygenation and/or high film homogeneity [40].

4.2.2 The irreversibility line

Resistance versus temperature characterization with applied magnetic field, where now the penetration of vortices into the specimen governs the superconducting state, allows a determination of the irreversibility field H_{irr} and irreversibility temperature T_{irr}. Both quantities combined represent the coordinates of the irreversibility line. Since the irreversibility line marks a solid-liquid phase transition in the $H - T$ map at which thermal energies give rise to a resistive vortex state and hence, it limits the appeal window for in-field applications. The expression that describes the irreversibility line when the magnetic field is applied along the c-axis is given by[139, 140]

$$\mu_0 H_{irr} = \mu_0 H_{irr}^0 (1 - \frac{T_{irr}}{T_c})^\beta, \tag{4.2}$$

where H_{irr}^0 and β represent fitting parameters.

In Fig. 4.4 (a), we show the resistive transition to the superconducting state for a Bruker sample at several magnetic fields applied normal to the substrate plane. The transition to the superconducting state broadens as the magnetic
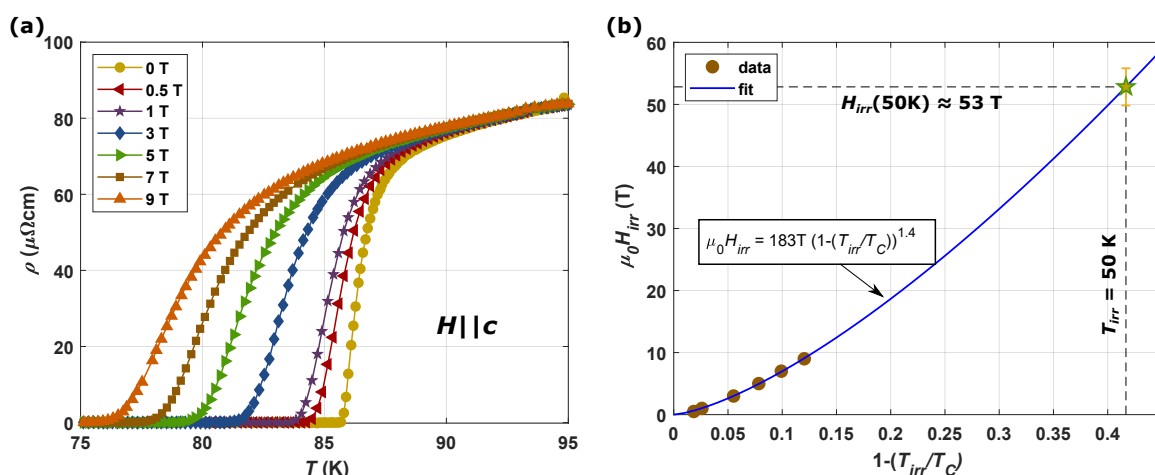
FIGURE 4.4: **(a)** Resistivity curves for Bruker sample at different magnetic fields applied along the c-axis **(b)** Shown are determined H_{irr} according to eq. (4.3) (markers) and a fit to the data with eq. (4.2). From the fit, we can estimate the irreversibility field to amount $\mu_0 H_{irr}(50\,\text{K}) = 53\,\text{T}$. The error on $H_{irr}(50\,\text{K})$ was estimated from T_{irr} criterion variations to be $\sigma_{H_{irr}(50\,\text{K})} = 3\,\text{T}$.

field increases. This phenomenon can be attributed to the presence of disorder that affects the vortex motion in the liquid state. In order to determine the irreversibility temperature T_{irr} at each field H_{irr} from the $\rho(T)$ data, we use the criterion

$$\rho(T_{irr})/\rho(95\,\text{K}) = 0.1\,\%. \tag{4.3}$$

We fit the irreversibility temperature and field with equation (4.2) to reconstruct the irreversibility line for the REBCO layer of the CC[2], as shown in Fig. 4.4 **(b)**. The fit with eq. (4.2) enables an estimation of the irreversibility field at 50 K, the operation temperature of the FCC-hh beam screen. For the Bruker specimen, we find that $\mu_0 H_{irr}(50\,\text{K}) = 52 \pm 3\,\text{T}$ surpassing the maximum 16 T by a good margin. Although, the extrapolation to 50 K is quite far away from our measurement points, we find reasonable agreement with literature. Experimentally determined values from 61 T-pulsed magnetic field measurements for a pristine YBCO crystal yield $\mu_0 H_{irr}(50\,\text{K}) \approx 43\,\text{T}$ [141, 142], while the inclusion of nanoparticles can lead to even higher irreversibility fields [43, 46, 143].

The fitting parameters for Bruker give $\mu_0 H_{irr}^0 = 183\,\text{T}$ and $\beta = 1.4$ and range for all CCs between $\mu_0 H_{irr}^0 = 97 - 190\,\text{T}$ and $\beta = 1.2 - 1.6$. It is proposed that eq. (4.2) could arise from the flux pinning model [140]. Hence, H_{irr}^0 and β

---

[2]For consistency reasons T_c was determined here with the criterion $\rho(T_c)/\rho(95\,\text{K}) = 0.1\,\%$.

vary according to the present defect pinning landscape and provide links to the microstructure of the material. In accordance with our results, many authors found β values spanning from 1 to 2[144–148]. The fitting values for all providers are given in table 4.2.

The irreversibility lines of all analyzed CCs, but Theva because the inclined *c*-axis prevents the validity of eq. (4.2) for these samples, are compared in Fig. 4.5.
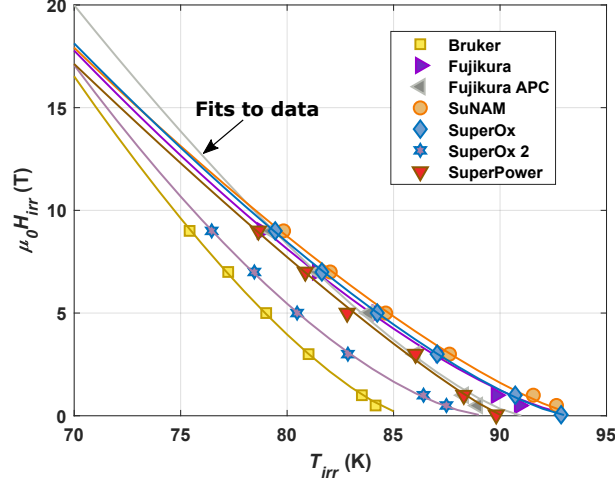
FIGURE 4.5: The irreversibility line for all analyzed CCs from resistive transitions (markers) and corresponding fits with eq. (4.2) (lines).

Two trends are observed. On the one hand, Y based CCs, Bruker and SuperOx 2, exhibit due to the decreased T_c smaller $\mu_0 H_{irr}$ at high temperatures, but surpass the irreversibility line of other CCs for temperatures > 70 K (see $H_{irr}(50\,\text{K})$ in table 4.2). Rare-earths with smaller ionic radius cause higher charge carrier densities n in the superconducting CuO_2 plane [138] and lower electronic anisotropy resulting in higher H_{irr} [104, 149].

On the other hand, the samples Bruker, Fujikura APC and SuperOx 2, all CCs with APCs, display the highest $\mu_0 H_{irr}^0$. As discussed earlier, the introduction of APC into the REBCO matrix causes various defects and thus affects β and H_{irr}^0, both determinants of the irreversibility line. SuperPower CC presents an exception to both observations, since it employs Y mixed with Gd as a rare-earth and uses BZO nanorods, without showing the characteristic features. Possibly, the MOCVD growth process generates a defect structure that undermines the characteristics associated to employing Y and nanorods APCs, see the low β and $\mu_0 H_{irr}^0$.

Discussed quantities derived from $\rho(T,H)$ are summarized for all CCs in table 4.2.

Provider	$\rho(300\,\text{K})$ ($\mu\Omega$cm)	$\rho(100\,\text{K})$ ($\mu\Omega$cm)	$T_c^{der.}$ (K)	ΔT_c (K)	$\mu_0 H_{irr}^0$ (T)	β	$\mu_0 H_{irr}(50\text{K})$ (T)
Bruker	272	91	86.7	1.1	183	1.42	53
Fujikura	280	90	94.1	0.8	126	1.42	43
Fujikura APC	395	150	91.6	0.7	145	1.35	49
SuNAM	255	82	93.9	0.3	109	1.32	43
SuperOx	290	94	93.4	0.5	119	1.36	45
SuperOx 2	329	108	89.9	0.6	190	1.58	52
SuperPower	258	81	91.0	0.3	97	1.16	38
Theva	1510	929	92.7	0.7	-	-	-

TABLE 4.2: Quantities derived from $\rho(T)$ curves at different magnetic fields applied parallel to the substrate plane of the CCs.

4.3 Critical current under applied magnetic field

HTS can sustain a limited current flow before the Lorentz-like force overcomes the pinning force and renders the material resistive. As shown in eq. (2.4), the Lorentz-like force is a function of current density and applied magnetic field. In the context of the FCC-hh, it becomes essential to check whether the CCs can sustain the 25 A peak mirror charges at 16 T and 50 K without being driven into the normal state. Before entering the experimental results, it is instructive to discuss the magnetic field intensity dependence of J_c.

4.3.1 Magnetic field dependence of J_c

Equation (2.3) describes a starting point to understand the phenomenology related to vortex penetration into the superconductor. The augment of applied magnetic field H is accompanied by a vortex density n_v increase which divides up $J_c(H)$ in three different pinning regimes as shown in Fig. 4.6.
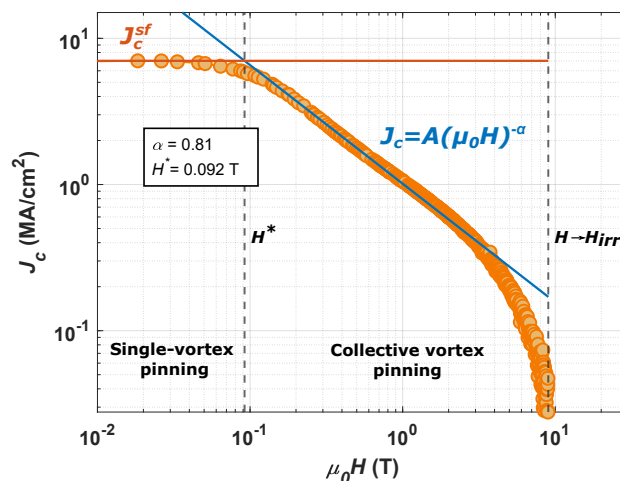
FIGURE 4.6: Typical magnetic field dependence of J_c with pinning regimes indicated in the plot. We define the characteristic field H^* as the crossing between the small magnetic field plateau J_c^{sf} (red line), which corresponds to single-vortex pinning, and the tangent to the power law decay at intermediate fields (blue line) associated with collective, or vortex-vortex, pinning where interactions between vortices dominate. Approaching the irreversibility field H_{irr}, an even faster drop of J_c is observed. As way of example, we picked the $J_c(H)$ that corresponds to SuNAM CC at 60 K.

In the single-vortex pinning regime, there are fewer vortices than pins. The vortex matter is characterized by large distances between fluxon lines resulting in weak vortex-vortex but strong vortex-defect interaction. All vortices are pinned individually. Here, $J_c(H)$ depends only weakly on the magnetic field and can be approximated with $J_c(H) \sim J_c^{sf}$, where J_c^{sf} is the critical current density that the HTS can withstand at self-field (sf), the magnetic field arising from the current itself [150, 151].

Upon increase of the magnetic field intensity, the crossover field H^* is reached that is associated with a transition in pinning regime. Beyond this boundary, collective effects become more relevant than the vortex-defect interaction. For correlated pinning sites [152] and without strong thermal excitation [153], H^* is often associated with the matching field H_Φ, the field at which the vortex line density n_v matches the defect density n_d. As a result, the mean distance between defects d_{pc} coincides approximately with the hexagonal side length $s \approx d_{pc}$.

Passing the crossover field H^*, collective pinning effects gain relevance and the magnetic field behavior changes from a plateau to a power law decay of the form

$$J_c(H) = A(\mu_0 H)^{-\alpha}, \tag{4.4}$$

where A and α are constants. Theoretical approaches analyzing the vortex-vortex interaction predict $\alpha = 0.5 - 1$ [154–156], which is in agreement with experimentally obtained values from fittings [157]. Nanostructuring of YBCO thin films lead to a even wider range in the power law exponent α reaching even values between 0.25 and 1.2 [157–160].

Approaching the irreversibility field H_{irr}, J_c's sensitivity to the magnetic field becomes stronger and it drops very fast to zero.

Phenomenologically, the entire J_c can be described by one single equation that includes the characteristic parameters [161]:

$$J_c(H) = J_c^{sf} \left[1 + \frac{H}{H^*} \right]^{-\alpha} \left[1 - \frac{H}{H_{irr}} \right]^2. \tag{4.5}$$

This equation will be later employed for J_c extrapolation to 16 T, the maximum field in the FCC-hh.

4.3.2 Experimental results

Comparing critical current density at 50 K

The critical current density as a function of magnetic field $J_c(H)$ of all analyzed CCs measured with a VSM at 50 K is displayed in Fig. 4.7 **(a)**. The CCs provided by the manufacturers are 12 mm in width. Owing to restricted sample
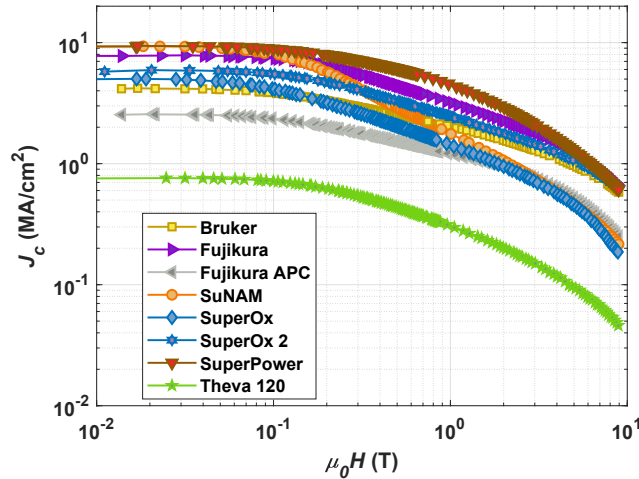
FIGURE 4.7: The critical current density variation with magnetic field $J_c(H)$ at 50 K for all analyzed CCs. Shown values are based on magnetization measurements acquired with a VSM.

dimensions for magnetometer measurements, the CCs were reduced to $\approx 4\,\text{mm} \times 4\,\text{mm}$ squares. The cutting technique plays a significant role for sample preparation since it determines how much area of the superconductor close to the cutting edges gets damaged. During the course of the PhD thesis, we optimized the preparation for minimal specimen destruction as discussed in section 6.1.2. For the samples presented in this chapter, cut by sharpened scissors far away from the pivot point in order to minimize shear forces, we estimated the sample damage to amount up to 30 %. We found that cutting damages impair the affected area absolutely, hence, J_c values are underestimated but the field

behavior represents the magnetic field response of not manipulated CCs. In addition, sticking to the very same cutting technique for all CCs legitimizes a comparison of absolute J_c values, when assuming a similar damage in all of them.

Among the CCs from different providers, we observe a wide variety. The critical current densities at self field J_c^{sf} span over more than one order of magnitude from about $0.85 \, \mathrm{MA/cm^2}$ in Theva 120, to $10 \, \mathrm{MA/cm^2}$ in SuperPower. In addition, the magnetic field behaviors $J_c(H)$ differ strongly in all CCs. Take for example Bruker. It has a moderate $J_c^{sf} \approx 4.5 \, \mathrm{MA/cm^2}$ which results to be the third smallest of the measured bunch but presents one of the least steepest $J_c(H)$ decrease and thus exhibits together with Fujikura, SuperPower and SuperOx 2 one of the highest J_c at 9 T. It should be noted that Fujikura APC reports much higher $J_c^{lit\cdot}(0\,\mathrm{T}, 50\,\mathrm{K}) \approx 5 - 8.3 \, \mathrm{MA/cm^2}$ than our measured values, but reported field behavior is in accordance with the one we measured [114]. This could suggest that our received sample batch is bad. A similar situation applies for Theva CCs. They added to the samples an information sheet with nominal I_c values that our samples do not match, maybe due to long length tape inhomogeneities [123] or sample deterioration. Taking possible cutting damage and tape inhomogeneities into account, our measured data shows good agreement with reported values of other providers [104, 112, 114, 116, 118, 119].

Extraction of pinning parameters

Fitting with eq. (4.4) allows the extraction of pinning defining parameters α and H^*. We demonstrate an example fit to the $J_c(H)$ of SuNAM CCs at 60 K in Fig. 4.6. We adjust the fitting range of eq. (4.4) for all CCs to cover the ranges where most linearity in log-log scale is observed, in particular, 0.3 T-2 T at 20-30 K, 0.3 T-0.8 T at 40-50 K and 0.25 T-0.7 T at 60-70 K. With this, we intend to highlight the characteristic power law decays in J_c, related by α, among the different CCs, while maintaining method consistency. The J_c^{sf} plateau is chosen to rest on the highest measured critical current density and its intersection with eq. (4.4) determines H^*.

We present the obtained J_c^{sf}, H^* and α for all CCs as a function of temperature in Fig. 4.8 **(a)**, **(b)** and **(c)**, respectively. The CC technology displays considerable adaptability to specific applications with its variety in $J_c(H)$ parameters which arises from the wealth of realizable pinning landscapes. The pinning behavior at specific temperature and field in the (T, H) diagram is determined by defect characteristics like the size, distribution and type of pinning defects [46].

Starting the discussion with the critical current density at 0 T J_c^{sf}, see Fig. 4.8 **(a)**, the best performing CC at 70 K is the one from SuNAM. The low supersaturation RCE-DR process generates 0D point-like defects, 2D grain boundaries and relatively big 3D nanoparticles, the last of which are reportedly effective to pin flux lines produced by the current at zero applied field and high temperatures [17]. The very high J_c^{sf} indicates that the defect density is controlled in a way that allows for high percolation currents. At higher temperatures, other CC technologies catch up. An explanation for this could be the as compared to the RCE-DR growth process (SuNAM) smaller 3D nanoparticles in the REBCO matrix of CCs grown by PLD (Bruker, Fujikura, SuperOx) and MOCVD (SuperPower) [17] which could allow better self-field pinning due to better vortex-defect matching because of the reduced correlation length at lower temperatures [162].

Important to mention is that the increase of normal conducting fraction in the microstructure can also have a detrimental effect on J_c. The addition of APCs into the REBCO matrix generally results in an elevated normal conducting defect density that, above a certain threshold, which is believed to amount around 30 % vol, gives rise to the phenomenon of superconducting current blocking and a decrease of J_c [163]. So, the optimal microstructure for high J_c^{sf} constitutes of many pinning centers that effectively pin self-field and a small enough normal conducting volume fraction to prevent supercurrent blocking. The MOCVD technique seems to generate in this regard with its 1D nanorods, 2D columnar grain boundaries and 3D nanoparticles a very advantageous microstructure since Superpower demonstrates across all
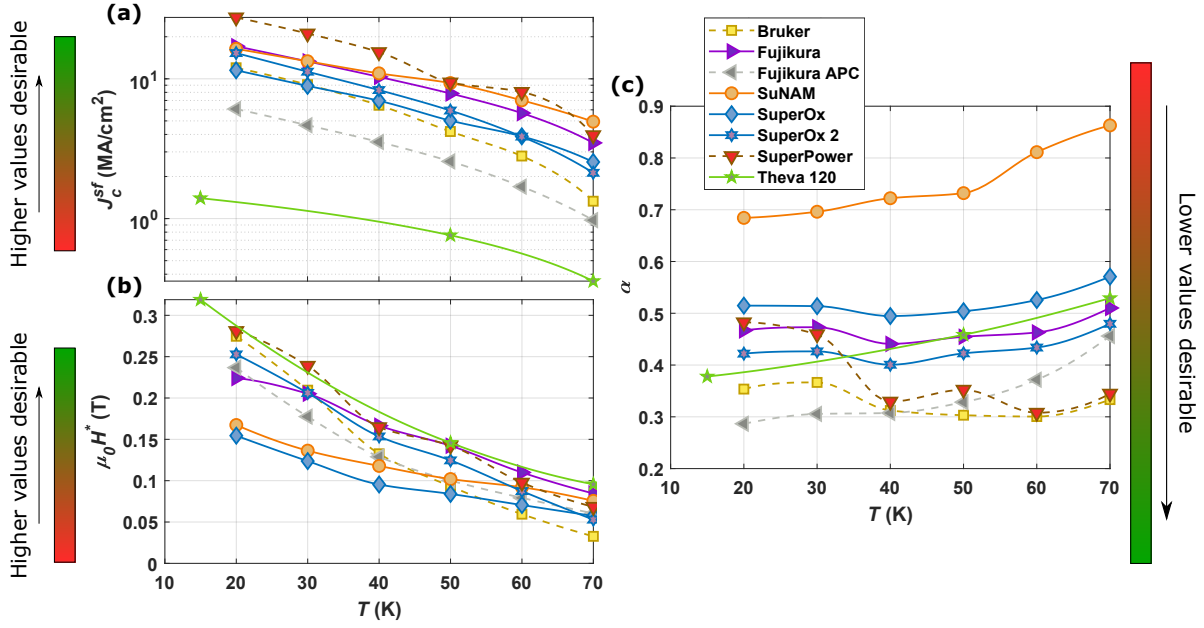
FIGURE 4.8: Critical current density at self field J_c^{sf} **(a)** and pinning defining parameters H^* **(b)** and α **(c)** as a function of temperature extracted from fittings with eq. (4.4). Dashed lines connecting the markers indicate the presence of APCs in CCs. The color bars visualize the desirable values for high field applications.

temperature a very high if not the highest J_c^{sf}. We remind that the measured Fujikura APC and Theva samples have suffered deterioration. Hence, their measured J_c^{sf} has limited meaningfulness.

Continuing with Fig. 4.8 **(b)**, the crossover field H^* exhibits an antiproportional dependence on the temperature T as reported in [160]. This suggests that the type of effective pinning centers change with temperature and that the density of the effective pinning centers decreases with increasing temperature. The spread in H^* amounts at 70 K around 0.7 T and increases at 20 K to approx. 1.5 T demonstrating again the importance of the REBCO microstructure to the superconducting performance. Below 50 K, a separation in terms of H^* occurs for SuNAM and SuperOx CCs with the other CCs. The temperature dependence of named CCs becomes quite weak in comparison with their competitors but similar to each other, although, SuNAM and SuperOx are grown by two entirely different processes (RCE-DR and PLD, respectively). This indicates that the microstructure is not only determined by the choice of growth technique but the subtle tuning within each growth process. Fuijkura, Fujikura APC and SuperOx 2, all grown by PLD, exhibit a much stronger temperature dependence below 50 K than SuperOx which support aforementioned argument.

Nevertheless, a trend that emerges is the improved H^* at temperatures below 50 K for samples with APCs in the REBCO matrix, whose primary (1D nanorods or 3D nanoparticles) and secondary (0D defects) imperfections give rise to extended single-vortex pinning regimes, as visible for Bruker, Fujikura APC, SuperOx 2 and SuperPower.

An interesting case represents the specimen by Theva since it shows the highest H^* over the entire temperature range. An explanation for it could be the effect of the inclined substrate technology. The applied magnetic field during the experiments is not directed along the REBCO's c-axis, but is tilted by $\theta \approx 27°$ away from it [122]. Due to the anisotropic nature of REBCO, this translates into the superconductor being exposed to an effective magnetic field along the c-axis (B_{eff}^c) which is lower than the applied one according to $B_{eff}^c = \varepsilon(\theta, \gamma)B$ [164], where $\varepsilon(\theta, \gamma) = \sqrt{cos^2(\theta) + \frac{1}{\gamma^2}sin^2(\theta)}$ and γ is the material electronic anisotropy, which for REBCO ranges between 5 and 8. In the case of Theva CCs $B_{eff}^c \approx 0.9B$ [14] whose decreased effective magnetic flux density could result in an extended single-vortex pinning regime.

Finally, we discuss the magnetic field dependence at elevated fields represented by the power law exponent α, as shown in Fig. 4.8 **(c)**. Different from the J_c^{sf} and H^*, low values are desirable for high field applications because it represents a weaker $J_c(H)$ decay and stronger vortex-vortex pinning. Again, a temperature dependence in the pinning parameter can be appreciated, although, it differs for most of the CCs.

SuNAM and Fujikura APC, exhibit one of the strongest temperature variations, in particular, decreasing α upon lowering the temperature from 70 K down to 20 K. Even though, the qualitative behaviors are alike, the absolute values of α differ widely between those two CCs. SuNAM CCs display between 20 K and 50 K an only weakly varying $\alpha \sim 0.7$ and rises above 50 K quite strongly to reach $\alpha \sim 0.85$ at 70 K. The effective pinning centers at higher temperatures relies in this case on isotropic, quite big 3D nanoparticles, while at lower temperatures (below 20 K) secondary 0D local disorder defects caused by fast growth take over [17, 165]. The effective defect landscape in the PLD based Fujikura APC samples is very different. Both, the employed 1D BHO nanorods [114] and the PLD characteristic 1D dislocation lines along 2D columnar grain boundaries, can be, depending on the defect size and distribution, effective across all temperatures [17, 166]. At very low temperatures, below 20 K, secondary, very small 0D defects become dominating. This defect landscape features less steep $J_c(H)$ decays with $\alpha(20\,\text{K}) \sim 0.3$ and $\alpha(70\,\text{K}) \sim 0.45$.

The conceptually similar grown Bruker CCs, with PLD and BZO nanorods, display also low α, but undercut Fujikura APC at high temperatures and resides with higher values at low temperatures, possibly, owing to alternative characteristics in defect size and spacing.

The other three PLD based CCs, Fujikura, SuperOx and SuperOx 2 have qualitatively resembling α, quite constant in the measured temperature range around $\alpha^{\text{Fuji}} \sim 0.45$, $\alpha^{\text{SO}} \sim 0.5$ and $\alpha^{\text{SO2}} \sim 0.42$, respectively. On the one hand, it highlights the commonalities in microstructure associated to the same PLD growth technique. On the other hand, it suggests again that within each processing method reside a lot of tuning parameter to change the type and effectiveness of a microstructure.

The CCs provided by SuperPower are grown by MOCVD. Owing to the lower degree of supersaturation during growth, when comparing to PLD, one would expect a less aggressive columnar growth associated with larger REBCO grains and thus less grain boundaries [167]. The loss in grain boundary density is counteracted by a high density of 1D BZO nanorods and employment of two rare-earth elements (Y and Gd) which can generate 0D defects. This microstructure results in a very low $\alpha \sim 0.31$ above 40 K and an increased but still strong $\alpha \sim 0.45$ below 40 K.

The ISD technique by Theva can be associated with high to moderate supersaturation and thus to 2D columnar grain boundaries and accompanying 0D defect pinning dominance, in addition to the inclined c-axis. The measured α follows above 40 K the trend line of Fujikura and below 40 K not enough measurement points are available to draw conclusions.

The here reported α are in reasonable accordance with values reported in literature [17, 120, 160].

Concluding this part, the overall shape of $J_c(H)$ determine all three here discussed parameters J_c^{sf}, H^*, α, in addition to H_{irr} (see eq. (4.5)). The tuning of these parameters is highly susceptible to microstructure changes and significant understanding of effective pinning centers at each temperature and field range was generated over the past years (see [17, 165, 166] and references within) that helped to link REBCO microstructure to superconducting performance in this section. Further, there is no such thing as a perfect microstructure. Depending on the targeted application, a more crystalline (low fields, high temperature) or defect rich (large fields, low temperature) REBCO body yields the highest performance.

Extrapolation to FCC-hh conditions

With all $J_c(H)$ defining parameters estimated, we can now extrapolate with eq. (4.5) the critical current per cm-width $I_c/width = J_c \cdot t$, where t is the REBCO layer thickness, up to 16 T in order to see if the analyzed CCs can sustain the prospected harsh conditions in the FCC-hh. During operation, the beam screen will face peaks of image currents up to 25 A. Taking into account the designed beam screen chamber dimensions, a tube with diameter $\varnothing \approx 2.7$ cm [10, 168], it translates into $I_c/width \approx 3$ A/cm.

For the extrapolation with eq. (4.5), we access the $J_c^{sf}(50 \text{K})$, $H^*(50 \text{K})$ and $\alpha(50 \text{K})$ as given in Fig. 4.8 and $H_{irr}(50 \text{K})$ form table 4.2. The critical current per cm-width calculated from VSM measurements can be found together with corresponding extrapolation in Fig. 4.9. Important to note are the not convincing fits to measurement data at large
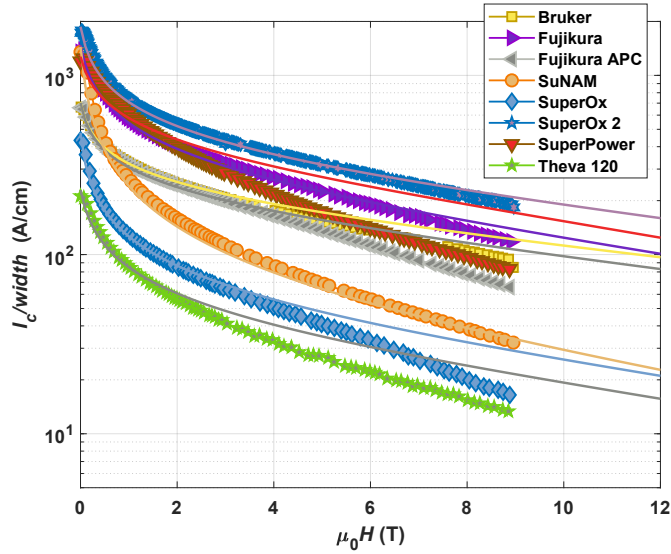
FIGURE 4.9: The critical current per cm-witdh $I_c/width$ of all analyzed CCs as a function of magnetic field up to 9 T at 50 K. Markers represent measurement points and the solid lines an extrapolation with eq. (4.5) to larger fields.

fields for some providers, see Bruker, Fujikura APC, SuperOx, SuperPower and Theva. This might have several reasons. For instance, estimated pinning parameters and real pinning parameters associated to VSM data might be distinct. VSM measurements are at large fields susceptible to flux creep, thus magnetization and J_c are in this range underestimated. Consequently, the irreversibility fields related to this data are underestimated in comparison with the real values and extrapolation based on transport deduced H_{irr} will lie above VSM data.

Moreover, the collective pinning regime cannot always be described with all its details by a simple power law decay with one exponent α as presented in eq. (4.5). Instead of a linear behavior in log-log scale, the collective pinning regime can consist of a more rounded $J_c(H)$ decay in log-log scale, as observed for Bruker, Fujikura APC, SuperOx, SuperPower and Theva. It is a consequence of highly complex defect landscapes present in the HTS whose pinning contributions of single defects do not add up to a simple linear decay in log-log scale. Thus, the model employed in eq. (4.5) might not account for the physical reality of complex microstructure and leads naturally to a mismatch with experimental data.

Nevertheless, the model still describe VSM data of Fujikura, SuNAM and SuperOx 2 quite well. Interestingly, these are all CCs with an rather classical microstructures, i.e. no incorporation of 1D nanorods nor inclined c-axes, which might outline the type of samples suitable to be modelled with eq. (4.5). To this end, we display the experimental data only together with the more trustworthy extrapolations and reported $I_c/width$ at 16 T in Fig. 4.10.
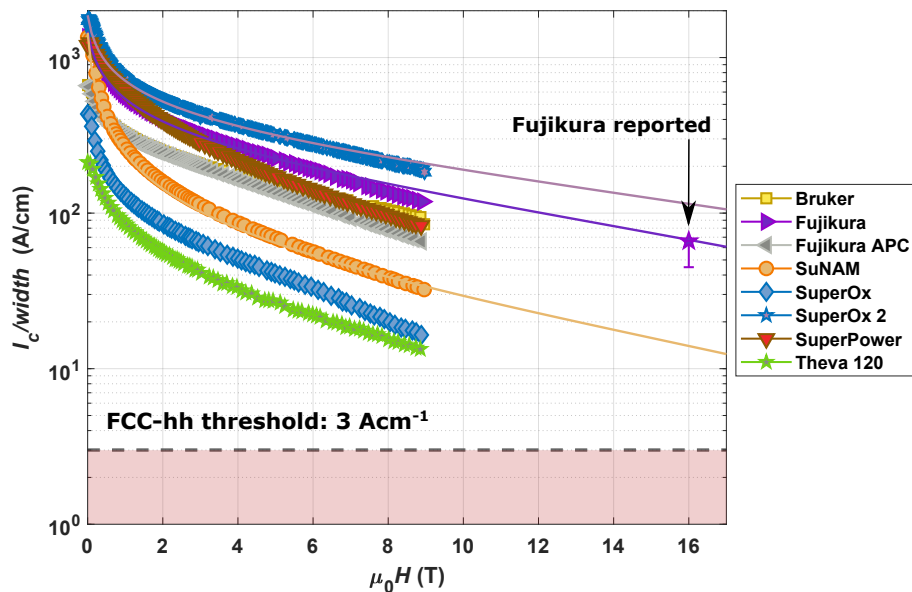
FIGURE 4.10: The critical current per cm-witdh $I_c/width$ of all analyzed CCs as a function of magnetic field up to 9 T at 50 K. Markers represent measurement points and the solid lines an extrapolation with eq. (4.5) to larger fields. The detached purple star at 16 T correspond to reported I_c data of Fujikura CC [114]. We added a bottom directed error bar to account for the fact that this data point was acquired with DC transport. Thus, it gives an upper limit of I_c when put into context with VSM data. The black dashed horizontal line corresponds to the maximum induced mirror charges when operating in the FCC-hh.

Assuming that the existing $I_c/width$ in-field trends will continue, all extrapolated CCs stand easily above the threshold of the FCC-hh. In contrast, the $I_c/width$ of SuperOx and Theva 120 might, judging from the data until 9 T, possibly not sustain the prospected peak image currents at 16 T. However, both SuperOx and Theva have by now higher performing series of their CC available, see sample SuperOx 2 and [169].

In order to evaluate the quality of the extrapolations, there is not much $I_c(H)$ of REBCO CCs at rather high temperatures and large fields in literature available because of the untypical operation window when comparing to conventional applications like large field magnets (low temperature at large fields) or power cables and fault current limiters (high temperature at small fields). However, comparing with one example, a published critical current per cm width at 50 K and 16 K measured with transport by Fujikura [114], indicated as a star in Fig. 4.10, we see good accordance with our extrapolation. This is quite an important result. On the one hand, it increases the credibility of generated pinning parameters and extrapolations performed for Fujikura, SuNAM and SuperOx 2. On the other hand, it confirms performance margins of the CC technology for the beam screen chamber.

In order to build upon our conclusions, significant importance should be attributed to the experimental critical current characterization of REBCO CCs at temperatures around 50 T and increased magnetic fields up to 16 T. It could further help to assess the quality of large field extrapolations, point out performance differences between CCs at larger fields and generate much needed accurate reference $I_c(50\,\text{K}, 16\,\text{T})$ data for all CCs that would quantify the margins available in the beam screen chamber of the FCC-hh. The abundance in current carrying capacity of a CC would allow for thinner REBCO layers which in turn would cause an investment drop for the FCC-hh project when engaging with the CC technology.

4.4   Conclusions

The main conclusion that should be drawn from this chapter can be broken down to two key points.

- **Commercially, in large-scales available CCs are performant enough to sustain superconductivity at extreme FCC-hh conditions, i.e.** 25 A **current flow at** 50 K **and** 16 T**.** We measured the critical temperatures T_c and irreversibility fields H_{irr} with transport and the critical current densities J_c with VSM characterization at several cryogenic temperatures and up to 9 T. Extrapolating the generated data with established models elucidate that the irreversibility field of all measured CCs are well above 16 T and the critical current of 25 A can be sustained by selected CCs at 50 K and 16 T. This finding is of great importance since it demonstrates the maturity and fitness of already available CCs technology for this specific application.

- **The CC technology proves its variety in a range of different architectures and most importantly, in rich REBCO microstructures variability that allows tailoring to specific applications.** Although all CCs are REBCO based, significant differences in optimal operation regimes were identified owing to microstructure differences. Rather simple factors like the employed rare-earth element or degree of oxygenation have already profound impact on the T_c and H_{irr}. More complex manipulation like the deliberate generation of non-superconducting defects affect the pinning behavior. For impurities to become effective for pinning, they have to match the size and distribution of vortex matter. Since the coherence length ξ, diameter of a single fluxon, depends on the temperature and the vortex density on the magnitude of applied magnetic field, one static defect landscape can only be optimized for one specific region in the $H - T$ coordinate system.
  This finding is of great importance because it emphasizes the potential for further REBCO microstructure tuning in order to increase the performance of already available CCs and hence decrease the technology price.

Chapter 5

High-frequency response of thick REBCO coated conductors

Motivated by REBCO CCs as a potential beam screen coating alternative, we evaluate the high-frequency response of HTS available on an industrial scale at FCC conditions. In particular, we compare the surface impedance $Z_s = R_s + iX_s$, where R_s and X_s denote the surface resistance and surface reactance, respectively, of several commercially available CCs with Cu in a wide cryogenic temperature range $T = 20 - 70\,\text{K}$ at $\nu_0 = 8\,\text{GHz}$ and up to 9 T. In-field analysis of it allows a discussion about vortex physics of CCs and its link to different microstructures. The vortex-motion parameters depinning frequency ν_p, vortex viscosity η and Labusch parameter $k_p = 2\pi\nu_p \cdot \eta$ are derived with two different methods, both of which are based on the Gittleman-Rosenblum model [65]. The model proposed by Gittleman and Rosenblum is a mean-field theory for vortices in a periodic pinning potential driven by high-frequency oscillating, subcritical currents without considering thermal activation. It modulates both the resistive and reactive response of vortices to the driving field.

In our first approach, we focus our analysis on the field behavior of the surface resistance R_s while neglecting the surface reactance X_s. The appeal of this procedure lies in the fact that the surface resistance is experimentally much easier and quicker obtainable than the surface reactance. However, by considering only the real part of the surface impedance, the vortex-response model remains underdetermined and has to be compensated by additional confinements. With a modified Bardeen-Stephen model [31], which describes the motion of vortices in a type-II superconductor, we can estimate the vortex viscosity η when taking flux-flow resistivities ρ_{ff} from DC-transport measurements into account. This reduces the Gittleman-Rosenblum model parameters to only one, the depinning frequency ν_p, and thus permits the determination of it by fitting the measured surface resistance R_s. The experimental surface resistance of characterized REBCO CCs is presented in section 5.1.2 and is followed up by the mentioned evaluation of microscopic vortex-motion parameters in subsection 5.1.3.

Prior to continuing with the second approach, we report about the challenging requirements facing the dielectric resonator setup to allow reliable surface reactance characterization of thick CCs. It is essential to guarantee a large frequency accuracy, a large stability of measurement temperature and a large mechanical stability of the resonating cavity. The latter has not been addressed in literature yet but is shown to be necessary in order to exclude external interfering effects to the intrinsic reactive response of the CC. After demonstrating experimentally the need for the setup requirements, we explain how to meet them. Finally, having the experimental prerequisites established, we disclose the reactive microwave response of several commercial REBCO CCs at 50 K and up to 9 T. All of this is described in section 5.2.

In the second approach to determine the vortex-motion parameters, we consider both the field response of surface resistance and surface reactance. While this method is experimentally more elaborate and expensive, it allows us to determine vortex-motion parameters consistently within the Gittleman-Rosenblum model using exclusively surface impedance data. Calculated parameters are compared to the values from our first approach and set into a wider context by referencing literature values and parameters of other superconductors. This paragraph is detailed in section 5.3.

Finally, we address the shortcoming of not having experimental surface impedance data at FCC-hh conditions available yet. With estimated vortex-motion parameters at hand, we can extrapolate the surface impedance of CCs down to 1 GHz and up to 16 T within the Gittleman-Rosenblum model. Those surface impedances are compared to the expected microwave response of Cu at FCC-hh conditions. The extrapolation and analysis of it is given in section 5.4.

We start this chapter by discussing how the different multi layers below the HTS in a CC contribute to the measured surface impedance.

5.1 Surface resistance of thick CCs

5.1.1 Influence of multilayered structure on surface impedance

In a general case, when exposed to a propagating microwave field, CCs' entire complex architecture consisting of a thick superconducting layer with $t_{SC} \geq 0.9\,\mu m$ on top of a buffer layer stack with $t_{dielectric} > 0.5\,\mu m$ backed by a metallic, flexible substrate with $t_m \sim 50\,\mu m$ contributes to the microwave response, where t stands for the thickness of specified layers. Following transmission line analogy and impedance transformation [170], the effective measured surface impedance of the CCs Z_{CC} can be written as

$$Z_{CC} = Z_{SC} \frac{Z_{stack} + iZ_{SC}\tan(k_{SC}t_{SC})}{Z_{SC} + iZ_{stack}\tan(k_{SC}t_{SC})}, \tag{5.1}$$

with

$$Z_{SC} = \sqrt{i\omega\mu_0\tilde{\rho}} \tag{5.2}$$

being the surface impedance of the superconductor (valid in the local limit) and $\tilde{\rho}$ the complex resistivity [69],[67]. Z_{stack} is the effective measured surface impedance of the layers below the superconductor (dielectric buffer layers/metallic substrate) and $k_{SC} = \frac{\mu_0\omega}{Z_{SC}}$ the propagation constant of the superconductor. So, when interested in the characteristic surface impedance of the superconductor Z_{SC}, knowledge about the microwave response of the entire multilayer stack below the superconductor Z_{stack} is necessary. However, equation (5.1) can be simplified, if considering the characteristic screening lengths in the material under study. In the framework of the two fluid model, $|k_{SC}t_{SC}| \gg 1$ implies $Z_{CC} \approx Z_{SC}$, where the influence of the layers below the superconductor can be ignored [171]. This is known as the thick film approximation. $|k_{SC}t_{SC}|$ can be estimated for samples in our experiments. By assuming $T_c = 93\,K$, $\rho_n(70\,K) = 60\,\mu\Omega cm$ and $\lambda_L(0\,K) = 150\,nm$, typical values for YBCO, and $T = 70\,K$, $\nu_0 = 8\,GHz$, as measurement conditions where the smallest propagation constant is expected, we get for our thinnest and thickest CC ($t_{min} \approx 0.9\,\mu m$, $t_{max} \approx 3.0\,\mu m$) $|k_{min}t_{SC}| \approx 5 > 1$ and $|k_{max}t_{SC}| \approx 16 > 1$, respectively, which does not clarify unambiguously if the thick film approximation is applicable. However, Silva et al. [171] provide a numerical example for the deviation of the thick film approximation from equation (5.1). For 1 μm YBCO on a LAO single crystal substrate at $\nu_0 = 30\,GHz$ and $T = 72\,K$, the error on the characteristic surface resistance by ignoring the substrate $R'_{SC+LAO} = R_{SC}$ is smaller than 5 %. This error becomes even smaller when decreasing ν_0. In conclusion, by applying the thick film approximation for the samples in this work, we make a systematic error on the characteristic surface resistance of the superconductor

and all values derived from it that is smaller than 5 %. With regard to specific microwave applications like the FCC-hh, the Z_{CC} is still a very relevant quantity, as it determines the effective microwave response of CCs in use.

5.1.2 Experimental surface resistance of commercially available CCs

The surface resistances are calculated based on the quality factors of the electromagnetic resonance in the cavity as described in section 3.1.2. In Fig. 5.1 **(a)**, we show measured forward transmission coefficient $|S_{21}|$, from which the quality factors are derived, as a function of frequency corresponding to SuNAM CC at 50 K and several applied magnetic fields starting from zero-field cooling (ZFC) state and ending at 9 T. The resonance curves exhibit a symmetric and noise-free shape with resonant frequencies ν_0 manifesting around 8 GHz. The symmetry and signal to noise ratio of $|S_{21}|$ data is of comparable quality for all high-frequency measurement sets acquired in this thesis. Upon increase of applied field, the resonant frequency drops and curves become wider, which results from smaller Q_l, i.e. larger dissipation in the resonating system. We present loaded quality factor Q_l of corresponding curves together with unloaded quality factors Q_0 (see eqs. (3.10)-(3.12)) as a function of magnetic field in Fig. 5.1 **(b)**.
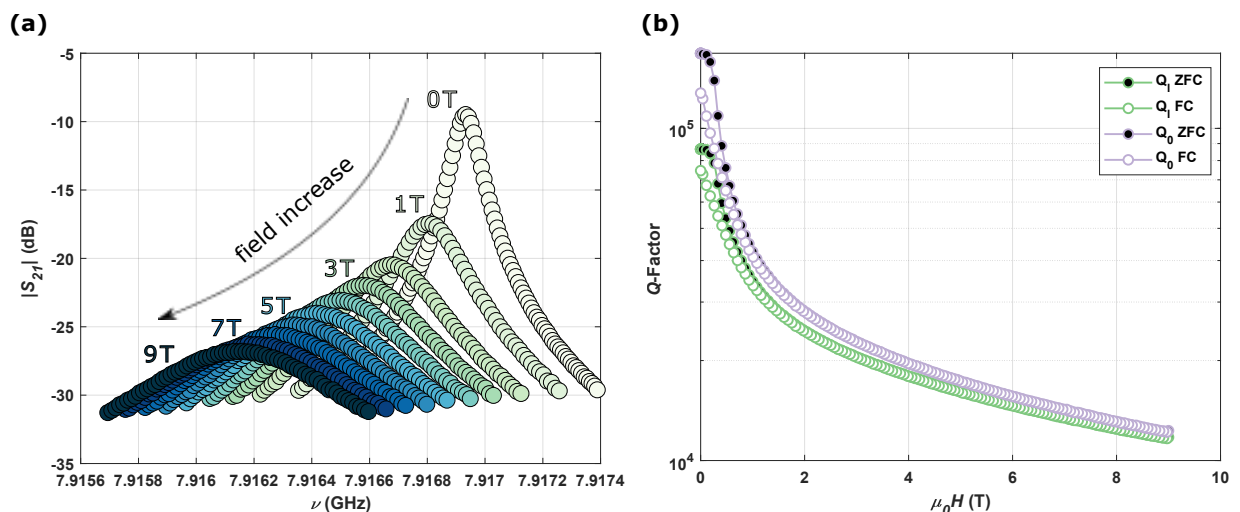
FIGURE 5.1: **(a)** The measured $|S_{21}|$ as a function of frequency corresponding to SuNAM CC at 50 K and several applied magnetic fields. We reduced the point density of the curves by a third for better depiction. **(b)** ZFC and FC (zero field cooling and field cooling, respectively) branches of loaded quality factor Q_l and unloaded quality factor Q_0. The data corresponds to the measurement from Fig. 5.1 **(a)**.

Over the field span 0-9 T, loaded Q-factor Q_l varies roughly in one order of magnitude, from about $Q_l^{\text{ZFC}}(0\,\text{T}) = 86000$ to $Q_l^{\text{ZFC}}(9\,\text{T}) = 11000$. At all measurement conditions, at 20 K-70 K with fields up to 9 T, the loaded quality factor stays within the range of $Q_l = 10^4 - 10^5$ or very close to it for all analyzed CCs. Having the small geometrical factor of the exposed twin samples in mind $G(50\,\text{K}) \sim 213\,\Omega$, the measured quality factors point towards low surface resistances of REBCO CCs.

In Fig. 5.2, we show R_s of three selected coated conductors as function of applied magnetic field $\mu_0 H$ at several cryogenic temperatures T. SuNAM represents a CC whose defect landscape is not adjusted for large-field applications, see $J_c(H, 50\,\text{K})$ in Fig. 4.7. Its microstructure relies on intrinsic growth defects including large 3D particles of Gd_2O_3 that were not converted to GdBCO (see Fig. 4.1) and can be associated in this context with medium vortex-pinning. On the contrary, the other two picked CCs by Bruker and SuperPower represent a group of CCs with high vortex-pinning microstructures that yield better performance when exposed to large magnetic fields. Usually, this is achieved by the deliberate incorporation of APCs, so non-superconducting secondary phases of diameter ξ, into the REBCO matrix

as it is done with BZO nanorods in Bruker and SuperPower, BHO nanorods in Fujikura APC or Y_2O_3 nanoparticles in SuperOx 2.
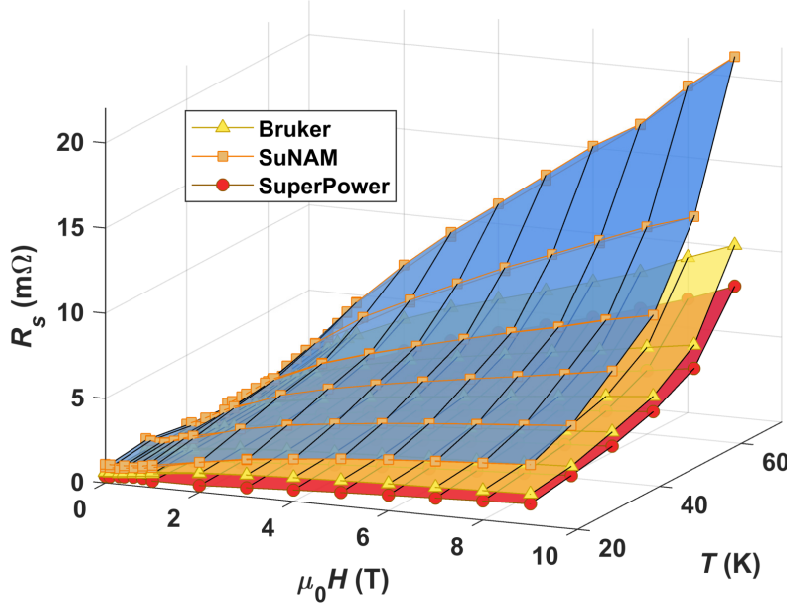
FIGURE 5.2: Absolute surface resistances R_s of three selected coated conductors as a function of magnetic field at $T = 20 - 70$ K. The markers (squares, triangles, circles) represent measurement points.

We see that the corresponding CC microstructures control the field behavior of the surface resistance. The SuNAM sample has a steeper increase in R_s with magnetic field $B \approx \mu_0 H$ especially at mid and high T as compared to SuperPower or Bruker. The higher in-field performance of APC based superconductors known from critical current measurements [48],[127] is encountered here, too. This points towards an influence of APCs on the surface resistance, hence, vortex dynamics where pinning is meaningful (pinning regime). As a reminder, at higher frequencies, precisely above the depinning frequency ν_p, pinning becomes ineffective and the vortex dissipation is governed by viscosity (flux-flow regime). From this we can already suspect that the depinning frequency of characterized CCs is likely to be greater than the resonant frequency.

Comparing Bruker with SuperPower, the field behavior at low and intermediate temperatures up to 50 K is fairly similar. At higher T, a slight difference in R_s emerges, visible particularly at 9 T. It is in accordance with Bruker's 'double disordered' coined microstructure which is designed to pin vortices strongly at 4.2 K and large fields at expense of performance at higher temperatures [112]. In particular, we observe lower T_c and $H_{irr}(70\,\text{K})$ in Bruker comparing with SuperPower, see Fig. 4.5, which is in accordance with its higher microwave losses at 70 K and 9 T.

The features of the surface resistance's field behavior that categorize the CCs into medium vortex-pinning and high vortex-pinning REBCO microstructure are observed for all measured samples. Figure 5.3 shows R_s as a function of magnetic field at $T = 50$ K for all considered CCs in comparison with Cu intended to be used in the FCC-hh beam screen chamber, i.e. 300 μm thick Cu on stainless steel colaminated by CERN. The surface resistance of Cu was measured without applied magnetic field and field-independence was assumed. In the plot, the field performance of CCs is colored into two regions, coined medium vortex-pinning and high vortex-pinning REBCO region, that refers to the type of microstructure, as already discussed above for a few examples. The materials belonging to the first group are REBCO CCs whose pinning capacity originates from defect landscapes that are not specifically adjusted for effectiveness at intermediate temperatures and large fields. Both, their increase in $R_s(H)$ and decrease in $J_c(H)$
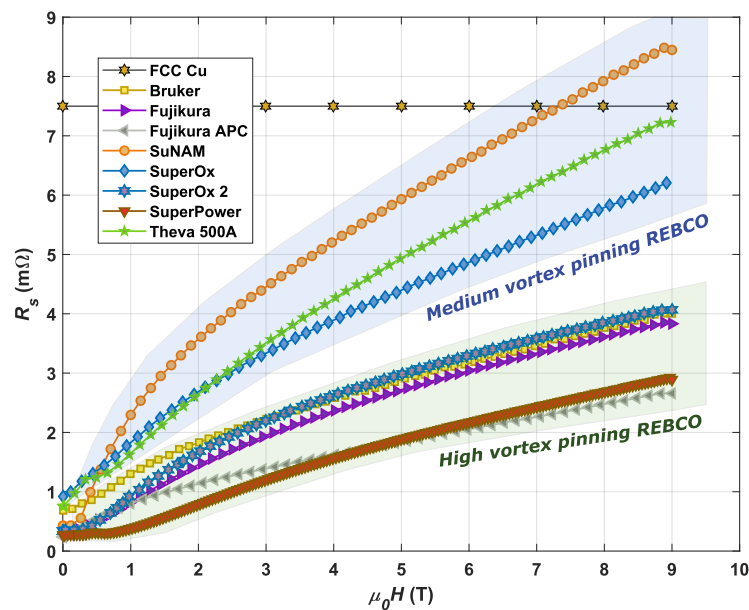
FIGURE 5.3: Surface resistance magnetic field dependence of all analyzed CCs in comparison with FCC Cu at 50 K. The field performance of CCs can be roughly categorized into two regions, coined medium vortex-pinning and high vortex-pinning REBCO region, that refers to the type of microstructure.

show a steeper magnetic field dependence. SuNAM, SuperOx and Theva belong to this group. The second group includes CCs with APCs (BZO and BHO nanorods or Y_2O_3 nanoparticles) based REBCO matrices, in particular, Bruker, Fujikura APC, SuperOx 2 and SuperPower. The Fujikura CC represents an exception with its high pinning performance despite the omission of APCs in its microstructure. For this CC, specific growth conditions must have been established that promote the generation of intrinsically occurring effective pinning defects. Its microstructure is 'simpler' through the omission of APC, however, not much less effective since it gives a weak field-dependence, similar to the one of Bruker.

Analogous to $J_c(H)$ (see Fig. 4.7), the spread in $R_s(H)$ comparing all CCs showcases the variety and richness of possible defect landscapes in REBCO and their profound impact on in-field microwave performance at 8 GHz.

CCs with high pinning microstructures outperform FCC-Cu widely up to 9 T. Even though the shown measurement conditions ($\nu \approx 8$ GHz, $\mu_0 H \leq 9$ T) do not represent the setting in the beam screen chamber ($\nu \approx 1$ GHz, $\mu_0 H \leq 16$ T), it is a good hint for what to expect at FCC-hh conditions. Later in section 5.4, we will extrapolate measured surface resistance to mentioned conditions by means of the Gittleman-Rosenblum model.

Figure 5.4 shows two $R_s(H)$ curves, one recorded after ZFC, the other one after FC, for each considered CCs at $T = 50$ K and smaller fields. The surface resistance at zero fields $R_s(0\text{T})$ varies between approximately 0.25 mΩ and 1 mΩ among all CCs. A hysteretic behavior associated to field cooled/zero field cooled measurement procedures occurs at fields < 2 T, which indicates an influence of trapped vortices. In Table 5.1, we present $\frac{R_s^{\text{fc}}(B=0\text{T}) - R_s^{\text{zfc}}(B=0\text{T})}{R_s^{\text{zfc}}(B=0\text{T})}$ for all measured samples. Interestingly, the hysteresis appears in different magnitudes for each CCs ranging between 5 % and 55 %. An in-depth study about the effect of trapped field on the surface resistance of CCs and its relation to the superconducting layer's architecture remains to be conducted. Nevertheless, in chapter 6 we already demonstrate that the as buffer layer employed $LaMnO_3$ influences the hysteretic $R_s(H)$ behavior at small fields significantly.
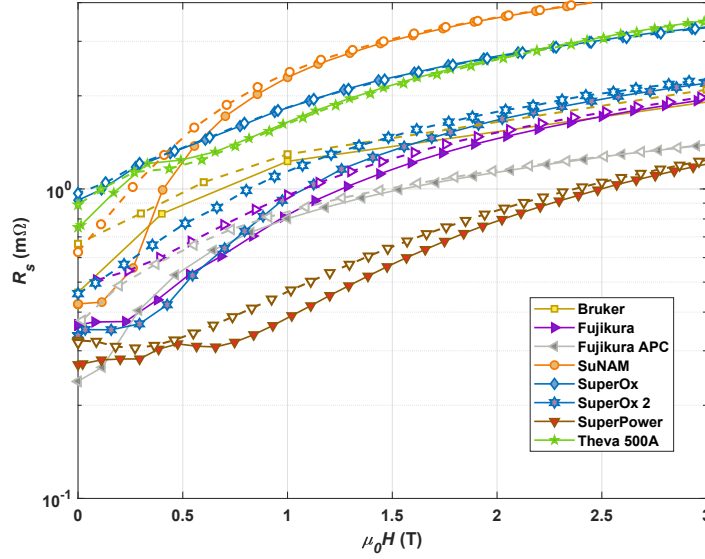
FIGURE 5.4: $R_s(H)$ of CCs measured at $T = 50\,\mathrm{K}$ and $\nu \approx 8\,\mathrm{GHz}$. The colored markers guide the zero-field cooled measurements, while the white markers connect the values recorded with field cooling. Below 2 T a hysteretic behavior can be observed that points towards influences of trapped vortices.

Provider	$\dfrac{R_s^{\mathrm{fc}}(B=0\mathrm{T}) - R_s^{\mathrm{zfc}}(B=0\mathrm{T})}{R_s^{\mathrm{zfc}}(B=0\mathrm{T})}$
Bruker	44 %
Fujikura	31 %
Fujikura APC	55 %
SuNAM	47 %
SuperOx	5 %
SuperOx 2	37 %
SuperPower	18 %
Theva	18 %

TABLE 5.1: Surface resistance hysteresis after exposing to 9 T for all CCs at 50 K.

5.1.3 Evaluation of microscopic vortex parameters

Determination of vortex viscosity

As shown in Fig. 5.2 and 5.3, it becomes evident that the vortex response, namely the field dependent part of the surface resistance dominates the total surface resistance under sufficiently high applied magnetic field. Hence, a good grasp of a superconductor's in-field performance under the influence of microwaves can be gained by estimating the vortex properties η and ν_p, which are function parameters of equation (2.56).

We start by determining the vortex viscosity η. Bardeen and Stephen derived for the approximation of a superconductor in the ideal local limit ($l > \xi_0$) an expression for the flux-flow resistivity ρ_{ff}. They assumed a normal conducting core of finite size with radius $\xi_0 \sim \frac{1}{\sqrt{B_{c2}}}$. The flux-flow resistivity is governed then by the normal-state resistivity ρ_n and the vortex core size, thus $\rho_{\mathrm{ff}} \sim \rho_n \frac{B}{B_{c2}}$ [31], [30]. This approximation was derived for s-wave superconductors. With the time dependent Ginzburg-Landau theory, Ivlev and Kopnin modified the flux-flow resistivity for YBCO by the factor $a = 1.45$ to account for the layered structure of the anisotropic uniaxial superconductor in the range

$\mu_0 H_{c1} \ll B \ll B_{c2}$ [172],[173] :

$$\rho_{\text{ff}} = \rho_n \frac{B}{a \cdot B_{c2}}. \tag{5.3}$$

Comparison of equation (5.3) with equation (2.56) yields for the vortex viscosity of REBCO superconductors

$$\eta = a \frac{\Phi_0 B_{c2}}{\rho_n}. \tag{5.4}$$

A possible way to determine the vortex viscosity is by DC transport measurements from which the normal-state resistivity ρ_n and upper critical field B_{c2} of the superconductors can be estimated. In Fig. 5.5 **a)**, we show the resistivity as a function of temperature in the range $T = 85 - 300\,$K at different applied magnetic fields up to $9\,$T for one exemplary CC. The magnitude of ρ follows values reported in literature [53].
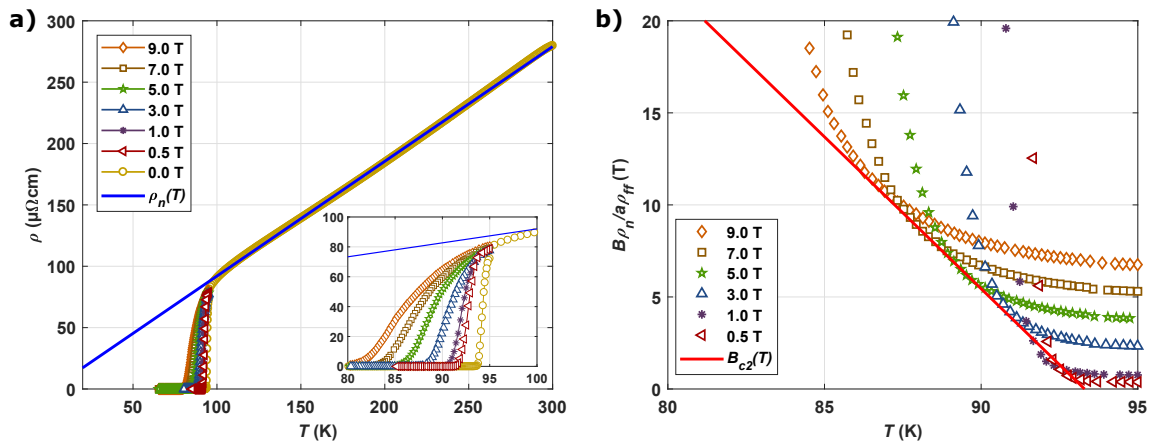
FIGURE 5.5: By way of example, data for Fujikura without APC is shown. **a)** ρ vs. T at various applied magnetic fields. The blue line is a linear fit to $\rho(T)$ well above T_c which is used to estimate ρ_n. The inset zooms into the range where $\rho = \rho_{\text{ff}}$. **b)** The ratio $B\rho_n/1.45\rho_{\text{ff}}$ as a function of temperature, as determined by flux-flow scaling. Solid red line in the figure represents the upper critical field $B_{c2}(T)$.

ρ_n below T_c can be characterized in a first approximation from a linear extrapolation of the metallic behavior well above the critical temperature T_c. It was demonstrated in [174] that the free flux-flow model applies for a considerable part of the resistive transition. For this reason, we can determine the magneto resistance measured close to T_c as $\rho(T \approx T_c, B) = \rho_{\text{ff}}(T, B)$. According to equation (5.3), the envelope of $\frac{B\rho_n(T)}{a\rho_{\text{ff}}(T)}$ represents points where $\rho(B) = \rho_{\text{ff}}(B)$ and gives an estimate for $B_{c2}(T)$ as shown in Fig. 5.5 **b)** for an example CC. As proposed in the theory of 3-D GL superconductors [30], the upper critical field follows a linear temperature dependence $\beta(T_c - T)$, with $\beta = 1.6 - 1.9\,$T/K depending on characterized CC. The slope coincides with values $\beta = 1.9 - 2.1\,$T/K given in previous reports [174],[175]. Even below $T = 78\,$K, where the upper critical field of YBCO crosses over to 2-D behaviour with $B_{c2} \sim (T_c - T)^{1/2}$ [30], our estimates of $B_{c2}(20\,\text{K}) = 115 - 135\,$T from the linear extrapolation yield reasonable accordance with reported values $B_{c2}^{\text{rep.}}(20\,\text{K}) \approx 120\,$T [176].

Equation (5.4) is fed with estimated ρ_n and B_{c2} in order to calculate the vortex viscosity for measured temperatures. The values are presented in Fig. 5.6 for all CCs but Theva. Vortex parameters of samples from THEVA Dünnschicht-technik GmbH are not presented in this section. The inclined REBCO c-axis in Theva CCs requires the consideration of anisotropy in quasiparticle and/or vortex dynamics which goes beyond the scope of presented elaborations and deserves a separate study. Error bars are derived from the determination of ρ_n and B_{c2} and then propagated to η. The vortex viscosity is for all samples inversely proportional to the temperature. While the magnitudes of η for most of the CCs are within the errors relatively close together, the sample Fujikura with APC significantly undercuts the other CCs by a factor of up to 4 depending on the temperature. Since η relates to the conversion of cooper-pairs to quasiparticles

and vice versa of a moving flux line [177], the entire microstructure of a CC may contribute to η and explain the variety between values of different providers. In the specific case of Fujikura APC, the normal-state resistivity ρ_n is unexpectedly high as seen in Fig. 4.2 which affects the present calculation of the vortex viscosity η. Later, in section 5.3, we will evaluate the vortex viscosity only with surface impedances, not taking the normal-state resistivity into account.
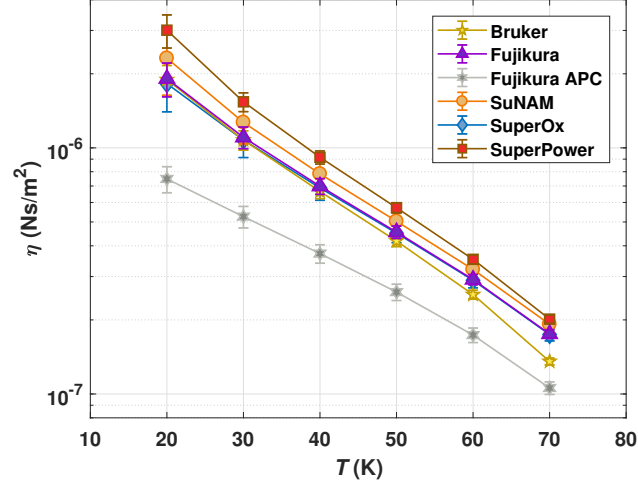
FIGURE 5.6: Vortex viscosity for all CCs but THEVA determined from equation (5.4) at $T = 20 - 70\,\text{K}$. The solid lines are guides for the eyes.

Determination of depinning frequency

The second vortex parameter ν_p in applied magnetic field can now be extracted from equation (2.60). When constraining the Gittleman-Rosenblum model with the determined vortex viscosities (see Fig. 5.6), we can employ ν_p as a fitting parameter to the measured field response of the surface resistance $R_{vm}(B) = \Delta R_s$. By way of example, ΔR_s of a Bruker sample is shown together with corresponding fits according to equation (2.60) for $T = 20 - 70\,\text{K}$ in Fig. 5.7. Up to
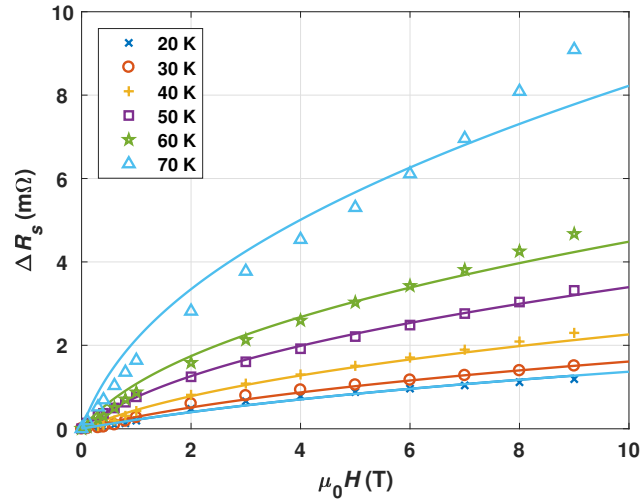
FIGURE 5.7: The markers show the dissipation under microwaves of $\nu_0 \approx 8\,\text{GHz}$ with applied magnetic field $\mu_0 H$ up to 9 T at different temperatures of a Bruker CC. Corresponding fits equation (2.60) are represented by solid lines. The lines follow the same color code as the markers.

$50\,\text{K}$, ΔR increases quite steadily with $\sqrt{B}$, as described by theory [73, 178]. At higher temperatures, especially at high

fields, measurement data deviates from the predictions with a steeper increase than $\sqrt{B}$. The Gittleman-Rosenblum model is limited to the mean-field regime, that is where the displacement of vortices from the pinning potential minima is small enough so that the flux tubes stay inside the wells and vortex-vortex interaction is infinite, resulting in a collective movement as a lattice [67],[69]. There are two possible explanations for the observed model deviation. On the one hand, thermal activation can excite hops between pinning sites, which a mean-field model cannot account for [179]. On the other hand, at high fields we are approaching B_{irr}. For example, $B_{irr}(T = 70\,\mathrm{K}) \approx 16\,\mathrm{T}$ for Bruker. In this case, the long-range order gets disturbed and the infinite vortex-vortex repulsion of mean-field models loses its validity.

Figure 5.8 **a)** shows the depinning frequency ν_p extracted from fits with Gittleman-Rosenblum model for all CCs at $T = 20 - 70\,\mathrm{K}$.
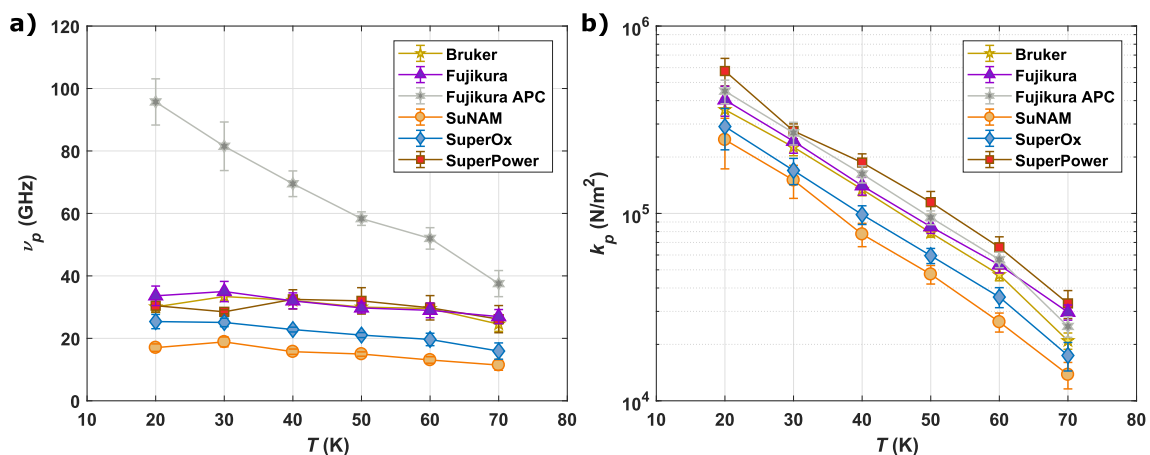
FIGURE 5.8: **a)** Depinning frequency determined from fits with equation (2.60) and **b)** Labusch-parameter for all CCs determined from the relation $k_p = 2\pi\nu_p \cdot \eta$ at $T = 20 - 70\,\mathrm{K}$ in $10\,\mathrm{K}$ steps. Error bars for ν_p are derived from the quality of the fittings and are propagated together with uncertainty of η to the error of k_p. The solid lines are guides for the eye.

Except for Fujikura with APC, the deviation of depinning frequencies as function of temperature is quite small and inversely proportional to temperature. A correlation between microstructure and depinning frequency can be observed. Bruker (double disorded), SuperPower (BZO nanorods) and Fujikura APC (BHO nanorods) characterized by the use of artificial pinning centers exhibit increased depinning frequencies as compared to SuNAM or SuperOx CCs that are not optimized for large field application. Remarkably, Fujikura without APC has within the errors the same depinning frequency as Bruker and SuperPower at all temperatures which points towards a nanoengineered microstructure that resembles the pinning properties of both CCs with APC. The determined values for all but one CC remain in accordance with literature which report mostly $\nu_p = 10 - 50\,\mathrm{GHz}$ in the given temperature range (see [180],[67] and references within). The depinning frequency of Fujikura with APC exceeds conventionally measured ν_p both in magnitude and steepness of the temperature dependence. As already mentioned above, Fujikura with APC is the only CC that incorporates Eu as the rare earth and BHO as the nano additive. Whether these two changes are the governing factors for the increased depinning frequencies cannot be concluded unambiguously without additional studies.

5.2   Challenging $\Delta X_s(B)$ measurements with rutile DR

Up to this point, we considered and analyzed exclusively the surface resistance derived from the quality factors of the resonance curves according to equation (3.14). The measurement procedures for acquiring the surface resistance of a superconducting film with a Hakki-Coleman type dielectric resonator are well documented in literature [81, 181]. More recent publications discuss in great detail the reliable determination including measurement limits of both surface resistance and surface reactance for superconducting thin films grown on single crystal or multilayered CC structures [86, 88].

To our knowledge, surface reactance measurements of thick REBCO CCs taken with a DR have not been the focus of studies yet. The correct resonator design and coupling tuning aside, we concluded the following features to be indispensable for reliable $\Delta X_s(B)$ characterization of thick REBCO CCs with a rutile DR:

1. **Large stability of temperature.**

2. **Large accuracy of frequency tracking.**

3. **Large mechanical stability of the cavity.**

The first two aspects are well known from thin film characterizations but are briefly reviewed, too, before moving to the third point which emerges as a new requirement for setups in which thick superconducting samples are employed as cavity endplates.

5.2.1   Large stability of temperature

For convenience, we give eq. (3.15) with applied approximations

$$-\frac{\Delta v_0(B,T)}{v_{0,\mathrm{ref}}(B,T)} = \frac{\Delta X_s^{\mathrm{CC}}(B,T)}{G^{\mathrm{CC}}(T)} + \frac{\Delta \varepsilon_r'(T)}{\varepsilon_{r,\mathrm{ref}}'(T)}. \tag{5.5}$$

There are three terms that influence the position of the resonance peak $v_{0,\mathrm{ref}}$ and its variation $\Delta v_0(B,T)$. First, the variation of surface reactance with temperature and field that is intrinsic to the superconductor $\Delta X_s^{\mathrm{CC}}(B,T)$. Second, the permittivity of the employed dielectric $\varepsilon_{r,\mathrm{ref}}(T)$ with its temperature variation $\Delta \varepsilon_r'(\Delta T)$. Third, the geometrical factor $G^{CC}(T)$ that is assumed to stay constant during magnetic field sweeps at fixed temperatures.

In order to employ the resonant frequency as a measurand for superconductor characterization, the contributions of the dielectric need to be negligible with respect to the superconductor response.

Let us estimate the governing term of equation 5.5, if a field sweep from 0 T to 0.5 T at 50 K was performed with a temperature instability of 1 K. Rutile has an extremely large permittivity $\varepsilon_{r,\mathrm{ref}}(50\,\mathrm{K}) \approx 111$, useful for confining the electromagnetic field in the crystal, but also steep $\Delta \varepsilon_r'(\Delta T)$ above 20 K [87]. With a temperature instability of 1 K at 50 K, $\Delta \varepsilon_r'(49.5\,\mathrm{K} - 50.5\,\mathrm{K}) \approx 0.05$ and thus, we would get $\frac{\Delta \varepsilon_r'(49.5\,\mathrm{K}-50.5\,\mathrm{K})}{\varepsilon_{r,\mathrm{ref}}(50\,\mathrm{K})} \approx 4.5 \cdot 10^{-4}$.

From eq. (2.59) and literature (see [67] and references within), we expect the magnitude of the surface reactance change with magnetic field $\Delta X_s(H)$ to coincide with $\Delta R_s(H)$ (the change of surface impedance with a temperature variation of 1 K can be neglected). With $R_s(50\,\mathrm{K}, 0.5\,\mathrm{T}) - R_s(50\,\mathrm{K}, 0\,\mathrm{T}) \sim 0.1\,\mathrm{m}\Omega$ (see Fig. 5.4), we can estimate $2\frac{\Delta X_s(50\,\mathrm{K},(0.5\,\mathrm{T}-0\,\mathrm{T}))}{G^{CC}(50\,\mathrm{K})} \approx 9.4 \cdot 10^{-7}$.

The term corresponding to the rutile permittivity is three orders of magnitude larger and would thus mask the reactive response of the superconductor in the resonant frequency. Ideally, a perfect temperature stability is desired when performing field sweeps so that $\Delta \varepsilon_r'(\Delta T \to 0) = 0$ and the resonant frequency holds only the intrinsic superconductor

response. Then equation (5.5) becomes

$$-2\frac{\Delta v_0(B,T)}{v_{0,\mathrm{ref}}(B,T)} = 2\frac{\Delta X_s^{\mathrm{CC}}(B,T)}{G^{\mathrm{CC}}(T)}. \tag{5.6}$$

Evidently, this condition cannot be practically achieved but we found that within the time, which it takes for ramping the magnetic field with $180\,\mathrm{Oe/s}$ from $0\,\mathrm{T}$ to $9\,\mathrm{T}$ and back to $0\,\mathrm{T}$, a temperature drift of about $50\,\mathrm{mK}$ at $50\,\mathrm{K}$ is acceptable. We reinforce the discussion by experimental data presented in Fig. 5.9.
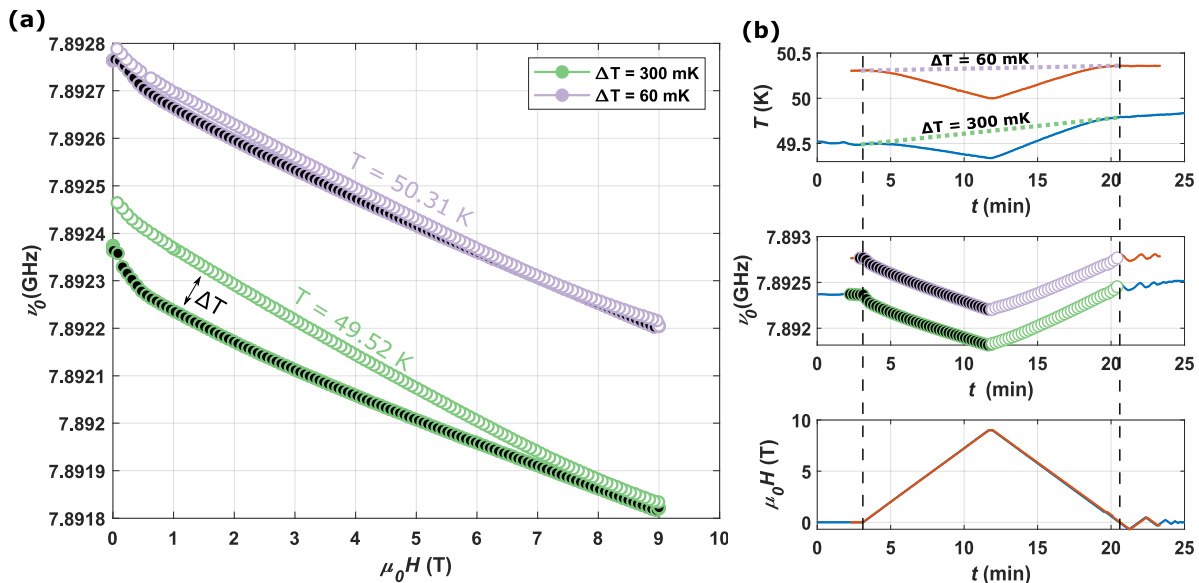
FIGURE 5.9: The influence of temperature instability on the resonant frequency. The measured samples are Theva CCs. **(a)** The resonant frequency as a function of magnetic field for two different temperature drifts at approximately the same temperature. The black and white filled markers represent the data points collected at sweeping the field up and down, respectively. **(b)** The time evolution of temperature T (upper subplot) in comparison with the time evolution of resonant frequency v_0 (middle subplot) and magnetic field $\mu_0 H$ (lower subplot) as shown in **(a)**. The stronger drift for the green data points becomes clear when comparing the temperature slopes (dotted lines) between starting and end (dashed lines) of the magnetic field sweep in the upper subplot.

The resonant frequency v_0, in this case $v_0(0\,\mathrm{T}) = v_{\mathrm{ref}}$, is given together with its magnetic field change $\Delta v(B)$ for two magnetic field sweeps with different temperature drifts at temperatures very close to $50\,\mathrm{K}$ in Fig. 5.9 **(a)**. The green and purple line color corresponds to a temperature drift of $\Delta T = 300\,\mathrm{K}$ and $\Delta T = 60\,\mathrm{mK}$, respectively, while the black and white filled markers represent the data points collected at sweeping the field up and down, respectively. The drifts have to be understood as temperature drifts per full magnetic field cycle ($0\,\mathrm{T} \to 9\,\mathrm{T} \to 0\,\mathrm{T}$).

We want to highlight the spreading between the ramping up and ramping down curve of the green data points. In this case, the temperature drift is significant enough in order to change the permittivity of the rutile $\Delta \varepsilon_r'(T)$ and superimpose the surface reactance signal of the superconductor $\Delta X_s^{\mathrm{CC}}(B)$, see equation (5.5). For a temperature drift of $\Delta T = 60\,\mathrm{mK}$ per magnetic field cycle, see purple data points, the ramping up and ramping down curves collapse almost perfectly on top of each other, indicating a negligible influence of the rutile crystal. The resonant frequency of the purple data points are slightly elevated because of the higher measurement temperature, $T_{\mathrm{purple}} = 50.31\,\mathrm{K}$ as compared to $T_{\mathrm{green}} = 49.52\,\mathrm{K}$.

For better understanding, we add in Fig. 5.9 **(b)** the time evolution of the magnetic field sweeps and resonant frequency shown in 5.9 **(a)** together with the monitored temperature. Focusing on the temperature subplot, the temperature drifts

for the corresponding field sweeps can be read as the difference between end- and start point of the field sweeps $\Delta T = T(H_{\text{end}} = 0\,\text{T}) - T(H_{\text{start}} = 0\,\text{T})$. The dips in temperature profiles during the field sweep result from the magnetoresistance of the used CERNOX temperature sensor.

We show in Fig. 5.10 how the instability in temperature translates into the according to eq. (5.6) calculated surface reactance change with magnetic field ΔX_s of a CC. The reference resonant frequency $\nu_{0,\text{ref}}$ is always chosen to be the highest measured frequency, so the value at zero field of the FC curve $\nu_0^{\text{FC}}(0\,\text{T})$, in order to fulfil $\Delta X_s(B = 0\,\text{T}) = 0$ and $\Delta X_s(B > 0\,\text{T}) > 0$.
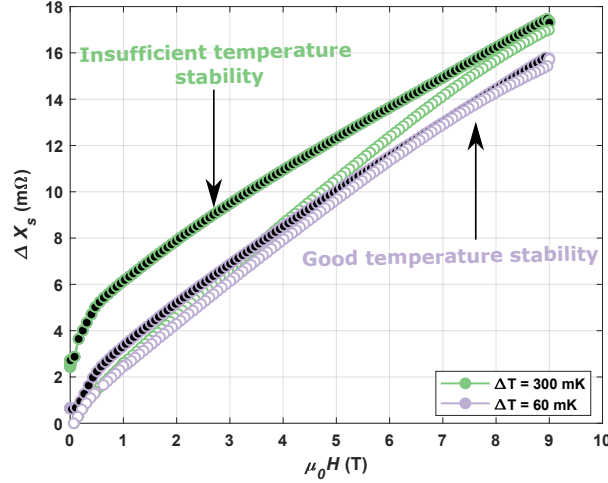
FIGURE 5.10: The according to eq. (5.6) calculated change in surface reactance with magnetic field ΔX_s of Theva CCs for two magnetic field sweeps with different temperature stabilities ΔT at 50 K. The larger temperature instability of the green measurement points accompanies an non negligible contribution from rutile's permittivity, larger total surface reactance values and larger spreading between curves corresponding to sweeping field up (black markers) and down (white markers), which results in masking of the intrinsic superconductor response (see purple data points).

For the greater temperature instability (green points), the permittivity change of rutile $\Delta \varepsilon_r'(T)$ is not negligible which masks the intrinsic superconductor's microwave response, see eq. (5.5).

In order to guarantee a stable enough temperature for reliable surface reactance measurements, we established a thermalization protocols before performing the magnetic field sweeps.

5.2.2   Large accuracy of frequency tracking

In the previous subsection, we already estimated the surface reactance sensitivity which would be desirable in order to resolve the surface reactance field behavior sufficiently well for REBCO CCs. It is $\delta X_s \approx 0.1\,\text{m}\Omega$ when analyzing $\Delta X_s(H)$ at small magnetic fields. With equation (5.6), we can determine the required frequency accuracy $\delta \nu$ required to resolve such small surface reactance changes:

$$\delta \nu = \nu_0 \cdot \frac{\delta X_s}{G^{\text{CC}}}$$
$$\Rightarrow \delta \nu = 8\,\text{GHz}\frac{0.1\,\text{m}\Omega}{213\,\Omega} \approx 3.8\,\text{kHz},$$

where we assume a resonant frequency $\nu_0 = 8\,\text{GHz}$ and $G^{\text{CC}} = 213\,\Omega$, which corresponds to the value at 50 K.

The accuracy in frequency tracking depends on the vector network analyzer and its optional add-ons. In table 3.1,

we detail the nominal frequency accuracy, which amounts (without taking time deterioration into account) $\delta v_{FF} = \pm 0.7\,\text{ppm} \cdot v_0$ and $\delta v_{ZNB20} = \pm 0.5\,\text{ppm} \cdot v_0$ for the FieldFox N9918A and R&S ZNB20, respectively. For a resonant frequency $v_0 = 8\,\text{GHz}$, we get $\delta v_{FF} = 5.6\,\text{kHz}$ and $\delta v_{ZNB20} = 4\,\text{kHz}$ which is in the same order of magnitude as the desired $\delta v \approx 3.8\,\text{kHz}$.

We confirmed the large frequency accuracy experimentally by tracking the sample temperature together with the resonant frequency of SuperPower CCs with the FieldFox VNA as shown in Fig. 5.11.
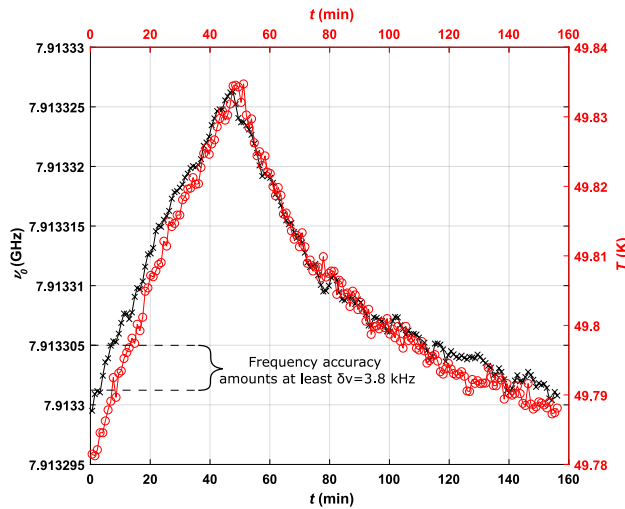
FIGURE 5.11: Experimental demonstration of FieldFox VNA's frequency accuracy. The resonant frequency as a function of time matches excellently the temperature reading of a CERNOX sensor and can be thus identified as a signal that corresponds to the sample temperature. Each tick on the frequency ordinate amounts 5 kHz which encompasses several distinguishable data points of temperature signal. This shows that the frequency accuracy of our FieldFox VNA is within the limit of desired accuracy $\delta v = 3.8\,\text{kHz}$.

In this experiment, we stabilized the temperature within a range of $\approx 100\,\text{mK}$ close to 50 K. For such small temperature variations, the change of surface reactance of the CCs samples is negligible, $\Delta X_s(T) \approx 0$, and equation (5.5) simplifies to

$$-\frac{\Delta v_0(T)}{v_{0,\text{ref}}(T)} = \frac{\Delta \varepsilon_r'(T)}{\varepsilon_{r,\text{ref}}'(T)}.$$

Within small temperature variations in the range of $100\,\text{mK}$ at $50\,\text{K}$, the permittivity change with temperature of rutile $\Delta \varepsilon_r'(T)$ is linear and antiproportional to the temperature, so that the change of frequency with temperature $\Delta v(T)$ tracks basically the change of sample temperature. Plotting the time evolution of resonant frequency (black crosses) together with the time evolution of temperature recorded with a CERNOX temperature sensor close to the samples (red circles), we observe an almost perfect alignment of both quantities. This implies that we indeed track the sample temperature with resonant frequency and that measured frequency changes correspond to a signal. In Fig. 5.11, each tick on the frequency ordinate amounts 5 kHz which encompasses several distinguishable data points of a signal. Thus, we can attest that the frequency accuracy of our FieldFox VNA is within the limit of desired frequency accuracy $\delta v = 3.8\,\text{kHz}$.

In this subsection, we have explained the need for a VNA with very large frequency accuracy in order to measure $\Delta X_s(B)$ with high resolution and demonstrated theoretically and experimentally that our employed VNAs fulfill this requirement.

5.2.3   Large mechanical stability of cavity

We found magnetic forces originating from the interplay between HTS and applied magnetic field to disturb surface reactance experiments.

From magnetostatics [182] one can derive the magnetization force, as known from levitating force experiments [183], on a HTS in a magnetic field as [184, 185]:

$$\vec{F}_m = \int\limits_{\text{HTS}} (\vec{M} \cdot \nabla)\vec{B}\, dV, \tag{5.7}$$

where $\vec{M}$ is the magnetization of the HTS and can be in our present setup, a loaded DR with sample planes normal to applied magnetic field, approximated with $\vec{M} = M(x,z)\vec{e}_z$. Then the vertical force component of equation (5.7) becomes

$$F_z = \int\limits_{\text{HTS}} M\frac{\delta B_z}{\delta z}\, dV, \tag{5.8}$$

where $\delta B_z/\delta z$ are field inhomogeneities in z-direction that corresponds to field perturbations induced by the metallic housing of the DR enclosed in a magnetic field.

The magnetic force direction depends on the cooling history of the sample. Adopted from literature [183, 186], we show in Fig. 5.12 how F_z acts on YBCO as a function of distance from a permanent magnet in a levitating force experiment. For samples cooled in zero field, the force F_z is repulsive, increases with the magnetic flux penetrating
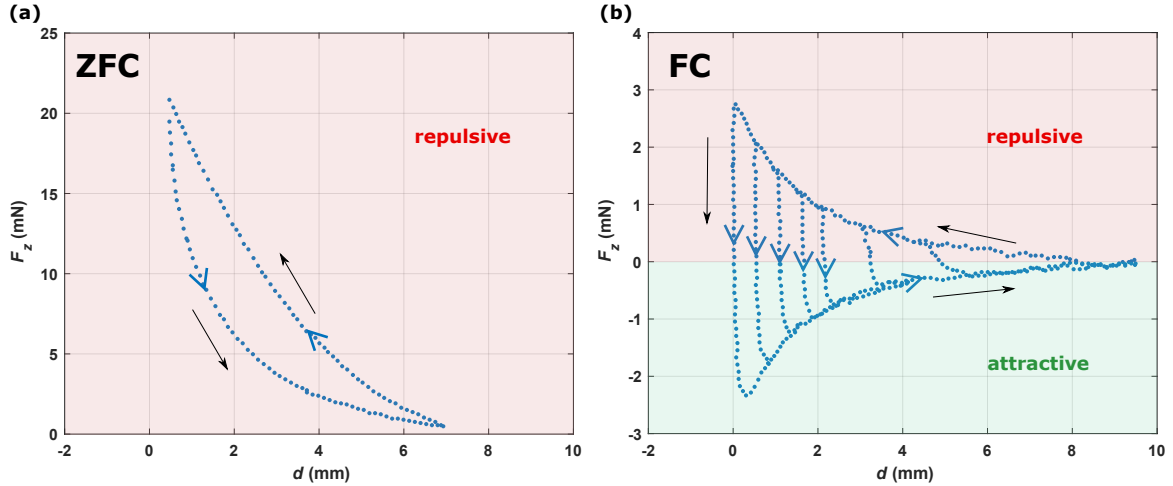
FIGURE 5.12: Levitation force F_z acting on YBCO as a function of distance from a permanent magnet at 77 K. **(a)** Varying the distance of a permanent magnet from a zero field cooled (ZFC) YBCO bulk sample, the force becomes hysteretic upon reversing the magnetic field motion but always repulsive. Data replotted from [183]. **(b)** Vertical force vs. distance from permanent magnet for a field-cooled thin film YBCO sample. Upon retreating the magnet, the force becomes an attractive retention force. Arrows indicate course of cycling. Data replotted from [186].

the sample and becomes smaller but still repulsive upon retracting the magnet. The magnetic hysteresis changes for field cooled HTS. Increasing the magnetic flux in the sample generates again a repulsive force, but causes a change in vertical force sign with decrease of magnetic flux through the sample.

The magnitude of the vertical force scales linearly with the superconductor's magnetization M, thus J_c, and its volume V, see eq. (5.8). The considerable CC sample volume $V_{\text{CC}} \approx 12\,\text{mm} \times 12\,\text{mm} \times 2\,\mu\text{m}$ and its excellent current-carrying

capabilities $J_c(77\,\text{K}) \sim 1 - 3\,\text{MA/cm}^2$ lead to significant pressure on the twin samples that can cause the endplates of the resonating cavity to move when applying a magnetic field. In the thesis, before reversing the field direction, applied magnetic fields reach 9 T and samples become fully penetrated with vortices, thus magnetic forces will follow the hysteretic curves of a field-cooled HTS as presented in Fig. 5.12 (**b**).

We show in Fig. 5.13 how ramping the applied magnetic field affects the cavity volume and consequently the measured resonant frequency $\nu_0(B)$ for a resonator loaded with Fujikura CCs at 20 K. Before moving forward, it is recommended to review the nomenclature of the resonator components in Fig. 3.3.
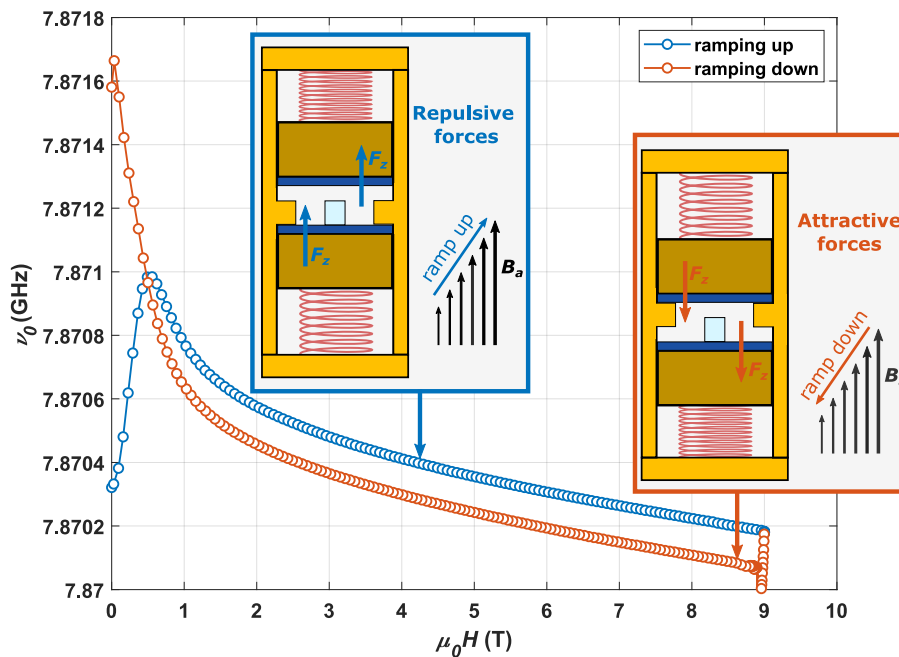
FIGURE 5.13: The variation of resonant frequency with magnetic field measured at 20 K for a DR loaded with Fujikura CC twin samples. Levitation forces cause cavity instabilities, depicted in the insets, that manifest as hysteretic resonance frequencies.

When changing the applied magnetic field in the PPMS, we are generating currents in the metallic frame of the resonator which create magnetic field inhomogeneities in its interior (where the CCs reside). These inhomogenieties $\frac{\delta B_z}{\delta z}$ are responsible for the appearance of the magnetization force F_z as described in eq. (5.8). Analogous to approaching a permanent magnet closer to the superconductor, the samples experience a repulsive force when we increase the applied magnetic field. The bottom sample hits the side walls of the cavity and stays immobile while the top sample pushes against the spring and, if the repulsive force is large enough to overcome gravity and the suspension of the spring, opens up new cavity volume through uplift of the top endplate. Upon reversing the magnetic field in the PPMS, analogous to pulling the permanent magnet away from the superconductor, the levitation force changes in direction. Given again that the force is large enough, the cavity volume change is reversed as the top sample hits the resonator body and the bottom endplate sinks (see inset of Fig. 5.13). The mechanical shifts of the cavity are allowed by the configuration used in the resonator and cause repercussions since the height of a cavity strongly affects the resonant frequency [54]. In consequence, the hysteresis in levitation forces propagates to the reference resonant frequency $\nu_{0,\text{ref}}$ which masks the intrinsic surface reactance response of the superconductor, see eq. (5.6). The resonant frequency curves from ramping the magnetic field up and down do not match at fields $> 2\,\text{T}$ as would have been expected for a resonant frequency signal originating from the CC's surface reactance (see Fig. 5.9). In total accordance with equation 5.8, this phenomenon is encountered more pronounced for samples with large thickness, high J_c and at lower temperatures.

As a proof of concept, we demonstrate in Fig. 5.14 that counteracting the levitation force, consequently increasing the mechanical stability of the cavity, reduces the hysteresis in the resonant frequency.
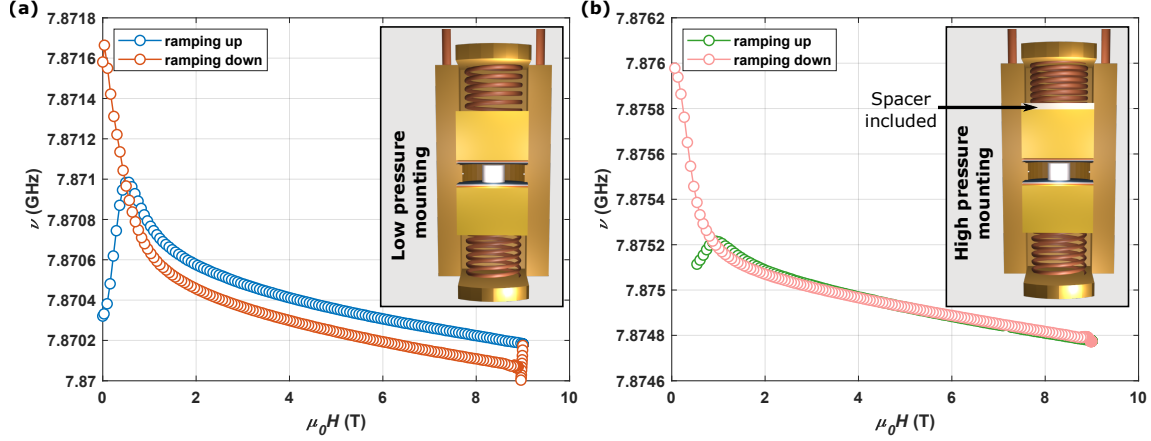
FIGURE 5.14: The resonant frequency with variation of magnetic field for two different resonator mountings loaded with Fujikura CC twin samples at 20 K. It is demonstrated how the inclusion of a spacer, referred to as high pressure mounting, reduces the hysteresis in resonant frequency which is associated with a larger stability of the resonance cavity.

As compared to the conventional sample mounting, denoted as low pressure mounting in the inset of Fig. 5.14 (a), a teflon spacer of $\approx 2\,\text{mm}$ thickness is placed between top sample block and spring, denoted as high pressure mounting in the inset of Fig. 5.14 (b), in order to compress the spring and apply a larger restoring force. The additional constraint on the upper sample movement restricts the change of cavity volume as indicated in the inset of Fig. 5.14 (b), i.e. improves the cavity stability. In this example, it was not necessary to include a spacer to the lower volume of the resonator, suggesting that the spring constant of the bottom spring is larger than the top spring's constant.

In order to form a better understanding about how the cavity expansions affect the resonant frequency $\nu(B)$ and consequently contribute to the magnetic field variation of surface reactance $\Delta X_s(B)$, we launched an additional study. The pressure on the top and bottom samples can be controlled by the spring constant of the used springs or by compressing the springs to provoke larger restoring forces according to Hooke's law. There are two adjustment parameters for the spring compression:

1. Thickness of spacers t.

2. Tightening of lid screws with torque D.

We fixed the spacers while controlling the torque on the lid screws to study the change in measured $\Delta X_s(B)$, calculated with eq. (5.6), for SuperOx 2 twin samples at 20 K as presented in Fig. 5.15. The corresponding resonator mounting specs are listed in table 5.2.

By increasing the tightening of the top lid screws with torque D, we increase the pressure on the top sample and thus the resistance of the cavity against mechanical expansions caused by levitation forces as shown in Fig. 5.13. This condenses in smaller hystereses between ZFC and FC cooled curves. Starting from a torque of $D \sim 2.5\,\text{Ncm}$, the hysteresis at large fields δ_1 drops almost to zero, rendering $\Delta X_s(B)$ reversible for fields $>1\,\text{T}$. The hysteresis at zero field δ_2 follows a similar pattern. It decreases with increase of torque D, however, it does not drop to zero within our line of experiments. So, the forces exerted by the springs on the samples are big enough to remove δ_1 but not δ_2.

Mount.	Top spacers t	Bot. spacers t	Top screws D	Bot. screws D
M1	$t_{\text{sample block}} + 2 \cdot t_{\text{teflon spacer}} =$ 6.99 mm+2·2.09 mm = 11.17 mm	$t_{\text{sample block}} + t_{\text{teflon spacer}} =$ 8.23 mm+2.11 mm = 10.34 mm	~ 0.01 Ncm	13 Ncm
M2	" "	" "	~ 0.1 Ncm	13 Ncm
M3	" "	" "	10 Ncm	10 Ncm
M4	" "	" "	11.5 Ncm	13 Ncm
M5	undocumented	undocumented	undocumented	undocumented

TABLE 5.2: The resonator mounting specifications for experiment shown in Fig. 5.15. Mounting M5 is not part of the initial experiment line, so its exact specs remain undocumented, however, it was a mounting with intention to exert extremely high pressure on the samples.
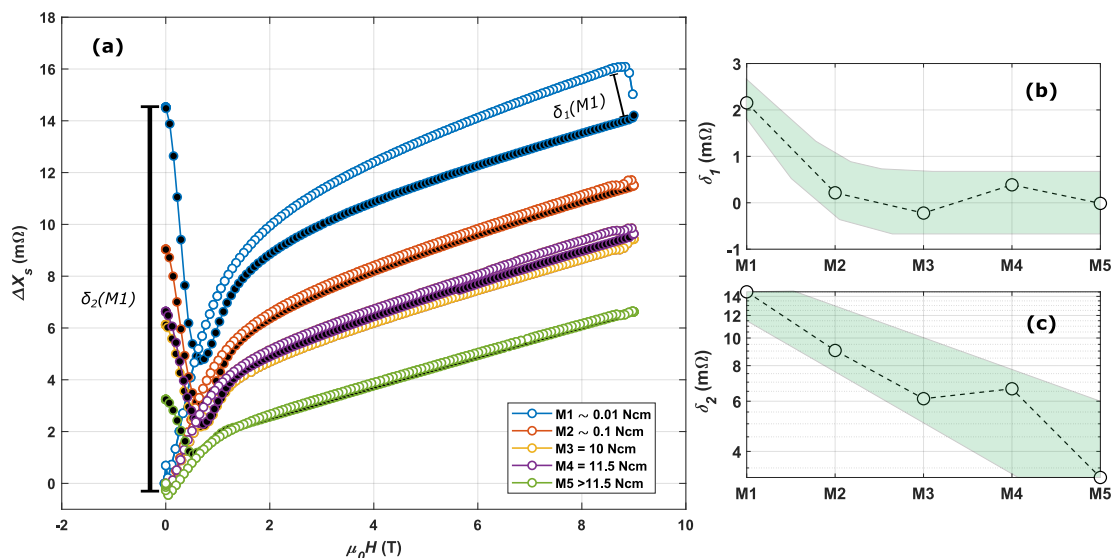
FIGURE 5.15: **(a)** The variation of surface reactance with magnetic field ΔX_s of SuperOx 2 samples measured at 20 K for different torques of top screws that correspond to mountings M1-M5 as detailed in table 5.2. For each mounting, we display two curves. One represents the ramping field up (ZFC) with black filled markers and the other ramping field down (FC) with white filled markers. $\delta_1 = \Delta X_s^{\text{FC}}(8.9\,\text{T}) - \Delta X_s^{\text{ZFC}}(8.9\,\text{T})$ and $\delta_2 = \Delta X_s^{\text{FC}}(0\,\text{T}) - \Delta X_s^{\text{ZFC}}(0\,\text{T})$ indicate the degree of hysteresis introduced to the surface reactance due to instability of the cavity as shown in Fig. 5.13. **(b)** The hysteresis δ_1 between ZFC and FC curves at large fields decreases and reaches values close to 0 rapidly with the mountings, thus with the pressure exerted on the top sample. **(c)** The hysteresis δ_2 between ZFC and FC curves at small fields decreases constantly with increasing the pressure on top sample. A saturation value was not achieved within performed experiments. Comparing with the hysteresis of the surface resistance R_s, which is at max about 0.4 mΩ (Fig. 5.4), the magnitude of $\delta_2 \approx 4$ mΩ in the mounting M5 appears to be big.

This suggests that the levitation forces F_z have their maximum at small magnetic fields causing the strongest cavity expansion, which is in line with the description in equation (5.8), since F_z scales linearly with the magnetization of the sample that has its maximum at zero field. A further increase of tightening of the lid screws would result in higher pressure on the samples and consequently a bigger stability of the cavity with respect to levitation forces. However, we remark that the pressure on the samples exerted by the springs should be limited to an extent where the dielectric crystal neither breaks or causes indentation in the samples.

We have demonstrated the necessity to counteract the mechanical expansion of the cavity caused by levitation forces, in order discount extrinsic effects to the measured resonant frequency and consequently the surface reactance. By

adjusting the pressure on the samples with thickness variation of spacers and torque change on lid screws, we could completely eliminate the irreversibility of ZFC and FC curves without damaging neither the samples nor the rutile crystal at fields >1 T. As shown in Fig. 5.15, a hysteresis δ_2, most likely originating from levitation forces, remains even for the mounting where we exerted maximum pressure. This extrinsic effect can be approximately discounted by a simple offset as discussed in the next section and shown in Fig. 5.17 **(c)**.

Finally, we show the surface reactances $X_s(B) = X_0 + \Delta X_s(B)$ as a function of magnetic field at 50 K for several CCs in comparison with FCC Cu in Fig. 5.16.
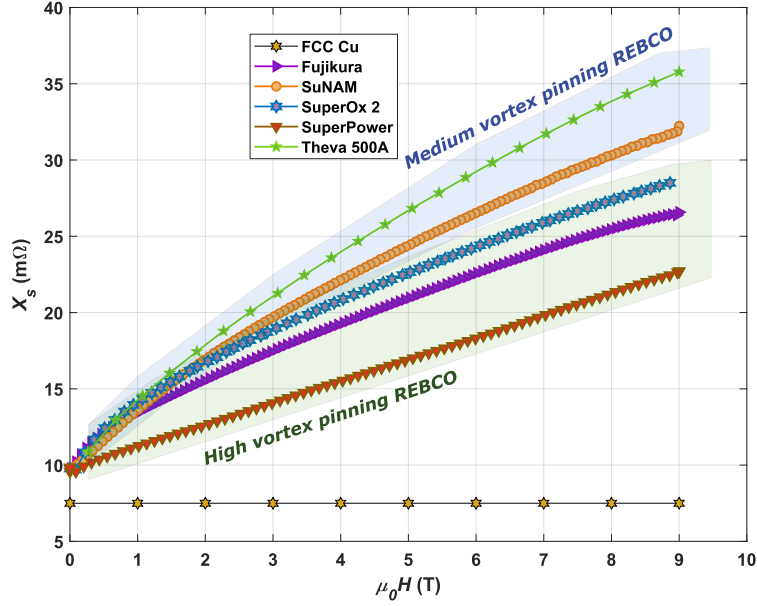
FIGURE 5.16: Surface reactance and its magnetic field dependence (displayed are the FC curves) of analyzed CCs in comparison with FCC Cu at 50 K. Similar to the surface resistance case, the field performance of CCs can be roughly categorized into two regions, medium - and high vortex-pinning REBCO, that refers to the type of microstructure.

The field independent surface reactance part of HTS can be written within the BCS theory as $X_0 = X_{\mathrm{BCS}} = 2\pi \nu \mu_0 \lambda_L$, where λ_L stands for the London penetration depth. The london penetration depth can be calculated by assuming the conventional temperature dependence [30]

$$\lambda_L^2 = \frac{\lambda_L^2(0\,\mathrm{K})}{1 - (T/T_c)^4} \tag{5.9}$$

with $\lambda_L(0\,\mathrm{K}) = 150\,\mathrm{nm}$ [53] and T_c the critical temperature measured by transport measurement of corresponding CCs. With this, we can estimate the expected surface reactance $X_{BCS}(T = 50\,\mathrm{K}, \nu = 8\,\mathrm{GHz}) \approx 10\,\mathrm{m\Omega}$. The field dependent part $\Delta X_s(H)$ is extracted from resonant frequency measurements, during which we established large temperature and cavity stability, according to equation (5.6). For the surface reactance of Cu, we have assumed that the Hagen-Rubens limit ($R_s = X_s$) [187] is appropriate.

Analogous to the field behavior of R_s, the REBCO microstructure of CCs influences the imaginary part of the surface impedance, too. Interestingly, the ranking at high fields among the providers stays unaffected with respect to $R_s(B)$. As a rule of thumb, we can derive experimentally that a microstructure engineered for high-field performance in R_s yields favorable results for X_s, too. This observation lines up with theoretical formulations as presented in eq. (2.59)

since both the real and imaginary part of the vortex-motion resistivity ρ_{vm}, see eq. (2.56), are governed by the same vortex parameters η and v_p that are directly linked to the REBCO microstructure.

At elevated frequencies around 8 GHz, HTS CCs present higher X_s whose gap to Cu grows larger with increasing magnetic fields. Depending on the provider, $X_s^{\text{CC}}(9\,\text{T}) \approx 3 - 5 \cdot X_s^{\text{FCC Cu}}(9\,\text{T})$. In section 5.4, we will compare the microwave performances of REBCO CCs with Cu at 1 GHz, a frequency closer to the prospected operation conditions of the FCC-hh.

5.3 Model consistent extraction of vortex-motion parameters

For samples where both the surface resistance R_s and the change of surface reactance with magnetic field ΔX_s was measured, we have two independent data sets available. Thus, we can determine the real and imaginary part of the vortex-motion (VM) resistivity $\rho_{vm} = \rho'_{vm} + i\rho''_{vm}$ within the Gittleman-Rosenblum model from eq. (2.59). As mentioned earlier, the GR model neglects thermal flux creep, thus errors on the VM parameters decrease with distance to T_c and H_{c2}. For temperatures where thermal effects become significant, the model provides lower boundaries for v_p and k_p and an upper limit for η [188]. Consequently, by neglecting thermal effects, we give pinning parameters that underestimate the pinning performance.

With some algebra one can express the VM resitivity as a funtion of surface impedance[1]

$$\rho'_{vm}(T,H) = \frac{2\Delta R_s(T,H) \cdot (\Delta X_s(T,H) + \omega\mu_0\lambda_L)}{\omega\mu_0} \tag{5.10}$$

and

$$\rho''_{vm}(T,H) = \frac{(\Delta X_s(T,H) + \omega\mu_0\lambda_L)^2 - \Delta R_s(T,H) - (\omega\mu_0\lambda_L)^2}{\omega\mu_0}. \tag{5.11}$$

The London penetration depth is calculated according to equation (5.9). We did not use any magnetic field dependence for λ_L as it does not significantly change the final result [189].

However, before calculating the vortex-motion resistivity ρ_{vm}, we should scrutinize the experimentally determined field change in surface resistance $\Delta R_s(H)$ and in surface reactance $\Delta X_s(H)$. From theory which considers only the intrinsic vortex-motion response of a superconductor, we would expect a power law increase of both surface resistance and surface reactance with magnetic field according to $R_s^{vm}(H) \propto H^{\alpha_1}$ and $X_s^{vm}(H) \propto H^{\alpha_2}$ with $\alpha_{1,2} = 0.5 - 1$ [73, 178]. In the course of this thesis, we have found that the $\Delta R_s(H)$ and $\Delta X_s(H)$ of a CC include external effects that superimpose the intrinsic vortex-motion response of the superconductor. To illustrate this mathematically, we can write the field change of the surface resistance as

$$\Delta R_s(H) = R_s(H) - R_s(0\,\text{T}) \tag{5.12}$$

$$= \left(R_s^{vm}(H) + R_s^{ext\cdot}(H)\right) - \left(R_s^{vm}(0\,\text{T}) + R_s^{ext\cdot}(0\,\text{T})\right). \tag{5.13}$$

Here, $R_s^{ext\cdot}$ represent the external contributions that mask the intrinsic superconductor response. Without applying a magnetic field, the superconductor is free of vortices so that $R_s^{vm}(0\,\text{T}) = 0$. With this, eq. (5.13) simplifies to

$$\Delta R_s(H) = \left(R_s^{vm}(H) + R_s^{ext\cdot}(H)\right) - R_s^{ext\cdot}(0\,\text{T}). \tag{5.14}$$

---

[1]The derivation is given in appendix B.

Analogously, we can write for the field change of the surface impedance

$$\Delta X_s(H) = \left(X_s^{vm}(H) + X_s^{ext\cdot}(H)\right) - X_s^{ext\cdot}(0\,\text{T}). \tag{5.15}$$

Two main sources have been identified that constitute $R_s^{ext\cdot}$ and $X_s^{ext\cdot}$ when characterizing CCs with a DR:

1. **Magnetic forces lead to mechanical expansion of the DR cavity which cause shifts in the resonant frequency ν_0, directly affecting the measured ΔX_s at small magnetic fields.**
   The effect manifests itself in a strong hysteresis between the ZFC and FC branches (ramping magnetic field up and down, respectively) of ΔX_s and is appreciable for small fields in Fig. 5.17 **(a)** or **(b)** (see subsection 5.2.3 for more detailed analysis of origin). This phenomenon is mainly contained in $X_s^{ext\cdot}$.

2. **Trapped fields and its interaction with a magnetic buffer layer or inferior REBCO seed layers mask the vortex-motion response, i.e. both ΔR_s and ΔX_s, of the HTS at small magnetic fields.**
   Referencing Fig. 5.17 **(a)** or **(b)**, at fields $\mu_0 H < 1\,\text{T}$, especially the surface resistance shows a more plateau-like behavior before it passes over to the expected power law increase. We will demonstrate in subsection 6.2.2 that the buffer layer $LaMnO_3$ present in some CCs alternates the measured surface impedance from the intrinsic vortex-motion response of the REBCO. Another example for small field contributions, comes from Theva which uses REBCO seed layer [190] of inferior superconducting quality as a growth template, which will affect the small field range of the high-frequency response. These phenomena are contained in $R_s^{ext\cdot}$ and $X_s^{ext\cdot}$.

As mentioned, both external effects affect mostly the small field range ($\mu_0 H < 1\,\text{T}$) while leaving the surface impedances at higher fields undisturbed. In consequence, we can discriminate the field change in surface resistance ΔR_s according to their field range as

$$\Delta R_s(H) = \begin{cases} \left(R_s^{vm}(H) + R_s^{ext\cdot}(H)\right) - R_s^{ext\cdot}(0\,\text{T}) & \text{for } \mu_0 H < 1\,\text{T} \\ R_s^{vm}(H) - R_s^{ext\cdot}(0\,\text{T}) & \text{for } \mu_0 H > 1\,\text{T}. \end{cases} \tag{5.16}$$

Knowing this, we can develop a strategy to eliminate the field independent constant $R_s^{ext\cdot}(0\,\text{T})$ coming from external effects. Since the determined ΔR_s above 1 T represent the pure vortex-motion response, we ignore the data below 1 T and approximately extrapolate the power law behavior from the field range $\mu_0 H > 1\,\text{T}$ down to zero field for ΔR_s. The crossing between the extrapolation and the ordinate has to be understood as the field independent constant $R_s^{ext\cdot}(0\,\text{T})$ to fulfill the boundary condition $R_s^{vm}(0\,\text{T}) = 0$, see Fig. 5.17 **(a)**. Now that $R_s^{ext\cdot}(0\,\text{T})$ is identified, it can be easily added to ΔR_s. After addition, we get

$$\Delta R_s^{\text{offset}}(H) = \Delta R_s(H) + R_s^{ext\cdot}(0\,\text{T}) = \begin{cases} R_s^{vm}(H) + R_s^{ext\cdot}(H) & \text{for } \mu_0 H < 1\,\text{T} \\ R_s^{vm}(H) & \text{for } \mu_0 H > 1\,\text{T}. \end{cases} \tag{5.17}$$

With this procedure we can isolate the intrinsic vortex-motion surface resistance R_s^{vm} of the REBCO for fields above 1 T, see Fig. 5.17 **(b)**.
An analogous case can be made for the field change of the surface reactance ΔX_s, where the field independent external contribution to the surface reactance $X_s^{ext\cdot}(0\,\text{T})$ is identified by extrapolating the field behavior of ΔX_s from higher fields to 0 T as illustrated in Fig. 5.17 **(a)**. This contribution can be eliminated at high fields by offsetting with $X_s^{ext\cdot}(0\,\text{T})$ according to

$$\Delta X_s^{\text{offset}}(H) = \Delta X_s(H) + X_s^{ext\cdot}(0\,\text{T}) = \begin{cases} X_s^{vm}(H) + X_s^{ext\cdot}(H) & \text{for } \mu_0 H < 1\,\text{T} \\ X_s^{vm}(H) & \text{for } \mu_0 H > 1\,\text{T}. \end{cases} \tag{5.18}$$

The demonstrated case in Fig. 5.17, corresponds to Fujikura CC measured at 40 K and we get for the field independent external offset $R_s^{ext\cdot}(0\,\text{T}) = 0.5\,\text{m}\Omega$ and $X_s^{ext\cdot}(0\,\text{T}) = -1.8\,\text{m}\Omega$. We have to note that this approach is to a considerable
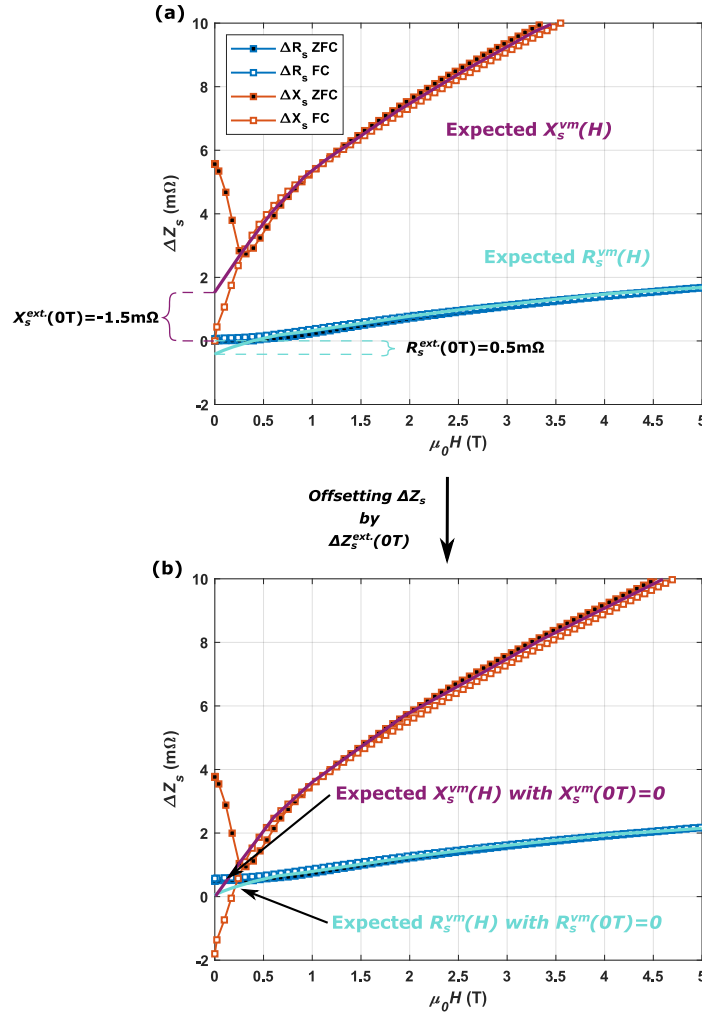
FIGURE 5.17: Comparing measured and offset surface impedance of Fujikura without APC at $T = 40\,\text{K}$. **(a)** Shown here is the measured change of surface impedance with magnetic field. **(b)** The corresponding offset ΔR_s and ΔX_s that discounts extrinsic influences on the vortex-motion response. The offset adjusts the measurement data, shown as transparent markers, to the expected field behavior intrinsic to a superconductor and amounts here $0.5\,\text{m}\Omega$ for ΔR_s and $-1.8\,\text{m}\Omega$ for ΔX_s. **(c)** Zoomed into small field area where offset ΔX_s data is shown together with expected $\Delta X_s(H)$ (pink dashed line). **(d)** Same field range with ΔR_s plotted together with expected $\Delta R_s(H)$ (light blue dashed line).

degree error-prone since predicting the correct field behavior for each individual sample and temperature turns out to be challenging, but it is necessary in order to isolate the vortex-motion response. In appendix B.2, we compare the vortex-motion parameters $\rho_{vm}(H)$, $\nu_p(H)$ and $\rho_{ff}(H)$ when either calculated from simply $\Delta R_s(H) = R_s(H) - R_s(0\,\text{T})$ and $\Delta X_s(H) = X_s(H) - X_s(0\,\text{T})$ (see eqs. (5.14) and (5.15)) or from the corrected data $\Delta R_s^{\text{offset}}(H) = \Delta R_s(H) + R_s^{ext\cdot}(0\,\text{T})$ and $\Delta X_s^{\text{offset}}(H) = \Delta X_s(H) + X_s^{ext\cdot}(0\,\text{T})$ (see eqs. (5.17) and (5.18)). There, it is shown that using $\Delta R_s^{\text{offset}}$ and $\Delta X_s^{\text{offset}}$ yield consistent results in terms of physical understanding and GR model. In the following, we only analyze the results where the deviation of $\Delta R_s(H)$ and $\Delta X_s(H)$ from the expected intrinsic superconductor response is small enough to allow a reasonable estimation of the field independent offset corrections $R_s^{ext\cdot}(0\,\text{T})$ and $X_s^{ext\cdot}(0\,\text{T})$.

In Fig. 5.18, we show how the offset $\Delta Z_s + Z_s^{ext\cdot}(0\,\mathrm{T})$[2] transforms into the vortex-motion resistivity ρ_{vm} according to equations (5.10) and (5.11) for SuNAM CC at 20 K. The field responses of the real and imaginary part of the vortex-
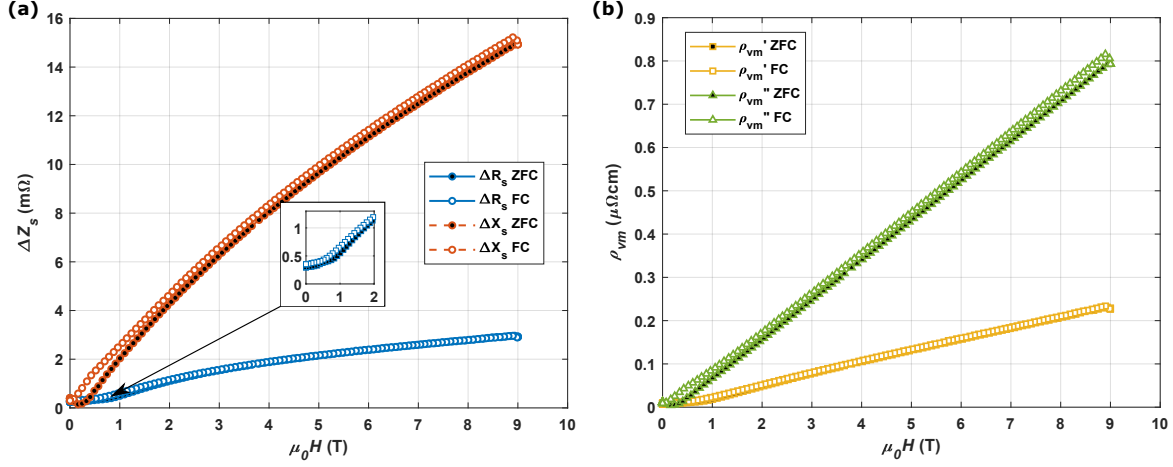
FIGURE 5.18: The vortex-motion response of SuNAM CC at 20 K up to 9 T. **(a)** measured change in surface impedance that is offset by $\Delta R_s = 0.3\,\mathrm{m}\Omega, \Delta X_s = 0.3\,\mathrm{m}\Omega$ to discount extrinsic effects. **(b)** The corresponding vortex-motion resistivity calculated with equations (5.10) and (5.11).

motion resistivity are almost perfectly linear as expected from equation 2.56. However, at fields $\mu_0 H < 1\,\mathrm{T}$, especially the real part ρ'_{vm} shows a more plateau-like behavior, which we associate with external effects, before it passes over to the expected linear increase. A similar field dependence is prominently present in the surface resistance of the sample as shown in the inset of Fig. 5.18 **(a)** and as already mentioned, it can be associated with the present buffer layer LaMnO$_{3+\delta}$. LaMnO$_{3+\delta}$ (LMO) as used in SuNAM CC can exhibit metallic properties when grown in its rhombohedral phase and wildly different magnetic properties depending on its oxygen stochiometry δ [191], which masks the intrinsic response of the superconductor. Later, in subsection 6.2.2, we will demonstrate that indeed the LMO give a considerable microwave signal. The signal of the buffer manifests in all measured temperatures as presented in Fig. 5.19 and requires a small offset.

With the variations in CC architectures, i.e. the variations in superconductor thickness or quality, type of buffer layers used and their corresponding thicknesses, each provider exhibits different degrees of masking of intrinsic superconductor response by extrinsic effects.

To our knowledge, no group reported the REBCO CC vortex-motion resistivity at 8 GHz yet. However, the ρ_{vm} from SuNAM CC at 20 K (see Fig. 5.18 **(b)**) is in line with results from similar measurement conditions. Alimenti et al. disclose $\rho'_{vm}(27\,\mathrm{K}, 9\,\mathrm{T}, 14.9\,\mathrm{GHz}) \approx 0.1 - 0.6\,\mu\Omega\mathrm{cm}$ and $\rho''_{vm}(27\,\mathrm{K}, 9\,\mathrm{T}, 14.9\,\mathrm{GHz}) \approx 0.3 - 0.8\,\mu\Omega\mathrm{cm}$ for $\sim 100\,\mathrm{nm}$ thick YBCO grown on single crystal substrates [192], while Tsuchiya et al. detail $\rho'_{vm}(30\,\mathrm{K}, 9\,\mathrm{T}, 31.7\,\mathrm{GHz}) \approx 3.5\,\mu\Omega\mathrm{cm}$ and $\rho''_{vm}(30\,\mathrm{K}, 9\,\mathrm{T}, 31.7\,\mathrm{GHz}) \approx 3.4\,\mu\Omega\mathrm{cm}$ for a $50\,\mu\mathrm{m}$ thick YBCO single crystal [178].

We compare the vortex-motion resistivity determined from the ZFC branch of several samples at 70 K, the temperature at which ΔX_s most of the CCs could be characterized due to moderate magnetic forces, in Fig. 5.20 **(a)-(b)**.
The errors considered in the plot correspond to the frequency accuracy of the VNA Rhode & Schwarz ZNB20 $\delta_\nu = 0.1\,\mathrm{ppm} \cdot \nu$ allowing an upper limit error estimation for the surface resistance $\sigma_{R_s} = 0.05\,\mathrm{m}\Omega$ and change in surface reactance $\sigma_{\Delta X_s} = 0.05\,\mathrm{m}\Omega$ which were propagated to the vortex-motion resistivity. Focusing primarily on the comparative aspect of the analysis, systematic errors originating from uncertainties in geometry factor, permittivity of the

---

[2]Offsetting $\Delta Z_s(H)$ by $Z_s^{ext\cdot}(0\,\mathrm{T})$ means explicitly offsetting $\Delta R_s(H)$ by $R_s^{ext\cdot}(0\,\mathrm{T})$ and $\Delta X_s(H)$ by $X_s^{ext\cdot}(0\,\mathrm{T})$.
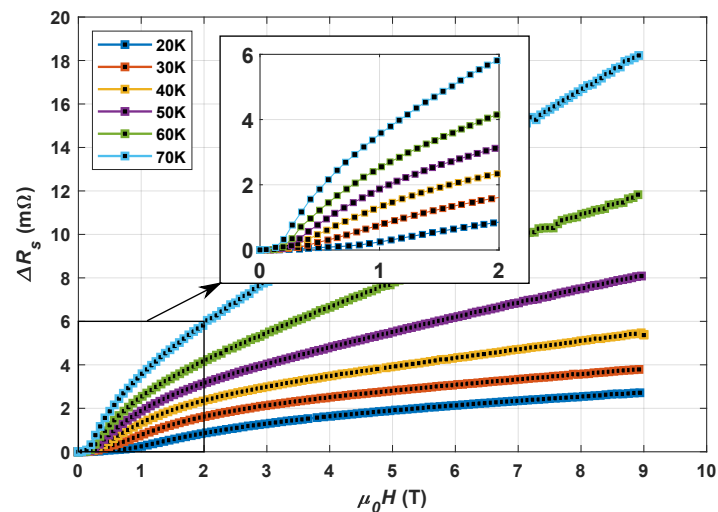
FIGURE 5.19: The change of surface resistance with magnetic field ΔR_s (ZFC branch) for SuNAM CCs at all measured temperatures. The inset highlights the plateau-like behavior at small fields owing to the magnetic properties of the LaMnO$_{3+\delta}$.

rutile or correct adjustment offsets in ΔR_s and ΔX_s are not included in the error bars as they affect approximately all samples in the same way.

The magnetic field behavior of ρ'_{vm} stay linear until approximately 7 T after which they take an upward swing, deviating from the model expectations. This phenomenon occurs only at higher temperatures 60-70 K and is stronger for samples without APCs, see SuNAM and Theva, suggesting that either, the pinning regime where vortex - pinning center interactions are dominant gets surpassed, or the irreversibility field is approached. Both phenomena would interfere with the GR model and are discussed in context of the surface resistance deviation from approximately power law behavior in subsection 5.1.3. In contrast, the imaginary part of the vortex resistivity ρ''_{vm} follows a linear behavior in the entire measurement range.

Again, the losses associated with the vortex-motion correlate with the microstructure of the samples. The CCs not optimized for large field operation, SuNAM, SuperOx and Theva, show the biggest losses both in real and imaginary part of ρ_{vm}. Interestingly, Fujikura without APC competes in the same low loss range as CC with APCs, a demonstration that the native GdBCO matrix allows for effective intrinsic pinning centers when sufficiently nano-engineered. At lower temperatures, for example at 50 K shown in Fig. 5.20 **(c)-(d)**, we find similar trends for the VM resistivity as a function of applied field $\rho_{vm}(H)$, as previously discussed. On the one hand, the CC performances follow the well described categorization into medium vortex-pinning and high vortex-pinning REBCO microstructures. On the other hand, the field increase is linear for fields > 1 T and exhibit a plateau-like behavior for smaller fields due to the magnetic properties of LMO or other extrinsic effects.

We present the temperature behavior of the complex VM resistivity of several CCs at 9 T in Fig. 5.21.
As expected, for all CCs the microwave losses, visible in both real and imaginary part of ρ_{vm}, drop with decreasing temperature since it is accompanied by increase of superconductor's pinning strength. CCs with high vortex-pinning microstructures exhibit a less steep temperature dependence than their medium vortex-pinning counterparts suggesting that high pinning microstructures comprise a balanced mix of weak pinning center, active at low temperatures, and strong pinning centers, active at high temperatures [43, 165]. Moreover, in comparison with medium vortex-pinning
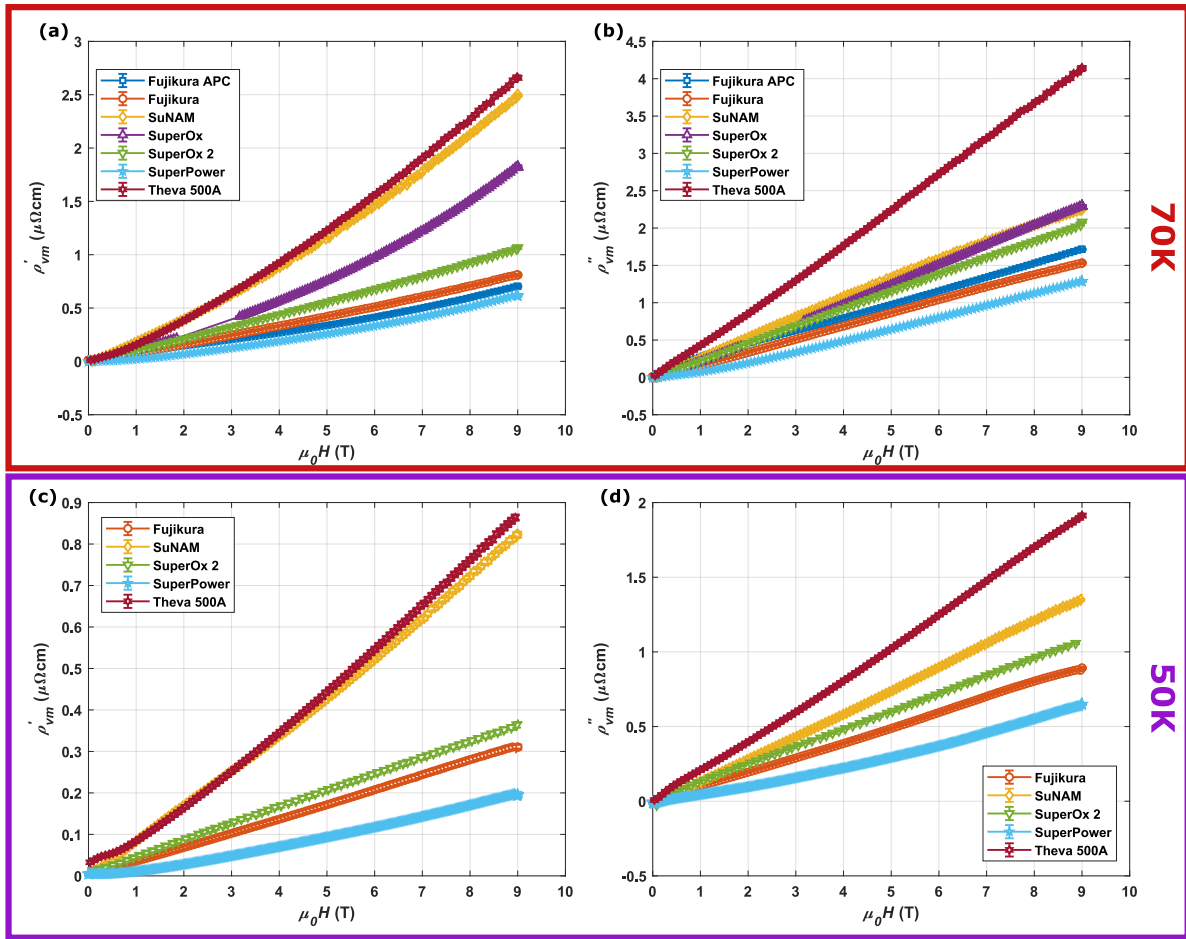
FIGURE 5.20: The real **(a),(c)** and imaginary part **(b),(d)** of the vortex-motion resistivity ρ_{vm} of several CCs as a function of magnetic field at 70 K (**(a)-(b)**) and 50 K (**(c)-(d)**).
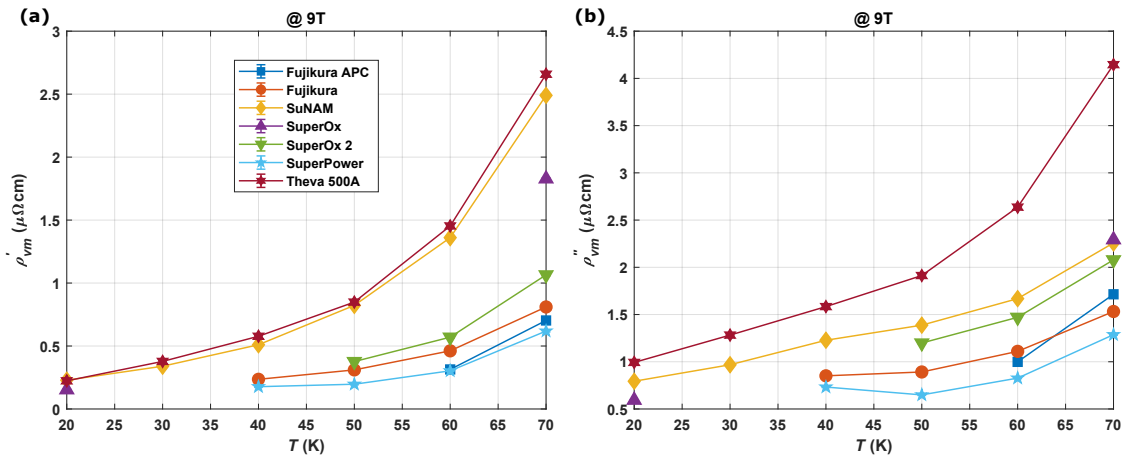
FIGURE 5.21: The real **(a)** and imaginary part **(b)** of the vortex-motion resistivity ρ_{vm} of several CCs at 9 T as a function of temperature.

CCs, the ρ_{vm} of CCs with defect rich microstructure remain in a smaller magnitude range across the entire temperature range. The ranking among the CCs for the VM losses reflects generally their pinning strengths as represented in form of $J_c(H)$ in Fig. 4.7.

5.3.1 Vortex viscosity and flux-flow resistivity

Within the GR-model, the vortex viscosity or viscous drag coefficient η can be calculated as a function of the VM resistivity. Starting from equation (2.56), equivalent transformations yield

$$\eta = \Phi_0 B \cdot \frac{\rho'_{vm}}{{\rho'_{vm}}^2 + {\rho''_{vm}}^2} = \frac{\Phi_0 B}{\rho_{ff}}. \tag{5.19}$$

The vortex viscosity based on measured Z_s and determined from equation (5.19) is presented in Fig. 5.22 **(a)** at 70 K for all studied CCs. Different from our previous analysis in subsection 5.1.3, where η originates from ρ_n and
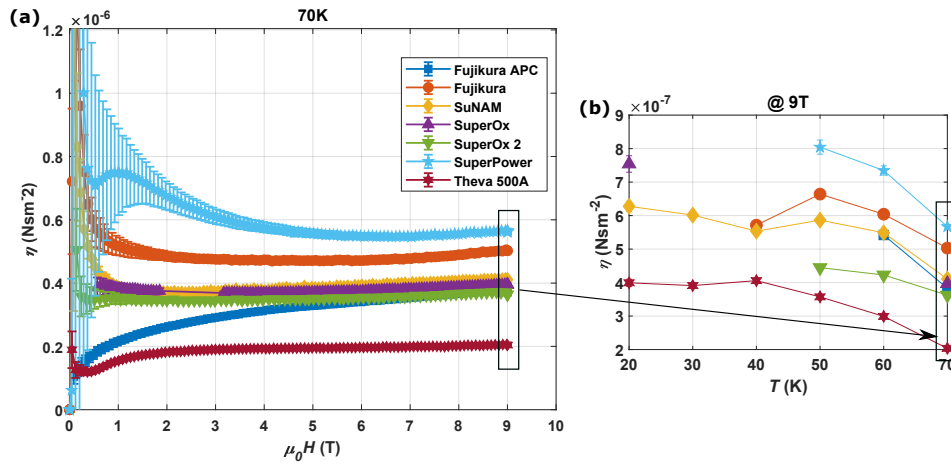
FIGURE 5.22: Viscous drag coefficients calculated from eq. (5.19) for all characterized coated conductors. **(a)** η as a function of magnetic field at 70 K. **(b)** $\eta(9\,\mathrm{T})$ as a function of temperature.

B_{c2} (Bardeen-Stephen model) estimated by transport, the given vortex viscosity can be displayed as a function of magnetic field. At intermediate and high magnetic fields, the field dependence is very weak, almost non existent. It falls into expectations with the Bardeen-Stephen model, since the upper critical field B_{c2} and the normal-state resistivity of REBCO ρ_n are field independent quantities. At lower magnetic fields, extrinsic effects superimpose the field dependence.

The introduction of APC into the REBCO matrix does not have a clear effect on the magnitude of η. Take for instance, Fujikura APC and SuperPower which are both based on nanorods. The former has one of the lowest, while the latter the highest vortex viscosity *eta* among all samples. Beyond APCs, the η must be influenced by additional factors like inhomogeneities and nanoscale defects. Microstructure analysis by transmission electron microscopy could reveal explicit links between defects and vortex viscosity.

In Fig. 5.22 **(b)**, the analysis of η at 9 T is extended to lower temperatures. For all providers, we observe generally an increase of the magnitude with decreasing temperature, in line with expected ρ_n and B_{c2} temperature behaviors. The calculated values are in excellent agreement with literature. For example at $T = 50\,\mathrm{K}$, the reported values range from $\approx 2 \times 10^{-7}\,\mathrm{Ns/m^2}$ measured with pulse transmission [193] to $\approx 10 \times 10^{-7}\,\mathrm{Ns/m^2}$ characterized with a parallel plate resonator at 5.5 GHz [194] for YBCO thin films. The vortex viscosities calculated from two different approaches, on the one hand the Bardeen-Stephen description [31] with $\eta = \frac{\Phi_0 B_{c2}}{\rho_n}$ and on the other hand Tinkham´s model [30] $\eta = \frac{\Phi_0 B}{\rho_{ff}}$, are presented together with literature results in Fig. 5.23. The black line approximates the results obtained for a YBCO thin film with microwave measurements, which are approximated with $\eta(T) = \eta(0)(1 - (\frac{T}{T_c})^2)/(1 + (\frac{T}{T_c})^2)$ with $T_c = 88\,\mathrm{K}$ and $\eta(0) = 1.2 \times 10^{-6}\,\mathrm{Nsm^{-2}}$, as
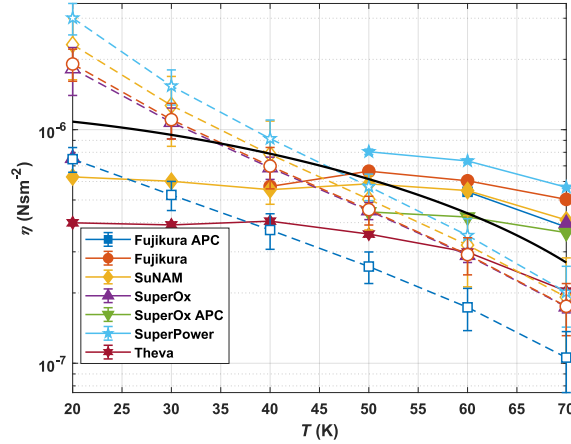
FIGURE 5.23: Comparison of vortex viscosity calculated from two different approaches. The filled markers relate to surface impedances based and the open markers to transport measurement based η. The black line approximates the results obtained for a YBCO thin film with microwave measurements as reported in [67].

reported in [67]. Independent of the chosen approach, our η is within the same order of magnitude to those reported values in thin films. This describes the limitations of the REBCO microstructure on η. The temperature dependence of the reported values is more akin to the one obtained from surface impedance which is not surprising considered that both result from microwave measurements. The deviation of values based on transport measurements from microwave results at low temperatures might arise from increasing uncertainties in estimation of ρ_n and B_{c2} with decreasing temperature. Comparing the vortex viscosities of our two approaches, interestingly, the succession among the CCs is quite similar. SuperPower samples display the highest values, while Fujikura, SuNAM and SuperOx stay in the intermediate range. Fujikura APC represents an exception. While from microwave measurements its $\eta(T, 9\,\text{T})$ lines up with the intermediate values from Fujikura, SuNAM and SuperOx, the η calculated within the Bardeen-Stephen model shows extremely low values. As already mentioned in section 5.1.3, the very low values for η arise from the high normal-state resistivity ρ_n that we estimated in Fujikura APC from the normal state. It seems that the ρ_n does not influence so much the η estimated from microwave measurements which is measured while the film remains in its superconducting state.

However, this exception aside, the two applied ways to determine η yield similar magnitudes and are consistent in predicting how different microstructures of REBCO compare to each other in terms of vortex viscosity.

The flux-flow resistivity $\rho_{ff} = \frac{\Phi_0 B}{\eta}$, see equation (2.58), shows a different perspective on the same aspect. While the vortex viscosity gives the drag or friction to move the vortex, the flux-flow resistivity marks the upper limit of possible microwave losses [69].

In Fig. 5.24, we disclose the flux-flow resistivity as a function of magnetic field at 50 K for several CCs. The almost linear in-field behavior implies the almost constant field behavior of the vortex viscosity that we already have seen in Fig. 5.19. The losses at 9 T can differ by a factor of two comparing SuperPower and Theva. However, we have to remember that Theva exhibits an inclined c-axis which will force microwave currents to exit the best conducting ab-planes and result in additional dissipation. All other CCs deviate by at most 30 % from each other.

Comparing the flux-flow resistivity with other superconductors, demonstrates the potential of REBCO in high-temperature, in-field microwave applications. Nb_3Sn was reported to show $\rho_{ff}(10\,\text{K}, 9\,\text{T}) \approx 8\,\mu\Omega\text{cm}$ and MgB_2 is expected to demonstrate even higher losses [189]. The characterized coated conductors perform at the same magnetic field but
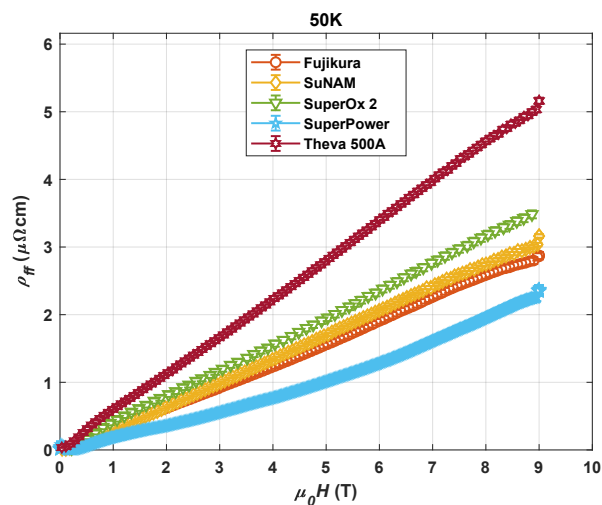
FIGURE 5.24: The flux-flow resistivity ρ_{ff} as a function of magnetic field at 50 K for all characterized CCs.

significantly higher temperature, 50 K, considerably better $\rho_{ff}(50\,\text{K}, 9\,\text{T}) \approx 2.3 - 5.1\,\mu\Omega\text{cm}$, as shown in Fig. 5.24.

5.3.2 Depinning frequency and pinning constant

The depinning frequency ν_p informs about the excitation frequency of a material above which the real part of the VM resistivity ρ'_{vm} exceeds half of its maximum. It basically separates the low-frequency, low-losses from the high-frequency, high-losses regime (see Fig. 2.12). With the VM response at hand, one can isolate the depinning frequency by forming a VM resistivity ratio in the following way

$$\nu_p(B) = \frac{\rho''_{vm}(B)}{\rho'_{vm}(B)} \cdot \nu. \tag{5.20}$$

Note that the vortex parameter is in this formulation expressed as a function of magnetic field. We disclose the depinning frequency as a function of magnetic field for several CCs at 70 K calculated according to equation (5.20) in Fig. 5.25 (a). The decrease of ν_p with magnetic field in the relevant field range is observed for all CCs but SuperOx 2. In the case of a constant vortex viscosity with changing magnetic field, this is approximately what we observe in Fig. 5.22 for analyzed CCs at 70 K, a field dependent depinning frequency suggests a pinning regime with many vortices per pinning site [67, 189, 192]. Consequently, it occurs at large magnetic fields or temperatures where few pinning sites are active. In this regime, depinning frequencies are smaller and field dependent.

Among the CCs, a quite wide range of depnning frequencies is covered, 7-20 GHz at 9 T, which is in accordance with the microstructure relevance to the vortex-motion parameters. The introduction of APC to the REBCO matrix seem to result in elevated values. Other groups report similar values for the depinning frequency. Alimenti et al. measure $\nu_p(67\,\text{K}, 9\,\text{T}) \approx 16\,\text{GHz}$ for a thin film of CSD-YBCO with 5 % BZO and $\nu_p(65\,\text{K}, 12\,\text{T}) \approx 20\,\text{GHz}$ for a thin PLD pristine YBCO [192]. Golosovsky et al. disclose $\nu_p(70\,\text{K}, 0 - 0.8\,\text{T}) \approx 15\,\text{GHz}$ for a thin YBCO film [67, 194].

We present the high-field depinning frequency as a function of temperature for all analyzed CCs in Fig. 5.25 (b). One can observe that ν_p scales inversely with temperature uniformly for all CCs. Especially relevant for the FCC-study are the values at 50 K. Depending on the sample, they are roughly between 12 GHz and 30 GHz which suggests a low-loss operation of CCs at excitation frequencies around 1 GHz, as foreseen for the FCC-hh, and up to fields of 9 T, given the validity of the GR-model.
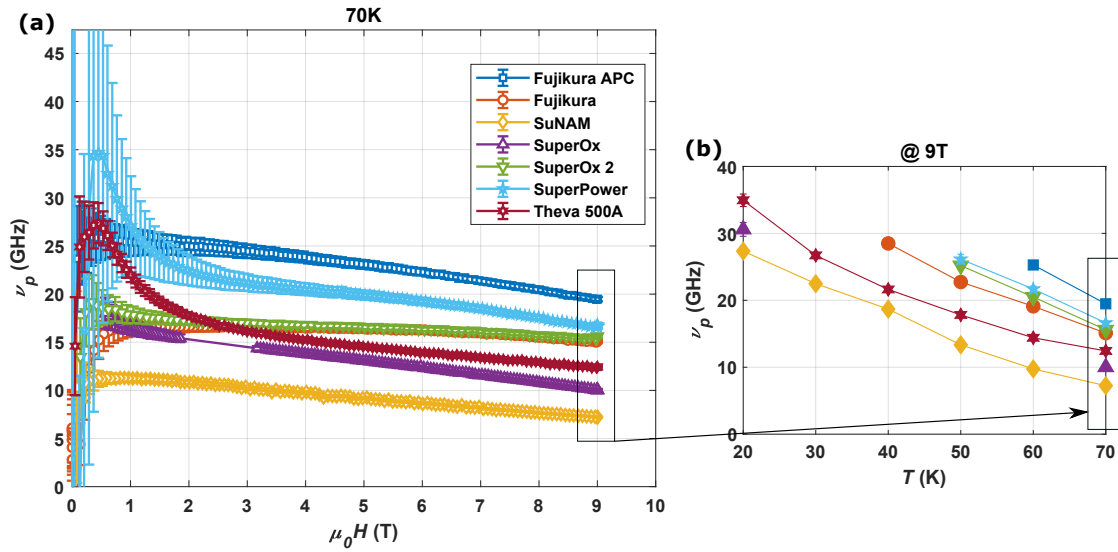
FIGURE 5.25: **(a)** The depinning frequency ν_p as a function of magnetic field at 70 K for several CCs.**(b)** The depinning frequency as a function of temperature at 9 T for all analyzed CCs.

We find quite good accordance with depinning frequencies obtained from fits of the surface resistance as presented in Fig. 5.26. On the one hand, the found magnitudes for the depinning frequencies of both approaches match. On the

FIGURE 5.26: Comparison of depinning frequency calculated from two different approaches. The filled markers relate to surface impedances based and the open markers to fits from surface resistance data.

other hand, independent of chosen approach, samples with APCs display higher values.

A main difference is the weaker temperature dependence of the depinning frequencies calculated from the fitting method. As shown previously in Fig. 5.23, the η estimated from transport displays a very strong temperature dependence which probably overestimates the real η at low temperatures because of the increasing uncertainties in determination of ρ_n and B_{c2} with decreasing temperature. The overestimated temperature dependence of η propagates then into an underestimated temperature dependence of ν_p obtained from ΔR_s fits since η is always a constraint in equation (2.56).

Finally, the pinning constant or Labusch parameter k_p, which defines, in the limit of no vortex-vortex interaction, the restoration force per displacement of a vortex from its pinning potential minimum, can be expressed as a product of vortex viscosity and depinning frequency

$$k_p = 2\pi v_p \cdot \eta. \tag{5.21}$$

We present k_p as a function of magnetic field at several temperatures for a SuNAM CC sample in Fig. 5.27 **(a)**. In the
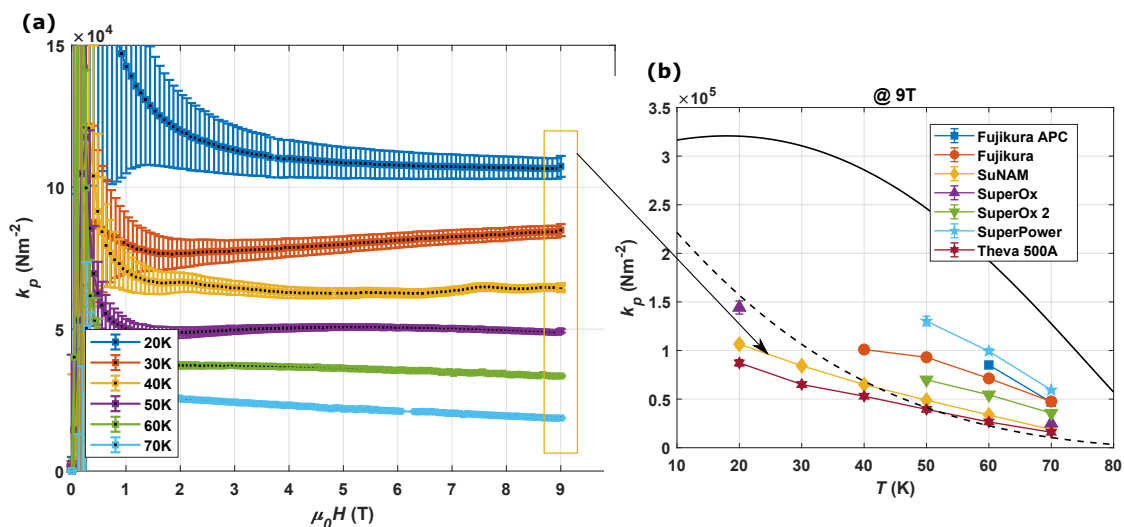
FIGURE 5.27: **(a)** The Labusch parameter k_p as a function of magnetic field at several cryogenic temperatures for SuNAM CCs. **(b)** The Labusch parameter at 9 T as a function of temperature for all analyzed CCs. The full black and dashed curves demonstrate approximations for $k_p(T)$ [67].

range between $20-70$ K, the Labusch parameters at large fields span roughly $(2-11) \cdot 10^4$ Nm^{-2} indicating varying pinning mechanisms with temperature.

At low temperatures, thermal vortex displacements are small enough that fluctuations in the uncorrelated point-like defect (e.g. oxygen vacancies which are weak pinning center) density contribute together with strongly correlated disorder like twin boundaries, screw dislocations or artificially introduced pinning centers (strong pinning center) to the overall pinning. With increasing temperature, thermal fluctuations cause a quick smearing out of the uncorrelated disorder potential so that this type of pinning becomes ineffective. At the same time, thermal vortex displacement becomes too large to allow vortex pinning of a single correlated defect, the vortex becomes delocalized and can only be pinned by an assembly of correlated defects. Now, only fluctuations in the correlated defect density lead to pinning of the vortex line, which reduces the overall pinning [164].

The field evolution of the pinning constant varies with temperature, too. The presence of various active pinning centers, weak and strong, at low temperatures allow for an individual pinning regime with many pinning sites per vortex. In this regime, k_p is constant in field since vortex - pinning center interactions are dominant over vortex-vortex interactions. At higher temperatures, uncorrelated defects and pinning through single correlated defects break away as active pinning centers. The pinning site per vortex distribution shifts towards an abundance of vortices, the vortex-vortex interaction kicks in and k_p decreases with magnetic field. This phenomenon becomes apparent at about 60 K for SuNAM CCs as demonstrated in Fig. 5.27 **(a)**. In addition, thermal energies cause smoothing of the pinning potential which reduces the overall magnitude of k_p with increasing temperature [164].

We compare the k_p at 9 T of various CCs as a function of temperature with approximations found in literature in Fig. 5.27 **(b)** [67]. The full black curve corresponds to $k_p^{lit}(T) = k_p(0)(1-(\frac{T}{T_c}))^{4/3}(1+(\frac{T}{T_c}))^2$ with $T_c = 90$ K and $k_p(0) =$

$3 \times 10^5 \, \text{N/m}^2$. The dashed line adds an exponential term to k_p^{lit} in the following way: $k_p^{lit,2} = k_p^{lit}(T) \cdot \exp(-T/T_0)$ with $T_0 = 30 \, \text{K}$ which is a characteristic temperature associated with thermal fluctuations. In the first case, the temperature dependence originates from the temperature dependence of the superconducting parameters, such as condensation energy, while in the latter, a term is added that accounts for thermal smearing of the pinning potential [67, 164, 195].

The experimental k_p of medium vortex-pinning CCs, like SuNAM, SuperOx or THEVA, match the $k_p^{lit,2}$ both in magnitude and temperature evolution quite well. The CCs with high vortex-pinning microstructures exhibit larger values, which might correspond to more active pinning centers, and although only high-temperature values are available, seemingly a temperature behavior that is more akin to $k_p^{lit}(T)$. The slower decrease of k_p with temperature of high vortex-pinning CCs would match the microstructure picture. Nanocolumns or 3D nanoparticles, trademarks of high vortex-pinning CCs, are strong pinning centers that are more effective at higher temperatures [164] which could smooth out the decay of k_p in temperature.

Finally, we compare the Labusch parameters as a function of temperature obtained from our two different approaches in Fig. 5.28. Since $k_p = 2\pi\nu_p \cdot \eta$, both quantities ν_p and η superimpose in order to constitute k_p. The calculated values of both approaches remain at all temperatures in the same order of magnitude. However, due to the very strong temperature sensitivity of η obtained from transport data, corresponding k_p undercuts the Labusch parameter from surface impedance data at high temperatures and overestimates it at low temperatures. The deviation between both approaches is minimal at 50 K, yielding, within error bars, the same values for Fujikura, Fujikura APC and SuperPower.
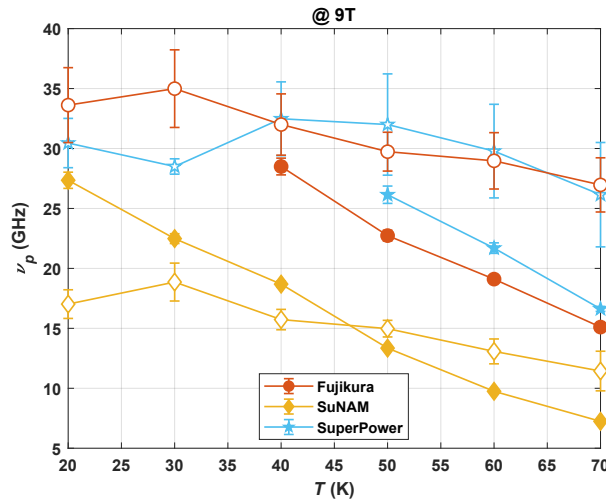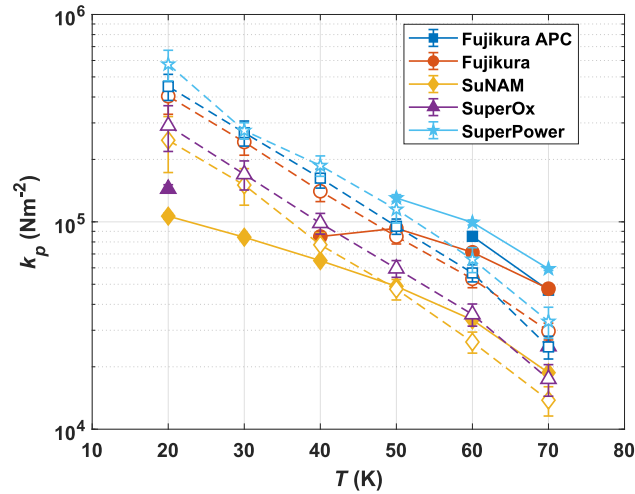

FIGURE 5.28: Comparison of Labusch parameters calculated from two different approaches. The filled markers relate to surface impedances based and the open markers to fits from surface resistance data.

5.4   Extrapolation of surface impedance to FCC-hh conditions

Transverse beam coupling between accelerated hadrons and the introduced image currents within the beam screen coating pose one of the performance limitations in the current FCC-hh design. The transverse beam coupling impedance is directly proportional to the surface impedance of the material facing the particle beam [12],[196].

In Fig. 5.3 and in [14], we compare the surface resistance of the potential FCC-hh beam screen coating Cu with the CCs presented here. At $T = 50 \, \text{K}$, $\mu_0 H = 9 \, \text{T}$ and $\nu \approx 8 \, \text{GHz}$, the best performing CC has a 2.5 smaller surface resistance than Cu. Aforementioned work and previous discussions enable extrapolation of the surface impedance of

Cu and CCs to FCC-hh conditions, so to lower frequencies and higher fields. The microwave response of $300\,\mu\text{m}$ thick Cu colaminated on stainless steel by CERN is measured with the presented dielectric resonator and amounts $R_s^{\text{FCC Cu}}(50\,\text{K}, 0\,\text{T}, 8\,\text{GHz}) \approx 7.5\,\text{m}\Omega$ (see Fig. 5.3). Since the surface impedance of a normal, non-magnetic metal is related to its skin depth, as derived in chapter 2 or in [197],

$$\delta = \sqrt{\frac{2\rho}{2\pi\nu\mu_0}} \tag{5.22}$$

by

$$Z_s^{\text{metal}} = (1+i)\frac{\rho}{\delta}, \tag{5.23}$$

we can deduce the surface resistance of Cu at FCC conditions to be

$$R_s^{\text{FCC Cu}}(50\,\text{K}, 0\,\text{T}, 1\,\text{GHz}) = \sqrt{\frac{1\,\text{GHz}}{8\,\text{GHz}}} \cdot R_s^{\text{FCC Cu}}(50\,\text{K}, 0\,\text{T}, 8\,\text{GHz}) \approx 2.65\,\text{m}\Omega.$$

The change with applied magnetic field is insignificant. As indicated by equation (5.23), $R_s = X_s$ for normal conductors.

Returning to equation (2.53), the field independent part for the surface resistance R_{BCS} of a superconductor in the dirty limit (short mean free path) has a quadratic frequency dependence for $T < T_c$ and not too high frequencies ($2\pi\nu \ll 2\Delta/\hbar$, Δ is the energy gap) [62]. R_{res} can exhibit different frequency dependencies [198], however, in high T_c superconductors quadratic frequency behaviors were observed [62],[63]. In this setting, it can be considered $R_{BCS}^{\text{CC}}(50\,\text{K}, 0\,\text{T}, 1\,\text{GHz}) + R_{res}^{\text{CC}}(50\,\text{K}, 0\,\text{T}, 1\,\text{GHz}) = \left(\frac{1\,\text{GHz}}{8\,\text{GHz}}\right)^2 \cdot R_s^{\text{CC}}(50\,\text{K}, 0\,\text{T}, 8\,\text{GHz}) \approx 10\,\mu\Omega$.

The field independent part of the surface reactance can be written within the BCS theory as $X_{\text{BCS}} = 2\pi\nu\mu_0\lambda_L$, where λ_L stands for the London penetration depth. Assuming the conventional temperature dependence [30] (see eq. (5.9)) with $\lambda_L(0\,\text{K}) = 150\,\text{nm}$ [53] and T_c the critical temperature measured by transport measurement of corresponding CCs, we can estimate the expected surface reactance $X_{BCS}(T = 50\,\text{K}, \nu = 1\,\text{GHz}) \approx 1.2\,\text{m}\Omega$.

Finally, the field dependent part of the superconductor's surface impedance at FCC conditions is calculated from equation (2.59) and estimated pinning parameters from surface resistance fits at $T = 50\,\text{K}$[3].

In Fig. 5.29, we present FCC conditions extrapolated surface impedance as a function of magnetic field for FCC Cu in comparison with all CCs covered in this work. The surface resistance of the CCs at 16 T is expected to be by a factor of 15-70 (depending on the provider) smaller than that of Cu. The surface reactance of CCs exceeds that of Cu by a factor of 1.5-2.3. So, the use of current state of the art CCs in the beam screen chamber results in highly decreased surface resistance with the trade off of slightly increased reactive microwave response as compared to Cu. Realized in practice, the decrease in surface resistance would equate to significant benefits in terms of beam stability margins and resistive power losses, while the increased surface reactance would result in a minor drop of maximum beam current within the FCC [73].

Furthermore, the CC technology offers room for optimization. As pointed out in the previous section, CCs under

---

[3]A discussion on the limits of this approach is given in the following. Presented calculations for the field dependence of CCs' surface impedance are performed within the mean-field approximation which are very successful in elevated frequency ranges $\nu \geq 8\,\text{GHz}$ [199]. Going to lower frequencies increases the excursion of the vortices, thus vortex-vortex interaction and thermal fluctuations become more relevant [179]. Close to conditions where the vortex-liquid transition is passed, data is better described by scaling models. Wu et al. found the crossover frequency $\nu_x \sim 8 - 9\,\text{GHz}$ at $T = 80.2\,\text{K}$ and $H = 0.4\,\text{T}$ for YBCO [179]. It defines the frequency at which the liquid-glass transition occurs. The crossover frequency ν_x at $T = 50\,\text{K}$ remains unknown but is expected to be dependent on microstructure and lower than at $80.2\,\text{K}$ since oscillations are less influenced by thermal activation.
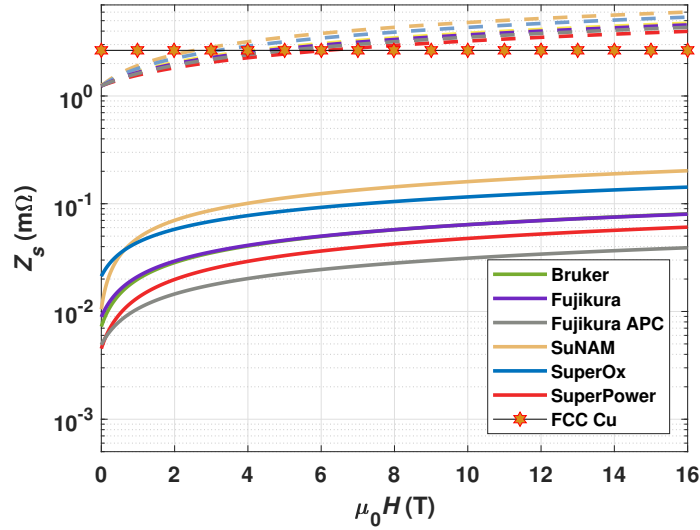
FIGURE 5.29: To $T = 50\,\mathrm{K}$ and $\nu = 1\,\mathrm{GHz}$ extrapolated surface impedance for $300\,\mu\mathrm{m}$ thick Cu sputtered on stainless steel, denoted here as FCC Cu, and several CCs as a function of magnetic field. The stars represent both the surface resistance and surface reactance values of FCC Cu. The solid lines are surface resistances, the dashed lines surface reactances of CCs. The provider of the CCs are color coded.

study perform at FCC conditions in the pinning regime. Hence, from an engineering point of view, it is desirable to use superconductors with large pinning constants $k_p = 2\pi \nu_p \cdot \eta$, that is, large depinning frequency and vortex viscosity for this particular application. As shown in Fig. 5.8 **a)**, incorporation of artificial pinning centers have positive impacts on the depinning frequency. The vortex viscosity η can be increased by either decreasing the normal-state resistivity ρ_n or increasing the upper critical field B_{c2} as indicated by equation (5.4).

5.5 Conclusions

In this chapter, we have studied the surface impedance, $Z_s = R_s + iX_s$, and vortex properties (ν_p, η and k_p) at microwave frequencies of several commercially available REBCO coated conductors as a function of magnetic field up to 9 T at $\nu = 8\,\mathrm{GHz}$ and 20 K to 70 K with a Hakki-Coleman type dielectric rutile resonator.

Comparing the surface resistance as a function of magnetic field $R_s(H)$ of the CCs with the one of copper, the beam screen coating standard, we found that the best performing CC outperforms copper by about a factor of 2.6 at 50 K, 8 GHz and 9 T, so at the closest FCC-hh conditions we can experimentally realize. This demonstrates the excellent microwave performance of CCs in large-field RF applications. Moreover, studied CCs have been categorized into medium and high vortex-pinning REBCO groups. The latter are, one exception aside, APCs based CCs and cause less microwave dissipation than their medium vortex-pinning counterparts. This underlines the link between REBCO microstructure and microwave in-field performance.

By calculating the vortex viscosity η of CCs based on flux-flow resistivity transport measurements, we were able to use it as a constraint in the GR-model and treat the second model parameter, the depinning frequency, as a fitting parameter to $\Delta R_s(H)$. The connection between microwave performance and REBCO microstructure propagates to the pinning parameter ν_p. High vortex-pinning REBCO matrices yield higher depinning frequencies which puts forward the usage of APCs as a viable technique for microwave performance improvement. Also the vortex viscosity shows some spread in its magnitude for different CCs. It can be increased by either increasing the upper critical field or

decreasing the normal-state resistivity of the REBCO microstructure. Mentioned findings provide material engineers a recipe to potentially improve the already outstanding microwave performance of CCs even further.

The reliable and reproducible measurement of CCs' surface reactances with a DR was a meaningful hurdle to take. Besides the required high accuracy in frequency and large temperature stability, we identified large mechanical cavity stability to be essential, since magnetic forces, as known from levitation experiments, expand the resonance cavity when characterizing $\Delta X_s(B)$ of CCs during magnetic field sweeps. We showed a save modification to the setup, meaning without damaging neither the setup nor the samples, to limit the mechanical movement of the cavity. This allowed the controlled measurement of $\Delta X_s(H)$ with the DR. We show that the surface reactance of studied CCs is $X_s^{\text{CC}}(9\,\text{T}) \approx 3 - 5 \cdot X_s^{\text{FCC Cu}}(9\,\text{T})$ at 50 K.

Having both the surface resistance and surface reactance available, we used the two data sets to calculate the characteristic vortex-motion resistivity ρ_{vm} and vortex-motion parameters η, v_p and k_p again with the GR-model, but this time without model constraints from transport measurements. In this instance, it was demonstrated that external microwave contributions like hysteresis in ΔX_s due to cavity movement or magnetic properties of the buffer layer LMO, mask the intrinsic superconductor response at small magnetic fields. This contribution can be removed for fields $\mu_0 H > 1\,\text{T}$ through a simple offset. The most significant difference between our two approaches is observable in the determined η, which is expected considering that it was determined from two completely different techniques. The η from surface impedance data shows a much milder temperature behavior than its tranport counterpart. Besides this, obtained vortex-motion parameters are quite consistent within the two approaches in terms of magnitudes and general trends.

Further, we have calculated the surface impedance of CCs at FCC conditions ($T = 50\,\text{K}$, $v = 1\,\text{GHz}$ and $16\,\text{T}$) by means of the Gittleman-Rosenblum model. The surface resistance is expected to be a factor 15-70 smaller (depending on the provider), while the surface reactance stays in the same order of magnitude with respect to the surface impedance of copper. Realized in practice, the decrease in surface resistance would equate to significant benefits in terms of beam stability margins and resistive power losses, while the increased surface reactance would result in a minor drop of maximum beam current within the FCC.

The estimated outstanding microwave performance of CCs at FCC conditions encourage to take next steps in the feasibility study. Namely, to determine experimentally the surface impedances at $1\,\text{GHz}$ and $16\,\text{T}$, study the different ways to attach tens of meter-long CCs to the beam screen chamber taking into account the mechanical properties of the stainless-steel/ CC ensemble, ensure magnetic field quality inside the beam-screen chamber, and study possible hazards such as a dipole magnet quench. Some of these factors will be examined in detail in the next two chapters as they represent essential puzzle pieces for a final, reliable cost-benefit assessment for this solution.

Chapter 6

Scalable technique to coat metallic surfaces with REBCO for large-field microwave applications

Promising as the high-frequency properties of REBCO CCs are, the practical issue of how to coat the beam screen chamber in large scales has not been addressed yet. In fact, until recently REBCO CCs did not play a significant role in the history of microwave applications.

Since the late 1960s, superconductors are employed as materials for radio-frequency (RF) cavities because of their operation at higher acceleration voltage gradient and lower AC power demand than normal conducting alternatives[18]. In this field, Nb films are the most widely used among the single element superconductors owing to its highest critical temperature T_c and highest RF critical field H_{sh} and the ease of coating even curved structures with Nb foils or sputtering. Usually, this is done without big performance compromises in contrast to its compound counterparts like Nb_3Sn. High purity Nb avoids thermal breakdowns and allows the achievement of ultra low surface resistances in the order of $1\,n\Omega$ [200]. The defects which are still present in the material let magnetic flux lines, originating from earth's magnetic field or stray fields from accelerator magnets, penetrate and cause with the movement of its normal core the residual resistance. So generally speaking, in the scenario of RF cavities with zero applied field, defect free superconductors are desired in order to minimize the losses.

Emerging high magnetic field RF applications, like next generation high energy accelerators [9, 11] or potential axion detection cavities [201, 202] call, however, for other superconductors because of niobium's low $H_{c2}(T = 5\,K) < 0.5\,T$. With applied magnetic field, penetration of magnetic field lines into the superconductor cannot be avoided and thus, the strategy becomes the immobilization of quantized magnetic vortices by means of defect pinning. The most mature superconductors for high field applications are nowadays Nb-Ti, Nb_3Sn and REBCO. The high-temperature superconductor REBCO offers opposed to NbTi and Nb_3Sn a larger technological flexibility due to its higher critical temperature $T_c^{REBCO} \approx 90\,K$ as compared to $T_c^{NbTi} = 9\,K$, $T_c^{Nb_3Sn} = 18\,K$ and larger upper critical field $H_{c2}^{REBCO}(4\,K) > 100\,T$ as compared to $H_{c2}^{NbTi}(4\,K) = 12\,T$, $H_{c2}^{Nb_3Sn}(4\,K) = 27\,T$ [53]. In addition, in a comparative study it was shown that REBCO exhibits promising microwave properties [189]. Unfortunately, its usage in RF cavities is impeded by complicated material growth that requires meticulous stochiometry control and biaxially textured templates, making it virtually impossible to grow REBCO directly on cavities with complex geometry.

To bypass the issue of direct REBCO growth on cavity walls, we initially envisioned to solder stripped coated conductors, so without their protecting Ag and Cu layers, with their metallic substrate side to the cavity [203]. Recently,

a similar idea has been put into practice. For axion search at large fields, Ahn et al. coated successfully a cavity with YBCO CCs by gluing the substrate side to the cavity walls [21, 204]. With the metallic substrate side attached to the cavity, the YBCO ends up being exposed as the topmost layer. Their cavity presents high Q-factors and it demonstrates a practical use of REBCO coated conductors for microwave applications.

In this chapter, we disclose a novel, non-destructive technique to coat REBCO coated conductors on metallic, curved surfaces compatible with large scale microwave applications like the beam screen chamber of the FCC-hh. As opposed to our initial idea and Ahn's attachment of coated conductors to metallic walls, our method involves 'face-down' soldering of the coated conductor and subsequent delamination of the superconductor from the tape. This results in the bottom side of the superconductor to be exposed to the cavity and has positive implications for the microwave performance.

This chapter is structured in the following way: In section 6.1, we start with describing the process steps that define the attachment technique. Subsequently, we assess the integrity of the technique. Potential damage, for example due to excessive heat during soldering or the mechanical exfoliation are analyzed with magnetization measurements. Finally, we compare the topography of exfoliated bottom surface with the standard top surface via scanning electron microscopy.

In section 6.2, we continue with high-frequency analysis by means of a dielectric resonator. Firstly, the surface sensitivity of this technique is quantified by calculating the penetration depths of the electromagnetic fields in REBCO CCs when exposed to large magnetic fields. Secondly, we compare the surface impedance of exfoliated REBCO bottom side with its top surface counterpart for several CCs in a wide cryogenic temperature range and up to 9 T. Thirdly, we report about the first results of a spin-off collaboration with the RADES (Relic Axion Detector Exploratory Setup) project at CERN. Here, we coated haloscopes, specially shaped Cu cavities, with REBCO CCs using our proposed attachment technique in order to achieve high Q-factors at large fields while searching for axion dark matter.

The delamination and soldering technique was developed in collaboration with other members of the SUMAN group at the ICMAB. My main contribution to it lies in the high-frequency characterization and analysis of exfoliated samples as presented in this chapter. As an ongoing work, our group studies the optimization of REBCO with the aim to induce as few damage to the REBCO layer as possible. The feedback is supplied by Hall Scan Microscopy, Scanning Electron Microscopy and optical microscopy. The conclusions of our labor can be soon found in [205] and PhD dissertations of Guilherme Telles and Neil Lamas.

6.1   Coating technique

6.1.1   Process steps

The coating technique to attach REBCO CC to a metallic and possibly curved surface can be broken down into two integral steps.

1. The fully protected coated conductor, find cross section of it in Fig. 6.3 **(a)**, needs to be soldered 'face down' (with face we refer to the top surface of the superconductor, see again Fig. 6.3 **(a)**) to the desired surface. Starting point is the pre-tinning of the CC surface with a Sn:Pb:Cu 60:38:2 solder that contains in addition some dissolved flux. For this, the sample is placed 'face up' on a heater, warmed up to $200\,^{\circ}$C and brought into contact with a solder wire in order to cover the surface with a thin layer of tin alloy. The amount and distribution of solder on the stabilizing Cu is shown to affect the quality of delaminated samples and both parameters were

optimized by spreading the solder with a tilted carbon fiber blade as reported in [205]. The soldering part is initiated by homogeneously pressing the pre-tinned side of the CC with ≈ 5 bar on a cleaned metallic surface. Note that the CC is here placed 'face down'. Then, the sample is heated for three minutes to $230\,^\circ$C. Once the sample is cooled off, it is soldered to the metallic surface and one can move to the next step.

2. The metallic substrate has to be delaminated off the oxide laminar structure, which will expose the bottom side of the superconductor, potentially covered with films or patches of buffer layers, see 6.3 **(d)**. In principle, this is achievable by mechanical upwards pulling without any additional process manipulation since the soldered interface is more robust than the oxide layer interfaces within the CC. However, the presence of the Cu jacket which holds the CC layers together, see 6.3 **(a)** or **(c)**, will result in inhomogeneous pulling direction and force distribution. Multilateral breaking within the oxide layers, including ripping REBCO from the sample, are the consequences. A key step to diminish this effect is to cut the sides of the Cu envelope in order to allow the pulling force to be evenly distributed across the entire CC width. Another optimization factor for homogeneous delamination is the way with which the substrate is detached from the oxide structure. For example, attaching the substrate to a cylinder and rolling it subsequently over the tape results in homogeneous peeling.

One positive aspects, intrinsic to our proposed technique, should be underlined here. The soldering process is carried out with CCs that are fully protected by their Ag and Cu layers. This facilitates the handling of the tapes, since it reduces mechanical damages to the REBCO. A more detailed description of the coating process is disclosed in [205].

6.1.2 Assessment of attachment technique integrity

A suitable attachment technique for CCs is distinguished by the preservation of the critical current after all manipulating steps were taken. On the one hand, soldering with too high temperatures and large time scales can lead to oxygen out-diffusion resulting in degradation of current carrying capabilities [206]. On the other hand, the mechanical exfoliation can take off some REBCO material and leave some small excavations in the REBCO layer of interest. The potential damage inflicted on the superconductor by these two steps can be assessed with magnetization measurements.

We soldered a $12\,\text{mm} \times 12\,\text{mm}$ SuperPower coated conductor sample 'face down' on a brass block, ripped the metallic substrate from the oxide structure and finally, unsoldered the exposed superconductor again by heating the brass block to $190\,^\circ$C. The unsoldered sample and the CC's substrate side counterpart are presented in Fig. 6.1.

Two observations are noteworthy. On the one hand, the exfoliated REBCO is bent due to solidified solder on the backside of the sample. Thus, care has to be taken in this process to not bend the tape beyond the critical bending radius which would damage the superconducting layer properties. On the other hand, the substrate side piece shows reflections in a purple and greenish color, pointing towards the possibility that the metal substrate has dragged some of the buffer layers together with it.

An $\approx 3.5\,\text{mm} \times 3.5\,\text{mm}$ piece was carefully cut out from the exfoliated REBCO center (see Fig. 6.1) and its magnetization measured up to $9\,$T at $T = 50\,$K. In Fig. 6.2, we compare its magnetization and the critical current density to a similar sized SuperPower CC sample, which was not subjected to the manipulating steps required for exfoliation of REBCO.

The exfoliated REBCO sample has an only $\approx 6\,\%$ larger volume but a $\approx 36\,\%$ larger magnetization at $0\,$T than its not delaminated counterpart. We assume that the superior magnetization stems from a less damaging cutting technique that we used for the exfoliated sample. It is known from literature that mechanically slitting CCs may deform the superconductor at the edges resulting in a degradation of the critical current [207]. For the sample preparation of the VSM experiment, the not delaminated CC was cut with a sharped scissor. Here, the end parts of the scissor blades were used in an attempt to minimize the shear force on the sample. In contrast to this, the exfoliated REBCO was

FIGURE 6.1: Bottom part: Exfoliated $12\,mm \times 12\,mm$ REBCO sample, which was soldered on a brass block, stripped off the metallic substrate and removed from the block again by melting the solder. We cut out a $\approx 3.5\,mm \times 3.5\,mm$ piece from the center (red dashed square) and measured its magnetization. Top part: The complementary substrate side CC piece of the exfoliated REBCO sample.
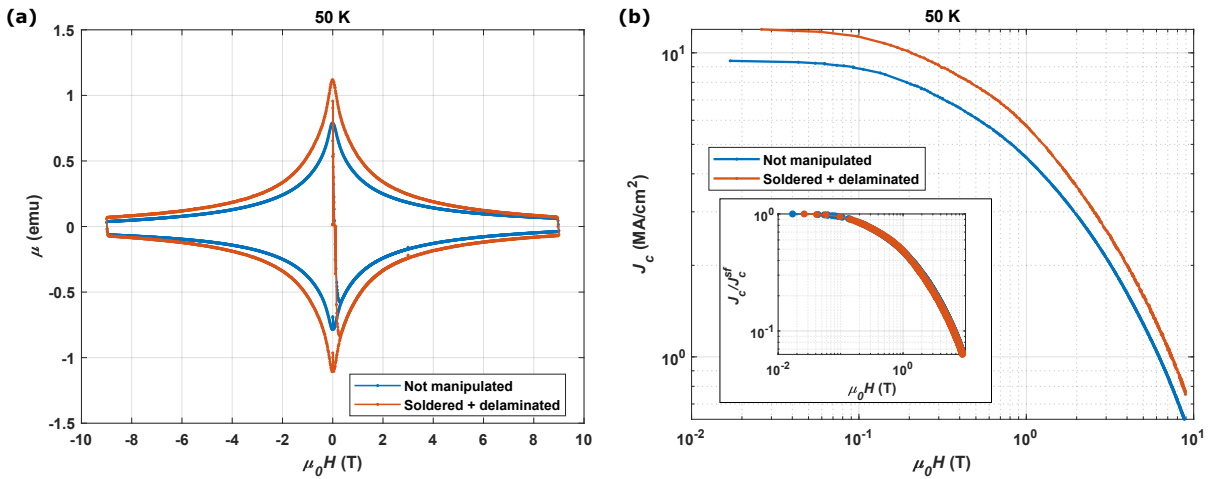
FIGURE 6.2: **(a)** Magnetization loops of a SuperPower CC sample as provided from the manufacturer cut to $3.3\,mm \times 3.4\,mm$ in comparison with a CC based REBCO sample that was soldered, exfoliated, unsoldered again before cut to $3.3\,mm \times 3.6\,mm$ at 50 K. **(b)** The critical current density of the corresponding magnetization measurement. The inset shows the normalized critical current.

split by a box knife blade which was aligned planar on the stabilizing Cu layer before being hammered trough the sample. From this we can conclude that if soldering and/or delamination deteriorates the carrying current capabilities, it is significantly less severe (for the sample center) than the damage we induce when cutting with scissors. For future CC cutting, it is recommended to stick to the blade plus hammer technique until a more profound study is undertaken.

We analyzed the effects of soldering and delamination on the critical current degradation with larger samples and spatially resolved scanning Hall probe microscopy. Our main findings establish that the sample edges are the most prone areas to degradation of critical current, while the central part of the samples usually preserves the superconducting properties. The work is summarized in [205] and is part of another PhD thesis.

6.1.3 Delaminated samples for DR measurements

In this chapter, it becomes necessary to introduce a new specification for measured samples. The customary surface impedances so far reported stems from CC stripped off their stabilizing Cu and Ag and glued 'face up' to a brass block as displayed in Fig. 6.3 **(b)**. In this instance, the side of the superconductor, which is furthest away from the metallic substrate, faces the cavity and characterizing electromagnetic fields. In the following, we denote these samples as the REBCO top surface.

Contrarily, when we solder the CC upside down on a brass block (see Fig. 6.3 **(c)**) and delaminate it, the superconductor's surface closer to the metallic substrate gets exposed to the cavity. These samples will be called REBCO bottom surface. The exposed surface can be quite complex after delamination. Depending on the CC provider and the delamination parameters (speed and pressure), several surfaces are present in different proportions such as closed buffer layer on top of the HTS (delamination between buffer layers), a layer of HTS with patches of buffer layers on top and/or trenches where thin layers of HTS got excavated (multi layered delamination between buffer layers and between last buffer and HTS layer) or a layer of HTS possibly with shallow craters (delamination between last buffer and HTS layer), see Fig. 6.3 **(d)**.

Fig. 6.3 supports the two described sample types with a visualization.
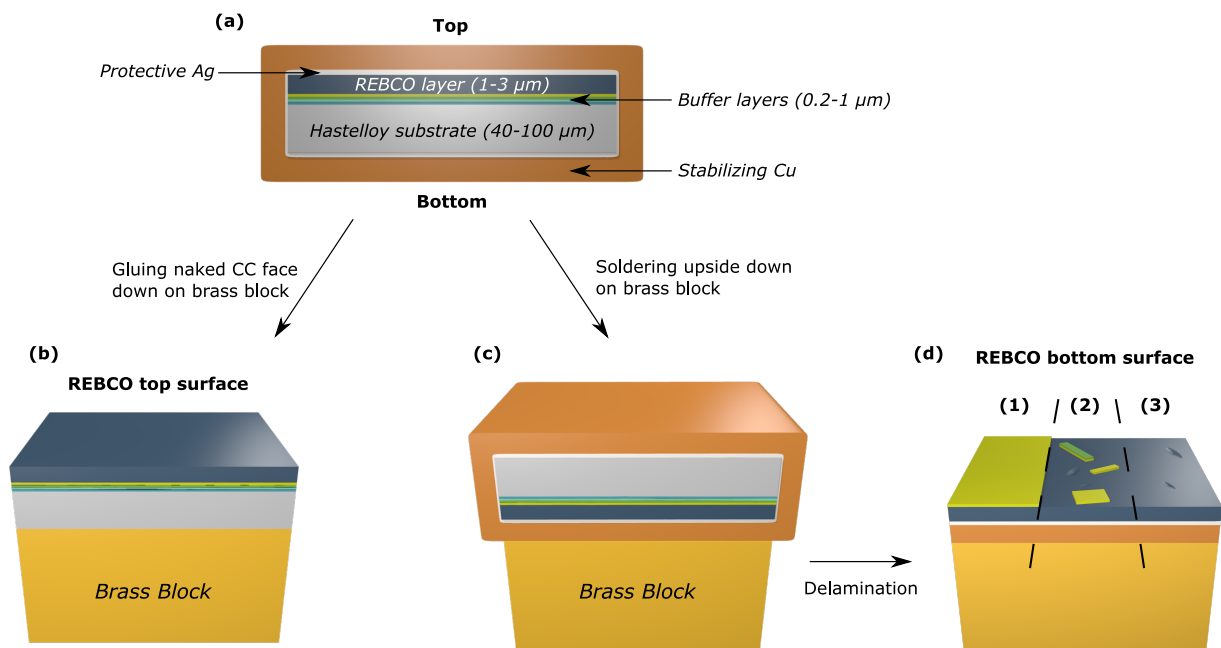
FIGURE 6.3: Schemes of characterized sample types. **(a)** Cross section of commercial available CC which serves as starting point for used samples. **(b)** CC stripped of the Cu and Ag protective layers and glued with top face up on a brass block for characterization in DR. **(c)** CC soldered upside down on brass block. **(d)** After delamination, the sample exposes either **(1)** a closed buffer layer on top of the HTS (delamination between buffer layers), **(2)** a layer of HTS with patches of buffer layers on top and/or trenches where thin layers of HTS got excavated (multi layered delamination between buffer layers and between last buffer and HTS layer) or **(3)** a layer of HTS possibly with shallow craters (delamination between last buffer and HTS layer).

We compare the topography of top and bottom surfaces for several CCs with scanning electron microscopy (SEM) and present in Fig. 6.4 the images corresponding to SuperOx with APC. The main features of the top surface, Fig. 6.4 **(a)**, are a dense YBCO film with several inclusions of secondary phases precipitates with diameter in the range of μm. Other than reported by the provider [104], we have not found (100)- and (010)-oriented YBCO grains on

the top surface. Moreover, in case of Theva, secondary phases and misaligned grains are known to be pushed to the top surface during growth processes leaving 'dead' surface layers, meaning layers devoid of good superconducting properties, behind [122].

The bottom surface , Fig. 6.4 (b), consists of a very dense, smooth and much cleaner YBCO film with terraces of buffer layers. The contrast of the SEM image suggests different buffer films to be exposed and energy-dispersive X-ray spectroscopy analysis confirms that both LaMnO$_3$ (LMO) and MgO can be the topmost layer.

CCs of all providers display similar trends in the topography of their corresponding top and bottom surfaces.
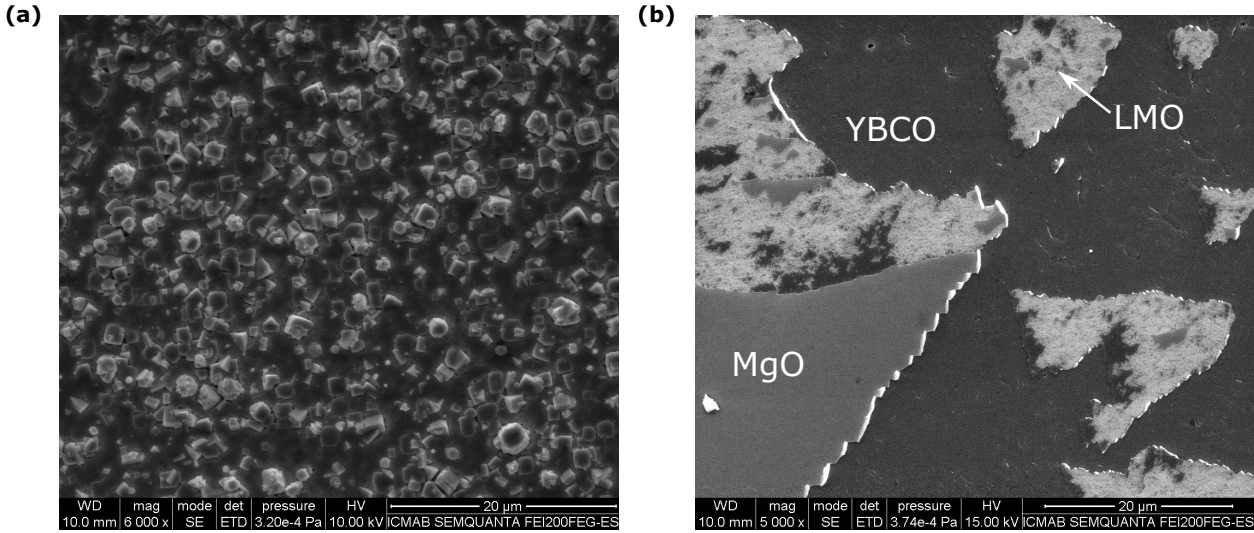
FIGURE 6.4: Scanning electron microscopy image of **(a)** the of Cu and Ag stripped top surface and **(b)** the delaminated bottom surface of a SuperOx APC coated conductor. The morphology of the top surface stands out because of its secondary phases precipitates, the bottom surface contains patches of MgO and LaMnO$_3$ buffer layers on top of smooth YBCO.

6.2 High-frequency response

6.2.1 Complex penetration depth

In order to quantify the probing depth of the electrodynamic RF field within a REBCO CC exposed to applied magnetic fields, we will turn to the concept of complex penetration depth $\tilde{\lambda}$. It describes the exponential decay of the magnetic RF field in the superconductor. The complex penetration depth $\tilde{\lambda}$ governs the entire surface impedance according to the following relation [30, 66]

$$Z_s = R_s + iX_s = i\omega\mu_0\tilde{\lambda}(\omega,B,T) = i\omega\mu_0\sqrt{\frac{\lambda_L^2 - \frac{i}{2}\delta_v^2(B,T,\omega)}{1+2i\frac{\lambda_L^2}{\delta_{nf}^2(B,T,\omega)}}}, \tag{6.1}$$

where μ_0 is the vacuum permeability. We see that $\tilde{\lambda}$ is composed of three other characteristics lengths. Firstly, the London penetration depth λ_L which describes the response of the superfluid. Secondly, the normal fluid skin depth δ_{nf} which corresponds to the response of the normal fluid and thirdly, the complex vortex motion skin depth δ_v arising from the movement of vortices. The explicit expressions of the two latter lengths are

$$\delta_{nf} = \sqrt{\frac{2\rho_n}{\omega\mu_0}}, \tag{6.2}$$

with ρ_n as the normal state resistivity and

$$\delta_v = \sqrt{\frac{2\Phi_0 B}{\mu_0 \omega} \frac{1}{\eta - i\frac{k_p}{\omega}}}, \qquad (6.3)$$

when flux creep can be neglected. The vortex viscosity η and the pinning constant k_p are the in chapter 2 introduced vortex motion parameters. For temperatures not too close to the critical temperature of the superconductor T_c, $\delta_{nf} >> \lambda_L$ and the complex penetration depth $\tilde{\lambda}$ from Eq. (6.1) can be simplified to

$$\tilde{\lambda}(\omega, B, T) = \sqrt{\lambda_L^2 - \frac{i}{2}\delta_v^2}. \qquad (6.4)$$

This expression is equivalent to the relation from equation (2.59). We estimate ρ_n, η and k_p of coated conductors used in this study for high fields and at low temperatures with DC transport and surface resistance characterization as described in chapter 5 and [15] and compute the penetration depths according to Eq. (6.3) and Eq. (6.4). In Fig. 6.5, we show the penetration depths of SuNAM coated conductor as a function of temperature at 9 T and 8 GHz which marks the upper limit of penetration depths that can occur for all examined CCs in the thesis.
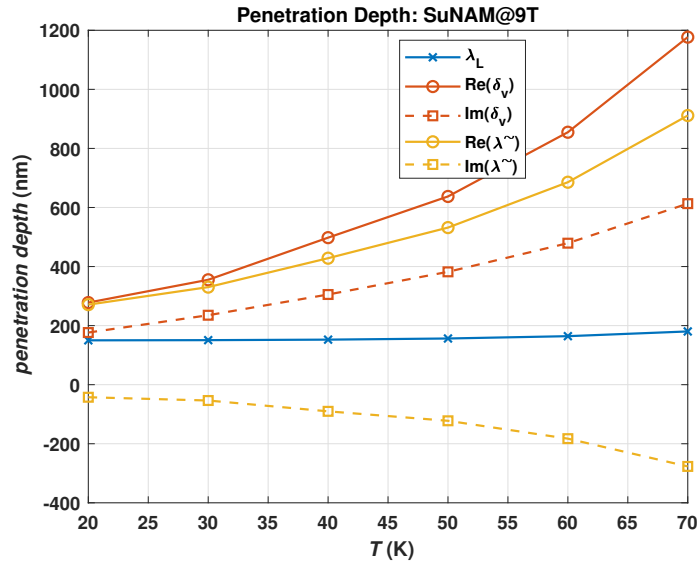
FIGURE 6.5: Penetration depths as a function of temperature at 9 T and 8 GHz. The estimation is shown for coated conductors provided by SuNAM. They exhibit the largest penetration depths among the samples under study.

Apart from the rather constant behavior of λ_L, the temperature dependencies of the penetration depths are quite strong. At 70 K, the real part of $\tilde{\lambda}$ reaches the three fold value of the ≈ 300 nm found at 20 K. The real part of the vortex motion penetration depth δ_v shows a similar behavior. At 70 K, the δ_v is increased by a factor of four with respect to the ≈ 300 nm encountered at 20 K.

With the thickness range ≈ 1.3 μm to 3.0 μm of the studied REBCO layers in mind, we can conclude two things. On the one hand, it becomes clear that the underlying substrate layers can contribute to the signal but the influence is small as already pointed out in subsection 5.1.1 of chapter 5. In addition, this influence decreases with decreasing temperature. Below $T = 40$ K the penetration depths become at least three times smaller than the REBCO film thickness, which is commonly considered as a good indicator for when layers below the film do not contribute significantly to the signal [208].

On the other hand, since the real parts of $\tilde{\lambda}$ and δ_v are mostly fractions of the REBCO film thickness, we are probing

different volumes of the film when characterizing a REBCO layer either from the top or bottom side. Assuming that the microstructure of the REBCO is not completely uniform along its film thickness, we could expect to measure different surface impedances that depend on the sampling side of the film. Indeed, this is what we experimentally observe as shown in the following section.

6.2.2   Surface impedance of top and bottom surface

Fig. 6.6 shows the real and imaginary part of the surface impedance $Z_s(H) = R_s(H) + iX_s(H)$ for the top and bottom surface of SuNAM coated conductor at 20 K and 70 K. We display the data which is recorded both during an up-sweep of the magnetic field starting at 0 T (colored markers) and the subsequent down-sweep to zero field (white markers). Comparing the two magnetic field branches, a hysteretic behavior can be observed below 1 T, most likely due to trapped fields and their contribution to the surface impedance. Interestingly, the hysteresis is much stronger at the bottom surface of samples. This points towards a magnetic influence of buffer layer LMO as will be discussed further below.

At both temperatures, the bottom surface exhibits a larger surface resistance at zero-field $R_s(\mu_0 H = 0 \text{T})$ than its counterpart on the top. At $\mu_0 H \approx 0.5 \text{T}$ a crossing between the surface resistances of top and bottom surface occurs, due to the weaker field dependence in R_s of the bottom surface. The situation for the surface reactance is similar. At small fields, the bottom surface shows larger surface reactances before it undercuts the values of the top surface at about 1 T as a consequence of better in-field performance.

The signal differences corresponding to top and bottom surface could be linked to a superconductor's microstructure quality gradient in thickness. For REBCO growth, microstructure gradients along their thickness are well known in the community. For example, misoriented YBCO grains are mostly located close to the top surface for SuperOx APC CC [104] and Fig. 6.4 **(a)**, Theva reports on differences in grain sizes between bottom surface ($\sim 200 \text{nm}$) and top surface (500-600 nm) [129], or YBCO layers closer to the substrate were observed with better epitaxy than upper layers for thick thick film growth on $SrTiO_3$ substrates [107]. All these effects could result in a microstructure that is less effective to pinning closer to its top surface. Taking into account the electromagnetic field penetration depths of our DR which are in the hundreds of nm range, the volumes which are probed when either top or bottom surface is characterized should comprise different thickness sections of the layer and therefore different microstructures. In chapter 5 and previous publications, we have already demonstrated that the microstructure of the superconductor's layer has a strong impact on the high-frequency response to an electromagnetic field [14, 15] and thus, this could explain the differences in surface impedance when comparing the top and bottom surface of film.

Differences in high-frequency properties of top and bottom surfaces of coated conductors were observed by another group, too. Yang et al. compared the surface resistance of the top and bottom surfaces of coated conductors as a function of temperature without an applied magnetic field [209]. They found the bottom surface to be by about a factor of 2.2 and 1.3 smaller than the top surface at 20 K and 70 K, respectively[1]. They ascribed the performance differences also to variations in microstructure with thickness of the superconducting layer.

The microstructure quality gradient in thickness has quite an interesting implication for the use of the coated conductors in microwave applications at large magnetic fields. Our generated results suggest that exposing the bottom surface of the superconducting layer to a RF cavity, which is native to our coating technique, gives rise to less losses at elevated fields as compared to when the standard top surface is facing the cavity. The performance difference between

---

[1]Although, we show at zero fields the opposite trend in Fig. 6.6, we have to remark that in our case the intrinsic response of the superconductor is masked by the LMO buffer layer in this field range. Removal of the LMO would render the surface resistance of bottom side lower than the surface resistance of the top side at zero fields.

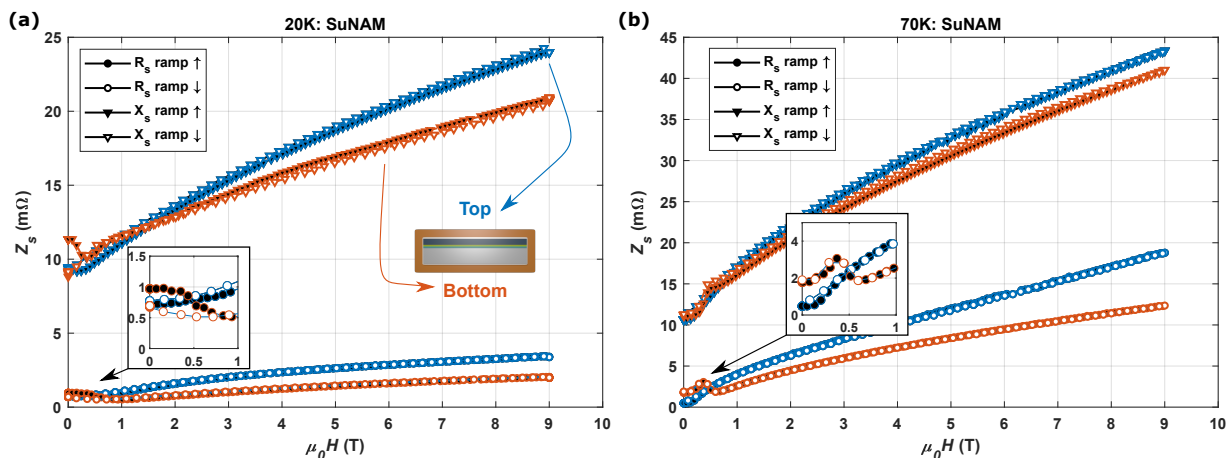top and bottom surface is provider dependent but increases always with magnetic field as shown in Fig. 6.8.

FIGURE 6.6: Measured surface impedance as a function of applied magnetic field at 20 K **(a)** and 70 K **(b)**. The top (blue line) and bottom surface (red line) of the superconducting layer are compared. Values recorded during ramping the magnetic field up and down are represented by black and white filled markers, respectively. Both the surface resistance and surface reactance of the bottom surface exhibit a stronger in-field behavior. The inserts zooms into the surface resistance at small fields.

Zooming into small fields, the inserts in Fig. 6.6 illustrate that $R_s^{\text{top}}(H)$ rises monotonously with magnetic flux enhancement, whereas $R_s^{\text{bottom}}(H)$ presents a curious sequence of increases and dips before it continues with an monotonous increase. The exact shape and positions of the increase-dip sequence is temperature and provider dependent as can be seen in Fig. 6.8. Ahn et al. observed similar field behaviors at small magnetic fields when characterizing their YBCO tape coated axion cavity. They etched the YBCO from the coated conductor and measured the magnetic signal of the tape. Indeed, they found a magnetization pattern of the tape that matches the signal from microwave measurements. They attributed the magnetization to the Ni-9W metallic layer [204].

Since we measure anomalous magnetic field behavior, arising on structures which are not comprised of the metallic substrate, we think that it originates from the interaction between vortices and the magnetic properties of coated conductor's buffer layers, not the metallic substrate itself. In case of measuring the top surface, buffer layers are covered by the superconducting layer which screens most of the probing microwave electromagnetic field. However, when probing the bottom surface of the superconductor, patches of buffer layers that remain after delamination on the HTS are directly exposed to the probing field and contribute thus stronger to the signal as can be seen in the inserts of Fig. 6.6.

In the following, we provide experimental support for our hypothesis. After soldering and delaminating a SuperOx APC CC, we first characterized the high-frequency response of the exposed bottom surface. We emphasize again, buffer layers, in this particular case MgO and $LaMnO_3$, remain on the bottom surface as seen in Fig. 6.4 **(b)**. In the next step, we ion milled the exposed surface with the intention to remove residual buffer layers. Indeed, the aspect of the samples, in particular the color of the reflected light on the sample surfaces, changed after ion milling them as can be seen in the inset of Fig. 6.7, which indicates a considerable thickness reduction or entire removal of the buffer layers.

The milled specimen are measured with the dielectric resonator and compared to the untreated pair in terms of surface impedance at 70 K in Fig. 6.7. We show the data corresponding to ramping the magnetic field up starting at 0 T (colored

markers) and down from 9 T (white markers). The most noticeable change after buffer layer thickness reduction is
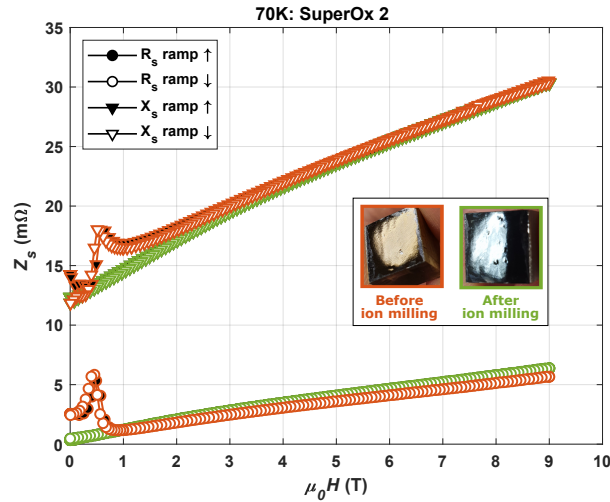
FIGURE 6.7: Depicted is the surface impedance, R_s in circles and X_s in triangles, for the exfoliated bottom side of SuperOx APC CC before (red) and after ion milling (green) as a function of magnetic field at $T = 70$ K. Data from both sweeping the field up (colored markers) and down (white markers) is shown. Clearly, the small field peak for R_s and X_s, which we associate with interaction of vortices and the LMO and/or MgO remains, disappears upon surface processing. The inset shows the sample surface aspect. The reflection hue changed after milling, a hint for removal or significant thinning of buffer layers.

the absence of the small field peaks for both surface resistance and surface reactance at about 0.5 T to 0.75 T. In fact, the field dependence at small applied fields of the milled sample resemble the ones that are measured for top surfaces (see Fig. 6.6 **(b)**), where the influence of the buffer layers is suppressed. For mid and large magnetic fields the surface impedance of milled sample shows a slightly stronger field dependence which might result from a minor REBCO deterioration caused by milling, but the overall surface impedance matching of milled and not-milled samples across this field range suggests that buffer layers impact the surface impedance primarily at fields < 1 T. The magnetic properties of buffer layers seem to interact with the trapped fields inside the superconductor since the hysteresis of ramping field up and down branches is much larger before ion-milling.

We compare the superconductor's top and bottom side of six different CCs in terms of $R_s(B)$ at 50 K in Fig. 6.8 **(a)** and its surface resistances at 9 T for several temperatures between 20 K to 70 K in Fig. 6.8 **(b)**.

The tendency of the bottom surface to perform better in-field prevails for all studied CCs. This trend is nuanced by the surface resistance difference between top and bottom side. At 50 K and 9 T, for example, SuperPower yields $R_s^{bottom} = 2.7$ mΩ and $R_s^{top} = 3$ mΩ, so a difference of only a few tenths of mΩ. In contrast, Theva gives $R_s^{bottom} = 4.0$ mΩ and $R_s^{top} = 7.3$ mΩ, which is a more significant variance. This observation could be explained by microstructure inhomogeneity in thickness which varies for different growth techniques. The CCs whose in-field performance is less dependent on the surface side of the superconductor, could have a more homogeneous nano defect landscape in its microstructure across the entire film thickness.

The full field sweeps corresponding to Fig. 6.8 **(b)** are archived in appendix C.

FIGURE 6.8: Comparing the surface resistance of several CCs. The marker edge color relates to the provider and the marker face color indicates the probed surface (white color–> bottom surface; other color–> top surface). **(a)** Displa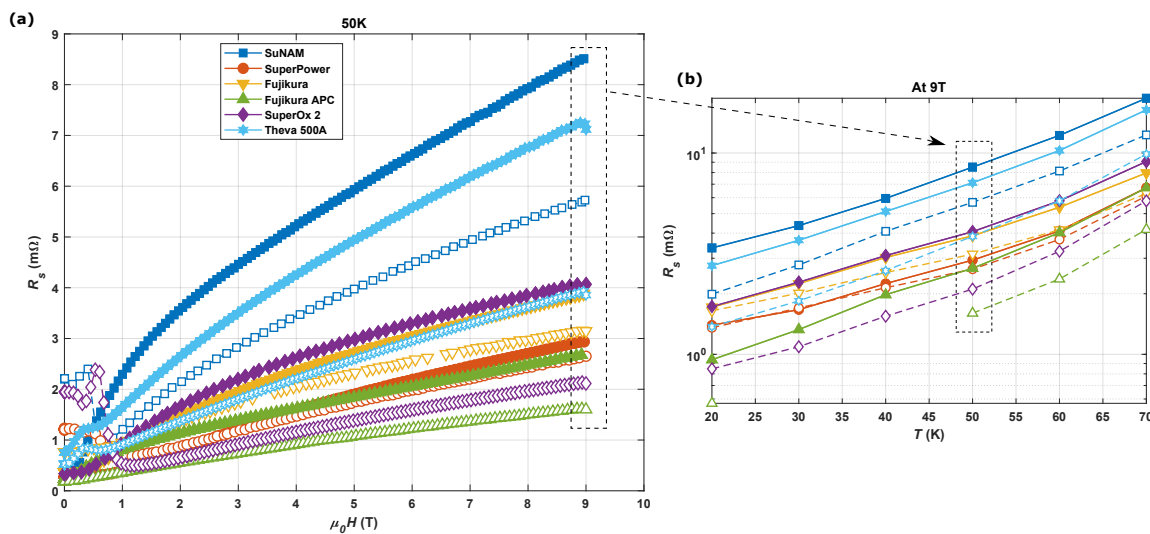yed is R_s as a function of magnetic field at 50 K. Just like in Figure 6.6, the top and bottom surfaces of each provider display different surface resistances, both in terms of zero-field values and field behaviors. **(b)** Here, we present the surface resistance of studied CCs at 9 T as a function of temperature. The trend of better performing bottom surfaces observed at 50 K, applies for a wide temperature range.

6.2.3 Spin-off collaboration with RADES group at CERN

The presented coating technique has been already applied for a large-scale microwave experiment. One of several techniques for dark matter search are axion haloscopes, a radio-frequency cavity embedded in magnetic fields acting as a detector [210]. Axions are proposed candidates for the building blocks of dark matter that could elegantly solve the strong-CP problem within the standard model of particle physics [211, 212]. Theory predicts a conversion of $\sim \mu$eV axions to two photons when transversing magnetic fields. Given a correct resonant frequency tuning, this conversion can be detected with a haloscope as a narrow linewidth signal [210, 213].

The sensitivity of axion detection scales with $\propto VQB^2$ where V corresponds to the cavity volume, Q the quality factor of the cavity and B the applied magnetic field [201, 214]. This relation indicates the preference for a low loss and high magnetic field sustainable coating material like type II HTS within the haloscope. A NbTi based superconducting cavity based haloscope has been already employed with success increasing the quality factor of the cavity and thus the potential axion signal with respect to copper cavity haloscopes [201].

The good results from our delaminated samples raised interest in other communities of high-energy physics, like the in the one of Axion detectors and sparked a spin-off collaboration with the RADES (Relic Axion Detector Exploratory Setup) team at CERN. Our proposed soldering and attachment technique was applied to a RADES cavity by members of the SUMAN group at the ICMAB. They coated the center of the Cu cavity with bending radius $r = 9$ mm using Theva CCs. Characterization of the REBCO coated haloscope at CERN yielded $Q(11\,\text{T}, 4.2\,\text{K}, 9\,\text{GHz}) \sim 60000$ in comparison with a pure Cu based haloscope $Q(11\,\text{T}, 4.2\,\text{K}, 9\,\text{GHz}) \sim 40000$ [215], thus an improvement of the quality factor by 50 %. With that in mind, we are interested in the microwave performance of CCs at even lower temperatures than previously relevant for the FCC-hh study.

In Fig. 6.9, we demonstrate the surface resistance sensitivity to magnetic fields at 10 K, close to the lower limit of achievable stable cooling temperatures with our setup, of several CCs. The full markers refer to the top surface and
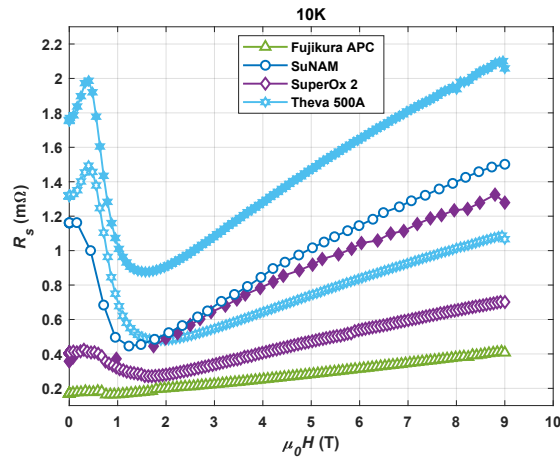
FIGURE 6.9: The surface resistance as a function of applied magnetic field 10 K for several CCs. The colored markers correspond to the top surface and the white markers to the bottom surface of the samples.

white markers to the bottom surface of corresponding samples. All CCs display extremely low R_s even up to 9 T demonstrating their suitability for low T, large H microwave applications. Informed by this plot, we can expect an improvement of the quality factor contribution from the REBCO in the RADES haloscope by at least a factor of 2.75 at 11 T and 4.2 K when coating with Fujikura APC instead of Theva. This factor is estimated as the lower bound since we assume that both CCs, Theva and Fujikura APC, perform as presented in Fig. 6.9 when assembled in the haloscope. However, we find that Theva suffers from considerable R_s increase when bent with radius $r = 9$ mm which
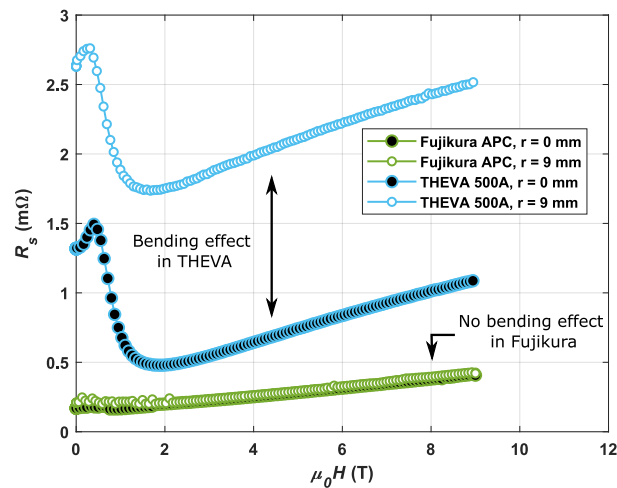
FIGURE 6.10: The effect of bending a CC on its surface resistance at 10 K and up to 9 T. Compared are samples from two different manufacturer. Fujikura APC exhibits virtually no change in R_s after bending with radius $r = 9$ mm. In contrast, Theva is harmed by the bending since it shows an almost field independent surface resistance increase that amounts ≈ 1.5 mΩ.

corresponds to the haloscope test cavity's curvature. In contrast, this bending effect is not encountered in Fujikura APC as shown in Fig. 6.10. We believe that Theva CCs are more susceptible to bending damages because of their inclined c-axis technology. When taking the one-sided deterioration due to curving into account, the improvement of cavity quality factor upon replacing Theva with Fujikura APC could amount a factor five at 10 K and 9 T.

Further details about the bending study will be disclosed in future works of our group.

6.3 Conclusions

Facing the issue of unattainable direct growth of REBCO on RF-cavities, on the one hand, and the demand for a high-performing and practical material for high-temperature, large magnetic field microwave applications, for example in the FCC-hh study, dark matter research or muon collider physics, on the other hand, we have introduced a technique to coat commercially available REBCO CCs on flat or curved, metallic surfaces compatible with large scale high-frequency applications. In this context, we detailed the procedure which is based on upside down soldering and delamination of the metallic substrate. This method brings advantages with respect to handling and lifetime of the samples.

We characterized small delaminated samples with a magnetometer in order to gauge the deterioration caused by the coating process. It was revealed that big parts of the sample center stay unaffected, thus $J_c(H)$ maintains the large values measured for samples as provided from the manufactures. An extended study about damage assessment, targeting especially the parts close to the sample edges and differences in breaking planes among the providers, is currently conducted by colleagues for samples in cm lengths.

Moving to the high-frequency characterization, we measured the surface impedance of delaminated samples in a wide cryogenic temperature range, up to 9 T and compared them to their top-surface counterparts. Not only do the delaminated samples display very low surface impedances, they even outperform their corresponding top surfaces. Other groups observed similar phenomena and attributed a gradient in the microstructure and thus varying pinning efficiencies across the film thickness to this effect.
The role of buffer layers which partially remain on the delaminated sample surface, as demonstrated by SEM, has been investigated in connection with microwave response. We found that, in particular, LMO features a peak in the surface impedance at fields < 1 T, while leaving higher fields unaffected.

The proposed attachment technique has been already put into practice in a spin-off collaboration with the RADES project at CERN. Colleagues have coated the center of an axion cavity with CCs by Theva. Large field characterization at CERN yielded an improvement of 50 % in cavity quality factor for the REBCO coated haloscope as compared to a copper haloscope. A bending study revealed that employed Theva CCs suffered damages in superconducting properties when applied to the haloscope. Since this bending effect does not occur for Fujikura APC CCs, we assume that it is related to the inclination of the *c*-axis found in Theva CCs.

All in all, the practicality of the proposed attachment technique supported by generated experimental results offer a possible solution to the critical issue of how to coat the beam screen chamber of the FCC-hh with REBCO CCs. To a greater extent, our study could lead to a wider penetration of coated conductors into other microwave applications where large magnetic fields are required.

Chapter 7

Requirements for use of CCs as a beam screen coating

Besides having a low surface impedance, a potential beam screen coating needs to fulfill many more compatibility points. In this chapter, we tackle three critical issues that arise when envisioning the use of CCs in a particle accelerator.

1. Persistent currents in the superconductor should not degrade the magnetic field homogeneity inside the beam screen, since it would endanger the trajectory stability of accelerated particles. Subdividing the superconducting coating into narrow parallel decoupled segments has been shown to effectively reduce superconducting persistent currents. Therefore, in order to avoid this undesirable effect, a hybrid coating composed of alternating longitudinal segments of REBCO superconductor and copper was suggested. Previous simulation studies bring additional relevance to this option [196, 216].

   In collaboration with group members, a finite elements numerical (FEM) analysis is carried out which formulates guidelines for hybrid coating geometries to comply with the field quality criterion imposed by CERN [217]. Within this chapter, we describe the production of CC based REBCO-Cu hybrid coatings which respect the geometry rules by the FEM simulations. The produced samples are analyzed in terms of their high-frequency response in a wide cryogenic temperature range and up to 9 T. In addition, we estimate the microwave losses expected from interruptions in the REBCO coating due to beam screen chamber segmentation.

2. Electron cloud build-up in the chamber, which depends significantly on the beam facing coating material, has to be suppressed during operation [218]. In cooperation with the Technology Department - Vacuum, Surfaces and Coatings (TE-VSC) group at CERN, we characterize the secondary electron yield (SEY) of pristine REBCO CCs and apply two surface treatments in order to lower the SEY to acceptable levels. On the one hand, CCs are conditioned with an e-beam, on the other hand, CCs are coated with thin films of amorphous carbon (a-C) and titanium. The compatibility of the a-C+Ti with CCs is assessed in terms of conservation of superconducting properties and low surface resistance. Part of presented results are published in [14].

3. The third aspect we explore is the impact of synchrotron radiation, the energy that charged particles emit when they are accelerated on a circular track, on the superconducting properties of coated conductors. In collaboration with ALBA Synchrotron, we expose CC samples to high-energy residual X-rays of low intensity for several weeks with the objective to estimate long term damages.

7.1   REBCO-Cu hybrid coatings for high field quality and low beam coupling impedance

Acceleration of proton bunches with 50 TeV in the FCC-hh requires extreme beam stability for unperturbed operation. One measure to decrease the beam coupling impedance, a source for beam disturbance, between accelerated beam and mirror charges is the coating of the beam screen chamber with superconductors [15]. This, however, introduces a new obstacle: the magnetic field generated by the persistent superconducting currents of the HTS will decrease the field homogeneity in the beam screen chamber, another important factor for beam stability.

A typical way to reduce AC-losses in YBCO is to decrease its aspect ratio, so the ratio between film width and thickness. For example, it has been shown that by dividing a YBCO film into narrow filaments, AC-losses could be decreased by two orders of magnitude owing to the decrease of film magnetization [219]. The striation strategy to decrease trapped fields within a superconductor has been picked up for the FCC study. Hybrid structures consisting of REBCO and Cu stripes are proposed as a possible beam screen coating solution to offer low beam coupling impedance without endangering the field quality. However, these two aspects of the coating are heavily dependent on its geometry.

In order to find the best compromise between high field quality and low coating surface impedance, we employed a finite element model that simulates the field quality inside the FCC-hh beam screen chamber for variable REBCO-Cu segmentation. Our approach parameterizes the REBCO-Cu hybrid structure into the ratio of superconducting material within the hybrid coating p and the number of superconducting segments that the hybrid structure is split into n. The model accounts for the inherent flux creep of HTS, the anisotropy of REBCO currents, the critical current dependency with the magnetic field, and beam-induced vortex shaking, while considering superconducting properties from commercially available CCs. The performed simulations are part of another PhD thesis and further details about it are disclosed in [217]. Grounded in the simulations, we formulated geometry guidelines for REBCO-Cu hybrid coatings that comply with the maximum allowed relative field disturbance of the order $\eta'_{max} = 1 \times 10^{-4}$ and produced several REBCO-Cu structures based on SuperPower CCs. This chapter section is structured as follows: First, we inform about the preparation of CCs based REBCO-Cu hybrid structures via photolithography. Then, we report on the surface resistance of hybrid samples with ring geometry. Subsequently, we demonstrate experimentally the importance of a correct hybrid structure layout by discussing the surface resistance of hybrid samples with stripe geometry. In the third subsection, we estimate the high-frequency contact resistance between REBCO and Cu. Finally, we draw conclusions.

7.1.1   Ring REBCO-Cu layout

Hybrid structure fabrication and sample choice

As we have reported in Chapter 6, the CC soldering to the beam screen and subsequent delamination of the metallic substrate from the REBCO layer can be employed as a non-destructive large scale coating technique for the FCC-hh. After the delamination procedure, the exposed REBCO sits on its Ag and Cu protective layers, see Fig. 6.3 **(d)** which can be exploited for hybrid REBCO-Cu samples fabrication, based entirely on CCs.
In Fig. 7.1, we disclose the process steps that involve photolithography and wet etching. The exfoliated sample, as it is depicted in Fig. 6.3 **(d)**, is first covered with a positive photoresist by spin coating (see Fig. 7.1 **(a)**). After curing the photoresist, the area desired for Cu representation is exposed to a laser light source in a microwriter and subsequently, the sample gets stirred in a developer solution resulting in a patterned photoresist (see Fig. 7.1 **(b)**). The remaining photoresist protects the underlying layers from etching, allowing propagation of the pattern. We use

a 1:10 diluted H_3PO_4:H_2O acid solution to decompose REBCO (Fig. 7.1 **(c)**) followed by a 1:1:5 NH_3:H_2O_2:H_2O solution for selective Ag removal (Fig. 7.1 **(d)**). The photoresist is dissolved in acetone to end up with narrow stripes of REBCO alternated by Cu, the structure simulating a REBCO-Cu hybrid coating for the beam screen chamber (Fig. 7.1 **(e)**). The shown stripe geometry is used for experimental characterization of trapped fields in striated CCs by means of scanning Hall probe microscopy, the results are reported in [217], and gives just an example for any possible hybrid structure layout.
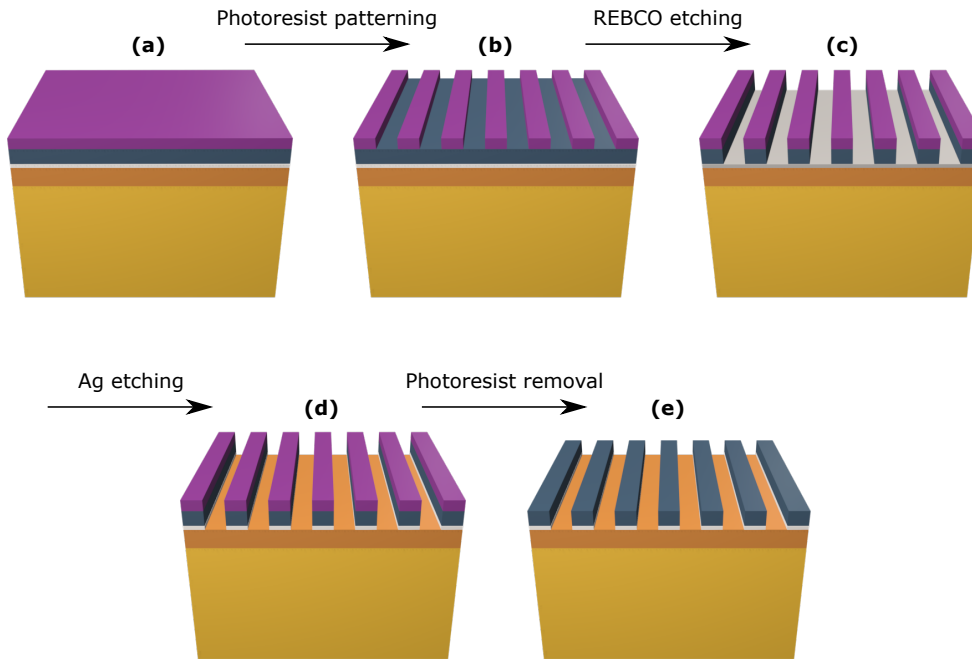
FIGURE 7.1: The fabrication steps that lead from a photoresist coated delaminated CC sample **(a)** to the finished REBCO-Cu hybrid structure **(e)**. The stripe geometry is just an example for any possible hybrid structure layout.

In fact, the layout has to be adopted for high-frequency measurements with a DR. We want the circular currents generated in a cylinder cavity, that resonates in the TE_{011} mode, to be confined within one material (either superconductor or Cu). This is needed in order to emulate the longitudinal stripes of the REBCO-Cu hybrid coating, which are translation-invariant under movement direction of accelerated particles, in the FCC-hh beam screen chamber. Such geometry avoids contact resistance contributions arising from driving currents from REBCO to Cu and vice versa whose phenomenology will be explained in subsection 7.1.2. To this end, following the electric field line distribution [83] in the cavity, the sample striation is realized in a ring pattern.

In order to point out the differences between sole REBCO and hybrid REBCO-Cu coatings, we created three specimen pairs. One coated conductor sample pair is not striated, here denoted as R0, whereas the other two pairs, R1 and R2, exhibit REBCO alternated by Cu grooves. The sample processing follows the steps described in Fig. 7.1.

The exact geometry of mentioned samples can be found in Table 7.1 and was chosen with the help of the simulations in such a way that the created REBCO-Cu hybrid structure complies with the field quality requirement within the FCC-hh beam screen chamber in the most demanding case of no dipole field correction by means of corrector magnets, see [220] for more details. In particular, we estimated the maximum relative field disturbance for a hybrid coating corresponding to the geometry of samples R1 and R2 with a finite element model as described in [217] and found a relative field disturbance of $\eta_{max} \approx 1.6 \times 10^{-4}$ for both samples which complies with the field quality target in the FCC-hh. The percentage of superconductor p given here refers to the relative amount of superconductor that is present

below the dielectric rutile disc with $\varnothing = 4\,\text{mm}$ in the center of the sample.

Sample name	p	$w(\mu m)$	$g(\mu m)$	$\eta_{max}(\times 10^{-4})$
R0	1	-	-	-
R1	0.92	121	10	1.56
R2	0.42	232	250	1.55

TABLE 7.1: Nomenclature of the samples produced to simulate hybrid coatings. R0 refers to a delaminated sample without any additional manipulation. R1 and R2 are delaminated and subsequently striated into rings by means of photolithograpy representing REBCO-Cu hybrid coatings. p corresponds to the amount of superconductor present in the sample center under the dielectric, w is the superconductor ring width and g the Cu groove width. η_{max} is the maximum relative field disturbance.

Figure 7.2 displays photographs of the R0, R1 and R2 samples taken through a magnifying glass where the ring striation can be appreciated.
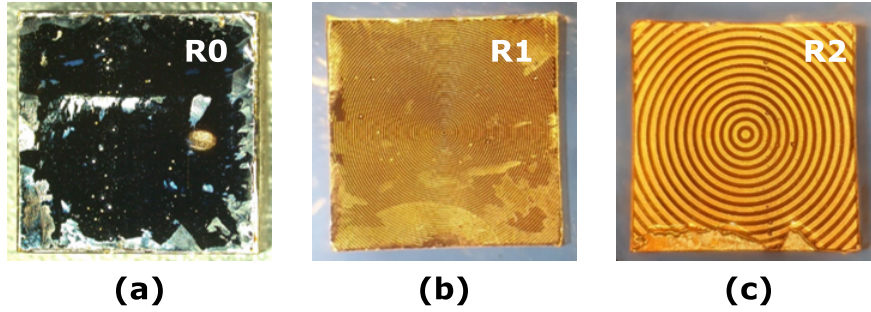

FIGURE 7.2: Top view of samples used for characterization in dielectric resonator. **(a)** Delaminated SuperPower coated conductor denoted as R0. After delamination of coated conductor, patches of buffer layers, shiny areas, remain on the REBCO surface. **(b)** First REBCO-Cu hybrid structure in ring geometry with $p = 0.92$, $w = 121\,\mu\text{m}$ and $g = 10\,\mu\text{m}$ denoted as R1. **(c)** Second REBCO-Cu hybrid structure in ring geometry with $p = 0.42$, $w = 232\,\mu\text{m}$ and $g = 250\,\mu\text{m}$ denoted as R2. The lower part shows REBCO that was ripped away during delamination of coated conductor. Since the EM-field in our cavity is mainly confined in the dielectric, a centered cylinder with $r = 2\,\text{mm}$, we do not expect a strong influence of the ripped HTS on measured surface resistance. The REBCO color on the picture of sample R0 (black) differs from the REBCO color of samples R1 and R2 (brownish) due to the from Cu grooves reflected light.

Surface resistance characterization

In Fig. 7.3, we present the surface resistance as a function of magnetic field of the two hybrid coatings R1 and R2 in comparison with a pure REBCO, R0, and pure Cu sample, electroplated copper that is used in the SuperPower CCs as a stabilizer, at $T = 50\,\text{K}$. For copper, we measured only $R_s(\mu_0 H = 0\,\text{T})$ and assumed no dependence on the field, whereas for the superconducting samples the magnetic field was ramped after zero-field cooling.

At $8\,\text{GHz}$ and $50\,\text{K}$, the microwave losses for both hybrid coatings are well below the ones of Cu in the measured field range. In the worst case at measurement conditions, the $92\,\%$ REBCO hybrid sample beats out Cu by a factor of 2.5. The difference between the two analyzed hybrid coatings are substantial. The $92\,\%$ sample R1 undercuts the surface resistance of its $42\,\%$ counterpart R2 by a factor 1.6-2.5 depending on the field. We observe that decreasing the REBCO ratio p in a hybrid coating has two contextual effects. It shifts the R_s to higher values but in return weakens the field dependence, the latter is better appreciated in Fig. 7.5 **(b)**.

Qualitatively, the field dependence for all superconducting samples is quite similar. Starting at intermediate fields, we observe an almost $\sqrt{B}$ behavior of the surface resistance for samples R0 and R1, typical for REBCO at high magnetic fields [73, 178], and a more linear behavior for sample R2. Below $\approx 1\,\text{T}$, the microwave signal peaks anomalously. As

shown in chapter 6, this peak can be attributed to remaining buffer layers after the delamination process, see Fig. 7.2 **(a)** for remaining buffer layer patches.

Finally, it is remarkable to see how close the 92 % hybrid sample R1 performs to the not striated sample R0. The surface resistance increase remains quite constant over the measured field range and amounts about 0.15 mΩ to 0.25 mΩ. Weighing this rather marginal increase in surface resistance against the decrease in trapped field, as seen from scanning Hall probe measurements [217] a reduction by one order of magnitude and more is feasible, the REBCO-Cu hybrid coating crystallizes itself out as a promising candidate for the FCC-hh beam screen coating. It should be noted that for large-scale applications the geometry parameters p and n of the presented hybrid coatings are limited by the minimum groove width that are realizable nowadays. A prominent large scale striation technique like laser scribing allows for groove widths $g \approx 23\,\mu\text{m}$ [221]. In any case, the potential of corrector magnets within the FCC-hh, see [220] for more details, could drastically relax the field quality constrain. Simulations suggest that hybrid coatings with parametric combinations $p = 0.95$ and $n < 10$ would be allowed in the beam screen chamber, if the dipole distortion component is corrected [217]. This translates to HTS segments close to the 2 mm or 4 mm width of some commercially available coated conductors. As a matter of fact, slightly decreasing the HTS ratio p would completely eliminate the need to striate the coating, benefiting the simplicity and cost of the production process.
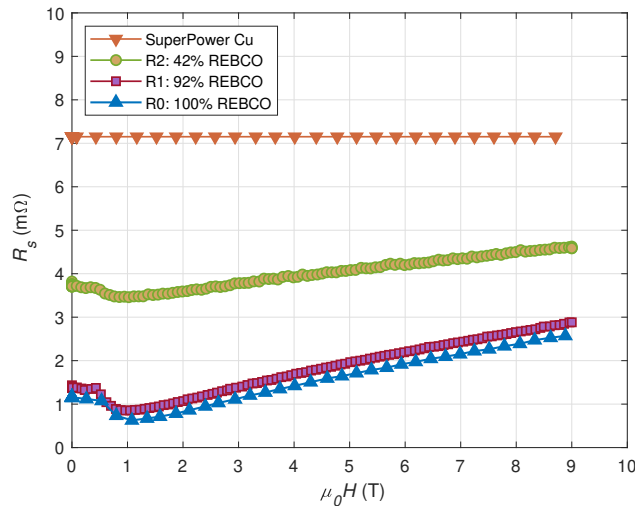
FIGURE 7.3: The surface resistance of pure Cu and pure REBCO in comparison with two hybrid samples as a function of applied magnetic field at $T = 50\,\text{K}$ measured with a dielectric resonator at $\nu \approx 8\,\text{GHz}$.

The high-frequency characterization for temperatures beyond $T = 50\,\text{K}$ is shown in Fig. 7.4. All described tendencies remain there valid, too. Thus, our conclusions can be extended to a wide cryogenic temperature window around $T = 50\,\text{K}$.

In order to understand the physics behind the microwave losses of hybrid coatings clearer, we employ an extremely simple, heuristic model. In a first approximation, one could assume that the present materials within a hybrid coating contribute linearly according to their exposed surface area to the total measured losses of a hybrid structure. In our case, this assumption translates mathematically to

$$R_s^{\text{hybrid}}(H) = p \cdot R_s^{\text{REBCO}}(H) + (1-p) \cdot R_s^{\text{Cu}}(H), \tag{7.1}$$

where R_s^{REBCO} and R_s^{Cu} denote the surface resistances of the hybrid sample constituents, i.e. the REBCO and Cu,
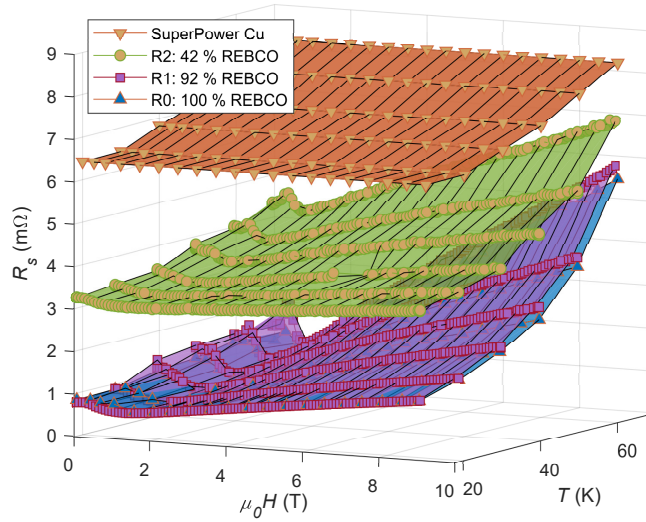
FIGURE 7.4: The surface resistance R_s of two hybrid coatings (42 % and 92 % REBCO) in comparison with Cu used in the SuperPower coated conductor and delaminated SuperPower as a function of applied magnetic field at several cryogenic temperatures. The trends for $T = 50$ K, described explicitly in the text, are valid for the shown temperature range.

respectively. This simplification arises from simulations of our DR loaded with a perfect conductor where the EM-field is focused spatially inside the rutile [96]. As a consequence, microwave currents are primarily driven through the conductor that is present below and above the dielectric rutile, letting the center area, presumably, of any sample govern the microwave losses.

The theoretical hybrid structure surface resistance, calculated according to eq. (7.1), is shown together with surface resistances of samples R0, R1 and R2 in Fig. 7.5. Our simple model predicts the experimental data qualitatively well.
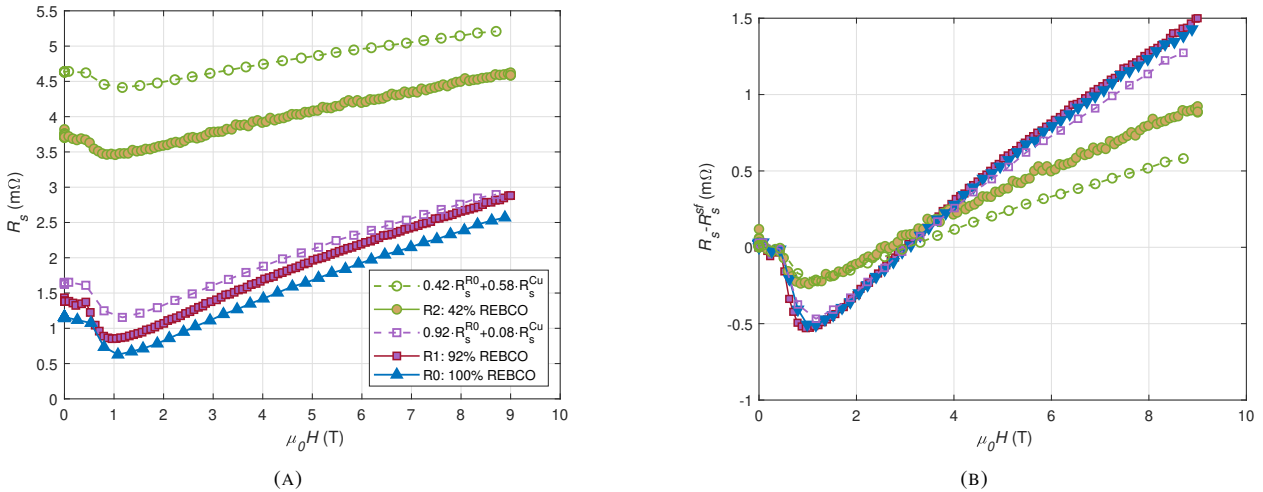
FIGURE 7.5: Measured surface resistances as a function of applied field at $T = 50$ K, $\nu \approx 8$ GHz (full points) and R_s curves of hybrid coatings calculated with a simple model described in the text (empty points). **(a)** Absolute values of the surface resistances. (b) Substracted surface resistances by the corresponding zero-field, or self-field value R_s^{sf} in order to highlight the field behaviors of the samples.

When decreasing the amount of REBCO p, the absolute R_s value of the hybrid coating increases, see Fig. 7.5 **(a)**, while the field behavior $R_s(H)$ of hybrid coatings flattens, see Fig. 7.5 **(b)**. Nevertheless, this model overestimates

absolute R_s values and underestimates the magnetic field dependence of R_s. We propose two possible explanations for the model mismatch. On the one hand, the ratio of the superconductor p we are using to calculate the $R_s(H)$ of the hybrid coating with eq. (7.1) is estimated from the approximate relative amount of HTS under a centered dielectric disk with $\varnothing = 4\,\text{mm}$. This is not necessarily the real percentage of superconductor that contributes to the total signal of the hybrid coating, since RF-currents are not evenly distributed under the dielectric according to simulations [96]. The error we are making in estimating p scales with the groove width g and could thus explain why the model diverts stronger from sample R2. On the other hand, the more superconductor-like behavior of the experimental as compared to model data (smaller total surface resistance values but stronger field dependence), could hint towards the assumption that microwave currents have a preferential flowing medium within the hybrid structure. The system could focus more microwave currents into the REBCO than Cu in the pursuit to reduce losses.

In conclusion, while our model, represented by eq. (7.1), yields quantitative mismatch between theory and experimental data, it is able to explain the main trends of $R_s(H)$ in striated hybrid coatings quite well.

7.1.2 Striped REBCO-Cu layout

Sample choice

In order to demonstrate experimentally the importance of correct hybrid coating patterning, we produced additionally two hybrid structure sample pairs with stripe layout. Denoted S1 and S2, they exhibit narrow REBCO filaments alternated by Cu grooves.

The exact dimensions of produced samples can be found in Table 7.2. Just like in the case of the ringed samples, we chose the stripe dimensions based on field quality simulations [217], in order to let the S1 and S2 comply with the field quality requirement within the FCC-hh beam screen chamber. More precisely, the maximum relative field disturbance for hybrid coatings corresponding to the dimensions of samples S1 and S2 is $\eta_{max} \sim 1 \times 10^{-4}$ for both samples.

Sample name	p	$w(\mu m)$	$g(\mu m)$	$\eta_{max}(\times 10^{-4})$
S1	0.91	122.6	12.4	~ 1
S2	0.50	239	251	~ 1

TABLE 7.2: Nomenclature of the samples produced to simulate hybrid coatings. S1 and S2 are delaminated and subsequently striated into stripes by means of photolithograpy representing REBCO-Cu hybrid coatings. p corresponds to the amount of superconductor present in a sample, w is the superconductor stripe width and g the Cu groove width. η_{max} is the calculated maximum relative field disturbance.

Fig. 7.6 depicts the top view of the two samples from Table 7.2 taken with a magnifying glass.

Surface resistance characterization

The surface resistances as a function of magnetic field of the two hybrid coatings in stripes layout S1 and S2 are shown together with the corresponding quantity of samples R0, R1, R2 and SuperPower Cu at $T = 50\,\text{K}$ in Fig. 7.7.

The stripe structures perform meaningfully worse than REBCO/Cu hybrid samples in ring configuration. While the in-field behaviors of hybrid samples with similar p but different layout match, i.e. R1 with S1 and R2 with S2, the absolute R_s differ at 9 T for samples R1 and S1 by 2.49 mΩ and for samples R2 and S2 by 0.88 mΩ. This suggests, as already alluded to, that misaligning the pattern of a hybrid coating to the current distribution causes contact resistances arising from longer surface current paths, see Fig. 7.9. Since the earlier introduced heuristic model to describe the surface resistance of hybrid structures does not account for contact resistances, see eq. (7.1), we can compare it with experimental data of striped hybrid structures and thus roughly estimate the contact resistance as the mismatch between model and experimental data.
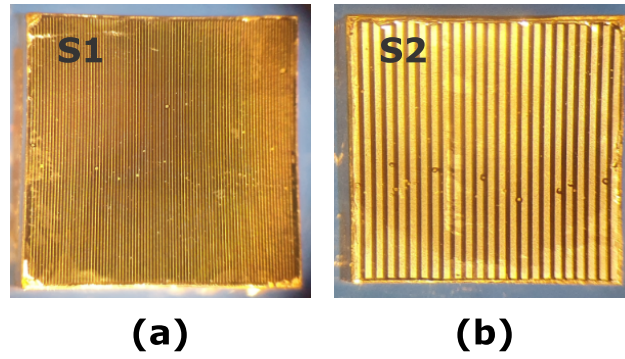
FIGURE 7.6: Top view of samples used for characterization in dielectric resonator. **(a)** First REBCO-Cu hybrid structure in stripe geometry with $p = 0.91$, $w = 122.6\,\mu m$ and $g = 12.4\,\mu m$ denoted as S1. **(b)** Second REBCO-Cu hybrid structure in stripe geometry with $p = 0.50$, $w = 239\,\mu m$ and $g = 251\,\mu m$ denoted as S2.
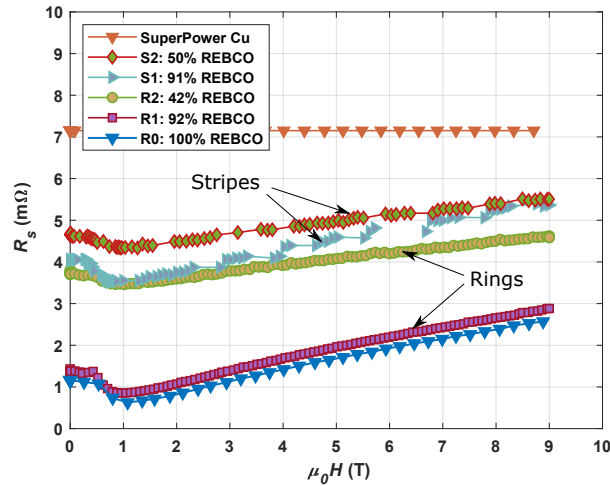
FIGURE 7.7: The surface resistance of pure Cu and pure REBCO in comparison with four hybrid samples of two different configurations as a function of applied magnetic field at $T = 50\,K$ measured with a dielectric resonator at $\nu \approx 8\,GHz$.

The theoretical hybrid structure surface resistance, calculated according to eq. (7.1), is shown together with surface resistances of samples R0, S1, S2 and copper in Fig. 7.8.

Our simple model predicts the qualitative differences between the two striped hybrid structure S1 and S2 quite well. When decreasing the amount of REBCO p, the absolute R_s value of the hybrid coating increases, see Fig. 7.8 **(a)**, while the field behavior $R_s(H)$ of hybrid coatings flattens, see Fig. 7.8 **(b)**. In addition, the field behaviors of hybrid coatings are matched outstandingly by the calculated values. Nevertheless, since the model does not account for contact resistances, it underestimates absolute R_s values depending on the samples in different severity. The experimental data is for sample S2 at 9 T 0.7 mΩ and for sample S1 at 9 T even 2.0 mΩ larger than the model. The increase is almost field independent.

Phenomenologically, the microwave contact resistance can be explained by taking the topography of the samples into account. According to the operation in the TE_{011} mode, the induced currents in our resonator flow in a circular path, mostly below the dielectric [83]. For samples in hybrid stripes configuration, the current flow direction is not parallel
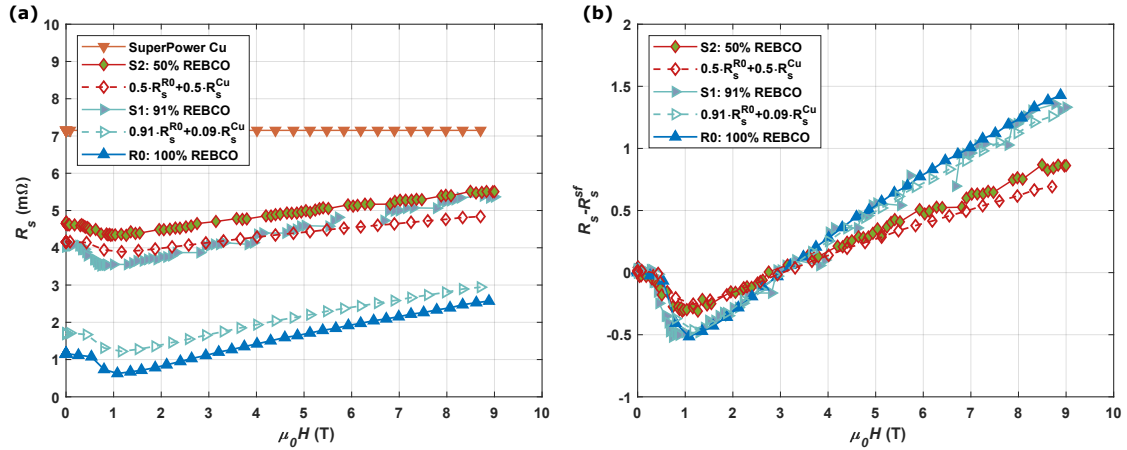
FIGURE 7.8: Measured surface resistances as a function of applied field at $T = 50\,\text{K}$, $\nu \approx 8\,\text{GHz}$ (full points) and R_s curves of hybrid coatings calculated with a simple model described in the text (empty points). **(a)** Absolute values of the surface resistances. (b) Substracted surface resistances by the corresponding self-field value in order to highlight the field behaviors of the samples.

to the striation and thus currents are driven through different materials of varying height, see Fig. 7.9 **(a)**, from REBCO to the lower laying Ag to the lower laying Cu and vice versa, see Fig. 7.9 **(b)**, where additional losses resulting from longer surface current paths occur. In particular, the topography becomes relevant to the measured surface resistance if $t \gg \delta$ [222, 223], where t is in our case the stripe thickness, so about 1.5 µm, and δ is the skin depth, for REBCO $\delta = \lambda_L \approx 150\,\text{nm}$. Engaging with direct current analogy, we can estimate the additional loss due to longer current path, which will depend on the interface materials, in form of a contact resistance $R_s^{\text{cont.}}$ expected at each REBCO/Cu interface.
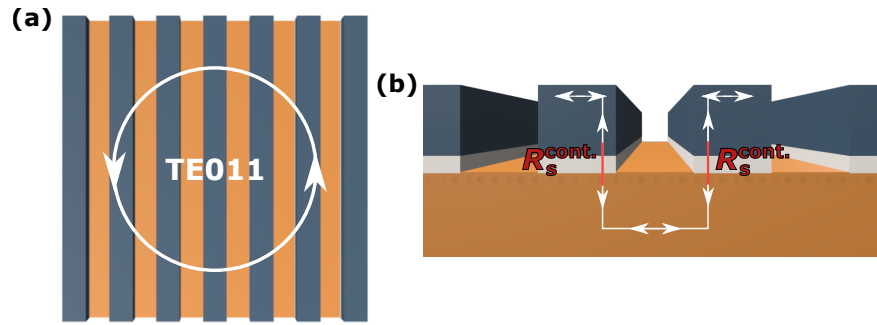
FIGURE 7.9: **(a)** Top view of stripe hybrid structure with the current flow direction associated to the TE_{011} mode represented as white arrows. **(b)** Cross section of striped hybrid structure with current flow direction represented as white arrows. In the REBCO/Cu interfaces additional losses resulting from contact resistance are expected which are visualized as red lines.

Assuming that the offset in experimental data as compared to model predictions arises only from losses associated to REBCO/Cu interfaces, we can estimate the mean contact resistance $R_s^{\text{cont.}}$ in the following way

$$R_s^{\text{hybrid, exp.}}(H) = R_s^{\text{hybrid model}}(H) + 4n \cdot R_s^{\text{cont.}}, \qquad (7.2)$$

where n is the number of HTS segments in the hybrid coating as introduced earlier. Multiplying n by 4 gives the number of interfaces that the current passes through per circular revolution, two times per REBCO-Cu interface on the upper sample half and the same amount on the lower sample half, thus the total number of times the contact resistance can contribute to the measured surface resistance of the hybrid structure $R_s^{\text{hybrid, exp.}}$. The contact resistance

can be normalized by the interface area A through which the surface currents flow in order to give a sample geometry independent quantity, the contact resistivity, or specific resistance:

$$\rho_s^{\text{cont.}} = R_s^{\text{cont.}} \cdot A. \tag{7.3}$$

We choose $A = w \cdot 4\,\text{mm}$, because w is the REBCO stripe width, so the width of the interface, and $4\,\text{mm}$ equals the diameter of the dielectric under which most of the surface currents in our DR flow. Table 7.3 shows the contact resitances and resistivities calculated for samples S1 and S2. It is remarkable how close together the calculated contact

Sample name	n	$R_s^{\text{hybrid, exp.}}(9\,\text{T})$ (mΩ)	$R_s^{\text{hybrid, model}}(9\,\text{T})$ (mΩ)	$R_s^{\text{cont.}}$ ($\mu\Omega$)	$\rho_s^{\text{cont.}}$ (nΩcm^2)
S1	88	5.4	2.9	7.1	35
S2	24	5.5	4.8	7.3	70

TABLE 7.3: The according to Eq.7.2 and Eq.7.3 calculated contact resistance and contact resistivity at 50 K.

resistances for samples S1 and S2 are, which actually follows expectations as both samples are based on CCs from the same batch. Although not completely comparable, interestingly, the calculated contact resistivity $\rho_s^{\text{cont.}}$ is in line with specific resistances found for soldered CC joints measured with IV-curves $\rho_c^{\text{CC joints}}(77\,\text{K}) = 20 - 300\,\text{n}\Omega\text{cm}^2$, where the main contribution to the specific resistance is associated to the REBCO-stabilizer and stabilizer-solder interfaces [224].

7.1.3 Estimation of high-frequency contact resistance

Within the FCC-hh arcs, the continuity of the beam screen chamber will be broken at about every 14 m because of dipole magnet interconnections [10]. The vacuum pipe will be held together by some flexible metallic connectors, known as RF-fingers, maintaining the electrical contact between magnets. Consequently, the potential HTS beam screen coating will be interrupted by non-superconducting elements.

In order to estimate the additional microwave losses caused by these interruptions, we picked up the contact resistance estimations from section 7.1.2 and launched a dedicated experiment based on the ring striated samples. The R1 sample pair was subjected to another patterning step with the purpose to create a centered cross of Cu grooves with width 10 μm superimposed over the ring patterning as shown in 7.10. This results in four REBCO-Cu joints per ring. These joints are supposed to emulate the interruptions expected in the REBCO coating within the beam screen chamber in a very simplistic manner.

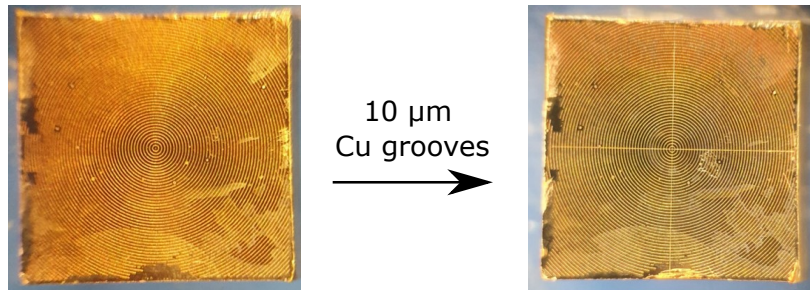FIGURE 7.10: Top view of sample R1 before and after patterning with a centered cross of 10 μm in order to create REBCO/Cu interfaces that are perpendicular to the current flow direction.

In Fig. 7.11, we compare the surface resistance as a function of applied magnetic field of sample R1 before and after the cross pattern at 70 K. Importantly, we see again an almost field independent increase for the manipulated R1
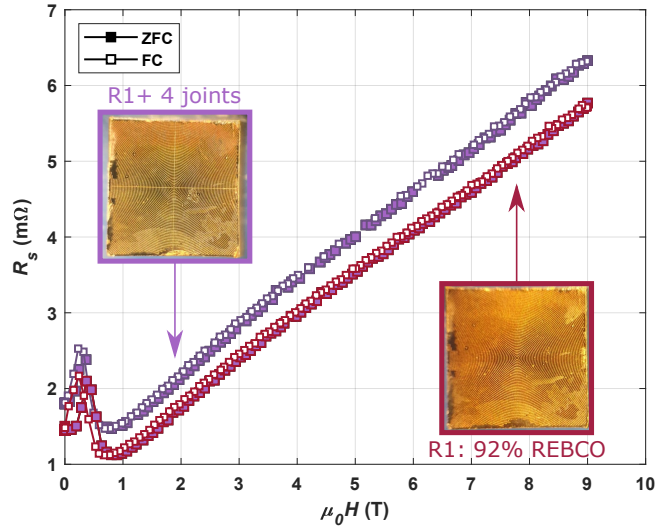
FIGURE 7.11: The surface resistance as a function of magnetic field of sample R1 before and after Cu cross pattern that results in four REBCO-Cu joints per ring. The colored and white faces of the markers represent measurements gathered from FC and ZFC, respectively.

sample, suggesting microwave losses at the interfaces that are normal to the current flow direction.

The total surface resistance of the new pattern with four REBCO-Cu joints $R_s^{4\,\text{joints}}$ can, analogously to eq. 7.2, be expressed as

$$R_s^{4\,\text{joints}}(T,H) = R_s^{\text{R1}}(T,H) + R_s^{\text{Cu cross}}(T) + 8n \cdot R_s^{\text{cont.}}(T), \tag{7.4}$$

where $R_s^{\text{R1}}(T,H)$ is the measured surface resistance of sample R1 at temperature T and applied magnetic field H, $R_s^{\text{Cu cross}}(T) = R_s^{\text{Cu}}(T) \cdot \frac{A_{\text{Cu cross}}}{A_{\text{sample}}}$, with $A_{\text{Cu cross}} = 2 \cdot 10\,\mu\text{m} \cdot 12\,000\,\mu\text{m}$ and $A_{\text{sample}} = 12\,000\,\mu\text{m} \cdot 12\,000\,\mu\text{m}$ corresponds to the additional surface resistance contribution arising from the new Cu grooves and n is the number of rings under the dielectric. We need to multiply n by 8, because the circular surface currents will encounter eight REBCO-Cu interfaces, two for each Cu groove, per ring. $R_s^{\text{cont.}}$ is the mean contact resistance per ring and can be normalized by the area A through which the surface currents flow when passing a REBCO-Cu interface in order to get the contact resistivity or specific contact resistance:

$$\rho_s^{\text{cont.}}(T) = A \cdot R_s^{\text{cont.}}(T). \tag{7.5}$$

As a first approximation, we estimate the REBCO-Cu interface width as the entire width of the REBCO ring w and the interface length to be 1 mm, thus $A = w \cdot 1\,\text{mm}$. The calculated mean contact resistances $R_s^{\text{cont.}}$ and specific contact resitances per ring $\rho_s^{\text{cont.}}$ at several cryogenic temperatures around 50 K are shown in table 7.4. Comparing the values

T (K)	n	$R_s^{4\,\text{joints}}(9\,\text{T})$ (mΩ)	$R_s^{\text{R1}}(9\,\text{T})$ (mΩ)	$R_s^{\text{Cu cross}}(9\,\text{T})$ (mΩ)	$R_s^{\text{cont.}}$ ($\mu\Omega$)	$\rho_s^{\text{cont.}}$ (nΩcm^2)
70	15	6.3	5.8	0.02	4.9	6.0
60	15	4.3	3.8	0.01	3.4	4.1
50	15	3.1	2.9	0.01	1.8	2.3
40	15	2.5	2.2	0.01	2.6	3.2
30	15	1.9	1.7	0.01	1.9	2.3

TABLE 7.4: The according to Eq.7.4 and Eq.7.5 calculated contact resistance and contact resistivity at 30-70 K.

at 50 K to the one calculated in subsection 7.1.2, we see a decrease in $R_s^{\text{cont.}}$ by half an one order of magnitude and in $\rho_s^{\text{cont.}}$ a decrease by one order of magnitudes. If one takes the simplicity of the used model and the crude estimations

of the to the high-frequency contact resistance contributing areas *A* into account, all calculated values coincide quite well. Beam coupling impedance simulations will need to assess the impact of the experimentally acquired contact resistances' magnitude on the beam stability.

7.1.4   Section conclusions

In this section, we addressed a major point of concern associated with the usage of superconductors as beam screen coating in the FCC-hh: persistent currents are expected to perturb the dipole field which guides the particle beam. A potential cure for this problem is the segmentation of the superconductor into narrow filaments which diminishes the trapped fields inside the HTS to a meaningful extent. However, removing superconducting material from the beam screen coating will necessarily result in deterioration of microwave performance. Looking for a compromise between high field quality and low surface impedance, we produced completely CC based REBCO-Cu hybrid structures whose dimensions are chosen in a way so that samples comply with the field quality target imposed by CERN. Two layouts were characterized, a ringed and a striped one.

To our knowledge as the first group, we disclose the surface resistance of these REBCO-Cu hybrid structures and in addition, compare them to the ones of pure Cu and REBCO samples, all measured with a dielectric resonator at 8 GHz, cryogenic temperatures and up to 9 T. We find a big difference in surface resistance between the two employed layouts. The striped REBCO-Cu configuration suffers as compared to the ring layout additional microwave losses associated to the longer surface current paths, when forced through the uneven height profile of different materials. These losses are denoted here as high-frequency contact resistances, due to the analogy in the DC regime. Its magnitudes are estimated with a simple, heuristic model to be similar to contact resistances found between CC joints measured with IV-curves. We identify tendencies, valid independent of the stripe or ring layout, for how alteration of hybrid structures affect its surface resistance: decreasing the REBCO content in the hybrid coatings renders the measured surface resistance, as someone would intuitively expect, more similar to the microwave response of pure copper, i.e. increasing the surface resistance but decreasing the magnetic field receptivity. With the 92 % REBCO sample in ring layout, outperforming pure Cu significantly while exhibiting only marginal trapped fields, we demonstrate the conceptual maturity of the hybrid coating technology to be used in the FCC-hh beam screen chamber.

In addition, we estimate the additional microwave losses expected from interruptions in the REBCO coating due to beam screen chamber segmentation. Calculated high-frequency contact resistances coincide quite well within our set of measurements. The impact of the additional losses on the beam stability have to be assessed by beam coupling impedance simulations.

For final considerations before usage in a high-energy particle accelerator, the entire surface impedance, both surface resistance and surface reactance, of REBCO-Cu hybrid structures has to be characterized at FCC-hh conditions, so at 1 GHz, around 50 K and up to 16 T, to exclude any unforeseen effects at altered frequencies and fields. Moreover, it has to be assessed what REBCO-Cu configurations are feasibly realizable at large scales. However, considering that the dipole component could be cancelled electronically within the FCC-hh, hybrid coatings with HTS segment widths of 2 mm or 4 mm could still comply with the field quality requirement. Since some manufacturer supply their CCs in the mentioned widths, it would allow a cost-efficient hybrid coating solution.

7.2 Surface treatments for low secondary electron yield

The build up of secondary electrons is a common barrier to overcome in designing high-energy particle accelerators. A secondary electron yield (SEY) of the beam screen material, defined as the number of secondary electrons emitted from one incident electron, well above unity is likely to generate electron clouds inside the chamber. The generation of electron clouds can be catastrophic for the stability of the proton beam. For this reason, among other challenges, we have to study the SEY of REBCO, a potential beam screen coating candidate. Seed electrons, for example photo-electrons generated from synchrotron radiation hitting the walls of the beam-screen chamber, can be slingshot by proton bunches back into the walls. In turn, these electrons will excite more electrons if the SEY of the wall (REBCO in our case) is high enough. This results in a positive feedback loop which produces a cascade effect [225]. These free electrons will be attracted by the proton bunches generating an electron cloud around the protons, highly disrupting the proton beam [218]. Other consequences of secondary electron multiplication are dynamic pressure rises and thermal load in cryogenic vacuum systems [226].

The SEY of REBCO CCs was measured in a customized SPECS UHV system (base pressure of 2×10^{-9} mbar) of the Technology Department - Vacuum, Surfaces and Coatings (TE-VSC) group at CERN which is based on the apparatus described in [227]. The SEY operational vacuum chamber consists of an electron gun (ELG-2/EGPS- 1022 from Kimball Physics) and a revolving sample holder. In standard measurements, the electron dose was estimated to be below 1×10^{-6} C/mm^2 on a 2 mm^2 area and assumed to have no surface conditioning effect. The SEY is determined by measuring the sample current in two consecutive steps. In the first step, the CC samples are positively biased (nominal 45 V). Primary electrons of variable energies E_{prim} between 100 and 1800 eV[1] impinge with normal incidence on the surface and are collected by the sample. It can be assumed that the sample current is the current of the primary electrons $I_{sample,1} = I_{pe}$. In the second step, the CC sample are negatively biased (nominal -45 V). All secondary electrons generated by the primary electron beam are forced to leave the sample. We define this sample current as the absorbed current $I_{sample,2} = I_{abs}$ and the amount of generated secondary electrons can be defined as $I_{se} = I_{pe} - I_{abs}$. With the above mentioned definitions, the SEY δ is determined by

$$\delta = \frac{I_{se}}{I_{pe}} = \frac{I_{pe} - I_{abs}}{I_{pe}}.$$

We chose two samples for SEY characterization, both of which are provided by SuperPower and were stripped off their stabilizing Ag and Cu layers, as they would be mounted in the beam screen chamber. Sample details are given in Table 7.5.

Sample name	Provider	History
Sample a	SuperPower	Stored in silica gel, cleaned in acetone
Sample b	SuperPower	Stored in alu foil, not cleaned

TABLE 7.5: Samples for SEY surface conditioning study.

7.2.1 SEY of pristine Coated Conductors

The SEY as a function of primary electron energies E_{prim} is given in Fig. 7.12. It should be noted that for sample a, δ is averaged over three different spots in the center of the sample, while for sample b, δ is averaged three times over the same sample spot in the sample center. In the as received state, the maximum SEY for sample a is $\delta_{max} = 2.95$ and for sample b $\delta_{max} = 2.81$. Both values surpass the maximum limit $\delta_{max}^{lim} = 1.0$, established for safe operation in

---

[1]In the context of particle accelerators especially the range between 0 and 1000 eV is of significance [10].
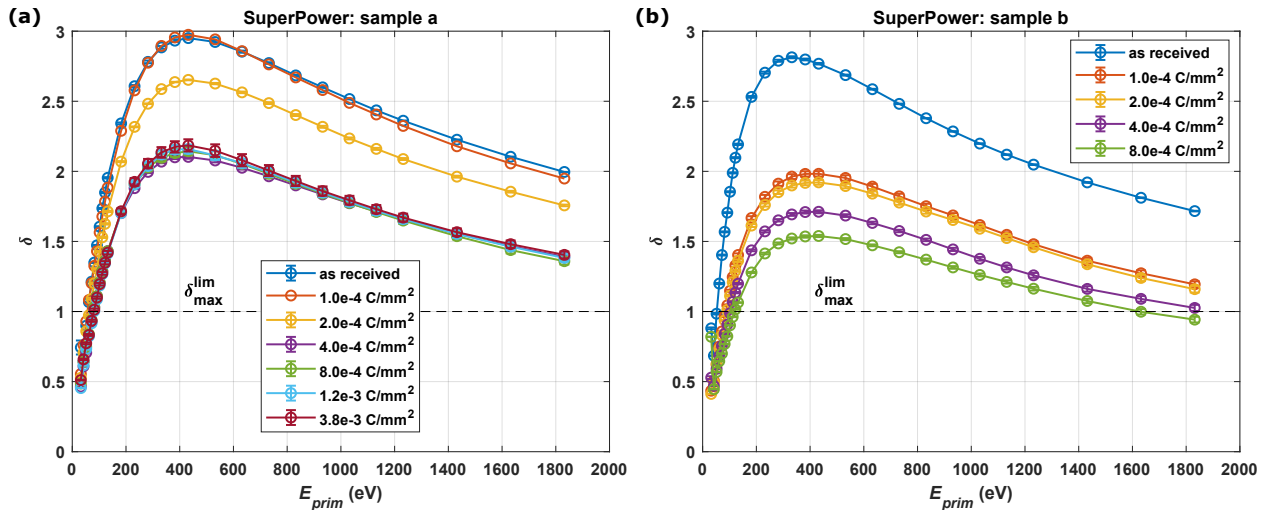
FIGURE 7.12: The SEY δ as a function of primary electron energies E_{prim} after several conditioning steps for **(a)** sample a and **(b)** sample b. The black dashed lines represent the SEY threshold $\delta_{max}^{lim} = 1.0$ for save operation in the FCC-hh.

the FCC-hh [9]), significantly. Over the past years, a number of surface treatments were tested in the beam pipes of several particle accelerators, some of which are surface conditioning, applying a thin coating with low SEY and chambers with grooves or slots [226]. In an attempt to enable compatibility with the e-cloud requirements of the FCC-hh, we engaged with the first two techniques.

7.2.2   Surface conditioning to decrease the SEY

In Fig. 7.12, we present the remeasured SEY of sample a and sample b after surface conditioning steps with increasing electron doses. Sample a shows constant suppression of the SEY for increasing doses until 8×10^{-4} C/mm^2 where it reaches in its maximum $\delta_{max} = 2.1$. Upon further increase of the dose, up to 3.8×10^{-3} C/mm^2, the δ_{max} saturates and no further suppression can be achieved.

For sample b, a more rapid and significant decrease of the SEY with increasing the conditioning dose is observed. The SEY could be decreased to $\delta_{max} = 1.54$ when conditioning the sample before measurement with a 8×10^{-4} C/mm^2 dose. The threshold of $\delta_{max}^{lim} = 1.0$ was not achieved here but the monotonous decrease of the SEY suggests that lower SEY values could potentially be realized upon increasing the dose. The dependence of δ_{max} with the conditioning dose for both samples is summarized in Fig. 7.13.

7.2.3   Thin a-C coatings to decrease the SEY

The second SEY mitigation strategy that was tried on REBCO coated conductors is the deposition of thin amorphous carbon (a-C) and titanium layers. For that, coated conductor samples were mounted onto a beam screen wall through which a short cylindrical magnetron sputtering source with a titanium and graphite target was pulled by cables, similarly as described in [223].

Either a thin layer of a-C was directly deposited on the HTS or a titanium interlayer was sputtered on the superconductor before depositing the a-C. The role of the Ti is the enhancement of the adhesion between superconductor and a-C. During the a-C deposition, Ti is also deposited simultaneously, in order to keep the hydrogen partial pressure low via the getter-pumping effect which guarantees low SEY of the a-C layer [228]. Important for low SEY is, moreover, a high roughness of the a-C layer in order to trap the secondary electrons which is achieved through low sputtering rates.
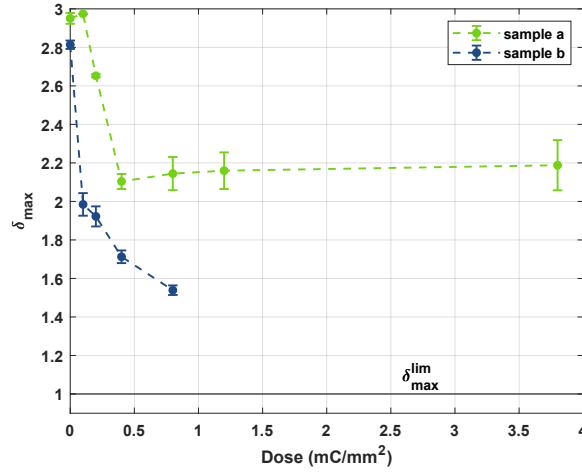
FIGURE 7.13: The SEY maximum δ_{max} as a function of conditioning dose for sample a and sample b. The black line represents the maximum allowed SEY $\delta_{max}^{lim} = 1.0$ in the FCC-hh.

The exact a-C deposition conditions are given in Table 7.6. It is noteworthy that a-C coatings have been already used in large scale applications. They were extensively validated and applied to the Super Proton Synchrotron accelerator [223].

Layer	Vacuum pressure	Sputter gas	Power	Voltage	Current	Sputter rate
a-C	1×10^{-6} mbar to 2.4×10^{-5} mbar	Ar	20 W	342 V	0.06 A	0.5 nm

TABLE 7.6: Sputter conditions for the a-C layer.

Several sputter depositions were run resulting in different SEY coatings for CCs provided by SuperPower and Bruker. The chosen film thicknesses had to account for a compromise between low SEY and small surface resistance R_s. The processed samples with their corresponding coating thicknesses are listed in Table 7.7. After deposition of the a-C films, the samples were wrapped in aluminum foil, a measure to prevent oxidation. The effect of the a-C coatings

Provider	Ti thickness	a-C thickness
SuperPower	-	50 nm
SuperPower	100 nm	50 nm
SuperPower	150 nm	100 nm
Bruker	150 nm	100 nm

TABLE 7.7: List of coated conductor samples that were coated with Ti and a-C films in order to decrease the SEY.

on the SEY is presented in Fig. 7.14. It is clearly appreciable how thin layers of a-C can decrease the SEY over the entire primary electron energy range. For 50 nm a-C layers, the maximum SEY δ_{max} is between 1 and 1.25 for the SuperPower sample, while for thicker a-C films (100 nm), the $\delta_{max} < 1$ for SuperPower and Bruker CCs. In the case of 100 nm thick a-C coatings, the maximum SEY is reduced below the acceptable threshold of the FCC-hh.

The damage of the sputter deposition on the superconductive properties is assessed from magnetization measurements using Bean's critical state model. We present the critical current density J_c as a function of magnetic field at $T = 77$ K of a CC before and after coating with a-C and a-C plus Ti in Fig. 7.15. Within the uncertainties, no deterioration of $J_c(H)$ is observed, neither for SuperPower nor Bruker coated conductors.
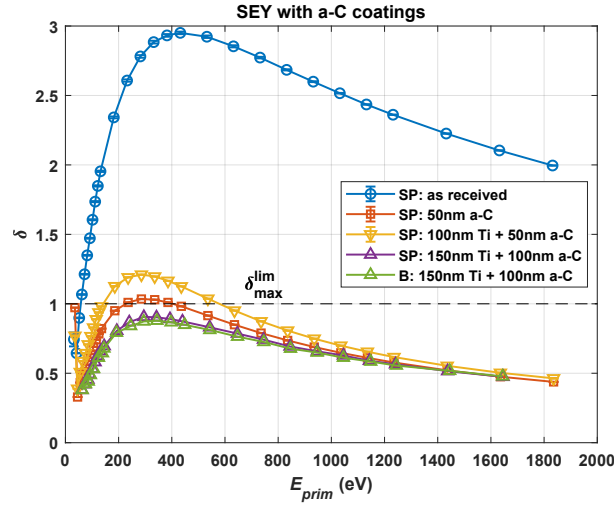
FIGURE 7.14: The SEY δ as a function of primary electron energies E_{prim} for CCs covered with thin layers of thin titanium and/or a-C layers. The black dashed lines represent the SEY threshold $\delta_{max}^{lim} = 1.0$ for save operation in the FCC-hh.

In addition, we measured the magnetization versus temperature in zero-field cooling conditions of mentioned samples. Fig. 7.16 displays the sample magnetization normalized by the magnetization at 50 K as a function of temperature. From this, we determined the critical temperature T_c, defined here as the onset of magnetization, and the superconducting transition width $\Delta T_C = T(\mu = 0.9 \cdot \mu_0) - T(\mu = 0.1 \cdot \mu_0)$.

With an estimated error of $\sigma_T = 0.3$ K on the determination of temperature values, the change in T_c and ΔT_c after sputter depositing thin layers of Ti and a-C are small. Tendentially, an increase of T_c upon sputter manipulation is discerned, while no consistent one-sided change in ΔT_c. Both observations point towards the assumption that variations in T_c and ΔT_c stem more likely from production dependent inhomogeneities in CCs than from sputtering induced deteriorations.

Finally, we characterized the surface resistance of the discussed multi-layer systems with a dielectric resonator. The surface resistance R_s as a function of temperature, measured in zero-field cooling, with resonant frequency $\nu_0 \approx 8$ GHz for uncoated, a-C and Ti plus a-C covered CCs in comparison with FCC Cu R_s is provided in Fig. 7.17. An almost temperature independent increment in R_s is observed for samples with e-cloud preventing coatings below T_c, when the superconducting state is reached. The surface resistance increase amounts $4\% \cdot R_s^{Cu}(50\,\text{K})$ and $11\% \cdot R_s^{Cu}(50\,\text{K})$ for 150 nm Ti + 100 nm a-C coated SuperPower and 150 nm Ti + 100 nm a-C coated Bruker, respectively. The explicit experimentally recorded increment

$$\Delta R_s^{\text{exp}} = R_s^{\text{coated,exp.}} - R_s^{\text{uncoated,exp.}}$$

at $T = 50$ K is given in table 7.8 for all coated samples.

Similarly to the calculation of the effective surface resistance of a layered structure like a CC, we can compute the theoretically expected surface resistance of a CC covered with thin layers of Ti and a-C $R_s^{\text{coated,theo.}}$ according to eq. (5.1). Important parameters for the estimations of the surface resistance of Ti and a-C are their electrical resistivities that are chosen to be $\rho_{\text{Ti}}(50\,\text{K}) = 4 \times 10^{-8}\,\Omega\text{m}$ [229] and $\rho_{\text{a-C}}(50\,\text{K}) = 3.9 \times 10^{-5}\,\Omega\text{m}$ [230], respectively. This results in the following skin depths: $\delta_{\text{Ti}}(50\,\text{K}) \approx 1.1\,\mu\text{m}$ and $\delta_{\text{a-C}}(50\,\text{K}) \approx 35\,\mu\text{m}$. With that we can compute $R_s^{\text{coated,theo.}}$ and hence also the expected rise in surface resistance

$$\Delta R_s^{\text{theo.}} = R_s^{\text{coated,theo.}} - R_s^{\text{uncoated,exp.}},$$
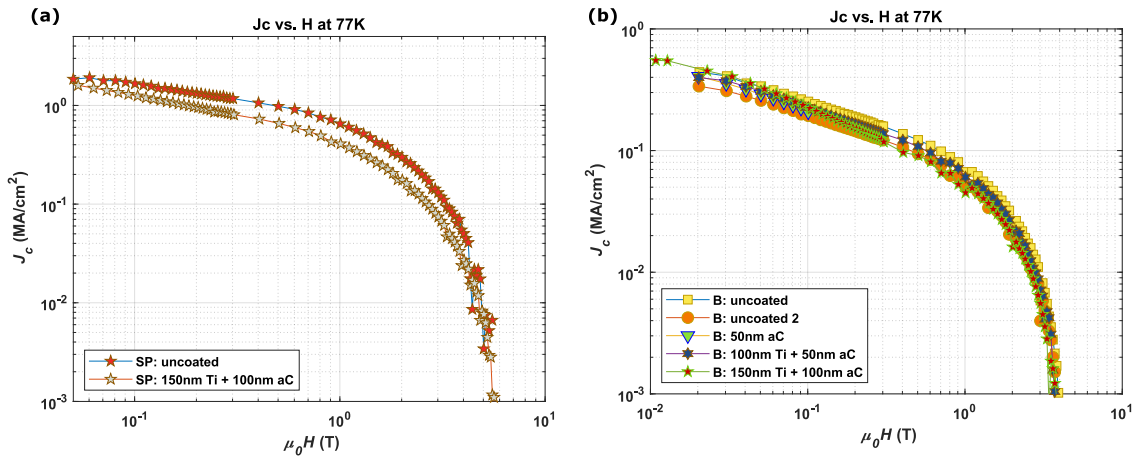
(a)

(b)

FIGURE 7.15: The critical current density J_c as a function of magnetic field at $T = 77\,\text{K}$ for **(a)** a-C covered SuperPower and **(b)** a-C covered Bruker samples in comparison with the corresponding uncoated counterparts.

(a)

(b)

FIGURE 7.16: The critical current density J_c as a function of magnetic field at $T = 77\,\text{K}$ for **(a)** a-C covered SuperPower and **(b)** a-C covered Bruker samples in comparison with the corresponding uncoated counterparts.

given at $50\,\text{K}$ in table 7.8. From the calculated values it becomes clear that a-C is almost transparent in terms of microwave response and that the Ti layer is governing the increase in the surface resistance. The mismatch between recorded and estimated ΔR_s is reasonable and can be explained by differences in titanium purity and thus its resistivity between deposited titanium and assumed Ti (Ti with $RRR = 30$). We reiterate that the microwave performance below T_c of Ti+a-C covered CCs is favorable as compared to FCC Cu, albeit the additional increase in R_s. Below the critical temperature, Bruker samples exhibit a surface resistance of several $\text{m}\Omega$ smaller than FCC Cu, while SuperPower samples undercut Cu by approximately one order of magnitude in surface resistance.

We present the in-field behavior of a-C coated samples at $50\,\text{K}$ in Fig. 7.18. Even in the worst case, at maximum applied field of $9\,\text{T}$, the superconducting samples cause less losses than Cu. The fully coated ($150\,\text{nm}$ Ti + $100\,\text{nm}$ a-C) Bruker and SuperPower samples have a by approx. $4\,\text{m}\Omega$ and $5\,\text{m}\Omega$, respectively, lower surface resistance than the metal. This equates to a performance gain of $50\,\%$ for Bruker and $63\,\%$ for SuperPower with respect to copper. Analogously to Fig. 7.17, the increase of surface resistance upon coating $\Delta R_s^{\text{exp.}}$ manifests itself as a constant over the entire field range. We can conclude that neither titanium's nor amorphous carbon's magnetic properties influence
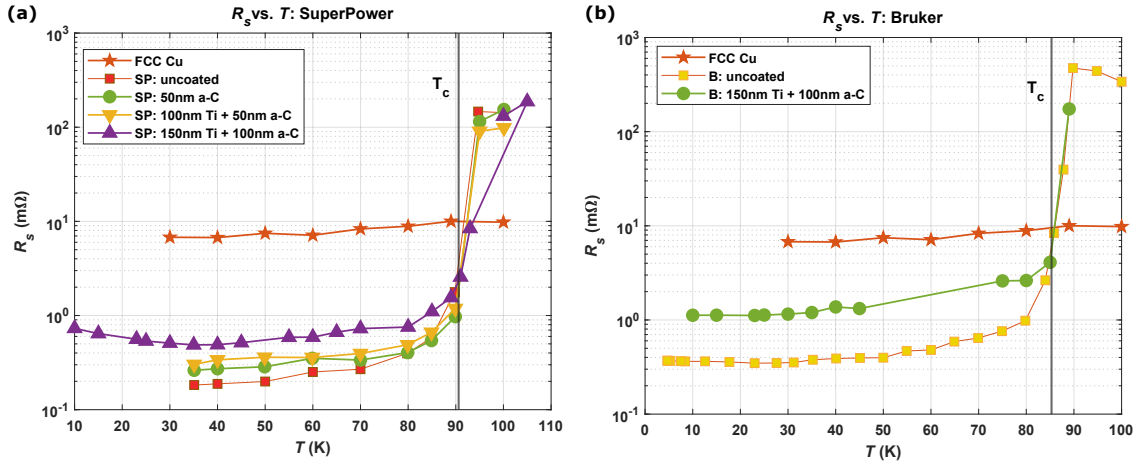
FIGURE 7.17: The surface resistance R_s as a function of temperature, without applied field, at 8 GHz, for **(a)** a-C covered SuperPower and **(b)** a-C covered Bruker samples in c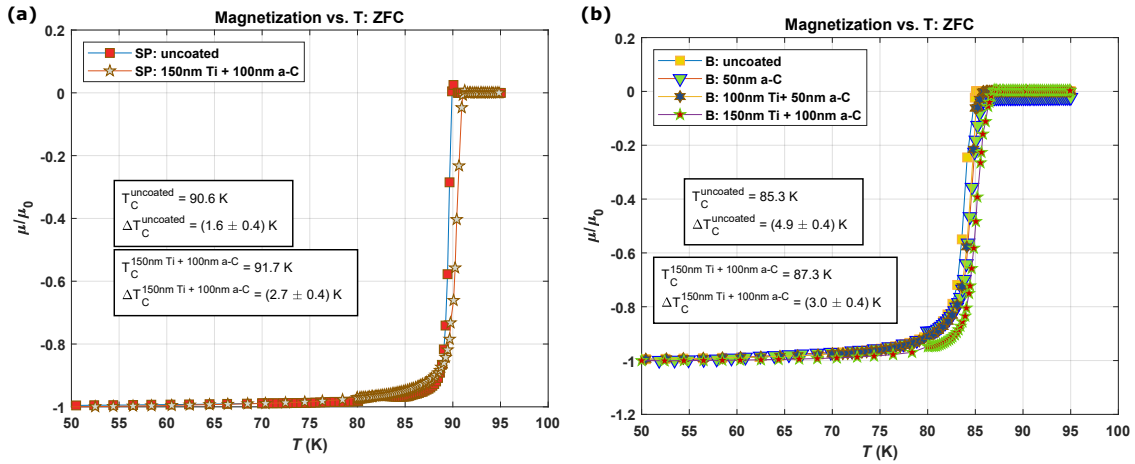omparison with the corresponding uncoated counterparts and FCC Cu. The critical temperature T_c determined from Fig. 7.16 is marked as a vertical line for both CCs.

Provider	Coating	$\Delta R_s^{\text{exp.}}(50\,\text{K})$	$\Delta R_s^{\text{theo.}}(50\,\text{K})$
SuperPower	50 nm a-C	0.09 mΩ	$1.4 \times 10^{-7}\,\Omega$
SuperPower	100 nm Ti + 50 nm a-C	0.16 mΩ	0.4 mΩ
SuperPower	150 nm Ti + 100 nm a-C	0.32 mΩ	0.7 mΩ
Bruker	150 nm Ti + 100 nm a-C	0.92 mΩ	0.7 mΩ

TABLE 7.8: A list of CC samples with e-cloud reducing coatings and its experimentally measured and theoretically calculated increase in surface resistance as compared to pristine CCs.

the measurement to a noticeable degree. The longevity of the thin Ti + a-C coatings in terms of $R_s(H)$ was tested as
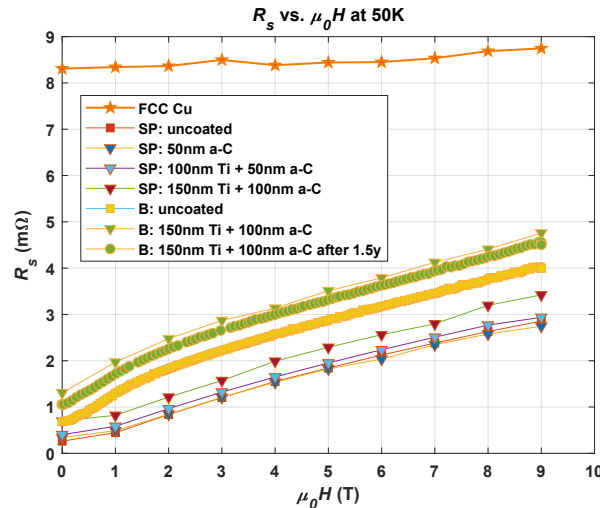
FIGURE 7.18: The surface resistance R_s as a function of applied magnetic field for a-C covered CC samples in comparison with the corresponding uncoated counterparts and FCC Cu at 8 GHz and 50 K

shown in Fig. 7.18. Storing the 150 nm Ti + 100 nm a-C coated Bruker sample for 1.5 y in silica gel, we repeated the R_s field sweep at 50 K and observed close to perfect reproducibility, suggesting no degradation of any of the involved layers.

7.2.4 Section conclusions

We have found that REBCO CCs show in their untreated state a too high SEY in order be used safely in the beam screen chamber of a particle accelerator. Possible cures for the e-cloud generations are conditioning of the sample surface with high-energy electrons or depositing an amorphous carbon coating on it.

The second means is especially promising as it is proven for large scale deposition and shows that an a-C layer as thin as $100\,\mathrm{nm}$ is enough to bring down the SEY to required levels. Titanium before a-C deposition acts as an hydrogen getter in the sputter chamber and an adhesion layer between carbon and HTS. We demonstrated that the applied sputter conditions do not deteriorate the superconducting properties of the CCs. Moreover, we show that thin layers of a-C have a negligible impact on measured surface resistance, whereas thin titanium layers cause a small increase. The contributions are found to be constant over the analyzed temperature and magnetic field range. In particular, a $150\,\mathrm{nm}$ Ti + $100\,\mathrm{nm}$ a-C coating that suppresses the SEY below the necessary threshold, increases the surface resistance by $R_s^{exp.}(50\,\mathrm{K}) = 0.32 - 0.92\,\mathrm{m\Omega}$ as compared to an uncovered CC. This increase equates $4 - 11\,\%$ of copper's surface resistance at $50\,\mathrm{K}$ and lets CCs outperfrom copper in the entire field range.

In conclusion, a-C is an utmost suitable coating candidate for CCs in order to enable compatibility of the HTS technology with particle accelerators like the FCC-hh since it decreases the SEY to required levels while causing only few additional microwave losses.

7.3 Impact of synchrotron irradiation on superconducting properties

Synchrotron radiation (SR) is understood as the emitted electromagnetic radiation of charged particles moving uniformly on a circular path [231]. In circular particle colliders, it is mainly generated when accelerated charged particles enter a magnetic dipole field where they get deflected by Lorentz force. For high-energy particles, relativistic effects become relevant and the SR is emitted forwardly as a collimated beam [232]. The spectrum of SR emission depends on the beam energy and the intensity of the particle deflecting magnetic field. With the unprecedented 50 TeV beam energy and 16 T bending magnets, the FCC-hh's SR linear power density is expected to be 160 times larger than in the LHC.

The detrimental effects of SR hitting the highly conductive beam screen coating were considered and tried to be mitigated by the new double chamber design of the FCC-hh beam screen. In full beam energy operation, most of the SR will exit trough the 7.5 mm aperture of the primary chamber where it hits the sawtooth Cu profile of the secondary chamber as seen in Fig. 1.2. Nevertheless, the potential HTS beam screen coating cannot be completely spared from synchrotron irradiation: at the sawtooth Cu, the majority of SR will be absorbed but a few can get reflected back into the primary chamber. In addition, low power tails of the SR will still touch the primary chamber. At last, during beam injection at 3.3 TeV, vertical beam alignment rises to 4 mm for short time causing SR to hit the interior of the primary chamber [10].

Two main concerns arise. On the one hand, SR causes heating which could potentially result into oxygen diffusion in the superconductor or quench-driving, local hot spots. On the other hand, high-energy photons can interact with superconducting charge carrier by breaking the cooper pairs. If the breaking rate surpasses the recombination rate of the cooper pairs, superconductivity will break down.
As a preliminary study, we analyzed possible long-term deterioration of the superconductor by irradiating CCs of several providers with high-energy SR of low intensity performed at ALBA Synchrotron Light Source.

7.3.1 Long term irradiation at ALBA Synchrotron

As shown in Fig. 7.19, the photon flux spectrum at the ALBA Synchrotron Light Source is in terms of energy spectrum quite comparable to the one expected at the FCC-hh. For the long term irradiation experiment, we tested the effect of
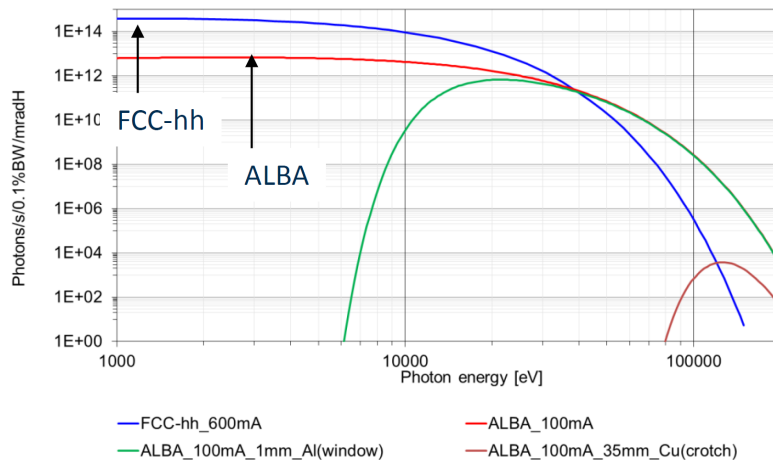

FIGURE 7.19: Photon flux vertically integrated per second, 0.1 % BW and mrad(H) spectra of the FCC-hh in comparison with the full and attenuated ones of ALBA Synchrotron Light Source. Adapted from [233] with permission.

the high-energy spectrum tail on the superconductor. Five different HTS-CC samples were mounted behind the ALBA crotch absorbers and irradiated by the high-energy residual X-rays that traverse the 35 mm copper absorber and 2 mm steel anti-chamber wall. The CCs were aligned in such way that the synchrotron beam passes through the entire sample cross section as it is demonstrated in Fig. 7.20. By making use of the normal operation of the Light Source for user, the irradiation time was in the order of several days and weeks. Table 7.9 summarizes the used irradiation parameters. The dose estimation was done internally at ALBA Synchrotron with the Monte Carlo simulation package FLUKA [233].
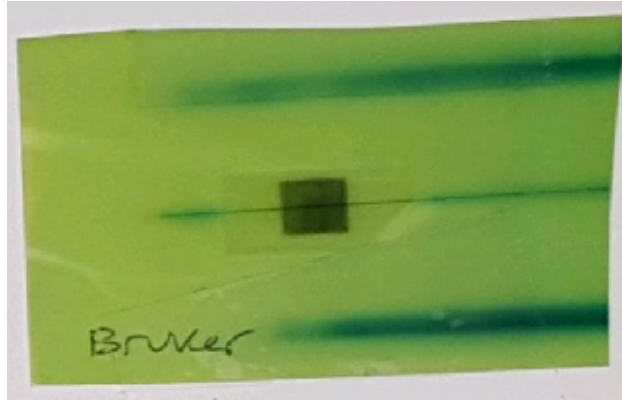
FIGURE 7.20: Irradiated $5\,\text{mm} \times 5\,\text{mm}$ Bruker sample attached to X-Ray sensitive paper. The synchrotron beam passes through the sample center.

SR current	Attenuator	Irradiation time		Photons at sample	
100 mA	Crotch absorber (35 mm Cu)	144 h	552 h	4.96e14	4.10e18

TABLE 7.9: Irradiation parameters used for experiment.

After irradiating the samples for 144 h and 552 h resulting in a deposition of 4.96e14 and 4.10e18 photons, respectively, we re-measured the magnetic moments. By way of example, the critical current density as a function of magnetic field $J_c(H)$ at 77 K, calculated from magnetization measurements, and the normalized magnetic moment recorded after zero-field cooling μ/μ_0 of SUNAM CCs is compared before and after irradiation in Fig. 7.21. The
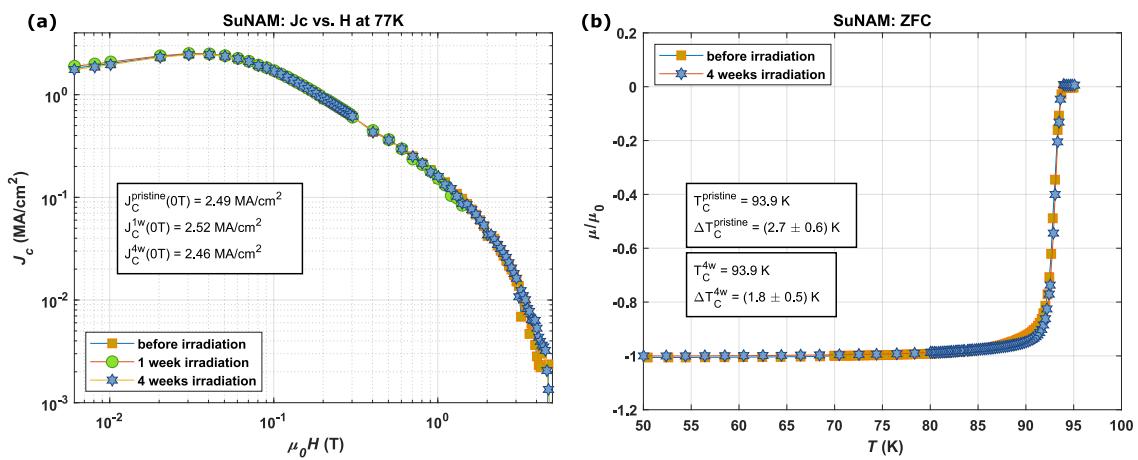
FIGURE 7.21: Effect of long term high-energy, low-intensity SR on the superconductive properties of SuNAM CC.**(a)** The critical current density as a function of magnetic field at 77 K of SUNAM CC before and after irradiation. **(b)** The magnetic moment after ZFC of the mentioned samples.

$J_c(H)$ curves collapse excellently on each other, suggesting that neither the photons, nor the exposure to air had any detrimental impact on the superconducting properties. The same picture is painted for the ZFC measurement. Within the measurement accuracy error, we find the same T_c and ΔT_c for the samples before and after SR exposure. The superconductive properties of all analyzed CCs stay unaffected after the high-energy, low-intensity SR irradiation for several weeks as shown in Fig. 7.22, where the critical current density at self-field J_c^{sf} before and after the experiment is given. Accounting for uncertainties in the determination of J_c^{sf}, within an estimated error of 5 %, no difference in
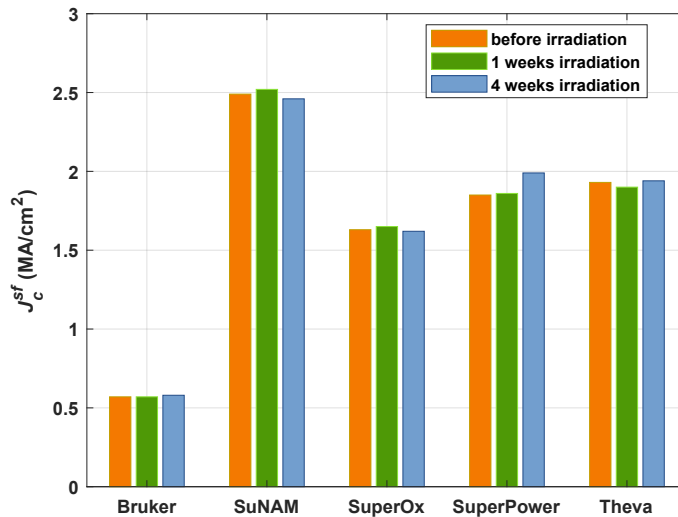
FIGURE 7.22: The critical current density at self-field J_c^{sf} at $T = 77\,\mathrm{K}$ before and after irradiation with SR for several CCs.

the magnetizing properties after SR irradiation can be reported.

7.3.2 Section conclusions

In order to assess possible long term damage on superconductors by SR, we irradiated several state of the art CCs for several hundred hours with an attenuated high-energy spectrum emitted in the ALBA Synchrotron Light Source. By comparing the superconducting properties of the samples before and after irradiation, we have demonstrated that all CCs stay unaffected in terms of their critical temperature T_c, their transition width ΔT_c and $J_c(H)$ up to $9\,\mathrm{T}$ at $T = 77\,\mathrm{K}$. Further work regarding the effect of synchrotron radiation on CCs' superconductivity was performed within our consortium under the lead of ALBA Synchrotron. Critical temperature and surface resistance were measured in-situ while being exposed to synchrotron radiation of a wider spectrum and higher photon intensity. The results are presented in [234] and discussed in the doctoral thesis of Patrick Krkotić.

7.4 Chapter conclusions

In this chapter, we addressed three major concerns associated with the usage of REBCO CCs as a beam screen coating.

1. **Persistent currents in the REBCO will degrade the magnetic field homogeneity inside the beam screen, endangering the trajectory stability of accelerated particles:** We analyzed a REBCO CCs based REBCO-Cu hybrid structure consisting of superconductor and copper filaments as a method to decrease the screening currents. By means of finite element simulations, we determined the exact REBCO and Cu filament widths,

in order to comply with the field quality requirements imposed by CERN and used them as guidelines for the dimensions of produced hybrid structures. Scanning Hall probe microscopy of hybrid structures attested excellent agreement with sample magnetizations predicted by finite element simulations, see [217]. Performing high-frequency characterization of hybrid structures in ring configuration, this layout was shown to be necessary to conduct electrical currents parallel to the material just like it will be done in the FCC-hh. Measurements with a 8 GHz DR illustrated that surface resistance depends significantly on the amount of REBCO present in the hybrid structure. We showed experimentally that a hybrid structure with 92 % REBCO exhibits extremely low surface resistances, comparable to a pristine REBCO sample, while satisfying field quality requirements. This sample represents a very profitable trade off between two competing attributes, low surface resistance and small persistent currents, and could serve as a geometry assembly blueprint for a REBCO-Cu hybrid coating in the FCC-hh beam screen chamber.

2. **A beam screen coating material with secondary electron yield above unity will generate electron clouds, disturbing the beam stability:** In collaboration with the TE-VSC group at CERN, we demonstrated that untreated REBCO CCs exhibit too high SEY, depending on the provider between 2.7 and 3.0, to be savely used in the beam pipe chamber. Coatings of 150 nm titanium plus 100 nm amorphous carbon on top of REBCO CCs were shown to decrease the SEY below the required level for CCs of two different providers. The compatibility of this Ti + a-C coating with REBCO CCs was validated by two means. On the one hand, sputter depositing the coating did not deteriorate the superconducting properties of REBCO. On the other hand, capping the REBCO layer with the low SEY coating increased the surface resistance only marginally. In particular, a 150 nm Ti + 100 nm a-C coating increased, independent of temperature and magnetic field, the surface resistance by $R_s^{exp.}(50\,\text{K}) = 0.32 - 0.92\,\text{m}\Omega$ with respect to an uncovered CC. This increase equates $4 - 11\,\%$ of copper's surface resistance at 50 K. In absolute terms this means that REBCO CCs capped with low SEY coatings outperform copper by a factor of 1.8-2.5 (depending on the provider and purity of Ti) at 50 K and 9 T. In conclusion, we experimentally verified the compatibility of the low SEY material a-C with REBCO CCs. Applied in the beam screen chamber, it would prevent electron cloud generation without sacrificing the microwave performance sharply.

3. **Interaction of beam emitted synchrotron radiation with REBCO could have detrimental effects on superconducting properties:** As a joint effort with ALBA Synchrotron Light Source, we analyzed the long term irradiation effect of attenuated high-energy photons on several REBCO CCs. The HTS were exposed for several hundred hours to mentioned synchrotron radiation at the ALBA Synchrotron Light Source, whereupon the samples were characterized in terms of their superconducting properties and compared to the state before irradiation. Within our analysis, we found unchanged properties. In particular, there was no effect on the critical temperature T_c, the transition width ΔT_c or the critical current density up to 9 T at 77 K. While this experiment excludes long term irradiation damages from attenuated high-energy synchrotron radiation as a show stopper, this study needs to be extended. A broader synchrotron energy range, closer to the one expected at the FCC-hh, has to be tested with REBCO CCs in terms of long term irradiation deterioration. More key experiments involve the measurement of superconducting and microwave properties during synchrotron irradiation. Preliminary studies addressing this point were already conducted by ALBA Synchrotron and will be disclosed in the future.

Chapter 8

General conclusions

Motivated by a key question the FCC-study wants to address, this work explores the advantages, potential risks and general feasibility of employing $REBa_2Cu_3O_{7-\delta}$ coated conductors (REBCO CCs), a tape structure based on a high temperature superconductor (HTS), as a beam screen coating for the next generation particle accelerator planned by CERN. The Institute of Materials Science of Barcelona has established a collaboration agreement with six international manufacturer, namely Bruker, SuNAM, SuperOx, SuperPower and Theva, that offered us their large scale produced REBCO CCs for superconducting properties and high-frequency characterization.

Laying the foundation of the study, we analyzed the architecture and electrical properties of all REBCO CCs. Not only vary the different HTS tapes in the thicknesses of the REBCO layers ranging from 0.9 μm to 3 μm but also in the REBCO microstructure whose complexity is constituted by for example, the choice of rare earth element, the incorporation of normal conducting nanoparticles or the growth technique. All these attributes impact the defect landscape in REBCO and consequently its electrical properties. Based on resistance as a function of temperature measurements, we found a spread in critical temperature T_c and normal state resistivity ρ_n among the CCs. Former originates from the doping state and utilized rare-earth element, while latter is tied to the doping state, too, and disorder in the REBCO matrix. By application of several magnetic fields to mentioned experiments, we were able to estimate the irreversibility fields $H_{irr}(T)$, a critical quantity that informs about the upper limit of in-field operation. At 50 K, the expected beam screen chamber temperature within the FCC-hh, REBCO CCs exhibit an irreversibility field between 38 T to 53 T, where two tendencies for larger irreversibility fields were identified. One is the incorporation of artificial pinning centers (APCs), BZO or BHO nanorods, and the other, the use of yttrium as rare earth element. The estimated H_{irr} agree with previously reported values, confirming a sustained superconducting state at expected maximum fields of 16 T in the FCC-hh.

Moreover, we performed magnetization measurements of CC samples in wide cryogenic range around 50 K and up to 9 T in order to extract the critical current densities $J_c(T,H)$. With a model that accounts for changing pinning regimes upon magnetic field increase, we extracted characteristic pinning parameters J_{sf}, H^* and α. The determined quantities vary in their magnitudes with the differences in the REBCO microstructures of analyzed tapes. An important observation for the FCC-hh study is that APC based CC exhibit weakest in-field dependence, indicating efficient pinning, at intermediate temperatures close to 50 K, as visible in their low α. Nevertheless, the total $J_c(50\,K, 9\,T)$ is not necessary lower for CCs that rely only on intrinsic pinning centers as represented by Fujikura, since the total performance draws from all mentioned parameters J_{sf}, H^*, H_{irr} whose entanglement with the microstructure is complex and requires further study.

With the aid of mentioned phenomenological pinning model, we extrapolated the critical current densities to fields up to 16 T, unattainable by our present magnet. CCs associated with 'classical' REBCO microstructures, i.e. no 1D nanorods or inclined c-axis, allow for quite decent model approximation of measurement data up to 9 T and gives J_c at 16 T which are credible since backed by accordance with reported values. Extrapolated results demonstrate that the

best performing CCs of our study will sustain the peak image currents of 25 A induced by proton acceleration when assembled in the beam screen pipe of the FCC-hh. They trump the FCC-hh threshold of $I_c/width(50\,\mathrm{K}, 16\,\mathrm{T}) = 3\,\mathrm{Acm}^{-1}$, a value that calculates from dividing the 25 A peak image currents by the circumference of the beam screen chamber, by more than one order of magnitude. The generated data attests the suitability of nowadays produced REBCO CCs for applications that require high-performing direct current properties at conditions as demanding as found in the FCC-hh.

Next, we move the discussion to the high-frequency characterization of the HTS samples. After the successful design and fabrication of a rutile loaded dielectric resonator (DR) with resonant frequency close to 8 GHz by ALBA Synchrotron and Polytechnic University of Catalonia (UPC), we collaboratively installed the DR in a 25 mm magnet bore of a Physical Property Measurement System (PPMS) for high-frequency response investigation of REBCO CCs at cryogenic temperatures and large magnetic fields up to 9 T. This allowed us to run a two-fold comparative microwave study.

For one thing, we measured the surface impedance, both the real (surface resistance) and imaginary (surface reactance) part, of eight thick REBCO CCs at cryogenic temperatures around 50 K, 8 GHz and large magnetic fields up to 9 T. High-frequency data of commercially available REBCO CCs at large magnetic fields was not available in literature at this point, marking it an important contribution to microwave applications which considers the use of this technology. We demonstrated that good pinning capabilities of the REBCO layer is the dominant factor that yields low surface impedances at high magnetic fields in presented experimental conditions. In consequence, analyzed REBCO CCs differ in high field performance as they are founded by microstructures with unique defect landscapes. Understanding this correlation opens the door to improvement of material's high-frequency properties through microstructure tailoring. Surface impedance data in the context of a mean-field vortex motion model unveils explicit relations between tuneable material properties and the two most relevant pinning parameters for high-frequency applications: depinning frequency ν_p and vortex viscosity η. The depinning frequency can be increased by the addition of APCs or the manifestation of additional intrinsic pinning defects as it is proportional to the critical current density. Whereas, the vortex viscosity augments with lower normal state resistivity ρ_n and higher upper critical field B_{c2}. The increase of both pinning parameters gives material scientists a leverage point to further optimize the performance of REBCO CCs at high frequencies and large magnetic fields. Regardless of future performance optimization, the determined pinning parameters attest already available REBCO CCs excellent microwave performance at large magnetic fields. The depinning frequencies amount depending on the sample $\nu_p(50\,\mathrm{K}) \approx 14 - 33\,\mathrm{GHz}$ and surpass the operational frequency in the FCC-hh significantly, thus reinforcing the use of REBCO in the beam screen chamber. The vortex viscosity $\eta(50\,\mathrm{K}, 9\,\mathrm{T}) \sim 5 \cdot 10^{-7}$ is higher than the vortex viscosity of Nb_3Sn or MgB_2 at 10 K and 9 T which equates to smallest microwave losses at large magnetic fields among all technologically relevant superconductors.

The correct measurement of the surface reactance in thick REBCO CCs deserves a special technical mention. The extremely strong magnetic forces within the superconducting layer cause the end plates of measurement cavity to shift when exposing to magnetic fields which only marginally affects the measured quality factor but significantly the resonant frequency. As a consequence, extracted field change of surface reactance is masked by this effect and does not represent the intrinsic HTS response. We modified the resonator to avoid the mechanical shifts and were able to obtain reliable surface reactance results.

For another thing, we confronted copper, the habitual beam screen coating, with the mature HTS technology in terms of surface impedance at conditions close to the accelerator environment. Copper gets outperformed by best performing CCs by a factor of roughly 2.5 (top surface) and 4.5 (bottom surface) at 50 K, 8 GHz and 9 T in terms of surface resistance, while the surface reactance of copper is significantly lower, more than by a factor 3, than the best performing CC at the same conditions. Within our study, however, the real competition takes place at lower

frequencies and higher fields, namely at 1 GHz and 16 T, the conditions present in the FCC-hh. Although we do not have the corresponding setup available yet (it is in construction) to measure the surface impedances in mentioned regime, we have extrapolated surface impedances to values expected in this situation using the vortex movement mean-field model. The performance advantage tilts further towards REBCO CCs as they expect to exhibit surface resistances by a factor of 15-70 (factor depends on the provider) lower than copper while maintaining their surface reactance in the same order of magnitude at 50 K, 1 GHz and 16 T. Realized in practice, it would mean significant benefits in terms of beam stability margins and resistive power losses but possibly a lesser maximum beam current limitation within the FCC. Disregarding potential improvement of high-frequency performance through microstructure tuning, the REBCO CCs tapes present themselves already in its current form as a mature candidate for high-frequency applications at large fields because of its low surface resistances unmet by competitors.

Practical challenges bother the wide spread usage of REBCO as a coating material for the beam screen chamber or, more generally, microwave cavities. The HTS material class requires epitaxial growth, so highly textured substrates, for useful superconducting properties to emerge. Having this in mind, a reasonable doubt that arises is how this material could coat metallic and curved surfaces. Instead of direct growth on the metallic surface, we proposed a scalable REBCO CC attachment technique which is based on upside down soldering and subsequent delamination of the tape between buffer layers and REBCO. Following this recipe, our technique exposes the bottom surface of REBCO, the first layers formed during growth, to the interior of the cavity. We demonstrated that the breaking of the multilayered architecture does not induce damage in the center of the superconducting sample. Moreover, scanning electron microscopy analysis was carried out to analyze the topography of exposed bottom surface. It showed, on the one hand, that parts of buffer layers remain after the delamination process on the superconductor and on the other hand, that the bottom REBCO layer is purer in comparison to its top surface where usually misaligned grains or secondary phases are found. High-frequency characterization of delaminated REBCO bottom surfaces revealed superior surface resistances as compared to its top surface counterpart. Reminding ourselves that the vortex penetration depth reaches only up to approximately 650 nm at 8 GHz and 50 K, different REBCO volumes are probed when measuring the surface impedance of either top or bottom surface. Hence, we associate the improved performance to a microstructure quality gradient in the REBCO film which decreases from the first formed layers at the buffer interface towards the last grown layers. This phenomenon is well known in the HTS community as it limits the growth of arbitrarily thick films with good properties.

We elucidated the role of LMO buffer layer, parts of which remain on the REBCO surface after delamination, in surface impedance measurements. It influences the field behavior at small magnetic field thus it is not of big relevance for the FCC-hh.

The benefits of the proposed coating technique like the reliance on already established REBCO CCs or the simplicity and scalability of attachment led to a collaboration with the RADES group in CERN with the aim to coat a haloscope with REBCO CCs for axion search. A first test coating yielded higher cavity quality factors than achieved by Cu or Nb_3Sn at 4.2 K and 11 T. Thanks to additional studies, we expect significantly higher cavity quality factors with the second coating trial.

The collaboration with the RADES group aside, our proposed coating blueprint could facilitate the penetration of CCs into other microwave applications where large magnetic fields are required, one of which is certainly the beam screen chamber in the FCC-hh.

Finally, we addressed an array of concerns associated with CC usage in the beam screen chamber. All our related experimental studies show compatibility of REBCO CC technology with the beam screen.

First, trapped vortices are expected to perturb the dipole field which steers the particle beam. As a first group, we

produced a completely CC based REBCO-Cu hybrid structure that consists of narrow HTS and Cu filaments. The striation strategy was demonstrated to diminish the trapped fields inside the REBCO meaningfully. In fact, the geometry for produced REBCO-Cu hybrid structures was directed by a numerical analysis model[1] in a way to keep the field disturbance caused by the trapped fields below a specific field quality threshold imposed by CERN. The high-frequency response of manufactured hybrid structures was measured with the 8 GHz DR in a wide cryogenic temperature range around 50 K and up to 9 T. We found that the percentage of HTS present in the hybrid structure drives measured surface resistance. The hybrid structure consisting of 92 % REBCO and 8 % Cu outperformed a pure Cu coating significantly, while exhibiting only marginal trapped fields because of the striation into filaments. This represents an experimental confirmation that REBCO CCs can be engineered into a coating that has an negligible impact on the magnetic field profile while maintaining the desired low surface resistance.

Second, the secondary electron build-up is a common problem to overcome in high-energy particle accelerators. The likelihood for electron cloud generation depends on the surface state of beam facing material, in our case REBCO, and is expressed numerically in the so-called secondary electron yield (SEY). A SEY well above unity leads to electron multiplication inside the beam screen chamber that can have catastrophic consequences for the beam stability. In collaboration with the Technology Department - Vacuum, Surfaces and Coatings (TE-VSC) group at CERN, we measured the peak SEY to range between 2.5 and 3 in two untreated CCs samples by SuperPower. Thus, a goal had to be the reduction of the SEY. Apart from conditioning the sample surface with an electron gun, another method to terminate seconday electrons is the application of a thin film consisting of a material with low intrinsic SEY. In the particle accelerator community, amorphous carbon (a-C) has proven itself as a suitable coating candidate because of its high roughness that prevents electrons from leaving the surface and its convenient large scale deposition. Consequently, REBCO CCs of two different providers were coated with thin films of a-C and titanium interlayers. We have demonstrated that the application of 150 nm thin a-C and 100 nm thin Ti on REBCO CCs is already enough to decrease the SEY to required levels. Further studies attested an extensive compatibility of a-C with REBCO CCs since the coating did neither cause degradation of the superconducting properties nor did it increase microwave losses meaningfully.

Third, synchrotron radiation aging effects were investigated. Collaborating this time with ALBA Synchrotron, CCs of several providers were exposed for up to 552 h to synchrotron radiation attenuated by a 35 mm Cu crotch. The energy spectrum of loaded synchrotron radiation is attenuated and on the high-energy range tail when comparing to the full spectrum expected in the FCC-hh. We have demonstrated that the magnetic properties of irradiated samples remain as high as before irradiation. In particular, we showed it for the critical temperatures, the transition width and the critical current density up to 9 T at 77 K.

All in all, generated results within this thesis not only encourage further investigation in the possibility to deploy REBCO CCs as a beam screen coating for a more efficient Future Circular Collider hadron-hadron but have demonstrated that REBCO CCs are attractive coating options for other microwave applications that require large magnetic fields. For this, it was important, on the one hand, to show experimentally that commercially available CCs exhibit excellent high-frequency properties at large magnetic fields and on the other hand, to offer a REBCO coating solution for metallic, curved surfaces.

However, before deciding whether REBCO CCs should be used as beam screen coatings, more experimental data is required. Especially interesting would be to measure the surface impedance of REBCO CCs at 1 GHz and up to 16 T. To this end, our consortium is working on extending its instrumental repertoire in form of a parallel plate resonator with 1 GHz resonant frequency and a new cryostat compatible with the bigger resonator and equipped with a 16 T

---

[1]This model was run by my PhD colleague Guilherme Telles.

magnet. The high-frequency response at those more extreme conditions should be recorded with increased excitation power amplitudes, as quite high powers are expected within the FCC-hh. Simulation work is required to assess how the surface impedance of the coatings translates into the beam coupling impedance which will quantify the real benefits for the FCC-hh when using REBCO CCs. Moreover, studies on the mechanical properties of REBCO CCs has to be intensified. Magnetic field ramping during accelerator operation will cause magnetic forces that act on the beam screen chamber and consequently on the soldered and already bent CCs. It has to be shown that these effects are not of concern for the operation of the HTS. Another important concern is the operation of superconductivity under synchrotron radiation. The energy spectrum has to be extended with respect to previous experiments and superconducting properties have to be measured during the actual irradiation. Having mentioned these aspects, all work should culminate in a proof-of-concept device, simulating as best as possible the operation in real FCC-hh conditions.

Appendix A

Appendix to chapter 3

In table A.1, we provide the reader with the geometry factor G determined by Patrick Krkotic as described in [82] corresponding to the DR used in this thesis, permittivity ε' and the loss tangent $\tan(\delta)$ of rutile adopted from [87]. For temperature conditions other than the ones given, values were intrapolated from the points in table A.1.

T (K)	$G(\Omega)$	ε'	$\tan(\delta)$
100	218.37	105.48	1.21e-5
95	217.73	106.10	1.03e-5
90	217.27	106.55	9e-6
85	216.70	107.12	8e-6
80	216.05	107.77	7e-6
75	215.46	108.36	6e-6
70	214.86	108.98	4.5e-6
65	214.38	109.51	3.71e-6
60	213.79	110.09	3.09e-6
55	213.32	110.67	2.31e-6
50	212.85	111.07	1.92e-6
45	212.51	111.37	1.56e-6
40	212.17	111.79	1.28e-6
35	211.91	112.07	9.5e-7
30	211.84	112.13	7.74e-7
25	211.77	112.22	6.34e-7
20	211.75	112.23	4.39e-7
15	211.74	112.27	2.7e-7
10	211.74	112.31	1.9e-7
6	211.74	112.31	1.5e-7

TABLE A.1: Geometrical factor G, ruile permittivity ε' and loss tangent of rutile $\tan(\delta)$ as a function of temperature that were used in the context of this thesis for the determination of REBCO CCs' surface impedances.

Appendix B

Appendix to chapter 5

B.1 Derivation of eqs. 5.10 and 5.11

Starting from eq. (2.59), we can write the following:

$$Z_s = R_s + iX_s = \sqrt{\omega\mu_0(-\frac{1}{\sigma_2} + i\rho_{vm})}, \qquad \text{with } \sigma_2^{-1} = \omega\mu_0\lambda_L^2 \tag{B.1}$$

$$\Rightarrow R_s + iX_s = \sqrt{\omega\mu_0(-\omega\mu_0\lambda_L^2 + i(\rho'_{vm} + i\rho''_{vm}))}$$

$$\Rightarrow (R_s + iX_s)^2 = \omega\mu_0(-\omega\mu_0\lambda_L^2 + i(\rho'_{vm} + i\rho''_{vm}))$$

$$\Longleftrightarrow R_s^2 - X_s^2 + i2R_sX_s = -\omega^2\mu_0^2\lambda_L^2 - \omega\mu_0\rho''_{vm} + i\omega\mu_0\rho'_{vm}. \tag{B.2}$$

If we now equate the real and the complex part of the expression (A.2), we continue with two equations:

$$\Rightarrow 2R_sX_s = \omega\mu_0\rho'_{vm}$$

$$\wedge \ R_s^2 - X_s^2 = -\omega^2\mu_0^2\lambda_L^2 - \omega\mu_0\rho''_{vm}$$

$$\Rightarrow \rho'_{vm} = \frac{2R_sX_s}{\omega\mu_0} \tag{B.3}$$

$$\wedge \ \rho''_{vm} = -\frac{R_s^2 - X_s^2 + \omega^2\mu_0^2\lambda_L^2}{\omega\mu_0}. \tag{B.4}$$

The surface impedance can be expressed as a field independent part and a term which describes the change of surface impedance with the magnetic field

$$Z_s = R_s + iX_s = (R_{s,0}(T) + \Delta R_s(T,H)) + i(X_{s,0}(T) + \Delta X_s(T,H)). \tag{B.5}$$

Without an applied field there are no contribution to the surface impedance from the vortex motion and $\rho_{vm} = 0$. With equation (A.5), we can write equation (A.1) as

$$Z_s(H = 0) = R_{s,0}(T) + iX_{s,0}(T) = i\omega\mu_0\lambda_L$$

This concludes

$$R_{s,0}(T) = 0$$

$$\wedge \ X_{s,0}(T) = \omega\mu_0\lambda_L$$

$$\Rightarrow \quad R_s = \Delta R_s(T,H) \tag{B.6}$$

$$\wedge \ X_s = \omega\mu_0\lambda_L + \Delta X_s(T,H). \tag{B.7}$$

Plugging equations (A.6) and (A.7) into (A.3) and (A.4) gives us equations (5.10) and (5.11).

B.2 The necessity for external effect removal when calculating vortex motion parameters

Based on the calculation of VM parameters, it can be demonstrated why offsetting $\Delta Z_s(H)$ by $Z_s^{ext\cdot}(0\,\mathrm{T})$[1] is necessary in order to extract the intrinsic response of REBCO. We present the vortex motion parameters $\rho_{vm}(H)$, $\rho_{ff}(H)$ and $\nu_p(H)$ when calculated from $\Delta R_s(H) = R_s(H) - R_s(0\,\mathrm{T})$ and $\Delta X_s(H) = X_s(H) - X_s(0\,\mathrm{T})$ (see eqs. (5.14) and (5.15)) in Fig. B.1 corresponding to Fujikura CC at 40 K. These can be compared with the same vortex motion parameters calculated from corrected data $\Delta R_s^{\mathrm{offset}}(H) = \Delta R_s(H) + R_s^{ext\cdot}(H)$ and $\Delta X_s^{\mathrm{offset}}(H) = \Delta X_s(H) + X_s^{ext\cdot}(H)$ (see eqs. (5.17) and (5.18)) in Fig. B.2. Moving to the VM resistivity ρ_{vm} in Fig. B.1 **(b)**, we see that linear fits to the field range $\mu_0 H > 2\,\mathrm{T}$ of ρ'_{vm} and ρ''_{vm} (see red line) highlight $\rho_{vm}(0\,\mathrm{T}) \neq 0$. This is certainly not consistent with neither the GR model (see eq. (2.56)) nor intuition, since in absence of vortices there should be no vortex motion resistivity. In contrast, when removing external contributions for field $\mu_0 H > 1$ from the ΔZ_s, so when applying the offset $Z_s^{\mathbf{ext\cdot}}(0\,\mathrm{T})$ to ΔZ_s, the vortex motion response has in first approximation no residual contribution at zero-field which establishes consistency with intuition and the GR model.

The consistency in ρ_{vm} propagates to both VM parameters flux-flow resistivity ρ_{ff} and depinning frequency ν_p. The flux-flow resistivity $\rho_{ff}(H)$ calculated from $\Delta Z_s(H)$, see Fig. B.1 **(c)**, exhibits a complicated field behavior for fields below 4 T which is at odds with the model prediction of a strict proportionality $\rho_{ff} \propto H$, see eq. (5.19). While determining $\rho_{ff}(H)$ from $\Delta Z_s^{\mathrm{offset}}(H)$, see Fig. B.2 **(c)**, the linearity in field is conserved for fields >1 T, so in the field range where external effects have been eliminated from the vortex motion response.

A similar picture is painted for the depinning frequency ν_p. For depinning frequencies calculated from ΔZ_s, see Fig. B.1 **(d)**, the field behavior of the depinning frequency decreases from high values at small fields and approaches asymptote-like a constant value close to 40 GHz at large fields. This field behavior is not predicted by the GR-model. It either foresees a constant field behavior for the regime where we have more pinning sites than vortices or a $\nu_p \propto H^{-1/2}$ decrease for the regime where the number of vortices surpass the number of effective pinning centers [67]. The field behavior of ν_p calculated from $\Delta R_s^{\mathrm{offset}}$, however, shows an almost constant field behavior for fields above 2 T, as expected from GR-model.

In conclusion, based on one example, we have demonstrated that eliminating the field independent external effect $Z_s^{ext\cdot}(0\,\mathrm{T})$ from $\Delta Z_s(H)$ renders calculated VM parameters much more in line with physical intuition and expectations of the GR model.

---

[1]Offsetting $\Delta Z_s(H)$ by $Z_s^{ext\cdot}(0\,\mathrm{T})$ means explicitly offsetting $\Delta R_s(H)$ by $R_s^{ext\cdot}(0\,\mathrm{T})$ and $\Delta X_s(H)$ by $X_s^{ext\cdot}(0\,\mathrm{T})$.
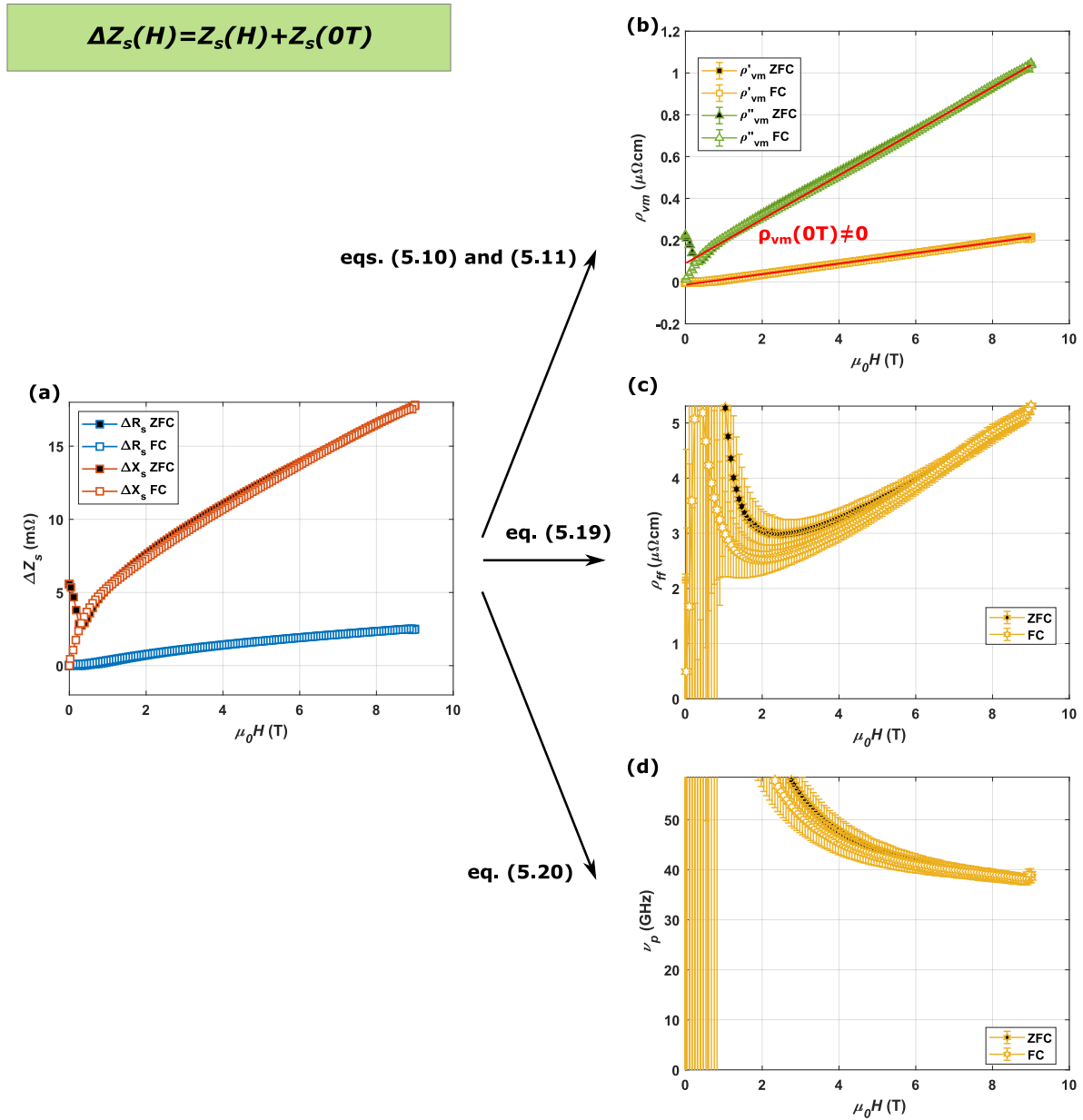
FIGURE B.1: **(a)** The experimentally determined field change of surface resistance $\Delta R_s(H)$ and surface reactance $\Delta X_s(H)$ corresponding to a Fujikura CC sample at 40 K. The vortex motion parameters calculated based on ΔR_s and ΔX_s are shown in **(b)-(d)**. The straight red lines in **(b)** are fits to ρ'_{vm} and ρ''_{vm} in the field range > 2 T and highlight by means of their crossing with the ordinate that $\rho_{vm}(0\,\text{T}) \neq 0$ which violates the GR-model and intuition.
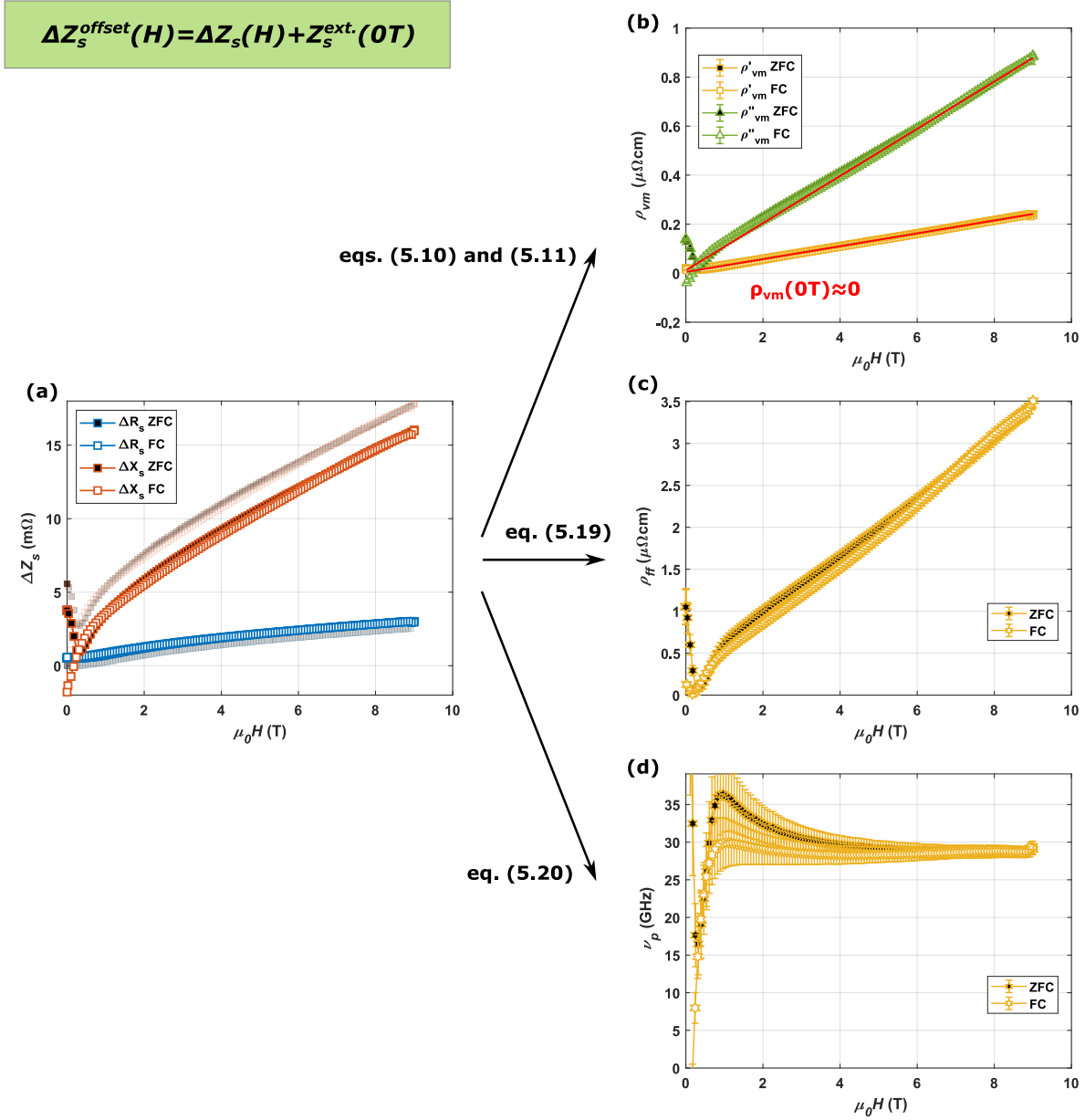
FIGURE B.2: **(a)** The experimentally determined field change of surface resistance $\Delta R_s(H)$ (transparent blue squares) and surface reactance $\Delta X_s(H)$ (transparent red squares) in comparison with $\Delta R_s^{\text{offset}}(H)$ (solid blue squares) and $\Delta X_s^{\text{offset}}(H)$ (solid red squares) corresponding to a Fujikura CC sample at 40 K. The vortex motion parameters calculated based on $\Delta R_s^{\text{offset}}(H)$ and $\Delta X_s^{\text{offset}}(H)$ are shown in **(b)-(d)**. The straight red lines in **(b)** are fits to ρ'_{vm} and ρ''_{vm} in the field range $> 2\,\text{T}$ and highlight by means of their crossing with the ordinate that $\rho_{vm}(0\,\text{T}) \approx 0$ which is in line the GR-model and intuition.

Appendix C

Appendix to chapter 6

We contrast here the surface resistance of top and bottom surface as a function of applied magnetic field for six different CCs. Presented are field sweeps at 70 K (see Fig. C.1), at 60 K (see Fig. C.2), at 50 K (see Fig. C.3), at 40 K (see Fig. C.4), at 30 K (see Fig. C.5) and at 20 K (see Fig. C.6).
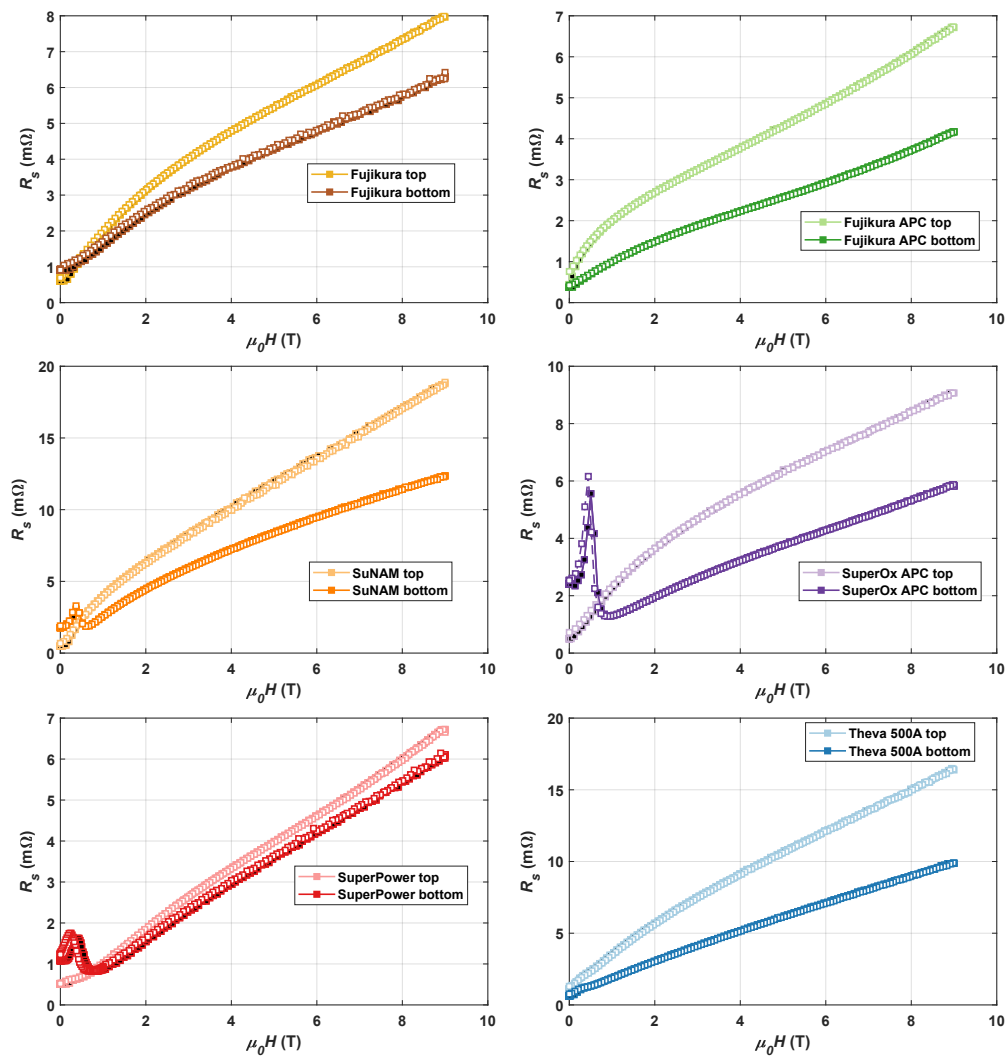

FIGURE C.1: How the surface resistance varies with magnetic field for several CCs at 70 K. The black filled and white filled markers correspond to ZFC and FC curves, respectively.

FIGURE C.2: How the surface resistance varies with magnetic field for several CCs at 60 K. The black filled and white filled markers correspond to ZFC and FC curves, respectively.
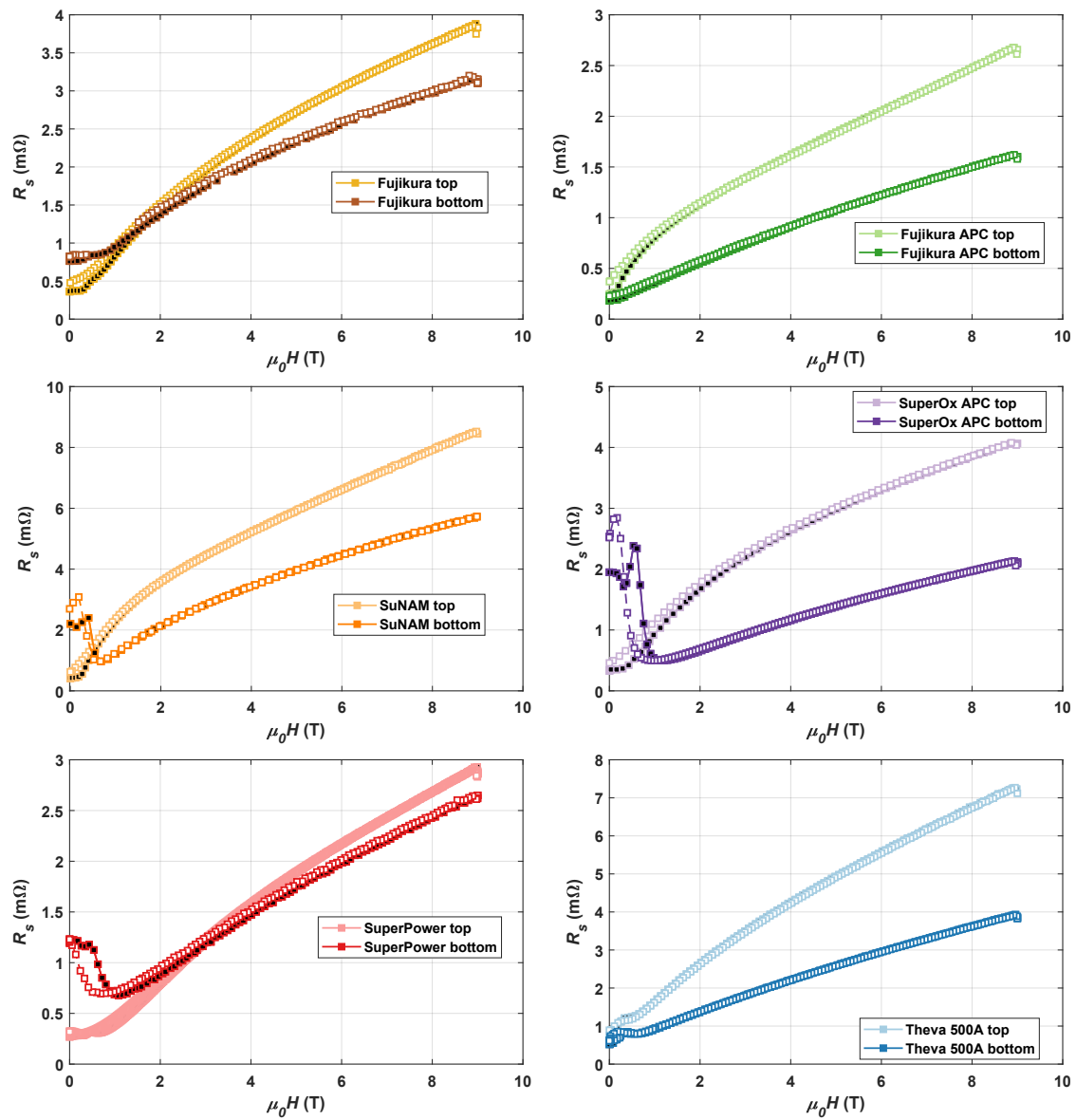
FIGURE C.3: How the surface resistance varies with magnetic field for several CCs at 50 K. The black filled and white filled markers correspond to ZFC and FC curves, respectively.

FIGURE C.4: How the surface resistance varies with magnetic field for several CCs at 40 K. The black filled and white filled markers correspond to ZFC and FC curves, respectively.
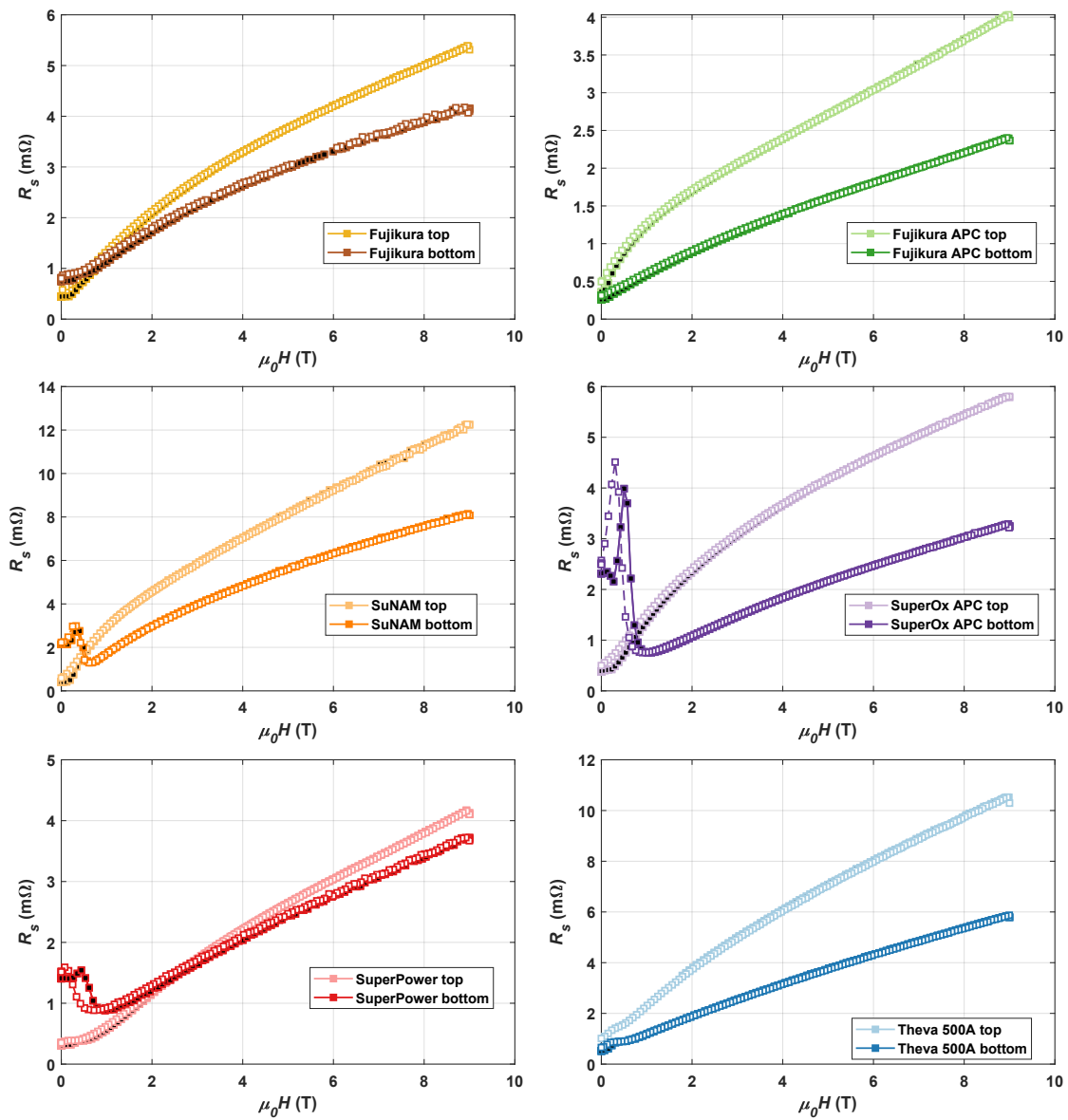
FIGURE C.5: How the surface resistance varies with magnetic field for several CCs at 30 K. The black filled and white filled markers correspond to ZFC and FC curves, respectively.

FIGURE C.6: How the surface resistance varies with magnetic field for several CCs at 20 K. The black filled and white filled markers correspond to ZFC and FC curves, respectively.
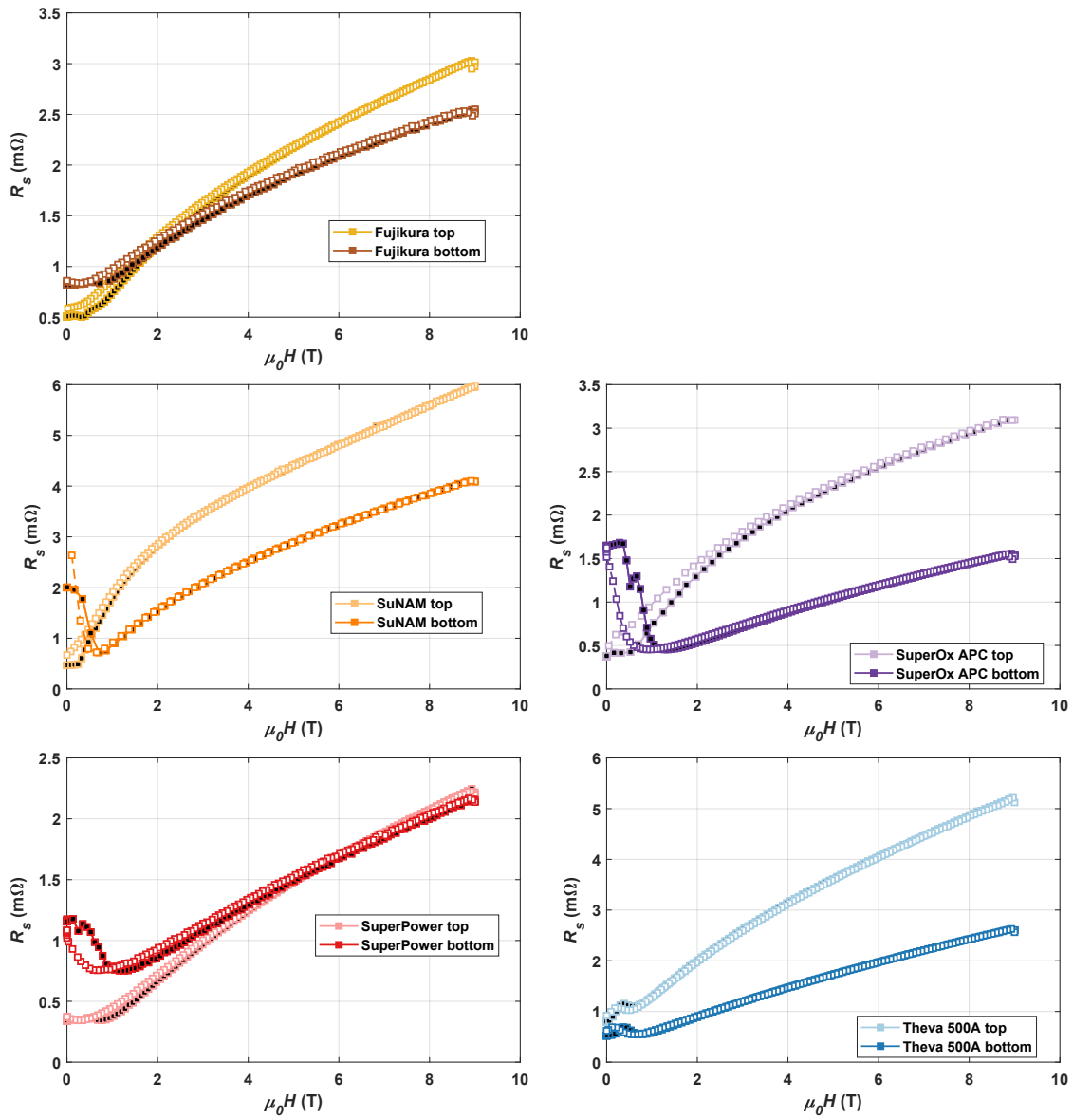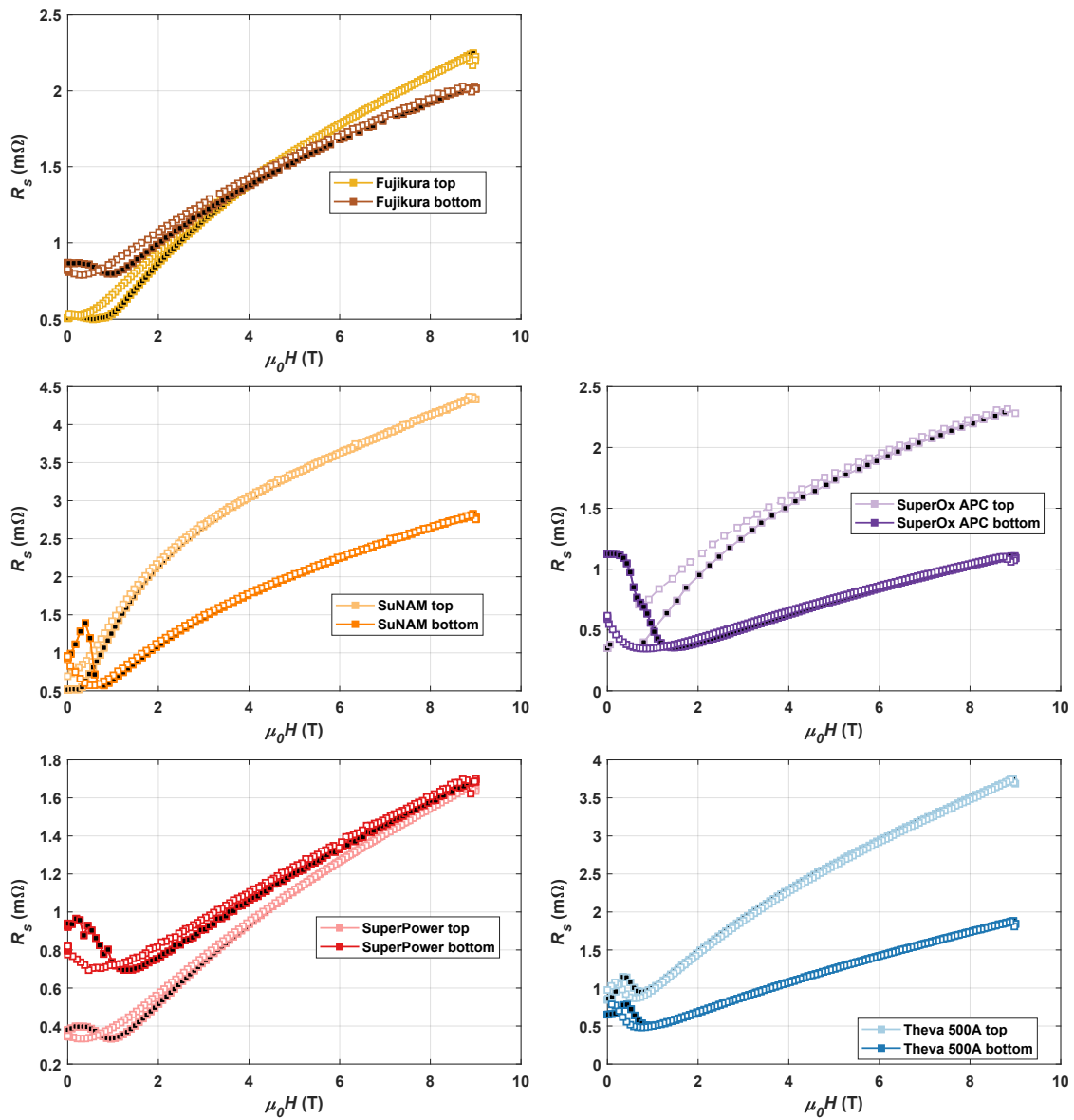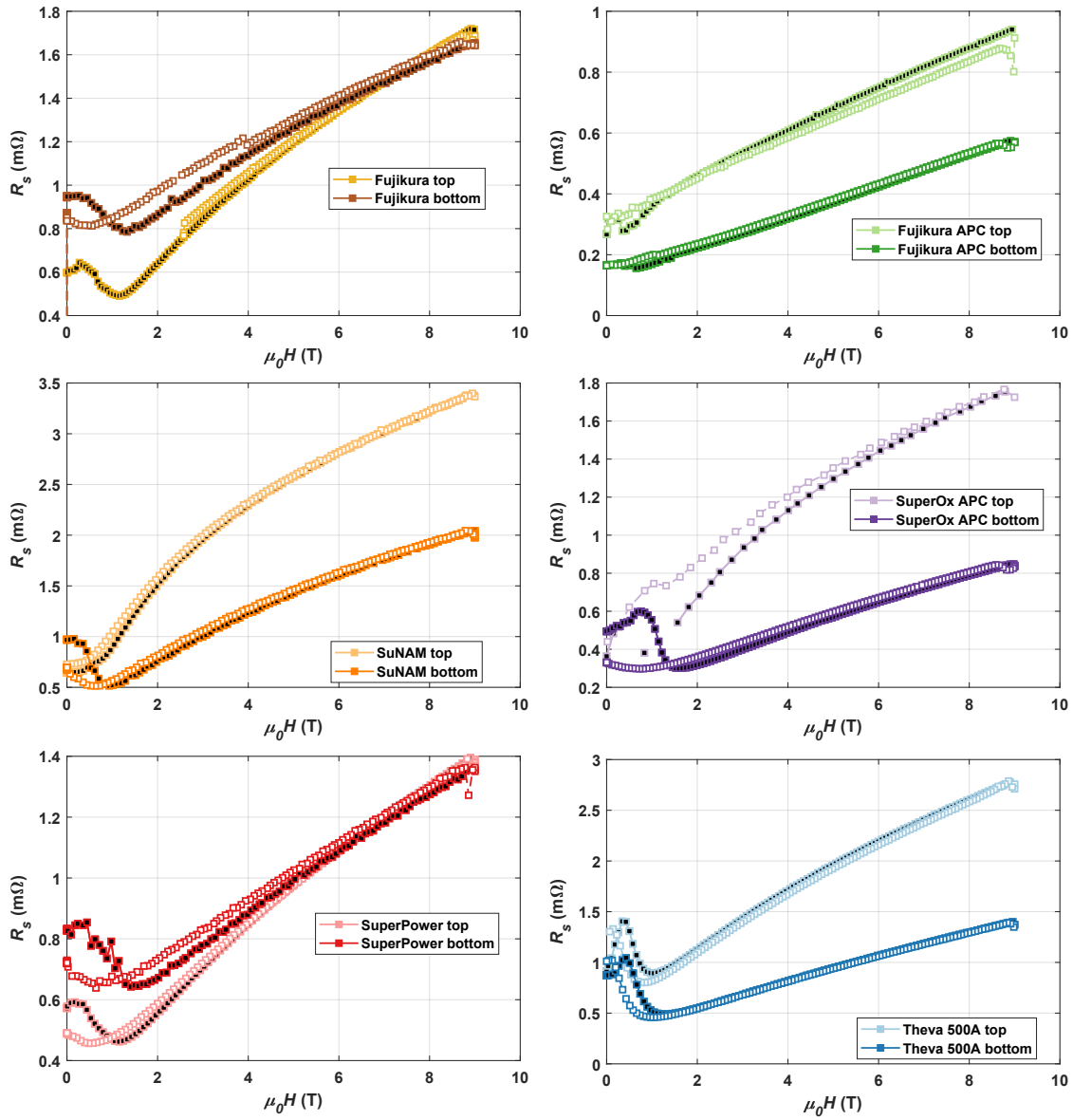
Bibliography

[1]   CERN. *The Large Hadron Collider*. 2022. URL: https://home.cern/science/accelerators/large-hadron-collider (visited on 11/02/2022).

[2]   Stephen Myers. "The large hadron collider 2008–2013". In: *International Journal of Modern Physics A* 28.25 (2013), p. 1330035.

[3]   Georges Aad et al. "Observation of a new particle in the search for the Standard Model Higgs boson with the ATLAS detector at the LHC". In: *Physics Letters B* 716.1 (2012), pp. 1–29.

[4]   Leon M Lederman and Dick Teresi. *The God particle: If the universe is the answer, what is the question?* Houghton Mifflin Harcourt, 2006.

[5]   *The Nobel Prize in Physics 2013*. 2013. URL: https://www.nobelprize.org/prizes/physics/2013/summary/ (visited on 11/02/2022).

[6]   FCC collaboration et al. "HE-LHC: The High-Energy Large Hadron Collider: Future Circular Collider Conceptual Design Report Volume 4". In: *European Physical Journal: Special Topics* 228.5 (2019), pp. 1109–1382.

[7]   CERN. *Future Circular Collider Study Kickoff Meeting, University of Geneva*. 2014. URL: http://indico.cern.ch/e/fcc-kickoff (visited on 11/02/2022).

[8]   FCC collaboration et al. "FCC Physics Opportunities: Future Circular Collider Conceptual Design Report Volume 1". In: *European Physical Journal C* 79.6 (2019), p. 474.

[9]   FCC collaboration et al. "FCC-hh: The Hadron Collider: Future Circular Collider Conceptual Design Report Volume 3". In: *European Physical Journal: Special Topics* 228.4 (2019), pp. 755–1107.

[10]   Ignasi Bellafont. "Study of the beam induced vacuum effects in the cryogenic beam vacuum chamber of the future Circular Hadron Collider". PhD thesis. UNIVERSITAT POLITÈCNICA DE CATALUNYA, 2020.

[11]   Sergio Calatroni. "HTS coatings for impedance reduction in particle accelerators: case study for the FCC at CERN". In: *IEEE Transactions on Applied Superconductivity* 26.3 (2016), pp. 1–4.

[12]   S Calatroni et al. "Thallium-based high-temperature superconductors for beam impedance mitigation in the Future Circular Collider". In: *Superconductor Science and Technology* 30.7 (2017), p. 075002.

[13]   A Leveratto et al. "Future Circular Collider beam screen: progress on Tl-1223 HTS coating". In: *Superconductor Science and Technology* 33.5 (2020), p. 054004.

[14]   T Puig et al. "Coated conductor technology for the beamscreen chamber of future high energy circular colliders". In: *Superconductor Science and Technology* 32.9 (2019), p. 094006.

[15]   Artur Romanov et al. "High frequency response of thick REBCO coated conductors in the framework of the FCC study". In: *Scientific reports* 10.1 (2020), pp. 1–12.

[16]   Pascal Tixador. "Development of superconducting power devices in Europe". In: *Physica C: Superconductivity and its applications* 470.20 (2010), pp. 971–979.

[17]		Judith L MacManus-Driscoll and Stuart C Wimbush. "Processing and application of high-temperature superconducting coated conductors". In: *Nature Reviews Materials* (2021), pp. 1–18.

[18]		Dieter Proch. "Superconducting cavities for accelerators". In: *Reports on Progress in Physics* 61.5 (1998), p. 431.

[19]		Steven M Anlage. "High temperature superconducting radio frequency coils for NMR spectroscopy and magnetic resonance imaging". In: *Microwave Superconductivity*. Springer, 2001, pp. 337–352.

[20]		HJ Chaloupka. "HTS antennas". In: *Microwave Superconductivity*. Springer, 2001, pp. 353–386.

[21]		Danho Ahn et al. "Maintaining high Q-factor of superconducting $YBa_2Cu_3O_{7-x}$ microwave cavity in a high magnetic field". In: *arXiv preprint arXiv:1904.05111* (2019).

[22]		Dirk Van Delft and Peter Kes. "The discovery of superconductivity". In: *Physics Today* 63.9 (2010), pp. 38–43.

[23]		Walther Meissner and Robert Ochsenfeld. "Ein neuer effekt bei eintritt der supraleitfähigkeit". In: *Naturwissenschaften* 21.44 (1933), pp. 787–788.

[24]		Allister M Forrest. "Meissner and Ochsenfeld revisited". In: *European Journal of Physics* 4.2 (1983), p. 117.

[25]		C Jo Gorter and H Casimir. "The thermodynamics of the superconducting state". In: *Z. tech. Phys* 15 (1934), pp. 539–42.

[26]		Fritz London and Heinz London. "The electromagnetic equations of the supraconductor". In: *Proceedings of the Royal Society of London. Series A-Mathematical and Physical Sciences* 149.866 (1935), pp. 71–88.

[27]		Fritz London and H London. "Supraleitung und diamagnetismus". In: *Physica* 2.1-12 (1935), pp. 341–354.

[28]		Vitaly L Ginzburg and Lev D Landau. "On the theory of superconductivity". In: *On superconductivity and superfluidity*. Springer, 2009, pp. 113–137.

[29]		Alfred Brian Pippard and William Lawrence Bragg. "An experimental and theoretical study of the relation between magnetic field and current in a superconductor". In: *Proceedings of the Royal Society of London. Series A. Mathematical and Physical Sciences* 216.1127 (1953), pp. 547–568.

[30]		Michael Tinkham. *Introduction to superconductivity*. Courier Corporation, 2004.

[31]		John Bardeen and MJ Stephen. "Theory of the motion of vortices in superconductors". In: *Physical Review* 140.4A (1965), A1197.

[32]		J George Bednorz and K Alex Müller. "Possible high T_c superconductivity in the Ba-La-Cu-O system". In: *Zeitschrift für Physik B Condensed Matter* 64.2 (1986), pp. 189–193.

[33]		EASItrain by CERN. *EASISschool 1 / ESAS Summer School*. 2018. URL: https://indico.cern.ch/event/663949// (visited on 02/15/2021).

[34]		Maw-Kuen Wu et al. "Superconductivity at 93 K in a new mixed-phase Y-Ba-Cu-O compound system at ambient pressure". In: *Physical review letters* 58.9 (1987), p. 908.

[35]		Alexei A Abrikosov. "On the magnetic properties of superconductors of the second group". In: *Sov. Phys. JETP* 5 (1957), pp. 1174–1182.

[36]		Juri Banchewski. "Transient Liquid Assisted Growth of YBCO Superconducting Films: Growth Kinetics, Physical Properties and Vortex Pinning". PhD thesis. Universitat Autònoma de Barcelona, 2020.

[37]		Paul Seidel. *Applied superconductivity: handbook on devices and applications*. John Wiley & Sons, 2015.

[38]		U Essmann and H Träuble. "The direct observation of individual flux lines in type II superconductors". In: *Physics letters A* 24.10 (1967), pp. 526–527.

[39]   AM Campbell and JE Evetts. "Flux vortices and transport currents in type II superconductors". In: *Advances in Physics* 21.90 (1972), pp. 199–428.

[40]   J Gutierrez. "Vortex pinning and critical currents in $YBa_2Cu_3O_{7-x}$ MOD-TFA thin films and coated conductors". PhD thesis. 2008.

[41]   JR Waldram. *Superconductivity of Metals and Cuprates Institute of Physics Publishing*. 1996.

[42]   David A Cardwell and David S Ginley. *Handbook of superconducting materials*. Vol. 1. CRC Press, 2003.

[43]   J Gutierrez et al. "Strong isotropic flux pinning in solution-derived $YBa_2Cu_3O_{7-x}$ nanocomposite superconductor films". In: *Nature materials* 6.5 (2007), pp. 367–373.

[44]   Ferran Vallès Pérez. *PhD Thesis: Vortex pinning and creep in YBCO nanocomposite films grown by chemical solution deposition*. Universitat Autònoma de Barcelona, 2019.

[45]   SR Foltyn et al. "Materials science challenges for high-temperature superconducting wire". In: *Materials For Sustainable Energy: A Collection of Peer-Reviewed Research and Review Articles from Nature Publishing Group*. World Scientific, 2011, pp. 299–310.

[46]   Kaname Matsumoto and Paolo Mele. "Artificial pinning center technology to enhance vortex pinning in YBCO coated conductors". In: *Superconductor Science and Technology* 23.1 (2009), p. 014001.

[47]   Co Po Bean. "Magnetization of hard superconductors". In: *Physical review letters* 8.6 (1962), p. 250.

[48]   J. Gutiérrez et al. "Strong isotropic flux pinning in solution-derived $YBa_2Cu_3O_{7-x}$ nanocomposite superconductor films". In: *Nature Materials* 6.5 (2007), pp. 367–373. ISSN: 14764660. DOI: 10.1038/nmat1893.

[49]   Víctor Rouco Gómez et al. "Controlling vortex pinning and dynamics of nanostructured YBCO thin films grown by chemical solution deposition". PhD thesis. 2014.

[50]   TH Johansen et al. "Measurements and model calculations of forces betpeen a magnet and granular high-T_c superconductor". In: *Applied superconductivity* 2.7-8 (1994), pp. 535–548.

[51]   Bernhard Keimer et al. "From quantum matter to high-temperature superconductivity in copper oxides". In: *Nature* 518.7538 (2015), pp. 179–186.

[52]   V Breit et al. "Evidence for chain superconductivity in near-stoichiometric $YBa_2Cu_3O_x$ single crystals". In: *Physical Review B* 52.22 (1995), R15727.

[53]   David Larbalestier et al. "High-T_c superconducting materials for electric power applications". In: *Materials For Sustainable Energy: A Collection of Peer-Reviewed Research and Review Articles from Nature Publishing Group*. World Scientific, 2011, pp. 311–320.

[54]   Lin-Feng Chen et al. *Microwave electronics: measurement and materials characterization*. John Wiley & Sons, 2004.

[55]   Sergey V Yuferev and Nathan Ida. *Surface impedance boundary conditions: a comprehensive approach*. CRC press, 2018.

[56]   Andrea Alimenti. "Advanced microwave resonant measurement techniques for the characterization and study of dielectrics, conductors and superconductors". PhD thesis. University Roma Tre, 2020.

[57]   Harold Weinstock and Martin Nisenoff. *Microwave superconductivity*. Vol. 375. Springer Science & Business Media, 2012.

[58]   Steven Anlage. "Microwave Superconductivity". In: *IEEE Journal of Microwaves* 1 (Jan. 2021), pp. 389–402. DOI: 10.1109/JMW.2020.3033156.

[59] Cornelis Jacobus Gorter and Hendrik Casimir. "On supraconductivity I". In: *Physica* 1.1-6 (1934), pp. 306–320.

[60] Daniel C Mattis and John Bardeen. "Theory of the anomalous skin effect in normal and superconducting metals". In: *Physical Review* 111.2 (1958), p. 412.

[61] J Halbritter. "Comparison between measured and calculated RF losses in the superconducting state". In: *Zeitschrift für Physik* 238.5 (1970), pp. 466–476.

[62] Carmine Attanasio, Luigi Maritato, and Ruggero Vaglio. "Residual surface resistance of polycrystalline superconductors". In: *Physical Review B* 43.7 (1991), p. 6128.

[63] JR Delayen and CL Bohn. "Temperature, frequency, and rf field dependence of the surface resistance of polycrystalline $YBa_2Cu_3O_{7-x}$". In: *Physical review B* 40.7 (1989), p. 5151.

[64] Cristoforo Benvenuti et al. "Study of the surface resistance of superconducting niobium films at 1.5 GHz". In: *Physica C: Superconductivity* 316.3-4 (1999), pp. 153–188.

[65] Jonathan I. Gittleman and Bruce Rosenblum. "Radio-frequency resistance in the mixed state for subcritical currents". In: *Physical Review Letters* 16.17 (1966), pp. 734–736. ISSN: 00319007. DOI: 10.1103/PhysRevLett.16.734.

[66] Mark W Coffey and John R Clem. "Unified theory of effects of vortex pinning and flux creep upon the rf surface impedance of type-II superconductors". In: *Physical review letters* 67.3 (1991), p. 386.

[67] M Golosovsky, M Tsindlekht, and D Davidov. "High-frequency vortex dynamics in". In: *Superconductor Science and Technology* 9.1 (1996), pp. 1–15. ISSN: 0953-2048. DOI: 10.1088/0953-2048/9/1/001.

[68] N-C Yeh. "High-frequency vortex dynamics and dissipation of high-temperature superconductors". In: *Physical Review B* 43.1 (1991), p. 523.

[69] Enrico Silva, Nicola Pompeo, and Oleksandr V. Dobrovolskiy. "Vortices at microwave frequencies". In: *Superconductors at the Nanoscale: From Basic Research to Applications* (2017), pp. 253–278. ISSN: 2365-6581. DOI: 10.1515/9783110456806-009.

[70] Sergio Calatroni and Ruggero Vaglio. "High-Temperature Superconductor Coatings for Beam Impedance Reduction in Particle Colliders: Nonlinear Effects". In: *IEEE Transactions on Applied Superconductivity* 31.3 (2021), pp. 1–8.

[71] Patrick Krkotić et al. "Evaluation of the nonlinear surface resistance of REBCO coated conductors for their use in the FCC-hh beam screen". In: *Superconductor Science and Technology* (2021).

[72] Andrea Alimenti et al. "Surface Impedance Measurements in Superconductors in DC Magnetic Fields: Challenges and Relevance to Particle Physics Experiments". In: *IEEE Instrumentation & Measurement Magazine* 24.9 (2021), pp. 12–20.

[73] Sergio Calatroni and Ruggero Vaglio. "Surface resistance of superconductors in the presence of a DC magnetic field: frequency and field intensity limits". In: *IEEE Transactions on Applied Superconductivity* 27.5 (2017), pp. 1–6.

[74] Robert E Collin. *Foundations for microwave engineering*. John Wiley & Sons, 2007.

[75] Rohde & Schwarz. *R&S ZNB/ZNBT Vector Network Analyzers User Manual, 1173.9163.02 , Version 60*. 2021.

[76] Kaneyuki Kurokawa. "Power waves and the scattering matrix". In: *IEEE transactions on microwave theory and techniques* 13.2 (1965), pp. 194–202.

[77] Keysight Technologies. *Data Sheet: FieldFox Handheld Analyzers 4/6.5/9/14/18/26.5/32/44/50 GHz*. 2020.

[78] Rohde & Schwarz. *Data Sheet: R&S ZNB Vector Network Analyzer Specifications Version 04.00*. 2021.

[79] Patrick Krkotić, Guilherme Telles, and Bernat Bozzo. *Drohms: Dielectric Resonator Surface Impedance Measurement System Version 1.0*. 2019.

[80] Terrabits. *Rohde & Schwarz python instrument control toolbox by Terrabits*. 2021. URL: https://github.com/Terrabits/rohdeschwarz (visited on 12/27/2021).

[81] BW Hakki and Paul D Coleman. "A dielectric resonator method of measuring inductive capacities in the millimeter range". In: *IRE Transactions on Microwave theory and techniques* 8.4 (1960), pp. 402–410.

[82] Patrick Krkotić, Albert Aguasca, and Juan M O'Callaghan. "Small footprint evaluation of metal coatings for additive manufacturing". In: *2018 48th European Microwave Conference (EuMC)*. IEEE. 2018, pp. 882–885.

[83] Steve Donovan et al. "Microwave cavity perturbation technique: part II: experimental scheme". In: *International Journal of Infrared and Millimeter Waves* 14.12 (1993), pp. 2459–2487.

[84] Z-Y Shen et al. "High-T/sub c/-superconductor-sapphire microwave resonator with extremely high Q-values up to 90 K". In: *IEEE transactions on microwave theory and techniques* 40.12 (1992), pp. 2424–2431.

[85] Nicola Pompeo et al. "Fitting strategy of resonance curves from microwave resonators with non-idealities". In: *2017 IEEE International Instrumentation and Measurement Technology Conference (I2MTC)*. IEEE. 2017, pp. 1–6.

[86] Andrea Alimenti et al. "Challenging microwave resonant measurement techniques for conducting material characterization". In: *Measurement Science and Technology* 30.6 (2019), p. 065601.

[87] N Klein et al. "Dielectric properties of rutile and its use in high temperature superconducting resonators". In: *Journal of applied physics* 78.11 (1995), pp. 6683–6686.

[88] N. Pompeo, K. Torokhtii, and E. Silva. "Dielectric resonators for the measurements of the surface impedance of superconducting films". In: *Measurement Science Review* 14.3 (2014), pp. 164–170. ISSN: 13358871. DOI: 10.2478/msr-2014-0022.

[89] Quantum Design. "PPMS Hardware Manual, 1070-150, Rev. B5". In: *PPMS Hardware Manual* (2008).

[90] Darko Kajfez and Pierre Guillon. "Dielectric resonators". In: *Norwood* (1986).

[91] Paul J Petersan and Steven M Anlage. "Measurement of resonant frequency and quality factor of microwave resonators: Comparison of methods". In: *Journal of applied physics* 84.6 (1998), pp. 3392–3402.

[92] Kenneth Leong and Janina Mazierska. "Precise measurements of the Q factor of dielectric resonators in the transmission mode-accounting for noise, crosstalk, delay of uncalibrated lines, coupling loss, and coupling reactance". In: *IEEE transactions on microwave theory and techniques* 50.9 (2002), pp. 2115–2127.

[93] Kenneth Levenberg. "A method for the solution of certain non-linear problems in least squares". In: *Quarterly of applied mathematics* 2.2 (1944), pp. 164–168.

[94] Donald W Marquardt. "An algorithm for least-squares estimation of nonlinear parameters". In: *Journal of the society for Industrial and Applied Mathematics* 11.2 (1963), pp. 431–441.

[95] Patrick Krkotić et al. "Algorithm for Resonator Parameter Extraction From Symmetrical and Asymmetrical Transmission Responses". In: *IEEE Transactions on Microwave Theory and Techniques* (2021).

[96] P. Krkotic et al. "RF Characterisation of HTS-CC Tapes as Alternative Coating for the FCC-hh Beam Screen". FCC week 2019. 2019. URL: https://indico.cern.ch/event/727555/contributions/3461230/.

[97] Quantum Design. "MPMS 3 User's Manual, 1500-100, Rev. F1". In: *MPMS Hardware Manual* (2016).

[98]   RL Fagaly. "Superconducting quantum interference device instruments and applications". In: *Review of scientific instruments* 77.10 (2006), p. 101101.

[99]   Quantum Design. "PPMS VSM Option User's Manual, Rev. A3". In: *PPMS VSM Option Hardware Manual* (2008).

[100]   D-X Chen and Ronald B Goldfarb. "Kim model for magnetization of type-II superconductors". In: *Journal of Applied Physics* 66.6 (1989), pp. 2489–2500.

[101]   Georg Simon Ohm. *Die galvanische kette: mathematisch*. TH Riemann, 1827.

[102]   Alexander Stangl. *PhD Thesis: Oxygen kinetics and charge doping for high critical current YBCO films*. Universitat Autònoma de Barcelona, 2019.

[103]   O Philips'Gloeilampenfabrieken. "A method of measuring specific resistivity and Hall effect of discs of arbitrary shape". In: *Philips Res. Rep* 13.1 (1958), pp. 1–9.

[104]   A Molodyk et al. "Development and large volume production of extremely high current density $YBa_2Cu_3O_7$ superconducting wires for fusion". In: *Scientific reports* 11.1 (2021), pp. 1–11.

[105]   Xiaoping Li et al. "The development of second generation HTS wire at American Superconductor". In: *IEEE transactions on applied superconductivity* 19.3 (2009), pp. 3231–3235.

[106]   Xavier Obradors and Teresa Puig. "Coated conductors for power applications: materials challenges". In: *Superconductor Science and Technology* 27.4 (2014), p. 044003.

[107]   A Berenov et al. "Microstructural characterization of $YBa_2Cu_3O_{7-\delta}$ thick films grown at very high rates and high temperatures by pulsed laser deposition". In: *Journal of materials research* 18.4 (2003), pp. 956–964.

[108]   Marilyn Hawley et al. "Growth mechanism of sputtered films of $YBa_2Cu_3O_7$ studied by scanning tunneling microscopy". In: *Science* 251.5001 (1991), pp. 1587–1589.

[109]   JL MacManus-Driscoll et al. "Strongly enhanced current densities in superconducting coated conductors of $YBa_2Cu_3O_{7-x}$+ $BaZrO_3$". In: *Materials For Sustainable Energy: A Collection of Peer-Reviewed Research and Review Articles from Nature Publishing Group*. World Scientific, 2011, pp. 327–331.

[110]   Yuh Shiohara, Takahiro Taneda, and Masateru Yoshizumi. "Overview of materials and power applications of coated conductors project". In: *Japanese Journal of Applied Physics* 51.1R (2011), p. 010007.

[111]   D Abraimov et al. "Double disordered YBCO coated conductors of industrial scale: high currents in high magnetic field". In: *Superconductor Science and Technology* 28.11 (2015), p. 114007.

[112]   Alexander Usoskin et al. "Double-disordered HTS-coated conductors and their assemblies aimed for ultra-high fields: large area tapes". In: *IEEE Transactions on Applied Superconductivity* 28.4 (2018), pp. 1–6.

[113]   M Igarashi et al. "Advanced development of IBAD/PLD coated conductors at FUJIKURA". In: *Physics Procedia* 36 (2012), pp. 1412–1416.

[114]   Wataru HIRATA et al. "Artificial Pinning Centers-doped RE-based Coated Conductors". In: *Fujikura Technical Review* (2019), p. 23.

[115]   Jae-Hun Lee et al. "RCE-DR, a novel process for coated conductor fabrication with high performance". In: *Superconductor Science and Technology* 27.4 (2014), p. 044018.

[116]   Soon-Mi Choi et al. "Characteristics of high-J_{c} GdBCO coated conductors fabricated by the RCE-DR process". In: *IEEE transactions on applied superconductivity* 23.3 (2012), pp. 8001004–8001004.

[117]   S Lee et al. "Development and production of second generation high T_c superconducting tapes at SuperOx and first tests of model cables". In: *Superconductor Science and Technology* 27.4 (2014), p. 044022.

[118] S Samoilenkov et al. "Customised 2G HTS wire for applications". In: *Superconductor Science and Technology* 29.2 (2015), p. 024001.

[119] D Turrioni et al. "Study of HTS wires at high magnetic fields". In: *IEEE transactions on applied superconductivity* 19.3 (2009), pp. 3057–3060.

[120] Carmine Senatore et al. "Field and temperature scaling of the critical current density in commercial REBCO coated conductors". In: *Superconductor Science and Technology* 29.1 (2015), p. 014002.

[121] Manuel La Rosa Betancourt and Markus Bauer. "Type 2G High Temperature Superconductors: Technology Trends and Challenges for Naval Applications". In: June 2018.

[122] W Prusseit et al. "Working around HTS thickness limitations–towards 1000+ A/cm–Class Coated Conductors". In: *Physics Procedia* 36 (2012), pp. 1417–1422.

[123] W Prusseit et al. "Long length coated conductor fabrication by inclined substrate deposition and evaporation". In: *Journal of Physics: Conference Series*. Vol. 43. 1. IOP Publishing. 2006, p. 054.

[124] K Kakimoto et al. "High-speed deposition of high-quality RE123 films by a PLD system with hot-wall heating". In: *Superconductor Science and Technology* 23.1 (2009), p. 014016.

[125] Run Zhao et al. "Precise tuning of $(YBa_2Cu_3O_{7-\delta})_{1-x}$:$(BaZrO_3)_x$ thin film nanocomposite structures". In: *Advanced Functional Materials* 24.33 (2014), pp. 5240–5245.

[126] B Maiorov et al. "Synergetic combination of different types of defect to optimize pinning landscape using $BaZrO_3$-doped $YBa_2Cu_3O_7$". In: *Nature materials* 8.5 (2009), pp. 398–404.

[127] JL MacManus-Driscoll et al. "Strongly enhanced current densities in superconducting coated conductors of $YBa_2Cu_3O_{7-x}$+ $BaZrO_3$". In: *Nature materials* 3.7 (2004), p. 439.

[128] W Prusseit et al. "Commercial coated conductor fabrication based on inclined substrate deposition". In: *IEEE transactions on applied superconductivity* 15.2 (2005), pp. 2608–2610.

[129] M Dürrschnabel et al. "Microstructure of monolithic $DyBa_2Cu_3O_{7-x}$ coated conductor thick films". In: *Physics Procedia* 36 (2012), pp. 1649–1654.

[130] V Selvamanickam et al. "MOCVD-based YBCO-coated conductors". In: *MRS bulletin* 29.8 (2004), pp. 579–582.

[131] JL MacManus-Driscoll et al. "Strong pinning in very fast grown reactive co-evaporated $GdBa_2Cu_3O_7$ coated conductors". In: *APL Materials* 2.8 (2014), p. 086103.

[132] A Sundaram et al. "2G HTS wires made on 30 μm thick Hastelloy substrate". In: *Superconductor Science and Technology* 29.10 (2016), p. 104007.

[133] T Ito, K Takenaka, and Shin-ichi Uchida. "Systematic deviation from T-linear behavior in the in-plane resistivity of $YBa_2Cu_3O_{7-y}$: Evidence for dominant spin scattering". In: *Physical review letters* 70.25 (1993), p. 3995.

[134] M Gurvitch and AT Fiory. "Resistivity of $La_{1.825}Sr_{0.175}CuO_4$ and $YBa_2Cu_3O_7$ to 1100 K: absence of saturation and its implications". In: *Physical review letters* 59.12 (1987), p. 1337.

[135] A Frolova et al. "Analysis of transport properties of MOD YBCO films with $BaZrO_3$ as artificial vortex pinning centers". In: *IEEE Transactions on Applied Superconductivity* 26.3 (2016), pp. 1–5.

[136] Nigel E Hussey. "Phenomenology of the normal state in-plane transport properties of high-T_c cuprates". In: *Journal of Physics: Condensed Matter* 20.12 (2008), p. 123201.

[137]   SL Drechsler and T Mishonov. "High-T_c superconductors and related materials". In: *Kluwer Academic Publishers* (2001).

[138]   JG Lin et al. "Origin of the R-ion effect on T_c in RBa$_2$Cu$_3$O$_7$". In: *Physical Review B* 51.18 (1995), p. 12900.

[139]   KA Müller, M Takashige, and JG Bednorz. "Flux trapping and superconductive glass state in La$_2$CuO$_{4-y}$:Ba". In: *Physical review letters* 58.11 (1987), p. 1143.

[140]   Yu Yeshurun and AP Malozemoff. "Giant flux creep and irreversibility in an Y-Ba-Cu-O crystal: an alternative to the superconducting-glass model". In: *Physical review letters* 60.21 (1988), p. 2202.

[141]   Yoichi Ando et al. "Resistive upper critical fields and irreversibility lines of optimally doped high-T c cuprates". In: *Physical Review B* 60.17 (1999), p. 12475.

[142]   BJ Ramshaw et al. "Vortex lattice melting and H_{c2} in underdoped YBa$_2$Cu$_3$O$_y$". In: *Physical Review B* 86.17 (2012), p. 174501.

[143]   Anna Llordes et al. "Nanoscale strain-induced pair suppression as a vortex-pinning mechanism in high-temperature superconductors". In: *Nature materials* 11.4 (2012), pp. 329–336.

[144]   WK Kwok et al. "Vortex lattice melting in untwinned and twinned single crystals of YBa$_2$Cu$_3$O$_{7-\delta}$". In: *Physical review letters* 69.23 (1992), p. 3370.

[145]   TK Worthington et al. "Observation of separate vortex-melting and vortex-glass transitions in defect-enhanced YBa$_2$Cu$_3$O$_7$ single crystals". In: *Physical Review B* 46.18 (1992), p. 11854.

[146]   Lifang Hou et al. "Dependence of the vortex-solid phase transition of YBa$_2$Cu$_3$O$_{7-\delta t}$ thin films on anisotropy: Evidence for a universal phase boundary". In: *Physical Review B* 55.17 (1997), p. 11806.

[147]   L Krusin-Elbaum et al. "Sudden irreversibility collapse in YBaCuO crystals: Possible evidence for thermal softening of the core pinning". In: *Physical review letters* 67.22 (1991), p. 3156.

[148]   CC Almasan et al. "Evidence for scaling invariance and universality of the irreversibility line of high temperature superconductors". In: *Physical review letters* 69.26 (1992), p. 3812.

[149]   Yukiko Yasukawa et al. "Consequence of isovalent rare earth substitution to magnetic irreversibility in cation-stoichiometric CuBa$_2$RECu$_2$O$_{6.93\pm0.01}$". In: *Applied Physics Letters* 78.19 (2001), pp. 2917–2919.

[150]   Alvaro Sanchez et al. "Self-fields in thin superconducting tapes: Implications for the thickness effect in coated conductors". In: *Applied Physics Letters* 96.7 (2010), p. 072510.

[151]   Evgeny F Talantsev and Jeffery L Tallon. "Universal self-field critical current for thin-film superconductors". In: *Nature communications* 6.1 (2015), pp. 1–8.

[152]   David R Nelson and VM Vinokur. "Boson localization and correlated pinning of superconducting vortex arrays". In: *Physical Review B* 48.17 (1993), p. 13060.

[153]   L Krusin-Elbaum et al. "Accommodation of vortices to columnar defects: Evidence for large entropic reduction of vortex localization". In: *Physical Review B* 53.17 (1996), p. 11744.

[154]   B Dam et al. "Origin of high critical currents in YBa$_2$Cu$_3$O$_{7-\delta}$ superconducting thin films". In: *Nature* 399.6735 (1999), pp. 439–442.

[155]   CJ Van der Beek et al. "Strong pinning in high-temperature superconducting films". In: *Physical Review B* 66.2 (2002), p. 024523.

[156]   Anota O Ijaduola et al. "Critical currents of ex situ YBa$_2$Cu$_3$O$_{7-\delta}$ thin films on rolling assisted biaxially textured substrates: Thickness, field, and temperature dependencies". In: *Physical Review B* 73.13 (2006), p. 134502.

[157] Wai-Kwong Kwok et al. "Vortices in high-performance high-temperature superconductors". In: *Reports on Progress in Physics* 79.11 (2016), p. 116501.

[158] M Miura et al. "Mixed pinning landscape in nanoparticle-introduced $YGdBa_2Cu_3O_y$ films grown by metal organic deposition". In: *Physical Review B* 83.18 (2011), p. 184519.

[159] FC Klaassen et al. "Vortex pinning by natural linear defects in thin films of $YBa_2Cu_3O_{7-\delta}$". In: *Physical Review B* 64.18 (2001), p. 184523.

[160] Elena Bartolomé et al. "Vortex pinning properties at dc and microwave frequencies of YBa2Cu3O7-x films with nanorods and nanoparticles". In: *Superconductor Science and Technology* 33.7 (2020), p. 074006.

[161] Tolga Aytug et al. "Analysis of flux pinning in $YBa_2Cu_3O_{7-\delta}$ films by nanoparticle-modified substrate surfaces". In: *Physical Review B* 74.18 (2006), p. 184505.

[162] NM Strickland et al. "Effective low-temperature flux pinning by Au ion irradiation in HTS coated conductors". In: *IEEE Transactions on Applied Superconductivity* 25.3 (2014), pp. 1–5.

[163] SI Kim et al. "Mechanisms of weak thickness dependence of the critical current density in strong-pinning ex situ metal–organic-deposition-route $YBa_2Cu_3O_{7-x}$ coated conductors". In: *Superconductor Science and Technology* 19.9 (2006), p. 968.

[164] Gianni Blatter et al. "Vortices in high-temperature superconductors". In: *Reviews of modern physics* 66.4 (1994), p. 1125.

[165] T Puig et al. "Vortex pinning in chemical solution nanostructured YBCO films". In: *Superconductor Science and Technology* 21.3 (2008), p. 034008.

[166] JPF Feighan, A Kursumovic, and JL MacManus-Driscoll. "Materials design for artificial pinning centres in superconductor PLD coated conductors". In: *Superconductor Science and Technology* 30.12 (2017), p. 123001.

[167] X Qi and JL MacManus-Driscoll. "Liquid phase epitaxy processing for high temperature superconductor tapes". In: *Current Opinion in Solid State and Materials Science* 5.4 (2001), pp. 291–300.

[168] Michael Benedikt et al. "FCC-hh: The Hadron Collider: future circular collider conceptual design report volume 3". In: *Eur. Phys. J. Spec. Top.* 228.CERN-ACC-2018-0058 (2018), pp. 755–1107.

[169] Theva Dünnschichttechnik GmbH. *Theva Homepage*. 2021. URL: https://www.theva.com/products/ (visited on 01/29/2021).

[170] Nicola Pompeo et al. "Vortex pinning and flux flow microwave studies of coated conductors". In: *IEEE Transactions on Applied Superconductivity* (2019).

[171] E. Silva, M. Lanucara, and R. Marcon. "The effective surface resistance of superconductor/dielectric/metal structures". In: *Superconductor Science and Technology* 9.11 (1996), pp. 934–941. ISSN: 09532048. DOI: 10.1088/0953-2048/9/11/003.

[172] BI Ivlev and NB Kopnin. "Flux flow in layered high-T_c superconductors". In: *Physical Review B* 42.16 (1990), p. 10052.

[173] BI Ivlev and NB Kopnin. "Flux-flow conductivity in anisotropic and layered high-T_c superconductors". In: *EPL (Europhysics Letters)* 15.3 (1991), p. 349.

[174] RM Langan et al. "Scaling behaviour of magneto-resistance in clean $YBa_2Cu_3O_{7-\delta}$ single crystals in the vortex liquid state". In: *Physica C: Superconductivity* 313.3-4 (1999), pp. 294–304.

[175] U Welp et al. "Magnetic measurements of the upper critical field of $YBa_2Cu_3O_{7-\delta}$ single crystals". In: *Physical review letters* 62.16 (1989), p. 1908.

[176]   T Sekitani et al. "Upper critical field for optimally-doped YBa$_2$Cu$_3$O$_{7-\delta}$". In: *Physica B: Condensed Matter* 346 (2004), pp. 319–324.

[177]   Alekse Alekseevich Abrikosov. *Fundamentals of the Theory of Metals*. Courier Dover Publications, 2017.

[178]   Yoshishige Tsuchiya et al. "Electronic state of vortices in YBa$_2$Cu$_3$O$_y$ investigated by complex surface impedance measurements". In: *Physical Review B* 63.18 (2001), p. 184517.

[179]   Dong Ho Wu, JC Booth, and Steven M Anlage. "Frequency and Field Variation of Vortex Dynamics in YBa$_2$Cu$_3$O$_{7-\delta}$". In: *Physical review letters* 75.3 (1995), p. 525.

[180]   Yoshishige Tsuchiya et al. "Estimation of vortex viscosity from the complex surface impedance measurement in the mixed state of YBa$_2$Cu$_3$O$_y$". In: *Physica C: Superconductivity and its Applications* 362.1-4 (2001), pp. 273–276. ISSN: 09214534. DOI: 10.1016/S0921-4534(01)00686-4. arXiv: 0102021 [cond-mat].

[181]   N Klein et al. "Microwave surface resistance of epitaxial YBa$_2$Cu$_3$O$_7$ thin films at 18.7 GHz measured by a dielectric resonator technique". In: *Journal of superconductivity* 5.2 (1992), pp. 195–201.

[182]   Francis C Moon. *Magneto-solid mechanics*. Wiley-Interscience, 1984.

[183]   FC Moon, MM Yanoviak, and R Ware. "Hysteretic levitation forces in superconducting ceramics". In: *Applied Physics Letters* 52.18 (1988), pp. 1534–1536.

[184]   Anjali B Riise, Tom H Johansen, and Harald Bratsberg. "The vertical magnetic force and stiffness between a cylindrical magnet and a high-T_c superconductor". In: *Physica C: Superconductivity* 234.1-2 (1994), pp. 108–114.

[185]   Anjali Bhatnagar Riise. *Levitation force and magnetization in bulk and thin film high T c superconductors*. Tech. rep. Oslo Univ., 1998.

[186]   P Schönhuber and FC Moon. "Levitation forces, stiffness and force-creep in YBCO high-T_c superconducting thin films". In: *Applied superconductivity* 2.7-8 (1994), pp. 523–534.

[187]   E Hagen and H Rubens. "Über Beziehungen des Reflexions-und Emissionsvermögens der Metalle zu ihrem elektrischen Leitvermögen". In: *Annalen der Physik* 316.8 (1903), pp. 873–901.

[188]   N Pompeo and E Silva. "Reliable determination of vortex parameters from measurements of the microwave complex resistivity". In: *Physical Review B* 78.9 (2008), p. 094503.

[189]   Andrea Alimenti et al. "Microwave measurements of the high magnetic field vortex motion pinning parameters in Nb$_3$Sn". In: *Superconductor Science and Technology* 34.1 (2020), p. 014003.

[190]   BH Stafford et al. "Tilted BaHfO$_3$ nanorod artificial pinning centres in REBCO films on inclined substrate deposited-MgO coated conductor templates". In: *Superconductor Science and Technology* 30.5 (2017), p. 055002.

[191]   J Töpfer and JB Goodenough. "LaMnO$_{3+\delta}$ Revisited". In: *Journal of Solid State Chemistry* 130.1 (1997), pp. 117–128.

[192]   Andrea Alimenti et al. "Microwave Surface Impedance Measurements in Nanostructured YBCO up to High Magnetic Fields". ASC 2020. 2020.

[193]   Beth Parks et al. "Phase-sensitive measurements of vortex dynamics in the terahertz domain". In: *Physical review letters* 74.16 (1995), p. 3265.

[194]   M Golosovsky et al. "Vortex depinning frequency in YBa$_2$Cu$_3$O$_{7-x}$ superconducting thin films: anisotropy and temperature dependence". In: *Physical Review B* 50.1 (1994), p. 470.

[195]   AE Koshelev and VM Vinokur. "Frequency response of pinned vortex lattice". In: *Physica C: Superconductivity* 173.5-6 (1991), pp. 465–475.

[196] Patrick Krkotić, Uwe Niedermayer, and Oliver Boine-Frankenheim. "High-temperature superconductor coating for coupling impedance reduction in the FCC-hh beam screen". In: *Nuclear Instruments and Methods in Physics Research Section A: Accelerators, Spectrometers, Detectors and Associated Equipment* 895 (2018), pp. 56–61.

[197] R.E. Collin. *Foundations for Microwave Engineering*. IEEE Press Series on Electromagnetic Wave Theory. Wiley, 2001. ISBN: 9780780360310. URL: https://books.google.es/books?id=2SxoQgAACAAJ.

[198] J Halbritter. *On RF residual losses in superconducting cavities*. 1984.

[199] JR Powell et al. "Field, temperature, and frequency dependence of the surface impedance of Y-Ba$_2$-Cu$_3$-O$_7$ thin films". In: *Physical Review B* 57.9 (1998), p. 5474.

[200] Hasan Padamsee. "The science and technology of superconducting cavities for accelerators". In: *Superconductor science and technology* 14.4 (2001), R28.

[201] D Alesini et al. "Galactic axions search with a superconducting resonant cavity". In: *Physical Review D* 99.10 (2019), p. 101101.

[202] TM Shokair et al. "Future directions in the microwave cavity search for dark matter axions". In: *International Journal of Modern Physics A* 29.19 (2014), p. 1443004.

[203] *HTS coated conductors for FCC beam screen: HTSCC-Beam Screen Proposal*. 2017. URL: https://indico.cern.ch/event/619380/contributions/2527436/attachments/1437344/2210760/HTS_CC_FCC_Z_MiniWorkshop_March2017.pdf.

[204] Danho Ahn et al. "First prototype of a biaxially textured YBa$_2$Cu$_3$O$_{7-x}$ microwave cavity in a high magnetic field for dark matter axion search". In: *arXiv preprint arXiv:2103.14515* (2021).

[205] SUMAN group collaboration. "Novel high-temperature superconducting coatings for large scale microwave applications". To be submitted. 2022.

[206] Shinjiro Yazaki et al. "Critical current degradation in high-temperature superconducting tapes caused by temperature rise". In: *IEEE transactions on applied superconductivity* 23.3 (2013), pp. 4602304–4602304.

[207] Kohei Higashikawa et al. "Lateral distribution of critical current density in coated conductors slit by different cutting methods". In: *IEEE transactions on applied superconductivity* 23.3 (2013), pp. 6602704–6602704.

[208] Juan Manuel O'Callaghan Castella. "Private conversation". 2019.

[209] Woo II Yang et al. "Depth profiling of the microwave surface resistance of high-J_c GdBa$_2$Cu$_3$O$_{7\delta}$ coated conductors grown using the RCE-DR process". In: *Superconductor Science and Technology* 29.10 (2016), p. 105004.

[210] A Álvarez Melcón et al. "Scalable haloscopes for axion dark matter detection in the 30 μ eV range with RADES". In: *Journal of High Energy Physics* 2020.7 (2020), pp. 1–28.

[211] Steven Weinberg. "A new light boson?" In: *Physical Review Letters* 40.4 (1978), p. 223.

[212] Roberto D Peccei and Helen R Quinn. "Constraints imposed by CP conservation in the presence of pseudoparticles". In: *Physical Review D* 16.6 (1977), p. 1791.

[213] Pierre Sikivie. "Experimental tests of the" invisible" axion". In: *Physical Review Letters* 51.16 (1983), p. 1415.

[214] Sergio Calatroni. "Goal of the meeting and presentation of the agenda". Close-up / kick-off meeting for the study of HTS-coated beam screens for the FCC-hh. 2020. URL: https://indico.cern.ch/event/857548/timetable/#20200116.detailed.

[215] J Golm et al. "Thin Film (High Temperature) Superconducting Radiofrequency Cavities for the search of axion dark matter". In: *arXiv preprint arXiv:2110.01296* (2021).

[216] S. Patsch et al. "Computation of the Magnetization of Type II Superconductors for Potential Beam Screen Coatings of the Future Circular Collider". In: *IEEE Transactions on Applied Superconductivity* 29.6 (2019), pp. 1–10. DOI: 10.1109/TASC.2019.2899767.

[217] Guilherme Telles et al. "Field quality and surface resistance studies of a superconducting REBCO - Cu hybrid coating for the FCC beam screen". To be submitted. 2022.

[218] Gianluigi Arduini et al. *Electron Cloud Effects in the CERN SPS and LHC*. Tech. rep. 2000.

[219] Coleman B Cobb et al. "Hysteretic loss reduction in striated YBCO". In: *Physica C: Superconductivity* 382.1 (2002), pp. 52–56.

[220] Stephan Russenschuck. "ROXIE: Routine for the optimization of magnet X-sections, inverse field calculation and coil end design. Proceedings". In: (1999).

[221] Francesco Grilli and Anna Kario. "How filaments can reduce AC losses in HTS coated conductors: a review". In: *Superconductor Science and Technology* 29.8 (2016), p. 083002.

[222] Samuel P Morgan Jr. "Effect of surface roughness on eddy current losses at microwave frequencies". In: *Journal of applied physics* 20.4 (1949), pp. 352–362.

[223] Sergio Calatroni et al. "Cryogenic surface resistance of copper: Investigation of the impact of surface treatments for secondary electron yield reduction". In: *Physical Review Accelerators and Beams* 22.6 (2019), p. 063101.

[224] Nadezda Bagrets et al. "Investigation of ReBCO conductor tape joints for superconducting applications". In: *IEEE Transactions on Applied Superconductivity* 25.3 (2014), pp. 1–5.

[225] P Chiggiato and P Costa Pinto. "Ti–Zr–V non-evaporable getter films: From development to large scale production for the Large Hadron Collider". In: *Thin Solid Films* 515.2 (2006), pp. 382–388.

[226] C Yin Vallgren et al. "Amorphous carbon coatings for the mitigation of electron cloud in the CERN Super Proton Synchrotron". In: *Physical Review Special Topics-Accelerators and Beams* 14.7 (2011), p. 071001.

[227] Iouri Bojko, Noël Hilleret, and Christian Scheuerlein. "Influence of air exposures and thermal treatments on the secondary electron yield of copper". In: *Journal of Vacuum Science & Technology A: Vacuum, Surfaces, and Films* 18.3 (2000), pp. 972–979.

[228] P Costa Pinto et al. "Carbon coatings with low secondary electron yield". In: *Vacuum* 98 (2013), pp. 29–36.

[229] Patxi Duthil. "Material properties at low temperature". In: *arXiv preprint arXiv:1501.07100* (2015).

[230] Raymond A Serway and Chris Vuille. *College physics*. Cengage Learning, 2014.

[231] A Hofmann. "CHARACTERISTICS OF SYNCHROTRON RADIATION". In: *CERN ACCELERATOR SCHOOL SYNCHROTRON RADIATION AND FREE ELECTRON LASERS*, pp. 1–30.

[232] Do H Tomboulian and PL Hartman. "Spectral and angular distribution of ultraviolet radiation from the 300-Mev Cornell synchrotron". In: *Physical Review* 102.6 (1956), p. 1423.

[233] Patrick Krkotić et al. "HTS REBaCuO coated conductors for the FCC-hh beam screen: Performance under photon irradiation at the ALBA Light Source". FCC week 2019 in Brussels. 2019. URL: https://indico.cern.ch/event/727555/contributions/3430768/attachments/1875329/3088389/POSTER_FCC19-SR_Irradiation_V7.pdf.

[234]   Patrick Krkotić et al. "Highlights of ALBA and UPC's Activities and Results". Project Meeting 16/01/20 at CERN. 2020.